

222 P.

{NASA-CR-177229) THE TELECOMMUNICATIONS AND
DATA ACQUISITION REPORT Progress Report,
Jan. - Mar. 1986 (Jet Propulsion Lab.)
222 p HC A10/MF A01 CACL 17B

N86-28275
THRU
N86-28294
Unclas
G3/32 43373

The Telecommunications and Data Acquisition Progress Report 42-85

January-March 1986

E. C. Posner
Editor

May 15, 1986



National Aeronautics and
Space Administration

Jet Propulsion Laboratory
California Institute of Technology
Pasadena, California

The Telecommunications and Data Acquisition Progress Report 42-85

January–March 1986

E. C. Posner
Editor

May 15, 1986

NASA

National Aeronautics and
Space Administration

Jet Propulsion Laboratory
California Institute of Technology
Pasadena, California

The research described in this publication was carried out by the Jet Propulsion Laboratory, California Institute of Technology, under a contract with the National Aeronautics and Space Administration.

Reference herein to any specific commercial product, process, or service by trade name, trademark, manufacturer, or otherwise, does not constitute or imply its endorsement by the United States Government or the Jet Propulsion Laboratory, California Institute of Technology.

Preface

This quarterly publication provides archival reports on developments in programs managed by JPL's Office of Telecommunications and Data Acquisition (TDA). In space communications, radio navigation, radio science, and ground-based radio astronomy, it reports on activities of the Deep Space Network (DSN) and its associated Ground Communications Facility (GCF) in planning, in supporting research and technology, in implementation, and in operations. Also included is TDA-funded activity at JPL on data and information systems and reimbursable DSN work performed for other space agencies through NASA. The preceding work is all performed for NASA's Office of Space Tracking and Data Systems (OSTDS).

In geodynamics, the publication reports on the application of radio interferometry at microwave frequencies for geodynamic measurements. In the search for extraterrestrial intelligence (SETI), it reports on implementation and operations for searching the microwave spectrum. The latter two programs are performed for NASA's Office of Space Science and Applications (OSSA).

Finally, tasks funded under the JPL Director's Discretionary Fund and the Caltech President's Fund which involve the TDA Office are included.

This and each succeeding issue of the TDA Progress Report will present material in some, but not necessarily all, of the following categories:

OSTDS Tasks:

- DSN Advanced Systems
 - Tracking and Ground-Based Navigation
 - Communications, Spacecraft-Ground
 - Station Control and System Technology
 - Network Data Processing and Productivity
- DSN Systems Implementation
 - Capabilities for New Projects
 - Networks Consolidation Program
 - New Initiatives
 - Network Sustaining
- DSN Operations
 - Network Operations and Operations Support
 - Mission Interface and Support
 - TDA Program Management and Analysis
- GCF Implementation and Operations
- Data and Information Systems

OSSA Tasks:

- Search for Extraterrestrial Intelligence
- Geodynamics
 - Geodetic Instrument Development
 - Geodynamic Science

Discretionary Funded Tasks

Contents

OSTDS TASKS DSN Advanced Systems TRACKING AND GROUND-BASED NAVIGATION

Total Ionospheric Electron Content Calibration Using SERIES GPS Satellite Data	1
G. Lanyi NASA Code 310-10-60-07-00	

COMMUNICATIONS, SPACECRAFT-GROUND

Planets as Background Noise Sources in Free Space Optical Communications	13
J. Katz NASA Code 310-20-67-59-00	
A Simple Method for Designing or Analyzing an Optical Communication Link	25
J. R. Lesh, W. K. Marshall, and J. Katz NASA Code 310-20-67-59-00	
Maximum Likelihood Estimation of Signal-to-Noise Ratio and Combiner Weight	32
S. Kalsou and S. J. Dolinar NASA Code 310-30-71-83-04	
A VLSI Pipeline Design of a Fast Prime Factor DFT on a Finite Field	42
T. K. Truong, I. S. Hsu, H. M. Shao, I. S. Reed, and H. C. Shyu NASA Code 310-30-70-84-08	

STATION CONTROL AND SYSTEM TECHNOLOGY

Fast Frequency Acquisition via Adaptive Least Squares Algorithm	53
R. Kumar NASA Code 310-30-70-84-02	
A Systolic Architecture for the Correlation and Accumulation of Digital Sequences	62
L. J. Deutsch and C. R. Lahmeyer NASA Code 310-30-70-87-02	

DSN Systems Implementation CAPABILITIES FOR NEW PROJECTS

VLBI Observations for 416 Extragalactic Radio Sources	69
D. D. Morabito, A. E. Niell, R. A. Preston, R. P. Linfield, A. E. Wehrle, and J. Faulkner NASA Code 314-30-51-38-45	
Parkes-CDSCC Telemetry Array: Equipment Design	85
D. W. Brown, H. W. Cooper, J. W. Armstrong, and S. S. Kent NASA Code 314-30-56-56-05	
DSA's Subcarrier Demodulation Losses	111
M. Simon and A. Mileant NASA Code 314-40-56-09-02	

SNR Estimation for the Baseband Assembly	118
M. K. Simon and A. Mileant	
NASA Code 314-40-56-09-02	

The New 34-Meter Antenna	127
M. F. Pompa	
NASA Code 314-40-41-81-15	

NETWORK SUSTAINING

The Deep Space Network Tracking System, Mark IV-A, 1986	139
J. A. Wackley	
NASA Code 314-40-41-81-12	

Mark IVA DSN Receiver-Exciter and Transmitter Subsystems	147
M. R. Wick	
NASA Code 314-40-41-81-13	

HVAC Modifications and Computerized Energy Analysis for the Operations Support Building at the Mars Deep Space Station at Goldstone	157
A. Halperin and P. Stelzmuller	
NASA Code 314-40-44-14-19	

Reverse Osmosis Water Purification System	181
H. G. Ahlstrom, P. S. Hames, and F. J. Menninger	
NASA Code 828-62-00-71-73	

DSN Operations

MISSION INTERFACE AND SUPPORT

The Venus Balloon Project	191
C. T. Stelzried, R. A. Preston, C. E. Hildebrand, J. H. Wilcher, and J. Ellis	
NASA Code 314-40-22-39-05	

The Venus Balloon Project Telemetry Processing	199
J. M. Urech, A. Chamarro, J. L. Morales, and M. A. Urech	
NASA Code 314-40-41-81-12	

OSSA TASKS

Geodynamics

GEODETIC INSTRUMENT DEVELOPMENT

The March 1985 Demonstration of the Fiducial Network Concept for GPS Geodesy: A Preliminary Report	212
J. M. Davidson, C. L. Thornton, T. H. Dixon, C. J. Vegos, L. E. Young, and T. P. Yunck	
NASA Code 676-20-20-10-20	

13145

Total Ionospheric Electron Content Calibration Using SERIES GPS Satellite Data

G. Lanyi

Tracking System and Applications Section

This article describes the current status of the Deep Space Network advanced systems research into ionospheric calibration techniques, based on Global Positioning System (GPS) data. A GPS-based calibration system is planned to replace the currently used Faraday rotation method by 1989. The SERIES receiver system used in this research determines the differential group delay of signals transmitted at two different carrier frequencies. This differential delay includes an ionospheric component and a GPS transmitter offset. The transmitter offsets are different for each GPS satellite. Tests have been conducted to assess the effect of the offsets on the ionospheric calibration accuracy. From the obtained data, the total electron content and GPS transmitter offsets are calculated by a least-squares estimation method employing a local model of total ionospheric electron content. The end product is an estimation of the total ionospheric content for an arbitrary line-of-sight direction. For the presented polynomial fitting technique, the systematic error due to mismodeling is estimated to be $\sim 6 \times 10^{16}$ el/m², while the formal error is $\sim 2 \times 10^{16}$ el/m². The final goal is an error of 3×10^{16} el/m² (~ 0.7 ns at 2.3 GHz).

I. Introduction

Electromagnetic waves traversing the Earth's ionosphere are delayed due to refractive properties of the ionosphere. For precise deep-space navigation, the calibration of the ionospheric delay is a required procedure. Also, certain radio-science experiments on space missions rely on precise calibration of the terrestrial total ionospheric electron content.

The Deep Space Network (DSN) monitors the ionospheric total electron content (TEC) by a Faraday rotation technique utilizing polarization of radio signals transmitted by quasi-geostationary satellites (Ref. 1). The Faraday receivers are in

the proximity of the DSN antennas. The line-of-sight TEC in the direction of a space probe to be calibrated is estimated from Faraday measurements by the program DIEN/TIEN described in Ref. 2. In the present DSN configuration, this algorithm estimates with an error of $\sim 10\%$, in the worst case, resulting in an error of 30×10^{16} el/m². Due to the declining number of Faraday satellites and increasing precision requirements for ionospheric calibration, the DSN plans to implement a Global Positioning Satellite (GPS)-based ionospheric calibration system (Ref. 3). The planned receiver network will also perform precise clock synchronization between the DSN stations. The following is a description of the GPS-based ionospheric calibration technique under consideration.

Presently, ionospheric delay data are obtained by the proof-of-concept SERIES and SERIES-X receivers developed by the Jet Propulsion Laboratory (Refs. 4, 5, and 6).¹ Here we report results obtained from SERIES data only, and SERIES-X data will be analyzed in the future. The ionospheric delays are obtained by measuring the differential arrival times of the P-code signals at L1 and L2 frequencies (Fig. 1). With the current GPS configuration, the SERIES receiver scans 5 satellites in a sequential manner, obtaining one 2-s observation per minute, for a total of ~ 300 observations in a 5-h observing session. The GPS observations cover only certain regions of the sky and the line of sight of a space probe to be calibrated might not overlap with the GPS observations. Therefore, in order to be able to estimate the total electron content at an arbitrary line-of-sight direction from the SERIES data, specific assumptions have to be made about the behavior of the ionosphere. We assume that the electron content is time independent for the duration of the observation session in a geocentric solar reference frame oriented along the Earth-Sun axis. This is to say that the electron distribution produced by ionization due to solar radiation (Ref. 7) is assumed to be in equilibrium and we deal with only the static part of electron density redistributed by the Earth's magnetic field. We then approximate the electron content by a second-order polynomial in the Earth-centered solar spherical coordinates for a given observation session. In other words, the functional form of the total ionospheric content is assumed to be a static paraboloid in coordinates of geocentric solar latitude and longitude where the origin of the coordinate system corresponds approximately to the middle of the observing session. The ionospheric region corresponding to an observing session spans ~ 15 deg in latitude and ~ 90 deg in longitude. The electron content parameters and GPS satellite offsets (see the description of transmitter errors in Appendix A) are determined by least-squares estimation. The separation of GPS transmitter offsets from effects due to ionosphere is facilitated by the dependence of ionospheric path delay on the elevation angle of observations.

The electron content, however, is only approximately time-independent in the chosen geocentric solar reference frame. Time-dependent effects are not modeled at present, though semiempirical estimation of some of these effects may be possible. In order to avoid possible confusion, we should note here that the typical diurnal variation observed in the terrestrial reference frame (Fig. 2) is due primarily to the fact that the observer looks at different points on the static ionospheric shell as the Earth rotates. On the other hand, the

time-variation effect in the solar reference frame is a correction to the static approximation of the ionosphere.

Ionospheric fluctuations due to inhomogeneities result in high-frequency temporal and spatial variations and the modeling of this effect could prove to be formidable. Consequently, with the current technique, the formal error of ionospheric estimation is always larger than the root-mean-square (rms) scatter of ionospheric fluctuations, unless the angular separation between the direction of prediction and observation is very small.

In order to demonstrate the capabilities of the static-model calibration algorithm, we display the errors due to all sources in a bar chart in Fig. 3. The first bar on the left represents the effect of uncertainties in the estimation of GPS transmitter offsets, and the next bar is primarily the sum of receiver calibration error and multipath effects. The third bar estimates the effect of ionospheric fluctuations and the following bar represents the ionospheric mapping errors. The last bar gives a summary of the line-of-sight ionospheric calibration error.

The experimental formal error of 1.5×10^{16} el/m² corresponds approximately to the rss of the transmitter and receiver errors and inhomogeneities; the modeling error is largely systematic in nature. The presented error budget assumes properly calibrated receivers and the GPS transmitter offset estimation. A more detailed description of these error sources is given in Appendix A.

In the following sections we will give a brief description of the estimation technique and experimental results. Section II will discuss the modeling and estimation techniques, and in Section III the results of this estimation will be presented. In Section IV, in addition to the summary of results, the possible improvements and additions will be discussed.

Finally, we should point out that while we are estimating total electron content, the instrument measures the difference in P-code group delays of transmission at L1 = 1.57542 GHz and L2 = 1.2276 GHz frequencies. Both of these quantities, TEC and differential delays, will be referenced in the text and figures. The physically measured delay will be in the units of nanoseconds (ns) and the TEC will have the units of electrons/meter² (el/m²). The conversion between these units is $1 \text{ ns} = 2.8 \times 10^{16} \text{ el/m}^2$.

II. Modeling and Statistical Estimation

Prediction of the ionospheric electron content along an arbitrary line of sight is difficult due to the complexity of underlying physical phenomena. Therefore, most prediction

¹See also Crow, R. B., Bletzacker, F. R., Najarian, R. J., Purcell, Jr., G. H., Statman, J. I., and Thomas, J. B., *SERIES-X Final Engineering Report*, JPL D-1476 (JPL internal document), Jet Propulsion Laboratory, Pasadena, Calif., 1984.

techniques are semiempirical in nature; semiempirical ionospheric electron content parameters are determined by the use of a large number of global ionospheric sounding data supplemented by the users own data. There are such computer programs in the public domain, e.g., the Bent program (Ref. 8) and the International Reference Ionosphere program (Ref. 9). There have also been attempts to characterize the global TEC behavior by a relatively simple semiempirical function fit to the mean of global ionospheric data, such as the work of Wu.² A comparison between ionospheric delay data obtained by dual-band (2.30 and 8.42 GHz) Very Long Baseline Interferometry (VLBI) data and Faraday rotation data mapped by the Wu method was given in Ref. 10.

In the planned DSN configuration, GPS receivers would take data continuously in the proximity of each DSN antenna. From the obtained ionospheric data, which covers only certain portions of the sky, the total ionospheric electron content in the direction of a space probe is then determined. Thus for the DSN, ionospheric models need only be local in contrast to global prediction methods. When the angular separation between the observed and predicted direction is very small, (<1 deg), then no ionospheric mapping is necessary, only the GPS transmitter offsets have to be removed.

Our knowledge about the value and the stability of GPS transmitter offsets is very cursory. GPS handbooks (Ref. 11) quote only a 1- σ level of 1 to 1.5 ns for these offsets. We have some secondary information about the prelaunch values (private communication by J.A. Klobuchar, February 1985), and these values we designate as "semiofficial prelaunch" values. Due to the lack of proper information, we chose to estimate these offsets from the data itself (therefore the tasks 1, 4, and 5 described at the end of this section are not separable; they are included in a single least-squares estimation procedure).

In the following we proceed to describe the model used in our estimation procedure. We define the "ionospheric shell" as the collection of maxima of ionospheric electron density profiles over the globe; we assume this to be a sphere, and we use currently $h = 350$ km for its height above the mean sea level (Figs. 4 and 5). The longitudes and latitudes of the observation site and the ray-path intersect point on the ionospheric shell coincides only when the observation is made at zenith. Otherwise the terrestrial longitude and latitude of the intersect position, ϕ' and θ' , are given by the following geometric transformation formulas

$$\sin \theta' = \sin \theta \cos \alpha + \cos \theta \cos A \sin \alpha \quad (1)$$

$$\sin (\phi' - \phi) = \sin \alpha \sin A / \cos \theta' \quad (2)$$

where the differential angle α between the observation and intersect position is determined by

$$\cos (\alpha + E) = \cos E / (1 + (h/R)) \quad (3)$$

and where θ and ϕ are the latitude and longitude of the observation site, A and E are the azimuth and elevation angle of the line-of-sight direction, and R is the mean radius of Earth. After the transformation from unprimed to primed quantities, the longitude ϕ' is then transformed into the solar reference frame, $\phi' \rightarrow \phi_{shell}$, where the Earth-Sun axis corresponds to 0 deg longitude on the shell.

The total electron content is modeled for vertical directions on the shell, then we map the vertical to the line-of-sight total electron content by a mapping function $M(E)$. At our current accuracy requirement for the mapping function, it is sufficient to use the simple geometric slant ratio at the shell height h :

$$M(E) = [1 - (\cos E / (1 + h/R))^2]^{-1/2} \quad (4)$$

For the least-squares estimation of ionospheric content, currently we use a second-order polynomial in Sun-referenced and Earth-centered spherical coordinates. These coordinates are the above-mentioned shell latitude θ_{shell} and longitude ϕ_{shell} being offset by a reference latitude and longitude corresponding to the middle of the observing session, so that both coordinates are zero at the reference point (see Fig. 5). These coordinates are designated as $\bar{\theta}$ and $\bar{\phi}$ and through Eqs. (1) through (3) they have an implicit dependence on E and A . The delays $\tau(E)$ then are modeled by the following expression:

$$\tau_i(E) = o_i + M(E) (c_1 + c_2 \bar{\phi} + c_3 \bar{\theta} + c_4 \bar{\phi}^2 + c_5 \bar{\phi} \bar{\theta} + c_6 \bar{\theta}^2) \quad (5)$$

where o_i is the sum of the offsets of i th GPS satellite and the receiver, and the polynomial in brackets represents the total vertical electron content. A least-squares fit applied for all observations can estimate the offsets and the six polynomial coefficients, c_1 through c_6 .

Having the polynomial coefficient determined, we can now estimate TEC to an arbitrary line-of-sight direction. First, the intersect position on the ionospheric shell is determined by using Eqs. (1) through (3). Then, transforming the intersect position into $\bar{\phi}$ and $\bar{\theta}$ and substituting these values and E into Eq. (5) with zero offset values, we obtain the predicted line-of-sight content. In summary, the local model consists of the following components:

²Wu, S. C., "Ionospheric Calibration for SEASAT Altimeter," Engineering Memorandum 315-34, 1977. Jet Propulsion Laboratory, Pasadena, California (JPL internal document).

- (1) Removing of GPS transmitter offsets from the measured delays.
- (2) Determining the effective intersect position of the ray path of GPS signals with the ionospheric shell in terrestrial coordinates.
- (3) Transforming these terrestrial coordinates into the geocentric solar reference frame.
- (4) Mapping the line-of-sight delays to the local vertical at the intersect point on the shell.
- (5) Estimation of the total ionospheric vertical content over the whole sky corresponding to a reasonable observation period; it should be long enough to contain a sufficient number of observations but short enough for describing the ionospheric content by a local model. Our experience indicates that a period of 4 to 6 h is sufficient.
- (6) Determining the effective intersect position of the ray path in the predicted direction with the ionospheric shell in terrestrial coordinates.
- (7) Transforming these terrestrial coordinates of the intersect point into the geocentric solar reference frame.
- (8) Mapping the estimated ionospheric vertical content at that shell position to the line-of-sight prediction.

In the next section we will present the currently available results of the estimation technique described in this section.

III. Results

Present results are based upon the reduction of ionospheric data obtained from two SERIES experiments carried out by L.E. Young and the SERIES team. The first experiment includes 14 days of nighttime data at various California locations (with the exception of one observing session at Harvard, Texas) between 15 January and 2 February of 1984 (Ref. 12). The data were taken by two receivers simultaneously with station separations ranging from 13 to 1300 km. In these observations, the receiver calibrators were not used. The L1 and L2 P-code signals are delayed relative to each other in the SERIES receiver, resulting, in these experiments, in an uncalibrated variable receiver offset with a mean value of ~ 25 ns ($\sim 70 \times 10^{16}$ el/m²). This offset is large compared to the nighttime ionospheric content of $\sim 4 \times 10^{16}$ el/m²; thus this experiment provided a good testing ground for the offset estimation technique.

The second experiment includes 4 days of daytime data taken during 27 to 31 August 1984. One receiver was stationed at DSS 12, Goldstone, California, and the other at the National

Bureau of Standards at Boulder, Colorado. Thus the two receivers were separated by about 1000 km. Both receivers were properly calibrated.

The average postfit rms scatter of all measurements is ~ 0.5 ns (1.5×10^{16} el/m²). The average formal error for TEC is also ~ 0.5 ns, while the formal error for GPS transmitter offsets is ~ 0.2 ns. However, due to modeling errors, our current estimation algorithm can result in incorrect ionospheric content values and thus the actual error is bigger than the formal ones. Estimation of TEC of the same daytime reference region on the ionospheric shell by two receivers separated by ~ 1000 km indicates an average line-of-sight discrepancy of 2 ns. Thus, we place the magnitude of current systematic errors at the 2-ns level. This value corresponds to 6×10^{16} el/m² in TEC units.

At nighttime the mean ionospheric content is spatially nearly homogeneous and small in value; thus modeling errors are less important and the systematic ionospheric mapping errors are smaller. Consequently, the total (receiver-plus-transmitter) offsets determined at night contain also smaller systematic errors. A comparison between the SERIES nighttime and the corresponding Goldstone Faraday data (Fig. 6) exhibits an rms difference of ~ 0.5 ns (1.5×10^{16} el/m²).

Since in these data the sum of transmitter and variable receiver (of the order of 25 ns) offsets were estimated, the agreement with the Faraday measurements is a good indication of small systematic errors in the nighttime estimation. At the same time this comparison gives an indication of the absence of cycle ambiguities in the Faraday data itself. Another comparison was given earlier in Ref. 6. In that study the transmitter offsets were not estimated nor known, and the Faraday TEC data were mapped to the SERIES TEC data by the Bent algorithm, giving a typical vertical content difference of $\sim 5 \times 10^{16}$ el/m² for an assumed separation of 2 h from the closest approach at midmorning. This value is somewhat larger than our current systematic daytime error of $\sim 3 \times 10^{16}$ el/m² for the vertical electron content (6×10^{16} el/m² typical line-of-sight prediction error).

A representative result of the statistical fitting procedure is shown in Fig. 7. The symbols correspond to measured delays obtained from the P-code signals of GPS satellites identified by their Space Vehicle (SV) numbers. The solid lines are the result of the fit. In Fig. 8 the intersect trajectories of the lines of sight of observations with the ionospheric shell are shown. The numeric labels represent the elevation angle of observations.

The estimated GPS transmitter offsets are shown in Figs. 9 and 10. Figure 9 represents the nighttime solution including

the large variable receiver offsets, while Fig. 10 represents the daytime solution with a calibrated receiver. The differenced offsets between satellites do only weakly depend on the model and are independent of the receiver offsets. One can observe from these plots that differenced offsets between satellites have little scatter even when the day and nighttime observations are compared. Noting that the day and nighttime observations are 7 months apart, our preliminary conclusion is that the GPS transmitter offsets are relatively stable.

While the semiofficial prelaunch offsets agree in sign and order of magnitude with our results, the values are different as can be seen in Fig. 10. Since we do not have at present well-calibrated nighttime data available, we cannot directly compare our offset values with the semiofficial prelaunch values. As can be seen on the daytime plot, the offsets can jump from day to day, presumably due to systematic modeling errors. However, our measured differenced offsets between satellites are directly comparable to the differenced semiofficial prelaunch values between satellites and they disagree in value (see Fig. 10). If, for example, we compare the differenced offsets for the satellite pair SV 9 and SV 11, the discrepancy is almost 5 ns.

IV. Discussion

Our results imply that the GPS P-code L1-L2 transmitter offsets can be determined by a least-squares estimation technique from the SERIES ionospheric data itself. At nighttime we can determine these offsets with a formal error of 0.2 ns. We can also estimate the line-of-sight total ionospheric electron content with a systematic error of 0.7 ns (2×10^{16} el/m²) for nighttime and 2 ns (6×10^{16} el/m²) for daytime. We plan to improve at least the static part of the mapping algorithm by using a more complex functional form for the ionospheric content and include the Bent program into our software and do further comparisons. We plan to analyze SERIES-X ionospheric delay data using differenced dual-band P-code and connected carrier-phase measurements. Recent phase-connected carrier delay data obtained by R. Neilan indicate the possibility of a sizable reduction of multipath errors. Such improvement would be very important, since omnidirectional antennas are planned to be used in the GPS-based calibration network. We should also point out that by using several GPS receivers, global ionospheric total electron content prediction, by mapping techniques similar to the one presented in this article, may become possible.

Acknowledgments

The SERIES ionospheric data was provided by L. E. Young, and H. N. Royden provided the Faraday rotation data. We wish to express our appreciation to L. E. Young, D. W. Trask, H. N. Royden, and C. L. Thornton for the helpful discussions and suggestions.

References

1. Green, D. W., Lam, V. W., and Royden, H. N., "Effects of the Charged Particle Environment on Voyager Navigation at Jupiter and Saturn," *AIAA/AAS Astrodynamics Conference*, Danvers, Massachusetts, 1980.
2. Yip, K. W., Winn, F. B., Reid, M. S., and Stelzried, C. T., "Decimeter Modeling of Ionospheric Columnar Electron Content at S-band Frequencies," in Proceedings of the Symposium on the Effect of the Ionosphere on Space Systems and Communications, Naval Research Laboratory, Washington, D. C., pp. 345-352, 1975.
3. Townes, S. A., "A Study of the Charged Particle Calibration Requirements for the Deep Space Network," *TDA Progress Report 42-75*, Jet Propulsion Laboratory, Pasadena, Calif., pp. 124-131, 1983.
4. MacDoran, P. F., Spitzmesser, D. J., and Buennagel, L. A., "SERIES: Satellite Emission Range Inferred Earth Surveying," in *Proceedings of the Third International Geodetic Symposium on Satellite Positioning*, Vol. 2, pp. 1143-1164, Las Cruces, New Mexico, 1982.
5. Buennagel, L. A., MacDoran, P. F., Neilan, R. E., Spitzmesser, D. J., Young, L. E., *Satellite Emission Range Inferred Earth Survey (SERIES) Project: Final Report on Research and Development Phase, 1979 to 1983*, JPL Publication 84-16, Jet Propulsion Laboratory, Pasadena, Calif., 1984.
6. Royden, H. N., Miller, R. B., Buennagel, L. A., "Comparison of NAVSTAR Satellite L-Band Ionospheric Calibrations With Faraday Rotation Measurements," *Radio Science*, Vol. 19, pp. 798-804, 1984.
7. Chapman, S., "The Absorption and Dissociative or Ionizing Effect of Monochromatic Radiation in an Atmosphere on a Rotating Earth," *Proc. Phys. Soc. (London)*, Vol. 43, pp. 26-45, 1931.
8. Bent, R. B., Llewellyn, S. K., *Description of the 1965-71 Ionospheric Model Used in the Definitive System (DODS)*, DBA-Systems, Melbourne, Florida, 1970.
9. *International Reference Ionosphere -IRI 79*, Word Data Center A for Solar-Terrestrial Physics, Report UAG-82, Boulder, Colorado, 1981.
10. Scheid, J. A., "Comparison of the Calibration of Ionospheric Delay in VLBI Data by the Methods of Dual Frequency and Faraday Rotation," *TDA Progress Report 42-82*, Jet Propulsion Laboratory, Pasadena, Calif., pp. 11-23, 1985.
11. *Interface Control Document*, 03953, Space Division, Rockwell International Corporation, Downey, California, 1975.
12. Goad, C. C., Sims, M. L., and Young, L. E., "A Comparison of Four Precise Global Positioning System Geodetic Receivers," *IEEE Transactions on Geoscience and Remote Sensing*, Vol. GE-23, pp. 458-466, 1985.

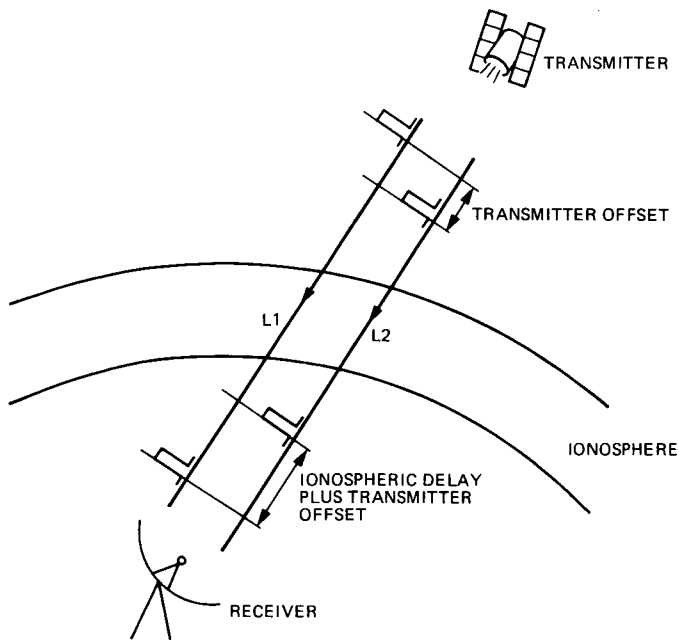


Fig. 1. Schematic view of GPS-based ionospheric calibration

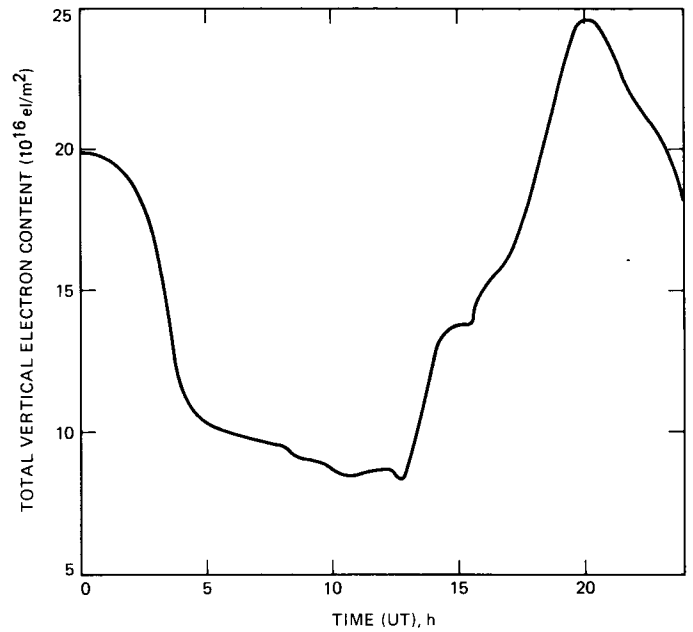


Fig. 2. Typical daily variation of the total vertical electron content measured by Faraday rotation at Goldstone, California, on 30 August 1984

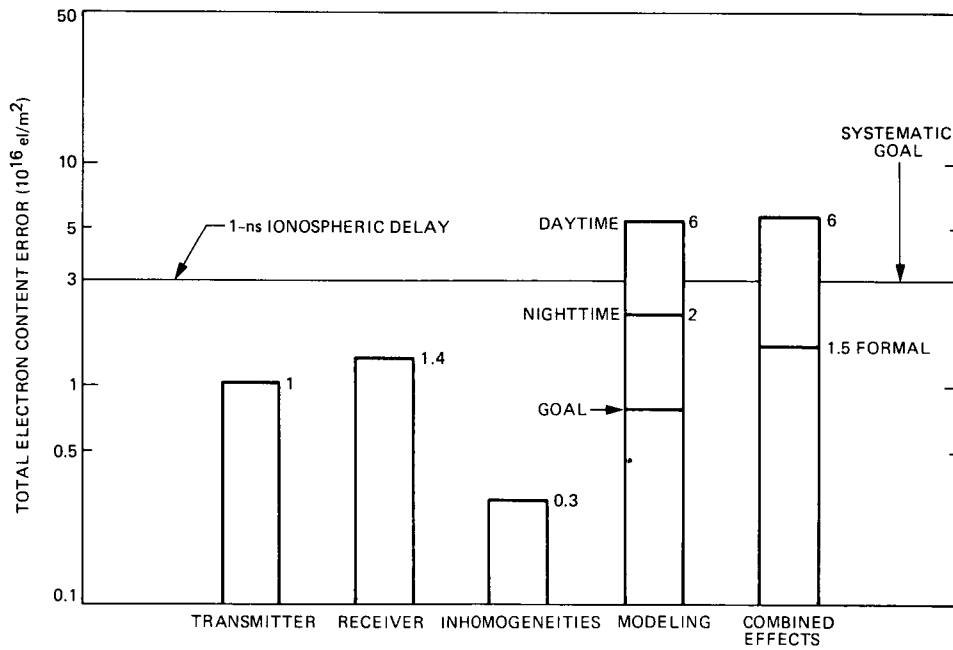


Fig. 3. Error budget of ionospheric prediction of the line-of-sight total electron content

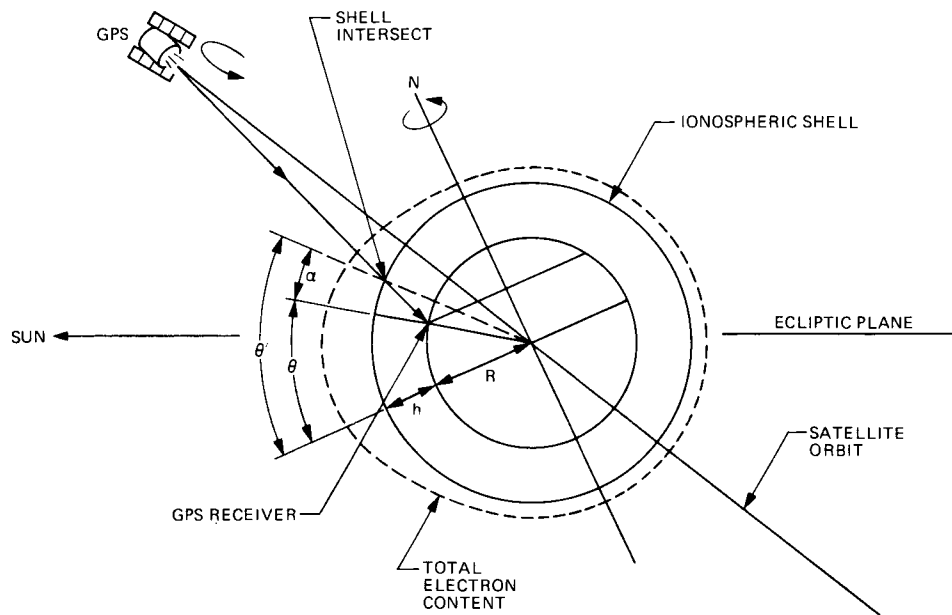


Fig. 4. Geometry of the ionospheric modeling. The height h of the "ionospheric shell" is exaggerated. The dotted curve is a schematic representation of vertical TEC values

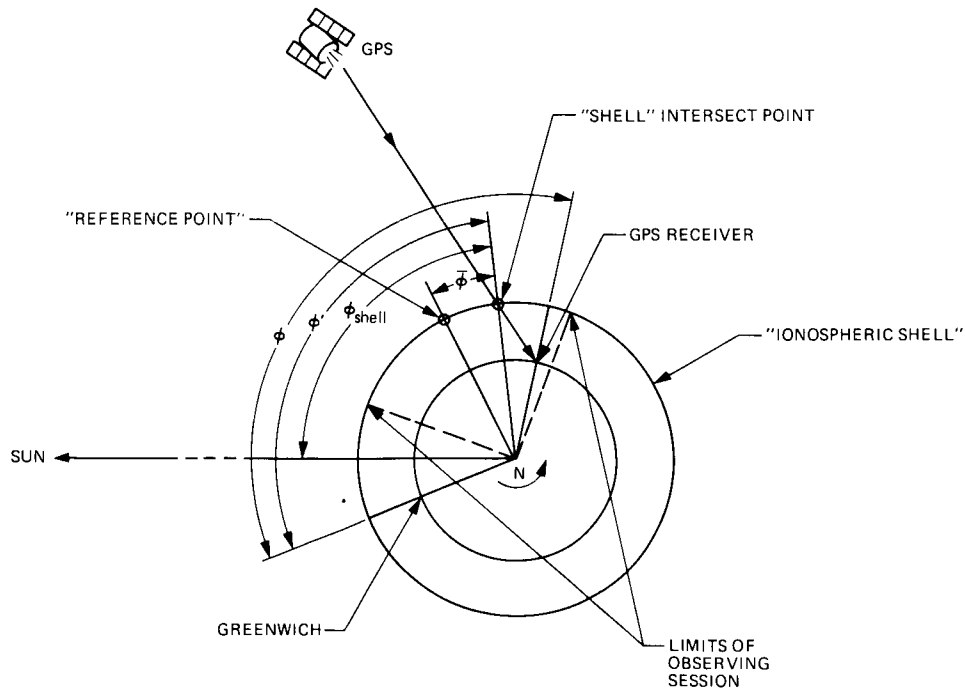


Fig. 5. Schematic view of coordinate transformations. The longitude ϕ of the observation site is transformed into the relative geocentric solar coordinate $\bar{\phi}$

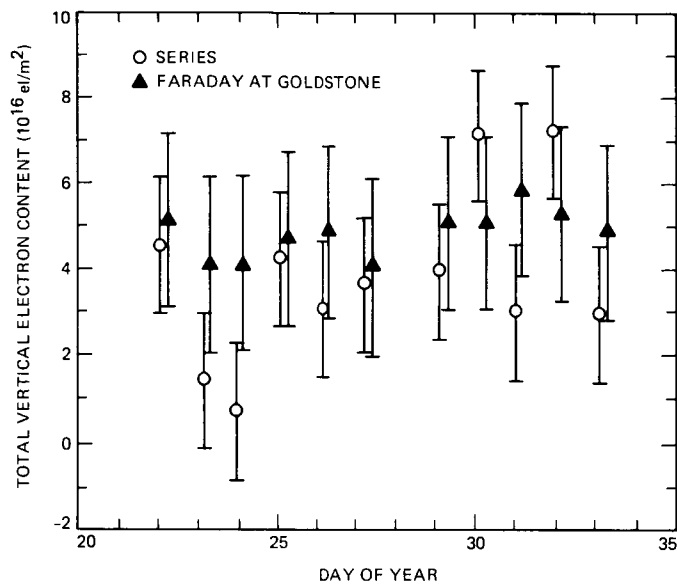


Fig. 6. Comparison of SERIES with Faraday rotation data at nights of January 1984

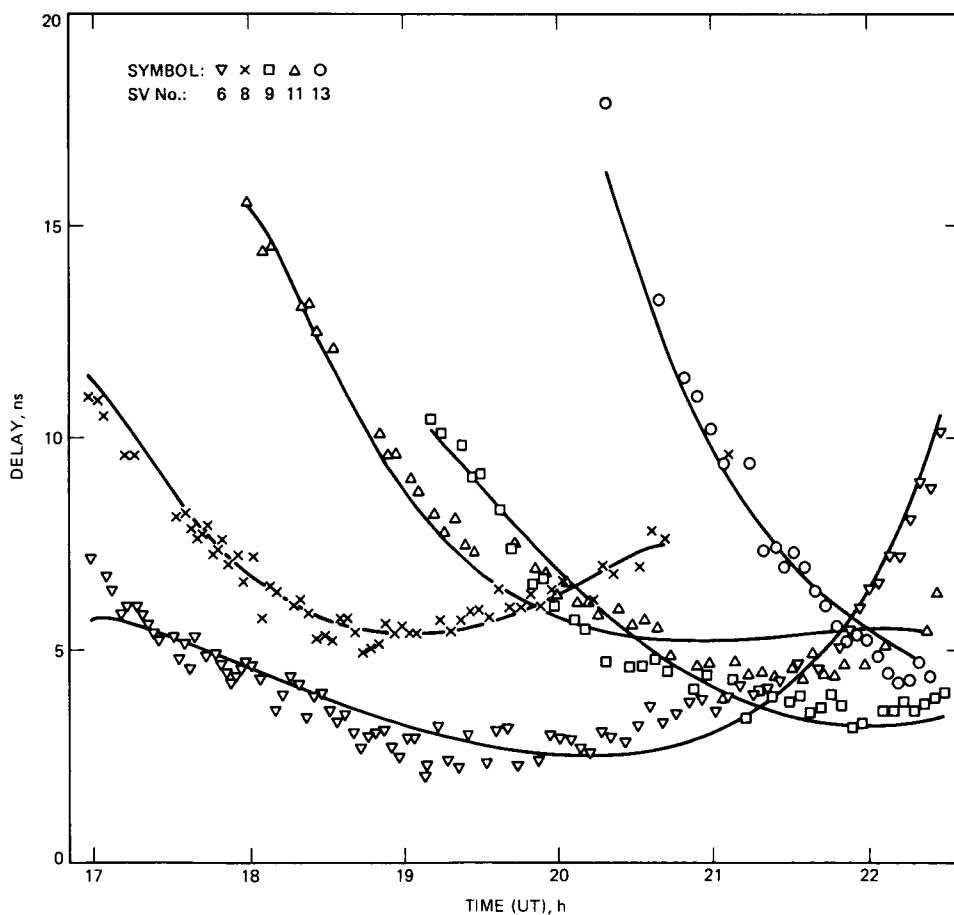


Fig. 7. SERIES observation of total line-of-sight electron content. Data were taken at Goldstone, California, 30 August, 1984

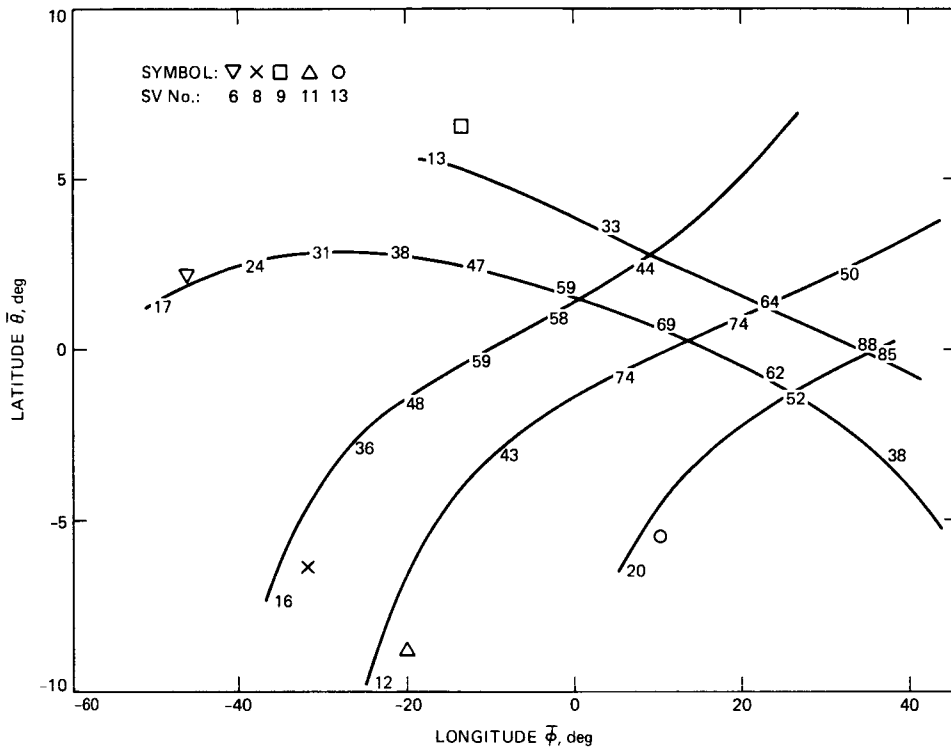


Fig. 8. Intersects of the observed lines of sights with the ionospheric shell corresponding to figure 7. The numeric labels represent the elevation angles of observations. The origin of the coordinate system corresponds to 35.30 deg equatorial latitude and 359.14 deg longitude referenced to the Sun-Earth axis

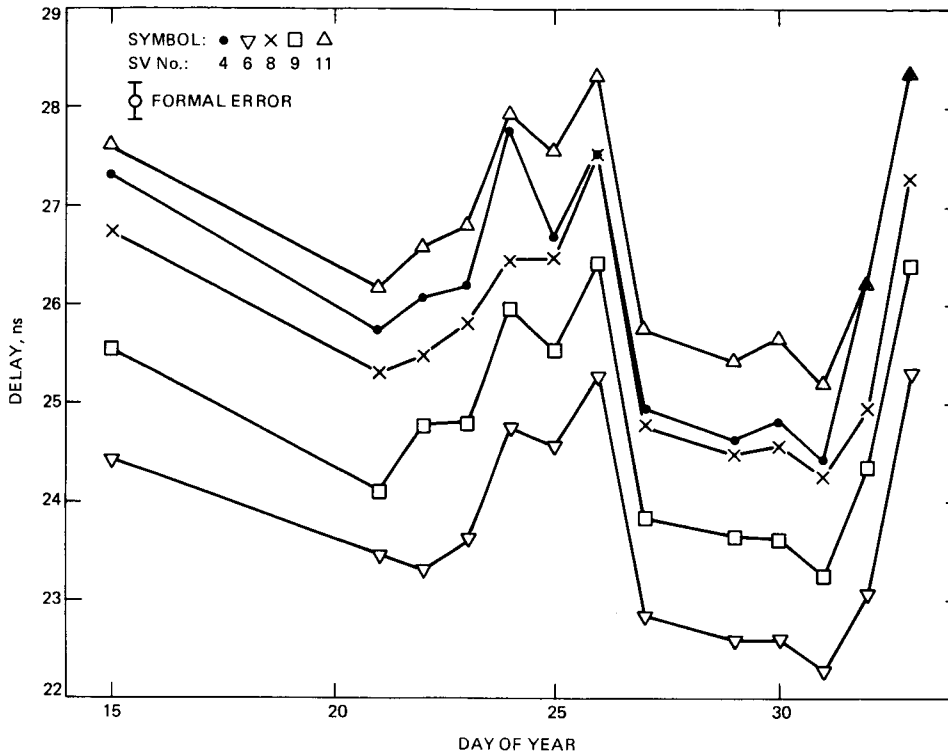


Fig. 9. Sums of GPS transmitter and receiver P-code L1-L2 offsets determined from SERIES nighttime data. The data contains receiver offsets of the order of 25 ns

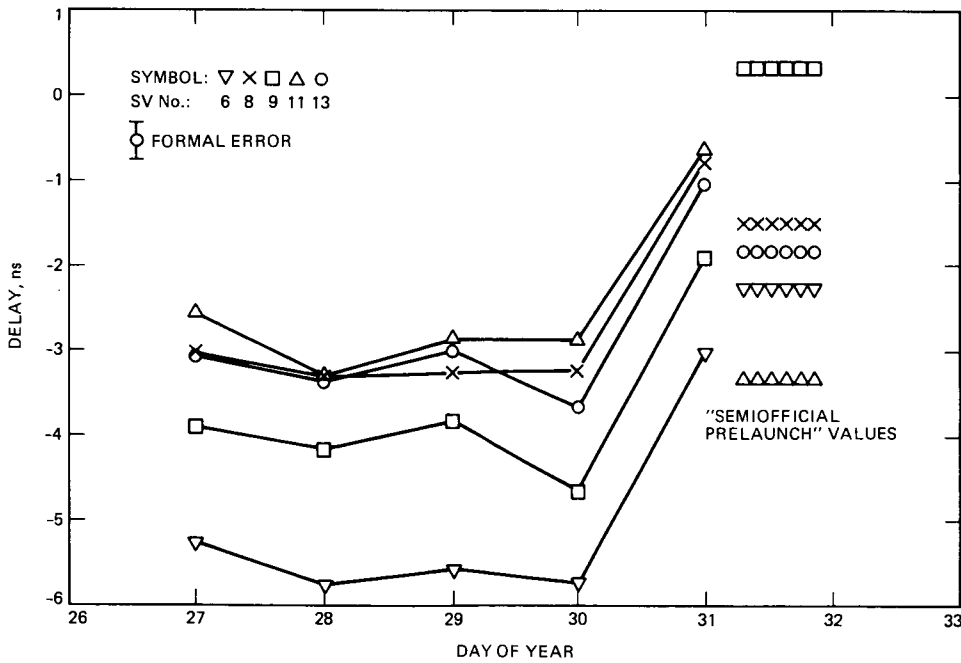


Fig. 10. Sums of GPS transmitter and receiver P-code L1-L2 offsets determined from SERIES daytime data. The receiver is calibrated. The semiofficial prelaunch values are marked on the right side of the plot

Appendix A

Instrumental Error Sources

1. Transmitter errors.

- (a) Multipath of radio signals by the satellite structure. The magnitude is unknown at present.
- (b) There is a time offset between the transmitted P-code signals at L1 and L2 frequencies. The value of this offset is different for each satellite. There are some semi-official prelaunch values for these offsets, though the official documentation quotes only an error estimate of 1.5 ns ($\sim 5 \times 10^{16}$ e/m²) at 1 σ .

2. Receiver errors.

- (a) *System noise*. This is a negligible effect compared to the other listed errors, its value is ~ 0.04 ns.

(b) *Temporal instabilities in the instrument*. The effect is ~ 0.1 ns.

(c) Multipath of radio signals by ground objects; the multipath's estimated value is ~ 0.3 ns. We should note here that the SERIES receiver employs a directional antenna which should significantly reduce multipath relative to the omnidirectional antenna used by SERIES-X.

(d) *GPS satellite interference in the receiver*. This effect is peculiar to the SERIES receiver, and occurs when more than one satellite appears in the beam pattern of the antenna. This error can be as high as 2 ns in magnitude. The observations corresponding to this effect were deleted from analysis.

13146

Planets as Background Noise Sources in Free Space Optical Communications

J. Katz

Advanced Electronic Materials and Devices Section

Background noise generated by planets is the dominant noise source in most deep space direct detection optical communications systems. Earlier approximate analyses of this problem are based on simplified blackbody calculations and can yield results that may be inaccurate by up to an order of magnitude. This article points out various other factors that need to be taken into consideration, such as the phase angle and the actual spectral dependence of the planet albedo, in order to obtain a more accurate estimate of the noise magnitude.

I. Introduction

Optical communications is considered as an alternative to conventional microwave links in future planetary (and exosolar) space missions (Ref. 1). For many typical deep space communications scenarios, the optical receiver which achieves maximum link sensitivity employs direct detection with a photon counting detector (e.g., photomultiplier tube) at the front end (Ref. 2). The performance of such receivers is limited by either the photon statistics of the received signal light or by background noise photons that appear in the receiving telescope field of view. In planetary space missions, the dominant background noise sources are the planets. Not only are they the brightest objects in the solar system (except the sun), but the highest demand on the communication link usually occurs during the planetary fly-by phase, where they are almost certain to be in the receiver field of view.

A first order approximation to the planet background noise is based on simplified blackbody calculations (for the spectral dependence), including the planet albedo as a single unique parameter (Refs. 3, 4, 5). As will be discussed in the following sections, the problem is much more involved, and the actual result can vary by more than an order of magnitude as compared to this simplified calculation. The purpose of this

article is to point out the other parameters that need to be taken into account and to demonstrate their effect through some illustrative examples. This article is not meant to be an exhaustive study of the problem. Such a detailed analysis is relevant only in the context of an actual planned mission.

Section II will briefly review the approximate basic theory. The following sections will consider the effects of the planet being an extended or a point source (Section III), phase angle (Section IV), and spectral dependence (Section V). Two other effects (polarization and temporal variations) will be briefly mentioned in Section VI.

II. Basic Theory

For the visible and near-infrared regions of the spectrum, virtually all the planet radiation is from reflected sunlight. The situation is different in the mid and far infrared (Ref. 3), but these cases will not be considered here.

If the planet is replaced by an ideal lambertian disk with a unit reflectivity facing the sun and with the same radius as the planet, the irradiance at the receiver plane is:

$$E_{\lambda} = \frac{H_{\lambda}}{R_{P_{\odot}}^2} \left(\frac{R_p}{Z} \right)^2 \frac{W}{\text{cm}^2 \mu\text{m}} \quad (1)$$

where H_{λ} is the solar flux at 1 AU (see Fig. 1 and Table 1), $R_{P_{\odot}}$ is the sun-planet distance in AU, R_p is the planet radius (in km), and Z is the distance between the planet and the receiver — usually earth — in km. Since the planets' orbits are not circular, there will be some variations due to the orbit eccentricity. The magnitude of this effect, with other basic parameters of the planets, are listed in Table 2. The ratio between the actual irradiance to the one predicted by Eq. (1) is the geometric albedo, p , of the planet.

By multiplying the actual irradiance by the receiver aperture area and by the bandwidth of its optical filter we obtain the background power level at the detector.

The simplified worst case calculations are given in Refs. 3, 4, and 5 (it should be noted that there is error in those references where the curves corresponding to Mars and Mercury are interchanged), where a single number is used to represent the albedo of each planet. In the following sections we will consider the various factors affecting the geometric albedo.

III. Planets as Extended Sources or Point Sources

Planetary optical communication receivers are usually envisioned to have narrow fields of view, usually in the micro-radian regime. Thus in many cases where the angular extent of the planet, θ_p , exceeds the receiver field of view, θ_r , the planet appears as an extended background source. Table 3 lists the approximate minimum, maximum and typical values of θ_p of each planet for near-earth reception. For uniformly reflecting planets the background irradiance dependence on θ_r is as shown in Fig. 2. Some planets, though, do not reflect uniformly, as shown, for example, for the planet Mars in Fig. 3, and thus when $\theta_r < \theta_p$, planetary features may have to be considered in greater detail. Of course, when $\theta_r > \theta_p$ (i.e., the planet is entirely encompassed by the receiver field of view) all the planet spatial features are averaged out.

IV. Phase-Angle Dependence

The phase angle is defined as the sun-planet-receiver (earth) angle. Even if the geometric albedo did not depend on the phase angle, the background contribution from the planet will vary because at the various phases different portions of the illuminated planet are seen from earth. This effect, which is

most important for the inner planets (and the moon), is analyzed in more detail in Appendix A and is depicted in Fig. 4.

In addition, there is a basic dependence of the geometric albedo on the phase angle α , because planets are not ideal lambertian reflectors. This dependence is expressed by a phase function $\phi(\alpha)$, which is shown in Fig. 5 for the planet Mars (Ref. 8) and the moon (Ref. 9). The typical features of the phase function are a linear part for phase angles exceeding approximately 10 deg, and a higher order component for phase angles smaller than approximately 5 deg. This enhanced reflectivity at small phase angles is called the "opposition effect." The exact shape of the phase function depends on the detailed light scattering properties at the planet (Refs. 8 and 9). Generally, albedos of planets with atmospheres have a smaller dependence on the phase angle than atmosphereless planets.

V. Spectral Dependence

In many cases the geometric albedo depends strongly on the wavelength. This may be caused, for example, by absorption lines in the planet's atmosphere or other processes such as Raman Scattering. Examples of the spectral variations of the albedo are shown in Fig. 3 (for Mars), Fig. 6 (for several planets in general low resolution detail) and in Fig. 7 for some other planets in more detail (Venus, Jupiter, Uranus, and Neptune). It is clearly seen that with all other parameters equal, a judicious choice of the communications link wavelength can significantly reduce the background noise by even more than an order of magnitude. For example, the Mars albedo at $\lambda = 1 \mu\text{m}$ is three to four times larger than at $\lambda = 0.5 \mu\text{m}$ (this is somewhat offset by the fact that the photon irradiance of the sun is 1.5 times larger at $0.5 \mu\text{m}$ than at $1 \mu\text{m}$). Furthermore, other outer planets which have atmospheres appear very dark at several wavelength regions, and they will contribute negligibly low background noise levels if these wavelengths are utilized in the communication link.

VI. Other Factors

In addition to the parameters discussed in the earlier sections, there are other factors that are usually of secondary importance, and are mentioned here for the sake of completeness. The first is the fact that planets — like most other objects — do not reflect equally both light polarizations. This effect is small (see data for Venus and Earth in Fig. 8) and completely unimportant in systems using unpolarized light or light with unknown polarization. The second factor is various temporal variations that can be caused by planetary climate patterns, solar flares, and other phenomena. Again, these are minor

effects compared with the effects of the Earth-Planet distance variation, phase angle and spectral dependence discussed earlier.

VII. Conclusion

As shown in the earlier sections, the simplified calculations of background noise generated by planets (Refs. 3, 4, 5) pre-

dict worst case situations and can thus serve in many cases only as a first order approximation to the actual magnitude of the background. While exact results can be obtained only when all the mission parameters are known (e.g., Planet and Earth location with respect to the Sun), this article points out the various parameters that play a role in determining this final result. The most important conclusion is that the noise magnitude strongly depends on the wavelength used for communication.

Acknowledgment

Discussions with S. Dolinar were helpful in ascertaining the dependence of received background noise from Venus on the Earth-Sun-Venus angle.

References

1. Posner, E. C., Grant, T., and Hortor, R., "Communications and Navigation for Galileo and Future Outer Planets Spacecraft," *IEEE Spectrum* (to be published), June 1986.
2. Lesh, J. R., Katz, J., Tan, H. H., and Zwillinger, D., "2.5 Bit/Detected Photon Demonstration Program: Description, Analysis, and Phase I Results," *TDA Progress Report 42-66*, Jet Propulsion Laboratory, Pasadena, Calif., pp. 115-132, 1981.
3. Ramsey, R. C., "Spectral Irradiance from Stars and Planets, above the Atmosphere, from 0.1 to 100.0 Microns," *Appl. Opt. 1*, 465-471, 1962.
4. Katz, J., "The Deep-Space Optical Channel: I. Noise Mechanisms," *TDA Progress Report 42-64*, Jet Propulsion Laboratory, Pasadena, Calif., 180-186, 1981.
5. Vilnrotter, V. A., "Background Sources in Optical Communications," *JPL Publication 82-73*, Jet Propulsion Laboratory, Pasadena, Calif., 1983.
6. "Solar Electromagnetic Radiation," NASA SP-8005, Washington, D.C., 1971.
7. "Surface Models of Mars (1975)," NASA SP-8020, Washington, D.C., 1975.
8. Egan, W. G., *Photometry and Polarization in Remote Sensing*, New York: Elsevier, 1985.
9. Lumme, K., and Bowell, E., "Radiative Transfer in the Surfaces of Atmosphereless Bodies," *Astron. J.* "I. Theory," 86 1694-1704, 1981; "II. Interpretation of Phase Curves," 86, 1705-1771, 1981; "III. Interpretation of Lunar Photometry," 87, 1076-1082, 1982.
10. Hartmann, W. K., *Moons and Planets: An Introduction to Planetary Science*, Tarrytown-on-Hudson, New York: Bogden and Quigley, 1972.
11. Moroz, V. I., "Stellar Magnitude and Albedo Data of Venus" (Ch. 3) in *Venus*, D. M. Hunten et al., Eds. Tucson: The U. of Arizona Press, 1983.
12. Taylor, D. J., "Spectrophotometry of Jupiter's 34100-1000Å Spectrum and a Bolometric Albedo for Jupiter," *Icarus*, 4, 362-373, 1965.
13. Irvine, W. M., and Lane, A. P., "Monochromatic Albedos for the Disk of Saturn," *Icarus*, 15, 18-26, 1971.
14. Neff, J. S., et al., "Absolute Spectrophotometry of Titan, Uranus and Neptune: 3500-10,500Å," *Icarus*, 60, 221-235, 1984.
15. Coffeen, D. L., and Hansen, J. E., "Polarization Studies of Planetary Atmospheres," from *Planets, Stars and Nebulae, Studied with Photopolarimetry*, T. Gehrels, Ed. Tucson: The U. of Arizona Press, 1974.

Table I. Solar spectral irradiance at 1 AU (from Ref. 6)

Wavelength (λ), μm	Average Irradiance* (P_λ), $\text{W cm}^{-2} \mu\text{m}^{-1}$	Wavelength (λ), μm	Average Irradiance* (P_λ), $\text{W cm}^{-2} \mu\text{m}^{-1}$	Wavelength (λ), μm	Average Irradiance* (P_λ), $\text{W cm}^{-2} \mu\text{m}^{-1}$
0.120	0.000010	0.425	0.1693	0.740	0.1260
0.140	0.000003	0.430	0.1639	0.750	0.1235
0.150	0.000007	0.435	0.1663	0.800	0.1107
0.160	0.000023	0.440	0.1810	0.850	0.0988
0.170	0.000063	0.445	0.1922	0.900	0.0889
0.180	0.000125	0.450	0.2006	0.950	0.0835
0.190	0.000271	0.455	0.2057	1.000	0.0746
0.200	0.00107	0.460	0.2066	1.100	0.0592
0.210	0.00229	0.465	0.2048	1.200	0.0484
0.220	0.00575	0.470	0.2033	1.300	0.0396
0.225	0.00649	0.475	0.2044	1.400	0.0336
0.230	0.00667	0.480	0.2074	1.500	0.0287
0.235	0.00593	0.485	0.1976	1.600	0.0244
0.240	0.00630	0.490	0.1950	1.700	0.0202
0.245	0.00723	0.495	0.1960	1.800	0.0159
0.250	0.00704	0.500	0.1942	1.900	0.0126
0.255	0.0104	0.505	0.1920	2.000	0.0103
0.260	0.0130	0.510	0.1882	2.100	0.0090
0.265	0.0185	0.515	0.1833	2.200	0.0079
0.270	0.0232	0.520	0.1833	2.300	0.0068
0.275	0.0204	0.525	0.1852	2.400	0.0064
0.280	0.0222	0.530	0.1842	2.500	0.0054
0.285	0.0315	0.535	0.1818	2.600	0.0048
0.290	0.0482	0.540	0.1783	2.700	0.0043
0.295	0.0584	0.545	0.1754	2.800	0.00390
0.300	0.0514	0.550	0.1725	2.900	0.00350
0.305	0.0603	0.555	0.1720	3.000	0.00310
0.310	0.0689	0.560	0.1695	3.100	0.00260
0.315	0.0764	0.565	0.1705	3.200	0.00226
0.320	0.0830	0.570	0.1712	3.300	0.00192
0.325	0.0975	0.575	0.1719	3.400	0.00166
0.330	0.1059	0.580	0.1715	3.500	0.00146
0.335	0.1081	0.585	0.1712	3.600	0.00135
0.340	0.1074	0.590	0.1700	3.700	0.00123
0.345	0.1069	0.595	0.1682	3.800	0.00111
0.350	0.1093	0.600	0.1666	3.900	0.00103
0.355	0.1083	0.605	0.1647	4.000	0.00095
0.360	0.1068	0.610	0.1635	4.100	0.00087
0.365	0.1132	0.620	0.1602	4.200	0.00078
0.370	0.1181	0.630	0.1570	4.300	0.00071
0.375	0.1157	0.640	0.1544	4.400	0.00065
0.380	0.1120	0.650	0.1511	4.500	0.00059
0.385	0.1098	0.660	0.1486	4.600	0.00053
0.390	0.1098	0.670	0.1456	4.700	0.00048
0.395	0.1189	0.680	0.1427	4.800	0.00045
0.400	0.1429	0.690	0.1402	4.900	0.00041
0.405	0.1644	0.700	0.1369	5.000	0.0003830
0.410	0.1751	0.710	0.1344	6.000	0.0001750
0.415	0.1774	0.720	0.1314	7.000	0.0000990
0.420	0.1747	0.730	0.1290	8.000	0.0000600

*Special irradiance averaged over small bandwidth centered at λ : 0.3 to 0.75 μm (bandwidth, 100Å), 0.75 to 1.0 μm (bandwidth, 500Å), and 1.0 to 5.0 μm (bandwidth, 1000Å)

Table 2. Orbital constants of the planets and solar irradiance at planetary distances (from Ref. 6)

Planet	Semi-Major Axis of Orbit		Sidereal Period, days	Eccentricity of Orbit 1971, ϵ	Solar Irradiance at Distance of Semi-Major Axis*		Ratio of Max to Min Irradiance,** $\left(\frac{1+\epsilon}{1-\epsilon}\right)^2$
	AU	10^6 km			Solar Constant	mW cm^{-2}	
Mercury	0.387 099	57.91	87.9686	0.205 629	6.673 5	902.9	2.303
Venus	0.723 332	108.21	224.700	0.006 787	1.911 3	258.6	1.028
Earth	1.000	149.60	365.257	0.016 721	1.000 0	135.3	1.069
Mars	1.523 69	227.94	686.980	0.093 379	0.430 7	58.28	1.454
Jupiter	5.2028	778.3	4 332.587	0.048 122	0.036 95	4.999	1.212
Saturn	9.540	1427	10 759.20	0.052 919	0.010 99	1.487	1.236
Uranus	19.18	2869	30 685	0.049 363	0.002 718	0.3678	1.218
Neptune	30.07	4498	60 188	0.004 362	0.001 106	0.1496	1.018
Pluto	39.44	5900	90 700	0.252 330	0.000 643	0.0870	2.806

*Solar irradiance is $1/R^2$ in units of the solar constant and $135.3/R^2$ in mW cm^{-2} where R is the semi-major axis of the planetary orbit.
 **Values of eccentricity change with time; the ratio of solar irradiance at perihelion to that at aphelion in the last column is computed on the assumption of constant eccentricity.

Table 3. Approximate angles (in microradians) subtended by planets ¹

Planet	Minimum ²	Maximum ³	Typical ⁴
Mercury	23	53	33
Venus	47	292	81
Mars	18	87	30
Jupiter	153	225	182
Saturn	76	94	84
Uranus	19	17	18
Neptune	6	6	6
Pluto	2	2	2

¹ Does not include the partially lit area effect which is primarily important for the inner planets as discussed in Appendix A.
² At maximum Earth-Planet distance.
³ At minimum Earth-Planet distance.
⁴ Earth-Planet distance equals 1 AU for the inner planets and Sun-Planet distance of the outer planets.

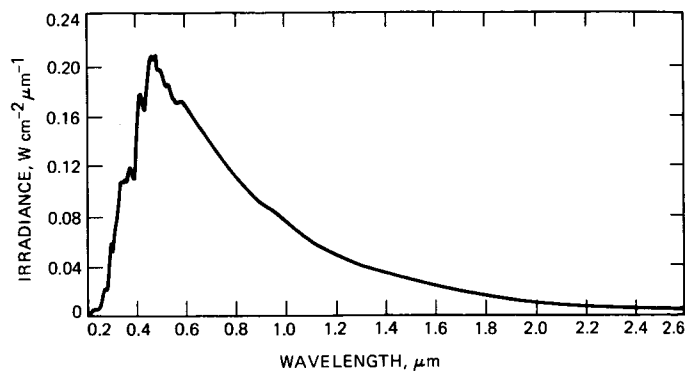


Fig. 1. Solar spectral irradiance (after Ref. 6)

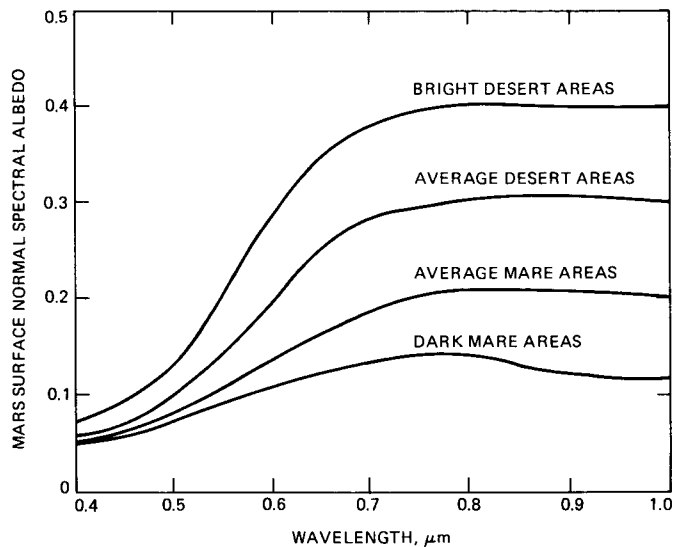


Fig. 3. Estimates of Mars surface normal albedo (after Ref. 7)

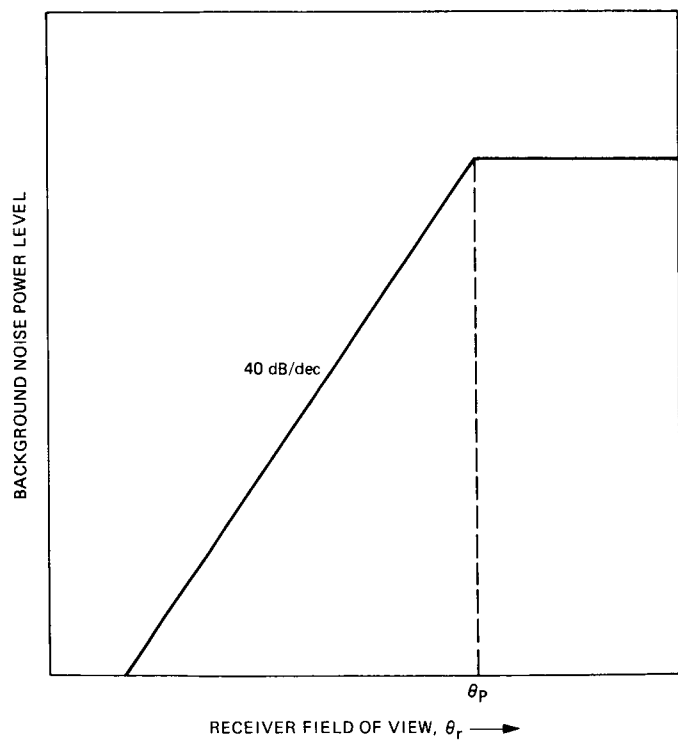


Fig. 2. Background noise power level from a planet vs. receiver field of view

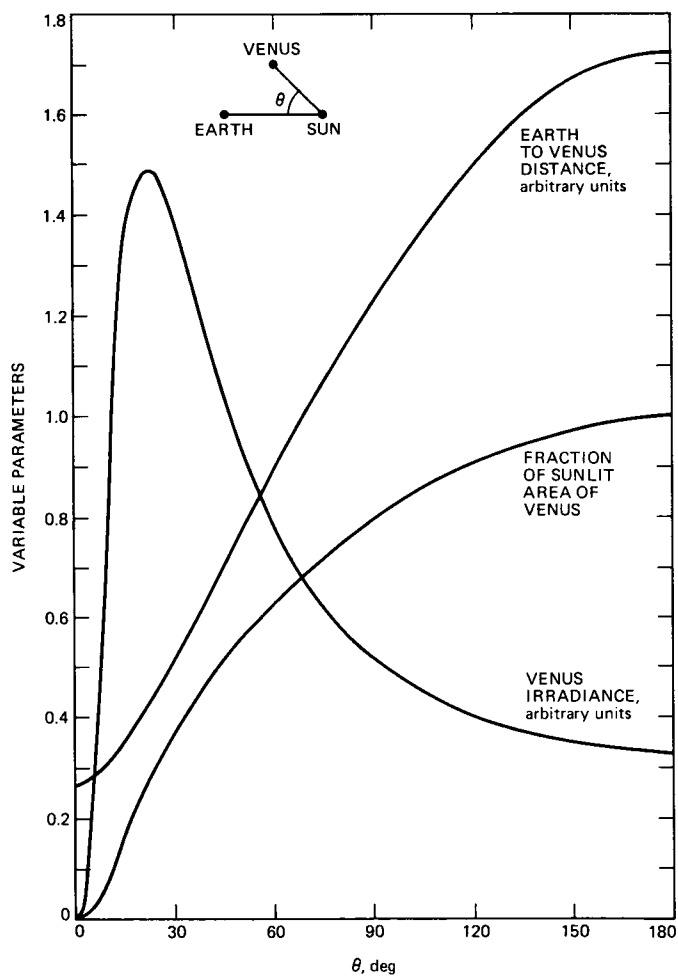


Fig. 4. Dependence of the received background noise from Venus on the Earth-Sun-Venus angle

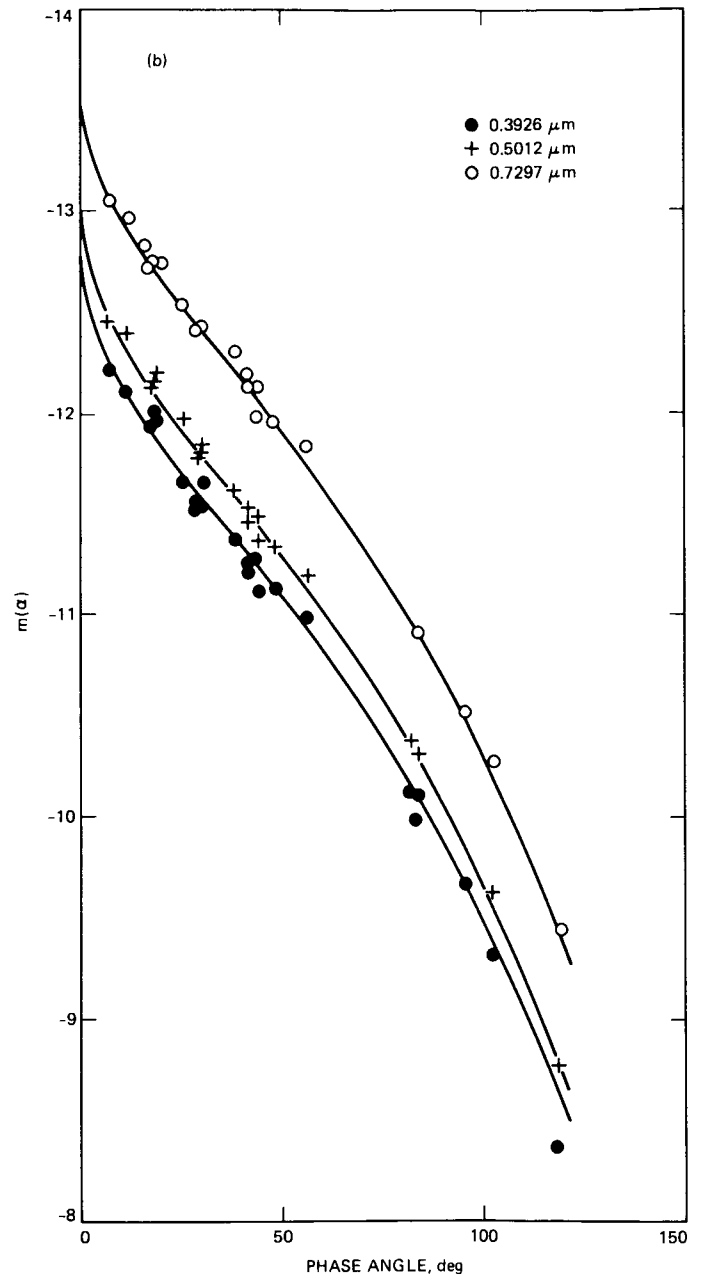
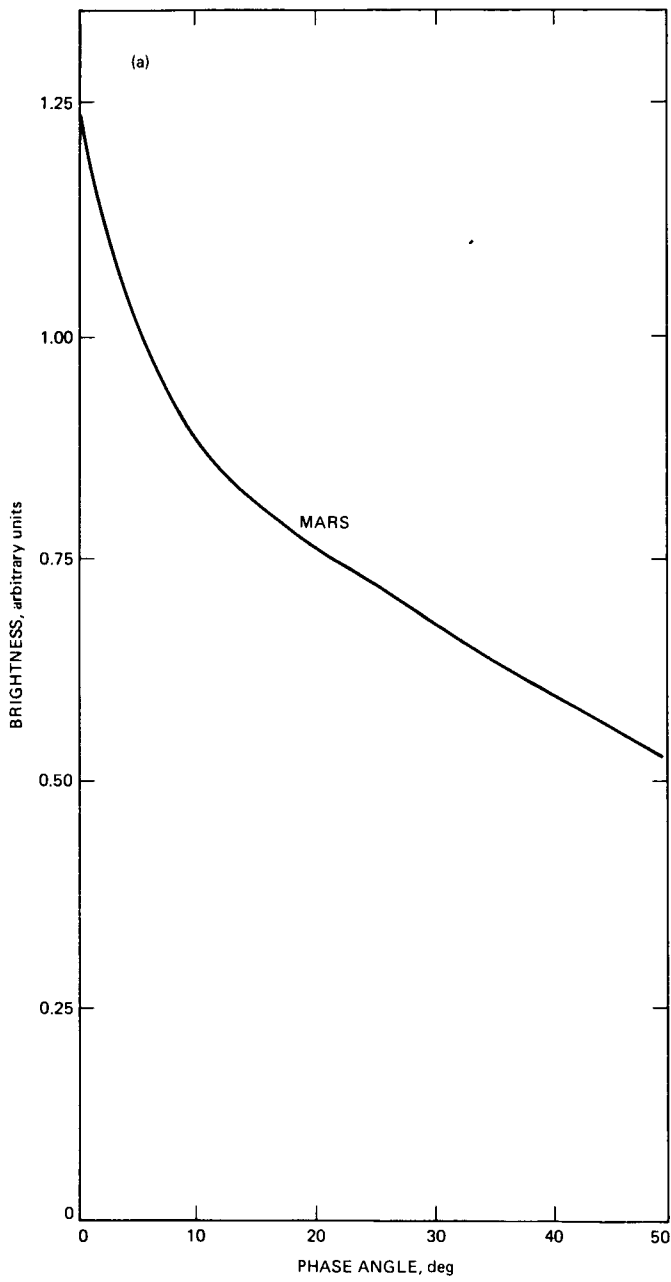


Fig. 5. Phase function (a) for Mars (after Fig. 16.4, Ref. 8) and (b) for Moon (in logarithmic magnitude units, after Fig. 2 in Ref. 9 [III])

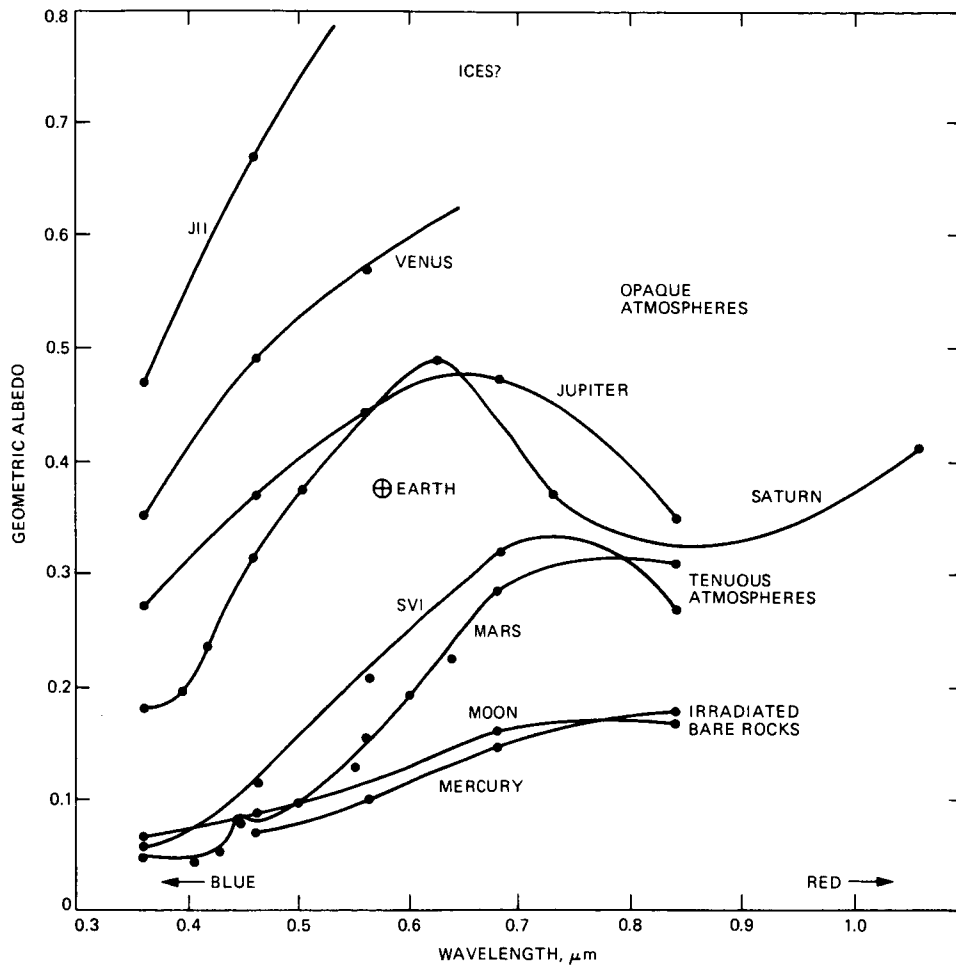


Fig. 6. Geometric albedo (low resolution) wavelength dependence for various planetary bodies (after Fig. 11.7 in Ref. 10 and Table IV in Ref. 13)

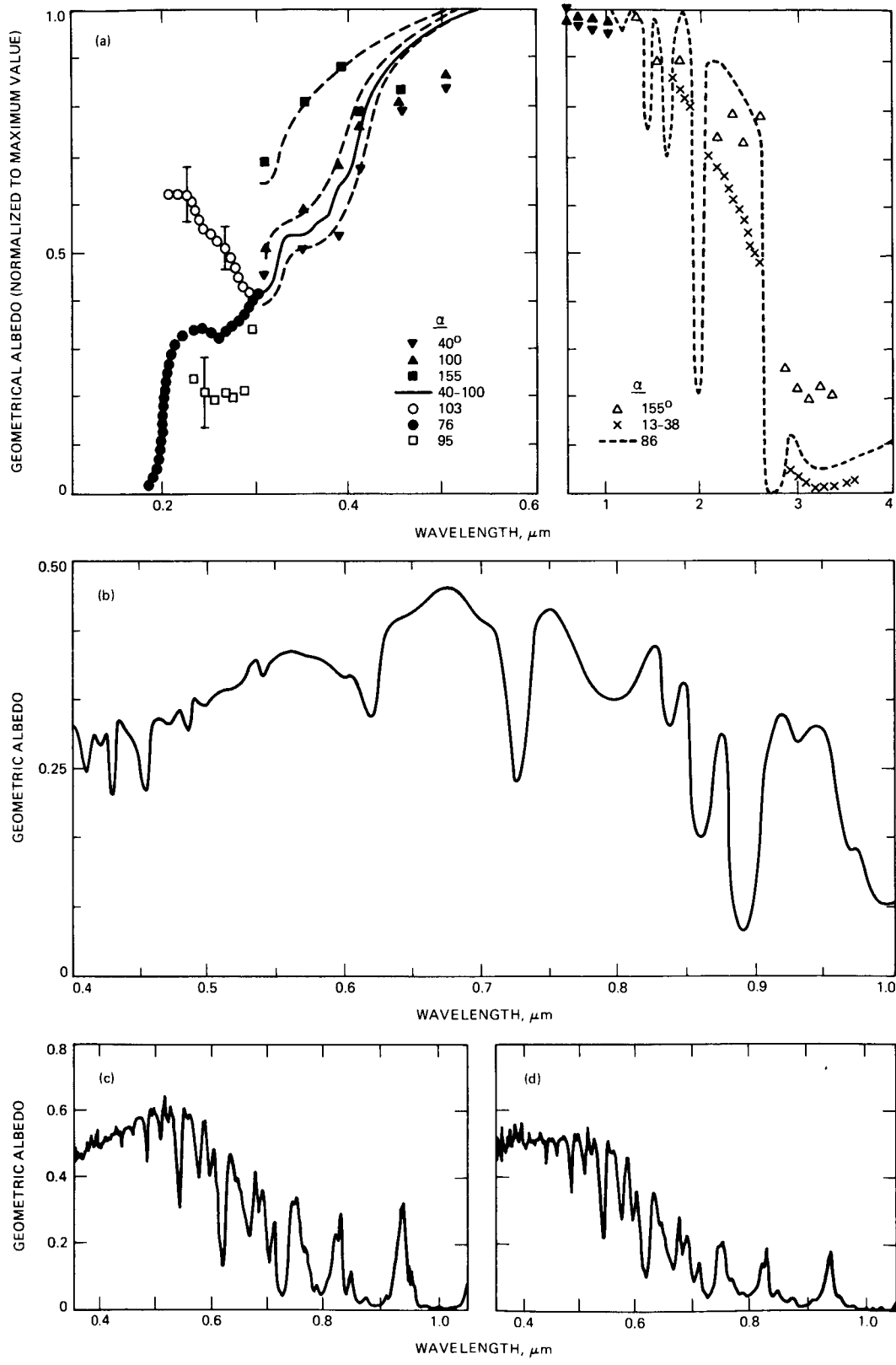


Fig. 7. Detailed geometric albedo for various planets: (a) Venus (after Fig. 1 in Ref. 11); (b) Jupiter (from data in Ref. 12); (c) Uranus (after Fig. 7 in Ref. 14); (d) Neptune (after Fig. 8 in Ref. 14)

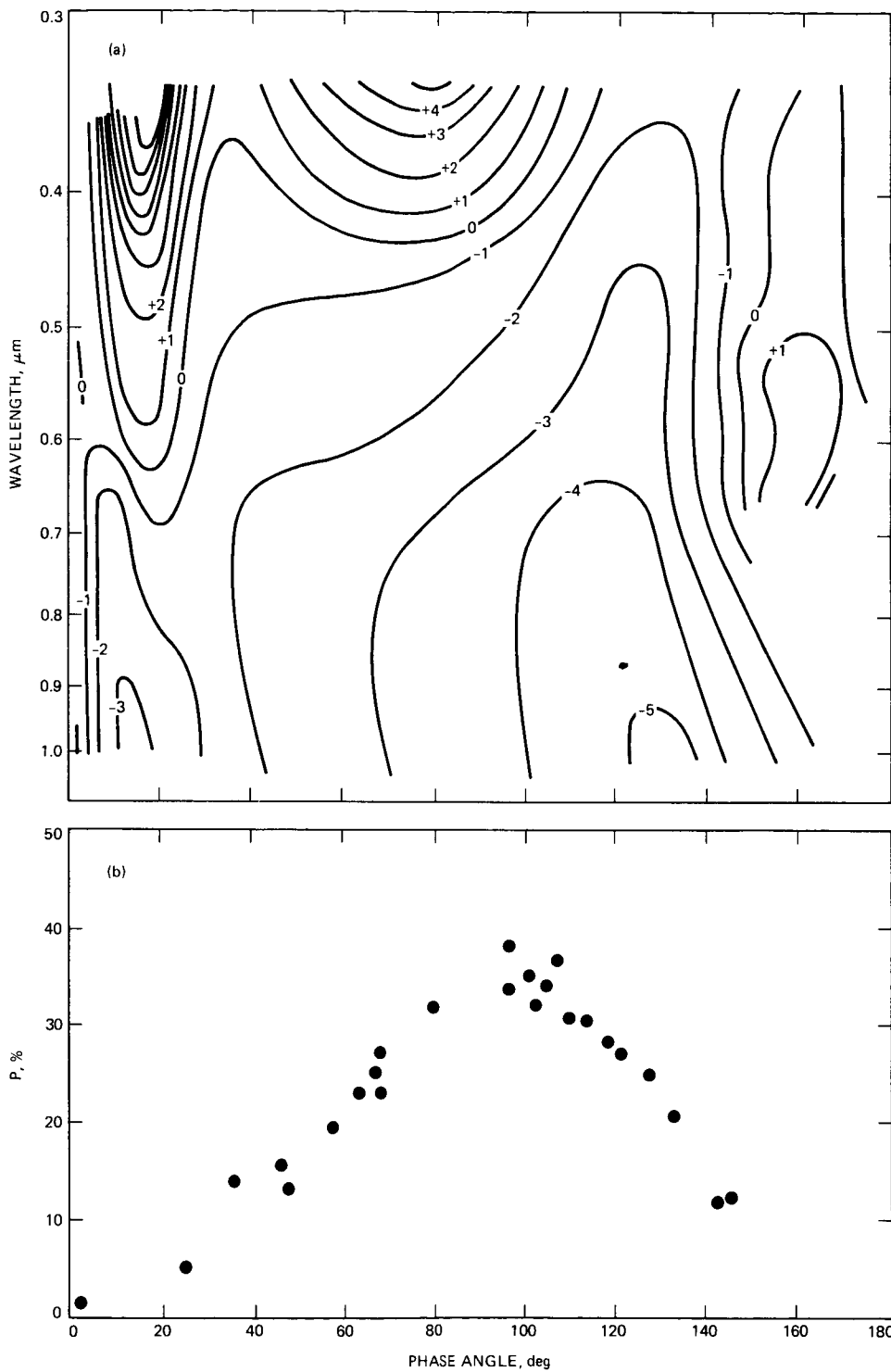


Fig. 8. Polarization: (a) degree of polarization (in percent) of Venus as a function of phase angle and wavelength (after Fig. 16 in Ref. 15) and (b) global earth degree of polarization (after Fig. 24 in Ref. 15)

Appendix A

Phase-Angle Dependence

Consider the sun-planet-earth system shown in Fig. A-1 (for an inner planet in this particular case). The lit angle of the cross sectional disc is $\pi - \alpha$, where α is the phase angle. Choosing θ (planet-sun-earth angle) as the natural coordinate for this problem, it is clearly seen that

$$\pi - \alpha = \theta + \gamma(\theta) \quad (\text{A-1})$$

where $\gamma(\theta)$ is the Sun-Earth-Planet angle, given by

$$\gamma(\theta) = \frac{1}{\sin \theta} \left[\frac{R_{E\odot}}{R_{P\odot}} - \cos \theta \right] \quad (\text{A-2})$$

Simple trigonometric calculations show that the fraction of the lit planetary disc is

$$\sin^2 \frac{\alpha}{2} = \sin^2 \left[\frac{\theta + \gamma(\theta)}{2} \right] \quad (\text{A-3})$$

and that the Earth-Planet distance is given by

$$Z = R_{E\odot} \left[\frac{\sin \theta}{\sin[\theta + \gamma(\theta)]} \right] = R_{P\odot} \frac{\sin \theta}{\sin[\gamma(\theta)]} \quad (\text{A-4})$$

As long as the planet appears as an extended background source, its noise contribution is not affected by the above considerations. However, when the planet is small enough to be considered as a point source, its actual noise is proportional to the ratio of the fractional area lit (Eq. [A-3]) to the distance (Eq. [A-4]). This dependence is strongest for the inner planets, as shown in Fig. 4. For the outer planets, though, the fractional area lit is always close to unity (for Mars the minimum is approximately 87% and the planets from Jupiter and beyond are always more than 99% lit), so the main effect on the noise variation is the Earth-Planet distance.

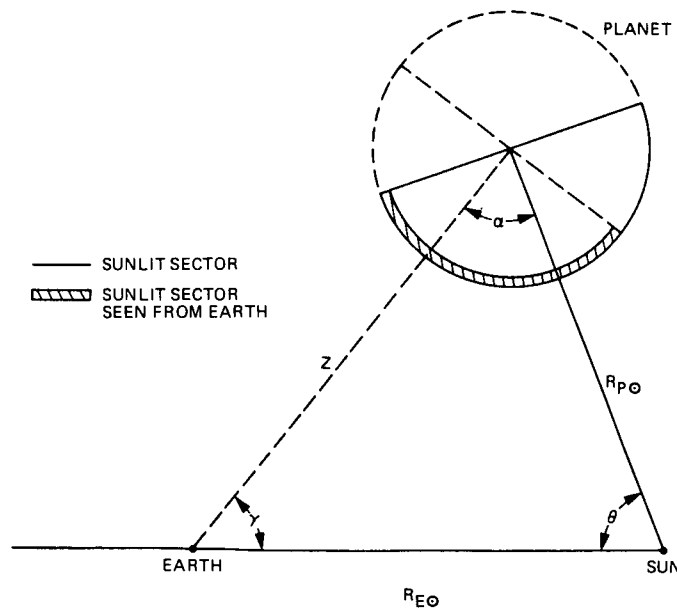


Fig. A-1. Sun-planet-earth system (for inner planet)

A Simple Method for Designing or Analyzing an Optical Communication Link

J. R. Lesh, W. K. Marshall, and J. Katz
Communications Systems Research Section

A simple method is described for determining the performance of a free space optical communication link. The method can be used either in the system design (synthesis) mode or in the performance evaluation (analysis) mode. Although restricted to photo counting (e.g., photomultiplier tube or equivalent) based detection of pulse position modulated signals, the method is still sufficiently general to accommodate space-based, as well as ground-based, reception.

I. Introduction

Experience over the years with the Deep Space Network has produced a high degree of familiarity and intuitive understanding of RF communications. Not only engineers but managers and scientific users as well generally appreciate that doubling signal power can double the data rates and that a bit SNR of 10 dB results in quite good, but most likely not over-designed, performance. This intuition is facilitated by the fact that an RF communications link is usually limited by the thermal noise of the communication receiver and the performance of the link is determined once the received signal-to-noise power ratio is specified.

For a deep space optical communications link, the dominant performance limitation is usually not related to noise in the receiver but due to received background noise (light). The performance of a link depends on the individual values of the signal and noise powers, not just on their ratio. Furthermore, there are meaningful examples for which a high "SNR" (defined here as a ratio of signal and noise powers or counts) can result in poor performance whereas there are likewise

examples where a poor "SNR" can result in essentially error-free performance. This latter point deserves explanation.

Consider a very benign optical communication channel where the background (noise) count rate is 0.001 over some characteristic decision time whereas the signal count rate over that time is one count. Such an example is not too unusual for a high data rate free-space optical channel. Despite the fact that the "SNR" is 1000 (30 dB), the system performance is dominated by the weak signal pulse erasure rate which is e^{-1} or 37%. Now consider a much noisier channel where both the signal and background count rates are 1000. Here, the "SNR" is 1 (or 0 dB). The detector's job is to distinguish the absence of a signal pulse (which is characterized by a mean noise count rate of 1000) from a signal pulse present condition where the mean count rate (signal + noise) is 2000. However, the Poisson statistics that govern the count processes produce RMS variations around these mean values, which equal the square roots of those mean values. The RMS spread around the 1000-count mean is 33 and that of the 2000-count mean is only 45. These two distributions are clearly distinguishable with very low probability of error.

The above results notwithstanding, it is very desirable that people affected by optical communication technology comfortably build intuition about its performance. The purpose of this article is to provide a simple means by which that intuition can be acquired. It should be emphasized that this is a first-order design tool useful for scoping an optical link and illustrating trends therefrom, and does not replace the more rigorous (and accurate) analysis techniques that have been developed elsewhere. The information provided should permit a relatively rich set of cases to be addressed.

In the next section we will describe the procedure and illustrate its use by analyzing an example. The example will involve ground-based reception of a spacecraft signal from Mars with that planet in the background. Following this, the rules for scaling the results to other parameter values will be presented. These scaling rules permit a rather wide set of parameter values and conditions to be accommodated. To illustrate this we will then use the rules to determine the required aperture size for a space-based receiver for the above example. It should be pointed out, however, that these results only apply to direct detection (not heterodyne) systems which utilize photomultiplier tube (or equivalent) based detectors.

II. The Simplified Design and Analysis Procedure

There are basically three steps to evaluating the performance of an optical link:

- (1) Determine the number of *detected* signal photons per pulse at the detector.
- (2) Determine the number of *detected* background or noise generated photons per PPM slot at that same detector.
- (3) Compare the number of detected signal photons per pulse with the number of detected noise photons per slot.¹

The operations may be done in any order and are routinely done so depending on whether the job is to analyze a given link or determine requirements on parameters to meet a specific level of performance. The following example uses the procedure in the specified (analysis mode) order.

¹From conventional PPM modulation, the slot width, τ_s (in seconds), is related to the data rate, DR (in bits/s), and the PPM word size M by $\tau_s = \log_2 M / DR * M$. However, for greater noise immunity, one can decrease the slot time by introducing dead time. Thus, τ_s is a free parameter as long as it is smaller than $\log_2 M / DR * M$.

A. Performance Analysis Example

In this example, we have assumed a 10-meter, *ground-based* receiver aperture with a rather broad ($5 \mu\text{rad}$) field of view to account for atmospheric turbulence broadening. This field of view admits about 100 times more background light into the detector than a spaceborne 10-meter aperture (assuming both apertures are non-diffraction limited at 10 times the diffraction limit), and it admits nearly 10^4 times more noise than a spaceborne diffraction limited aperture of the same size. The example also assumes a 400-milliwatt laser operating at a wavelength of $0.532 \mu\text{m}$ through a 10-cm transmitter telescope from Mars with the sunlit planet in the background. We assume a data rate of 30 kbps and 256-ary PPM modulation. All of the values used in the example are quite conservative, and will *realistically* permit variations on both sides of the parameter values.

1. **Determine number of detected signal photons/pulse.** A diffraction limited (transmit) telescope of diameter D meters produces a useable beamwidth (diameter) θ_t of approximately $1.5 \lambda/D$ radians, where λ is the optical wavelength in meters.² For $D = 10$ cm and $\lambda = 0.532 \times 10^{-6}$ meters, $\theta_t \sim 8.0 \mu\text{rad}$. At an Earth-Mars distance, R , of 2.3×10^8 km, the footprint diameter at the Earth is 1835 km. If light is collected by a 10-meter-diameter aperture, then the geometric signal level reduction factor is

$$\left(\frac{10 \text{ m}}{1.84 \times 10^6 \text{ m}} \right)^2 = 3 \times 10^{-11}$$

If 400 milliwatts is transmitted, then (assuming for the moment no losses other than beam spread), the power at the receiver is 1.2×10^{11} watts. At 30 kbps and PPM word size of 256 (8 bits/pulse), the pulse rate is 3750 pulses/second. Thus, each signal pulse has 3.2×10^{-15} joules of energy. If the energy per photon is $h\nu = hc/\lambda = 3.7 \times 10^{-19}$ joules, then each pulse contains 8.6×10^3 photons. Additionally, one must consider other (non-space) losses. Let us assume the following efficiencies:

Transmit optics	50%
Receive optic	50%
Atmospheric attenuation	50%
Detector quantum efficiency	30%
<hr/>	
Total <i>detected</i> photon efficiency	3.75%

Then, the number of *detected* photons per pulse is 321.

²The factor of 1.5 takes into account the effects of Gaussian beam illumination of the aperture and 20% subreflector blockage. For details, see the appendix.

2. Determine number of detected noise photons/slot. The next task is to determine the number of background-generated noise photons which the detector senses (on the average) per PPM slot time. Table 1 shows the approximate count rates for a variety of extended sources (i.e., bigger than the detector field of view) as well as a number of point sources (those smaller than the detector field of view). The parameters assumed in the calculations are shown in the lower portion of the table.

By referring to this table we see that unless the Sun, or a very bright star (of which there are very few), is in the field of view, the background count rate, even with daytime viewing, will be only about 0.2 counts/slot (0.1 from Mars and 0.1 from daytime sky).

3. Compare detected signal photons per pulse with detected noise photons per slot. The final step involves assessing the performance of the link given the appropriate signal and noise count rates. Figure 1 shows a curve of the number of detected signal photons per pulse required to achieve an uncoded error rate of 10^{-3} as a function of the number of detected noise photons per slot. The curve was calculated for a PPM word size, M , of 256, but is "first-order accurate" for word sizes as small as $M = 2$ or as large as many thousands. Furthermore, the error rate can be reduced very substantially by even rudimentary coding. (For example, an 8-bit Reed-Solomon code used at this uncoded bit error rate would produce a coded error rate of $\sim 10^{-22}$.) From this curve we see that for a detected noise count rate of 0.2 counts/slot, the required number of signal photons per pulse is approximately 11. Comparing this with the available number of detected signal photons from above, we see that this example link provides a margin of 14.6 dB!

B. Design Procedure Example

The above example was calculated based on the number of geometrically intercepted signal photons at the receiving aperture (reduced by the appropriate set of inefficiencies) and the corresponding background count rates from Table 1. For different situations, the geometry and efficiencies still determine the signal counts per transmitted pulse. However, the noise count rates must be scaled to the new set of conditions. Table 2 gives the scaling rules for this operation. To see how these rules are used, we will now calculate the aperture size required for spaceborne reception in the above example which will produce approximately a 3-dB link margin.

We note that moving the receiver outside the Earth's atmosphere will reduce the background count rate by a factor of two due to deletion of the daylit sky. However (see Table 2), the count rate from Mars will double due to the loss of the

Earth's atmospheric attenuation. Thus, a 10-meter aperture in space will have the same background count rate as one on the ground (in this particular example and assuming the same detector fields of view). Recall that in the previous example the link was more than 10 dB overdesigned and the detector field of view ($5 \mu\text{rad}$) was limited by atmospheric seeing. Let us assume that for spaceborne reception the field of view is reduced to $2 \mu\text{rad}$ (which is still substantially larger, i.e., worse, than diffraction limit). Note from Table 2 that reducing the field of view to 40% of its original value reduces the background noise effects by a factor of 0.16, and reducing the aperture diameter (anticipated due to the overdesign of the previous example) further reduces noise quadratically. However, from Fig. 1 we see that reducing the background count by several orders of magnitude still leaves the required count rate relatively unchanged at around 8 counts per pulse. Thus, we can use this count rate to determine the required aperture size.

Recall that atmospheric attenuation affects both signal as well as background. Thus, the 321 counts/pulse of the previous example, which corresponds to 642 counts/pulse outside the atmosphere, can be reduced to 16 (3-dB margin over the 8) by reduction of the aperture. This corresponds to a receiver aperture diameter of 1.6 meters. Using this diameter to further refine the background count rate estimates we have that

$$N_b = \underbrace{(0.2 \text{ cts/slot})}_{\substack{\text{Mars count rate} \\ \text{at 10-m and} \\ \text{5-}\mu\text{rad FOV}}} \underbrace{(2/5)^2}_{\substack{\text{FOV} \\ \text{reduction}}} \underbrace{(1.6/10)^2}_{\substack{\text{Aperture} \\ \text{reduction}}} = 8 \times 10^{-4} \text{ cts/slot}$$

which, from Fig. 1, implies that only 7 detected photons per pulse are actually required. Note also from Fig. 1 that the detector field of view could be increased substantially (and thereby greatly reducing the cost of the receiver aperture) without requiring more than 8 detected photons per pulse (16 with a 3-dB margin).

III. Concluding Remarks

We have shown a simplified procedure for analyzing or designing a direct detection, photon counting optical link with background noise. The procedure consists of a simple geometric calculation of the received signal pulse intensity, a table look-up method for background noise, and a single curve against which to compare the two. Additionally, scaling rules for calculating other situations were given and their use illustrated through an example. This method will aid those who prefer not to dig more deeply into the theory of optical communications to easily build an intuitive understanding of the field.

Reference

1. Klein, B. J., and Degnan, J. J., "Optical Antenna Gain. 1: Transmitting Antennas," *Appl. Opt.*, Vol. 13, No. 9, pp. 2134-2141, September 1974.

Table 1. Background noise counts in ground-based optical communications

Extended sources	Number of noise counts/slot
Sun	10^5
Mercury	0.8
Venus	3.0
Earth (typical)	0.6
Mars	0.1
Jupiter	0.03
Saturn	0.01
Uranus	0.003
Neptune	0.001
Moon	0.2
Clear sky:	
Day	0.1
Moonlit night	10^{-7}
Moonless night	10^{-8}
Background noise outside the atmosphere	10^{-8}

Point Sources	Number of noise counts/slot
Zero magnitude star	6
6th magnitude star	0.02
Pluto	3×10^{-5}

Parameter values assumed for the calculations:

1. Wavelength: 0.5 μm
2. Slot time: 10 ns
3. Receiver diameter: 10 m
4. Detector field of view: 5 μrad
5. Receiver optics efficiency: 0.5
6. Detector quantum efficiency: 0.3
7. Optical filter bandwidth: 10 \AA
8. Atmospheric transmission: 0.5

Table 2. Scaling rules for Table 1

The number of noise counts varies according to the following rules:

1. Linearly with the optical filter bandwidth, slot time, detector quantum efficiency, atmospheric transmission, and receiver optics efficiency.
2. Quadratically with the receiver diameter.
3. Quadratically with the detector field of view (only for noise generated by extended background sources). Note, however, that for space-based reception, and assuming constant surface figure requirements, the field of view scales inversely with receiver diameter.
4. According to Blackbody radiation law (illumination by Sun at 5900 K) with the wavelength. Typically, noise counts in the 0.8–1- μm region will be 2 to 3 times smaller than in 0.5 μm .

Notes:

1. Planets appear as extended sources only for fields of view smaller than their own angular extent. Thus, the field of view scaling should be checked for values above 10 μrad and below 2 μrad .
2. For space-based reception extraterrestrial background sources (as well as the desired signal source) should be increased by a factor of two.
3. Noise contributions from planets vary substantially with wavelength, phase angle, and other factors (e.g., contributions from Saturn's rings). Values used are believed to represent the worst case situation.

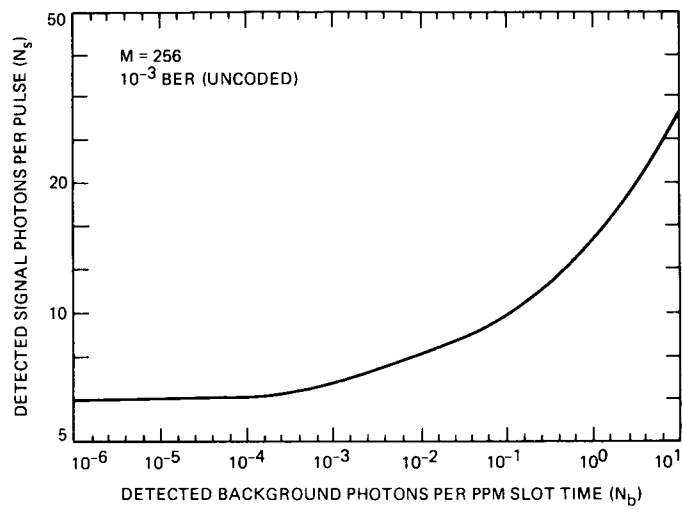


Fig. 1. Required signal pulse intensity at detector vs detected background count rate

Appendix

Equivalent “Uniform Cone” Beamwidth

In the first-order analyses of communications links, it is sometimes desirable to calculate the signal power density at the receiver by means of a “cone of uniform intensity” approximation for the transmitted beam. To use this approach, however, it is necessary to choose the proper beamwidth for a given transmitter aperture size. The analysis below indicates that the beam diameter should be assumed to be $1.5 \lambda/D$ (radians). Results obtained using this approach should be accurate to within 1 dB in most cases.

Consider an antenna/telescope which transmits power over a uniform cone of half-angle θ . The on-axis gain of such an antenna would be

$$\begin{aligned}
 g &= \frac{4\pi L^2}{\text{spot area at distance } L} \\
 &= \frac{4\pi L^2}{\pi(\theta L)^2} \\
 &= \frac{4}{\theta^2} \tag{A-1}
 \end{aligned}$$

Consider now an “ideal” circular antenna of diameter D . This antenna would have an on-axis gain of

$$\begin{aligned}
 g &= \frac{4\pi(\pi D^2/4)}{\lambda^2} \\
 &= \frac{\pi^2 D^2}{\lambda^2} \tag{A-2}
 \end{aligned}$$

Hence, an *ideal* transmitting antenna (with no pointing losses) can be modeled *exactly* via the “uniform cone” method by choosing the beam *half-angle* to be

$$\theta = \frac{2\lambda}{\pi D} = 0.637 \frac{\lambda}{D} \tag{A-3}$$

so that the on-axis gains given by Eqs. (A-1) and (A-2) are equal.

Now note that a real antenna of diameter D has a gain lower than that given by Eq. (A-2), due to several effects:

- (1) Transmission/reflection losses.
- (2) Pointing losses.
- (3) Beam truncation and aperture obscuration losses.

Losses due to (1) are usually handled explicitly in calculating the received signal. Losses due to (2) are usually assumed to be small, for example, less than 1 dB. Losses due to (3) can be handled easily within the “uniform cone” method by using an effective aperture size in Eq. (A-3) rather than the actual diameter. For realistic telescopes with Gaussian beams,

	Factor	
Truncation loss	0.81	(0.9 dB)
Obscuration loss	<u>0.85</u>	(0.7 dB)
Total	0.69	(1.6 dB)

Hence, one typically has $D_{\text{eff}} = \sqrt{0.69} D = 0.83 D$

Equation (A-3) becomes

$$\begin{aligned}
 \theta &= 0.637 \frac{\lambda}{D_{\text{eff}}} \\
 &= 0.637 \frac{\lambda}{0.83 D} \\
 &= 0.77 \frac{\lambda}{D}
 \end{aligned}$$

Therefore, when using the “uniform cone” method, the diametrical beamwidth should be $2 \times 0.77 \lambda/D \sim 1.5 \lambda/D$.

As a final note, it is important that the telescope be pointed accurately compared to the width of the central far-field lobe. This width is typically about $2.4 \lambda/D$ (diameter), so the requirement is

$$\text{pointing error} \ll 2.4 \lambda/D$$

For more information see Ref. 1.

U4-32
108

N86-28279

13148

Maximum Likelihood Estimation of Signal-to-Noise Ratio and Combiner Weight

S. Kalson and S. J. Dolinar
Communications Systems Research Section

An algorithm for estimating signal-to-noise ratio and combiner weight parameters for a discrete time series is presented. The algorithm is based upon the joint maximum likelihood estimate of the signal and noise power. The discrete-time series are the sufficient statistics obtained after matched filtering of a biphas modulated signal in additive white gaussian noise, before maximum likelihood decoding is performed.

I. Introduction and Problem Model

This article investigates maximum likelihood estimation of signal-to-noise ratio and combiner weight parameters for a discrete time series. The discrete time series are the sufficient statistics obtained after matched filtering of a biphas modulated signal (Ref. 1). In order to show the underlying assumptions and limitations of the estimation problem, we first examine the communication system that gives rise to the discrete time series.

We take as our model that given in Fig. 1. The channel encoder maps the binary digital source encoder output $\{I_k\}$ into the binary channel symbols $\{C_k\}$, where the channel symbols are produced with rate $1/T$. The modulation is biphas. That is, the modulator produces the baseband signal

$$s(t) = \sum_k A_k q_k(t) \quad (1)$$

where the $\{A_k\}$ are chosen according to

$$A_k = \begin{cases} -\sqrt{E_s}, & C_k = "0" \\ +\sqrt{E_s}, & C_k = "1" \end{cases} \quad (2)$$

Here, E_s is the channel symbol energy, and the $\{q_k(t)\}$ are orthonormal basis functions. We assume that the $\{q_k(t)\}$ are time-displaced replicas of a single function of duration T , namely,

$$q_k(t) = q(t - (k-1)T) \quad (3)$$

where

$$q(t) = 0, \quad t < 0 \text{ or } t > T \quad (4)$$

$$\int_0^T q(t)^2 dt = 1 \quad (5)$$

The baseband signal $s(t)$ is transmitted over an additive white gaussian noise channel with one-sided noise spectral

density N_0 . The received baseband signal is represented by $x(t)$ in Fig. 1. This received signal is demodulated by matched filtering (integrate and dump) to produce a discrete time series $\{x_k\}$:

$$x_k = \int_{(k-1)T}^{kT} x(t)q(t - (k-1)T) dt \quad (6)$$

Assuming such ideal channel and receiver characteristics as perfect phase tracking and channel symbol synchronization, no channel symbol interference, etc., the output time series from the demodulator are the sufficient statistics for maximum likelihood decoding. Referring to Eqs. (1)–(6), we see that this time series can be written in the form

$$x_k = m_{\text{true}} a_k + \sigma_{\text{true}} b_k \quad (7)$$

where the $\{a_k\}$ are either +1 or -1 depending upon whether the channel symbol transmitted was a “1” or “0,” $\{b_k\}$ are independent and identically distributed gaussian random variables with zero mean and unit variance, and m_{true} and σ_{true} are given by

$$m_{\text{true}} = \sqrt{E_s} \quad (8)$$

$$\sigma_{\text{true}} = \sqrt{N_0/2} \quad (9)$$

The parameters m_{true} and σ_{true} represent the true values of the signal and noise amplitudes, respectively. We note that σ_{true} and m_{true} are by definition non-negative.

In order to make the problem mathematically tractable, we make the assumption that the $\{a_k\}$ are independent and take on the values +1 and -1 with equal probability. For a communication system employing coding, this assumption is not correct. Thus, the effect of coding on the estimation algorithm given here needs to be determined.

II. Parameters to be Estimated

Our starting point for all further analysis is the time series $\{x_k\}$ defined in Eq. (7), with the assumed probabilistic models for the sequence of random variables $\{a_k\}$ and $\{b_k\}$. Our objective is to find maximum likelihood estimates of the signal and noise parameters m_{true} and σ_{true} or of other parameters of interest that are embedded in the model. Two such parameters are signal-to-noise ratio and combiner weight.

The signal-to-noise ratio (SNR) at the receiver is defined as

$$\text{SNR} = E_s/N_0 \quad (10)$$

SNR is a fundamental parameter of interest for a variety of reasons. For example, SNR is needed to optimally choose the quantization levels of the demodulator so that the “best” discrete channel is provided to the channel encoder-decoder (Ref. 2). We find it convenient to define a signal-to-noise ratio parameter ρ_{true} for the demodulated time series as

$$\rho_{\text{true}} = m_{\text{true}}^2/\sigma_{\text{true}}^2 \quad (11)$$

In terms of ρ_{true} , the SNR at the receiver is simply

$$\text{SNR} = \rho_{\text{true}}/2 \quad (12)$$

Another quantity of interest is the combiner weight needed for symbol stream combining. For example, suppose L different time series (or symbol streams) are available from L different receiver-demodulators,

$$x_{ik} = m_i a_k + \sigma_i b_{ik}, \quad i = 1, 2, \dots, L \quad (13)$$

where, as before, $\{a_k\}$ are either +1 or -1, and $\{b_{ik}\}$ are independent, identically distributed gaussian random variables with zero mean and unit variance. It can be shown (Ref. 3) that maximum likelihood decoding of the L time series $\{x_{ik}\}$ is equivalent to maximum likelihood decoding of a single time series $\{y_k\}$, where

$$y_k = \sum_{i=1}^L \alpha_i x_{ik} \quad (14)$$

and the combiner weights $\{\alpha_i\}$ are chosen to be proportional to $\{m_i/\sigma_i^2\}$. Thus, we are interested in estimating for any given time series a combiner weight parameter defined by

$$\alpha_{\text{true}} = m_{\text{true}}/\sigma_{\text{true}}^2 \quad (15)$$

In different applications, we may desire to estimate one, two, or several parameters simultaneously. However, we should always be aware that our assumed problem model has exactly two independent unknown parameters. This implies that any estimate of a single parameter (such as SNR) must be aided by an implicit estimate of an independent auxiliary parameter, and that simultaneous estimates of more than two parameters are not all independent. In particular, maximum likelihood estimation as applied to our problem must produce a joint maximum likelihood estimate of a *pair* of independent parameters.

Fortunately, it is not necessary to re-solve the maximum likelihood equations for every combination of parameters of interest. If two pairs of parameters are related by a one-to-one

transformation, then the corresponding joint maximum likelihood estimates are related by the same transformation (Ref. 4). Thus, we propose finding the joint maximum likelihood estimate of the signal and noise parameters m_{true} and σ_{true} , which we denote as \hat{m} and $\hat{\sigma}$, respectively. Then (ignoring a singularity at $\sigma_{\text{true}} = 0$ or $\hat{\sigma} = 0$) we can define the corresponding maximum likelihood estimates of the signal-to-noise ratio parameter ρ_{true} and the combiner weight parameter α_{true} as

$$\hat{\rho} = \hat{m}^2 / \hat{\sigma}^2 \quad (16)$$

$$\hat{\alpha} = \hat{m} / \hat{\sigma}^2 \quad (17)$$

III. The Log-Likelihood Function

Let us denote a set of N measurements (x_1, x_2, \dots, x_N) by the vector \mathbf{x} . The probability density function of \mathbf{x} conditioned on $m_{\text{true}} = m$ and $\sigma_{\text{true}} = \sigma$ is

$$p(\mathbf{x}|m, \sigma) = \prod_{k=1}^N \frac{1}{2} \frac{1}{\sqrt{2\pi\sigma^2}} \left\{ \exp \frac{-(x_k - m)^2}{2\sigma^2} + \exp \frac{-(x_k + m)^2}{2\sigma^2} \right\} \quad (18)$$

which after a little algebra becomes

$$p(\mathbf{x}|m, \sigma) = \prod_{k=1}^N \frac{1}{\sqrt{2\pi\sigma^2}} \exp \frac{-x_k^2}{2\sigma^2} \exp \frac{-m^2}{2\sigma^2} \cosh \frac{mx_k}{\sigma^2} \quad (19)$$

Taking the natural logarithm of both sides of Eq. (19) gives the log-likelihood function:

$$\ln p(\mathbf{x}|m, \sigma) = -N \ln \sqrt{2\pi} - N \ln \sigma - \frac{1}{2\sigma^2} \sum_{k=1}^N x_k^2 - \frac{Nm^2}{2\sigma^2} + \sum_{k=1}^N \ln \cosh \frac{mx_k}{\sigma^2} \quad (20)$$

IV. The Set of Feasible Solutions

Consider the $\sigma - m$ plane where σ is the abscissa and m is the ordinate. The joint maximum likelihood estimate (MLE)

of σ_{true} and m_{true} is the ordered pair $(\hat{\sigma}, \hat{m})$ in the $\sigma - m$ plane where $\ln p(\mathbf{x}|m, \sigma)$ obtains its maximum. Let us define a set of feasible solutions to the MLE problem as a set of ordered pairs in the $\sigma - m$ plane of which the MLE $(\hat{\sigma}, \hat{m})$ is a member. We wish to find a set of feasible solutions that is as small as possible. Since σ_{true} and m_{true} are non-negative, we can restrict the set of feasible solutions to lie in the first quadrant, including the non-negative σ and m axes.

A necessary condition for a function to obtain its maximum at some point in the *interior* of a closed, bounded region is that its partial derivatives at that point are zero. Although the first quadrant of the $\sigma - m$ plane is not bounded, one can observe from Eq. (18) that for finite $\{x_k\}$, $p(\mathbf{x}|m, \sigma)$ approaches zero for large σ and m . Thus, the maximum of $\ln p(\mathbf{x}|m, \sigma)$ must be contained in some bounded region. Therefore, we include in our set of feasible solutions those points in the first quadrant (excluding the non-negative axes) at which both partial derivatives of $\ln p(\mathbf{x}|m, \sigma)$ with respect to σ and m vanish.

We must separately consider if the maximum might occur on the non-negative axes. Thus, a set of feasible solutions consists of those points in the first quadrant of the $\sigma - m$ plane where both partial derivatives of $\ln p(\mathbf{x}|m, \sigma)$ vanish, and those points on the non-negative axes where $\ln p(\mathbf{x}|m, \sigma)$ obtains a local maximum. Let us first consider the latter.

A. m -Axis Solutions

In the limit as $\sigma \rightarrow 0$ (m -axis), we see from Eq. (18) that $p(\mathbf{x}|m, \sigma)$ is proportional to the product of delta functions given below:

$$\lim_{\sigma \rightarrow 0} p(\mathbf{x}|m, \sigma) \sim \prod_{k=1}^N \{\delta(x_k - m) + \delta(x_k + m)\} \quad (21)$$

In this case, one can see that if there exists some constant c such that $|x_k| = c$ for all k , then $p(\mathbf{x}|m, \sigma)$ is zero everywhere on the m -axis except at $m = c$, where it is unbounded. Conversely, if the $\{x_k\}$ are not all equal in magnitude, then $p(\mathbf{x}|m, \sigma)$ is zero on the entire m -axis. Thus, since $p(\mathbf{x}|m, \sigma)$ is bounded everywhere except possibly the m -axis, we can state that

$$(\hat{\sigma}, \hat{m}) = (0, c) \quad (22)$$

if and only if there exists a c such that $|x_k| = c$ for all k .

B. σ -Axis Solution

For $m = 0$ (σ -axis), we have from Eq. (18) that

$$p(\mathbf{x}|m, \sigma) = \prod_{k=1}^N \frac{1}{\sqrt{2\pi\sigma^2}} \exp \frac{-x_k^2}{2\sigma^2} \quad (23)$$

This is just a unimodal gaussian density function with mean zero. It is well known (Ref. 4) that this function obtains its maximum at

$$\sigma = \sqrt{\frac{1}{N} \sum_{k=1}^N x_k^2}$$

Thus, the only point on the σ -axis that we need to include in the set of feasible solutions is

$$\left(\sqrt{\frac{1}{N} \sum_{k=1}^N x_k^2}, 0 \right) \quad (24)$$

C. Interior First Quadrant Solutions

The other members of the set of feasible solutions are the points in the first quadrant of the $\sigma - m$ plane (excluding the non-negative axes) where the partial derivatives of $\ln p(\mathbf{x}|m, \sigma)$ with respect to σ and m vanish. Thus, we must find those ordered pairs (σ, m) for which both σ and m are positive and simultaneously satisfy

$$\frac{\partial}{\partial \sigma} \ln p(\mathbf{x}|m, \sigma) = 0 \quad (25)$$

and

$$\frac{\partial}{\partial m} \ln p(\mathbf{x}|m, \sigma) = 0 \quad (26)$$

Performing the indicated partial derivatives on Eq. (20) leads to

$$\begin{aligned} \frac{\partial}{\partial \sigma} \ln p(\mathbf{x}|m, \sigma) &= -\frac{N}{\sigma} + \frac{N}{\sigma^3} m^2 + \frac{1}{\sigma^3} \sum_{k=1}^N x_k^2 \\ &\quad - \frac{2m}{\sigma^3} \sum_{k=1}^N x_k \tanh \frac{mx_k}{\sigma^2} \end{aligned} \quad (27)$$

$$\frac{\partial}{\partial m} \ln p(\mathbf{x}|m, \sigma) = \frac{-Nm}{\sigma^2} + \frac{1}{\sigma^2} \sum_{k=1}^N x_k \tanh \frac{mx_k}{\sigma^2} \quad (28)$$

Setting Eq. (28) equal to zero leads to the relation between m and σ :

$$m = \frac{1}{N} \sum_{k=1}^N x_k \tanh \frac{mx_k}{\sigma^2} \quad (29)$$

Using Eq. (29), we can simplify the rightmost term in Eq. (27). Consequently, setting Eq. (27) equal to zero leads to the second relation between m and σ :

$$\sigma^2 + m^2 = \frac{1}{N} \sum_{k=1}^N x_k^2 \quad (30)$$

For simplicity of notation, let us make the definition

$$\langle x^2 \rangle_N \triangleq \frac{1}{N} \sum_{k=1}^N x_k^2 \quad (31)$$

For now, since we are only considering positive σ and m , we see from Eq. (30) that the feasible solutions (σ, m) in the first quadrant (excluding the non-negative axes) must satisfy $0 < \sigma < \sqrt{\langle x^2 \rangle_N}$ and $0 < m < \sqrt{\langle x^2 \rangle_N}$. Using Eq. (30) to solve for σ in terms of m and substituting into Eq. (19), we obtain a transcendental equation in one unknown:

$$m = \frac{1}{N} \sum_{k=1}^N x_k \tanh \frac{mx_k}{\langle x^2 \rangle_N - m^2}, \quad 0 < m < \sqrt{\langle x^2 \rangle_N} \quad (32)$$

Thus, given the measurements $x_k, k = 1, 2, \dots, N$, a set of feasible solutions in the interior first quadrant consists of ordered pairs of the form $(\sqrt{\langle x^2 \rangle_N - m^2}, m)$, where m satisfies Eq. (32). Equivalently, m is one of the roots of the function $F(m, \mathbf{x}) = m - f(m, \mathbf{x})$, where

$$f(m, \mathbf{x}) \triangleq \frac{1}{N} \sum_{k=1}^N x_k \tanh \frac{mx_k}{\langle x^2 \rangle_N - m^2} \quad (33)$$

V. Finding the Roots of $F(m, \mathbf{x})$

Rather than finding the roots of $F(m, \mathbf{x})$ in the range $0 < m < \sqrt{\langle x^2 \rangle_N}$, let us extend this range to $0 \leq m \leq \sqrt{\langle x^2 \rangle_N}$. At first, one may think that we have needlessly increased the size of the set of feasible solutions defined in the last section. However, we will see in this section that finding the roots of $F(m, \mathbf{x})$ in this new range of m includes the feasible solutions on the σ and m axes.

Finding the roots of $F(m, \mathbf{x})$ can be tricky. For example, looking for roots by investigating when $F(m, \mathbf{x})$ changes sign may fail since $F(m, \mathbf{x})$ may contain two or more roots very close together, or may in fact not change sign at a root. However, insight can be gained by observing that the roots of $F(m, \mathbf{x})$ are just the intersection of the curves:

$$z = m \quad (34)$$

and

$$z = f(m, \mathbf{x}) \quad (35)$$

where m is restricted to $0 \leq m \leq \sqrt{\langle x^2 \rangle_N}$.

It is interesting to note that $f(m, \mathbf{x})$ is an even function in x_k . That is, $f(m, \mathbf{x})$ depends on each x_k via its absolute value. This is not surprising since one can see that the conditional probability density function $p(\mathbf{x}|m, \sigma)$ in Eq. (18) depends only on $|x_k|$. Thus, the absolute values of $\{x_k\}$ constitute a sufficient statistic and the sign bit of x_k is not needed. Important properties of $f(m, \mathbf{x})$ are listed in Table 1, where for notational convenience we have made the definitions:

$$\langle |x| \rangle_N = \frac{1}{N} \sum_{k=1}^N |x_k| \quad (36)$$

$$\langle x^4 \rangle_N \triangleq \frac{1}{N} \sum_{k=1}^N x_k^4 \quad (37)$$

We shall now show that the roots of $F(m, \mathbf{x})$ in the range $0 \leq m \leq \sqrt{\langle x^2 \rangle_N}$ include the feasible solutions on the m and σ axes, as given in Eqs. (22) and (24). First, we verify Eq. (24), which specifies the feasible solution on the σ -axis. We see from Table 1, property (i), that $m = 0$ is always a root of $F(m, \mathbf{x})$ for all \mathbf{x} . But when $m = 0$, we have from Eq. (30) that $\sigma = \sqrt{\langle x^2 \rangle_N}$. Thus, the feasible solution $(\sqrt{\langle x^2 \rangle_N}, 0)$ on the σ -axis can be obtained from finding the roots of $F(m, \mathbf{x})$ in the range $0 \leq m \leq \sqrt{\langle x^2 \rangle_N}$.

Next, we show that finding the roots of $F(m, \mathbf{x})$ within the range $0 \leq m \leq \sqrt{\langle x^2 \rangle_N}$ also specifies the feasible solution on the m -axis as given by Eq. (22). It is not too difficult to see from Eq. (22) that $(0, \sqrt{\langle x^2 \rangle_N})$ is the joint MLE if and only if there exists a c such that $|x_k| = c$ for all k . However, it is easily verified that $|x_k| = c$ for all k implies;

$$\sqrt{\langle x^2 \rangle_N} = \langle |x| \rangle_N \quad (38)$$

in which case we have using property (ii) of Table 1:

$$f(\sqrt{\langle x^2 \rangle_N}, \mathbf{x}) = \langle |x| \rangle_N = \sqrt{\langle x^2 \rangle_N} \quad (39)$$

Thus, $m = \sqrt{\langle x^2 \rangle_N}$ is a root of $F(m, \mathbf{x})$ whenever $|x_k| = c$ for all k . Furthermore, for $m = \sqrt{\langle x^2 \rangle_N}$, we have from Eq. (30) that $\sigma = 0$. It thus follows that whenever the ordered pair $(0, \sqrt{\langle x^2 \rangle_N})$ is the joint MLE, it can always be obtained by looking for the roots of $F(m, \mathbf{x})$ in the range $0 \leq m \leq \sqrt{\langle x^2 \rangle_N}$.

Having justified extending the search for the roots of $F(m, \mathbf{x})$ to the range $0 \leq m \leq \sqrt{\langle x^2 \rangle_N}$, let us state what we currently know regarding the roots within this range. As mentioned before, $m = 0$ is always a root of $F(m, \mathbf{x})$. Are there any nonzero roots? To answer this question, we first note that the curve $z = f(m, \mathbf{x})$ is not above the curve $z = m$ at $m = \sqrt{\langle x^2 \rangle_N}$. This is easily verified by invoking Jensen's inequality

$$\langle |x| \rangle_N \leq \sqrt{\langle x^2 \rangle_N} \quad (40)$$

and using property (ii) of Table 1 to yield

$$f(\sqrt{\langle x^2 \rangle_N}, \mathbf{x}) = \langle |x| \rangle_N \leq \sqrt{\langle x^2 \rangle_N} \quad (41)$$

Next, we observe that from property (vi) of Table 1, the curve $z = f(m, \mathbf{x})$ rises above the curve $z = m$ sufficiently near $m = 0$ if and only if the following critical condition is satisfied:

$$\langle x^4 \rangle_N < 3 \langle x^2 \rangle_N^2 \quad (42)$$

Thus, if Eq. (42) is satisfied, the curve $z = f(m, \mathbf{x})$ must intersect the curve $z = m$ for some nonzero m less than or equal to $\sqrt{\langle x^2 \rangle_N}$.

The condition in Eq. (42) is interesting because it parallels an easily verifiable relationship between the corresponding ensemble averages, namely, $E\{x^4\} < 3E\{x^2\}^2$ for $m_{\text{true}} > 0$, and $E\{x^4\} = 3E\{x^2\}^2$ for $m_{\text{true}} = 0$. Thus, a nonzero root of $F(m, \mathbf{x})$ is guaranteed whenever the sample moments $\langle x^4 \rangle_N, \langle x^2 \rangle_N$ bear the same relationship as that relationship between ensemble moments which distinguishes the nonzero-mean case from the zero-mean case.

Finally, we state one more property that is known concerning the roots of $F(m, \mathbf{x})$. As mentioned before, $|x_k| = c$ for all k implies that $m = \sqrt{\langle x^2 \rangle_N}$ is a root of $F(m, \mathbf{x})$. The converse is also true. If $\sqrt{\langle x^2 \rangle_N}$ is a root of $F(m, \mathbf{x})$, then

$$f(\sqrt{\langle x^2 \rangle_N}, \mathbf{x}) = \sqrt{\langle x^2 \rangle_N} \quad (43)$$

and thus from property (ii) we have

$$\langle |x| \rangle_N = \sqrt{\langle x^2 \rangle_N} \quad (44)$$

which implies $|x_k| = c$ for all k , because this is the only condition under which Jensen's inequality, Eq. (40), can be satisfied with equality.

We summarize our results in this section in the following theorem:

Theorem 1

- (1) The feasible solutions are of the form $(\sqrt{\langle x^2 \rangle_N - m^2}, m)$, where m is a root of $F(m, \mathbf{x})$ in the range $[0, \sqrt{\langle x^2 \rangle_N}]$.
- (2) (a) $F(m, \mathbf{x})$ always has the root $m = 0$ for all \mathbf{x} .
 (b) $F(m, \mathbf{x})$ has the root $m = \sqrt{\langle x^2 \rangle_N}$ if and only if $|x_k| = \sqrt{\langle x^2 \rangle_N}$ for all k .
 (c) If $\langle x^4 \rangle_N < 3 \langle x^2 \rangle_N^2$, then there exists a non-zero root of $F(m, \mathbf{x})$ less than or equal to $\sqrt{\langle x^2 \rangle_N}$.

In Fig. 2, we have sketched $z = m$ and a hypothetical $z = f(m, \mathbf{x})$ satisfying Eq. (42). For sake of simplicity, we have drawn the curves so that there are only two intersections.

Unfortunately, Theorem 1 is all that we know regarding $F(m, \mathbf{x})$. Several pertinent questions are: If Eq. (42) is satisfied, is there only one non-zero root? If Eq. (42) is not satisfied, are there any non-zero roots? And, finally, when there is more than one root, which one corresponds to the MLE? These questions have been very difficult to answer analytically. It would be "nice" if there were only one non-zero root when Eq. (42) is satisfied, and no non-zero roots otherwise. A few plots of $F(m, \mathbf{x})$ indicate that this might be so. Properties of $F(m, \mathbf{x})$ which might give some indication about the number of roots are currently being investigated. We are also in the process of looking for counterexamples.

VI. An Algorithm for an Upper Bound of the MLE

Although Theorem 1 is somewhat incomplete concerning the number of roots of $F(m, \mathbf{x})$, we can nevertheless give an algorithm for finding the largest root, which provides an upper bound to our signal-to-noise ratio and combiner weight estimators. We suspect that this upper bound is indeed the MLE and we show later that this is true in the large SNR case.

Let m^* denote the largest root of $F(m, \mathbf{x})$, where $0 \leq m^* \leq \sqrt{\langle x^2 \rangle_N}$. A graphical representation of the algorithm for finding m^* is given in Fig. 3. At the i th iteration, $m^{(i)}$ is some estimate of m^* , where $m^{(i)} \geq m^*$. As the figure indicates, the better estimate $m^{(i+1)}$ is obtained by following the paths labeled (1), (2), and (3). One can see that the estimate $m^{(i+1)}$ is closer to m^* than the previous estimate $m^{(i)}$, but is still larger than m^* . From Fig. 3, we see that $m^{(i+1)}$ is given simply by the recursion

$$m^{(i+1)} = f(m^{(i)}, \mathbf{x}) \quad (45)$$

The zeroth estimate of m^* is

$$m^{(0)} = \sqrt{\langle x^2 \rangle_N}$$

Thus, performing Eq. (45) for $i = 0, 1, \dots$, generates the sequence of estimates $m^{(1)} > m^{(2)} > \dots$. It can be shown that this sequence converges to m^* . Since m^* is the largest root of $F(m, \mathbf{x})$, we see that upper bounds to our estimators are

$$\hat{\rho} = \frac{\hat{m}^2}{\hat{\sigma}^2} \leq \lim_{i \rightarrow \infty} \frac{[m^{(i)}]^2}{\langle x^2 \rangle_N - [m^{(i)}]^2} \quad (46)$$

$$\hat{\alpha} = \frac{\hat{m}}{\hat{\sigma}^2} \leq \lim_{i \rightarrow \infty} \frac{m^{(i)}}{\langle x^2 \rangle_N - [m^{(i)}]^2} \quad (47)$$

To obtain a qualitative understanding of how the rate of convergence of such an algorithm depends on SNR, let us make the definition:

$$\Delta^{(i)} \triangleq m^{(i)} - m^* \quad (48)$$

By the mean value theorem, there exists some m_0 between m^* and $m^{(i)}$ such that

$$\Delta^{(i+1)} = m^{(i+1)} - m^* = f(m^{(i)}, \mathbf{x}) - f(m^*, \mathbf{x}) = \left. \frac{\partial f}{\partial m} \right|_{m=m_0} \Delta^{(i)} \quad (49)$$

Equation (49) gives us some idea about the rate of convergence of the algorithm. For example, in the case of high SNR, m^* should be close to $\sqrt{\langle x^2 \rangle_N}$ and in this case the partial derivative of $f(m, \mathbf{x})$ should be close to zero. Thus, one can see from Eq. (49) that $\Delta^{(i)}$ would approach zero very rapidly. On the other hand, for low SNR, one would expect that m^* would be closer to zero, and consequently the partial derivative of $f(m, \mathbf{x})$ would be closer to its derivative at the origin, which is one. In this case the convergence would be very slow.

An algorithm for finding a root close to m^* is given by the flow diagram in Fig. 4. The variable TOL is a pre-assigned tolerance for the difference between two successive estimates of m^* . Also, a limit to the number of iterations of the algorithm is set by the variable NUM. This is needed in the low SNR case where the convergence of the estimate to m^* may be asymptotically slow.

VII. The High SNR Case

It is interesting to consider the high SNR case, especially since this serves as a check on our method. In the high SNR case, the $\{x_k\}$ will most likely be nearly equal in magnitude. Then, from Jensen's inequality, Eq. (40), $\langle |x| \rangle_N$ would be close to, but less than $\sqrt{\langle x^2 \rangle_N}$. Thus, from Fig. 3, we expect the intersection of the curves $z = m$ and $z = f(m, \mathbf{x})$ to be close to $\sqrt{\langle x^2 \rangle_N}$, in which case just one iteration of the algorithm of Fig. 4 would yield a close estimate of m^* , given below.

$$m^* \approx m^{(1)} = f(\sqrt{\langle x^2 \rangle_N}, \mathbf{x}) = \langle |x| \rangle_N, \text{ for SNR} \rightarrow \infty \quad (50)$$

If we use the above for m^* , then the signal-to-noise ratio estimate is

$$\hat{\rho} \approx \frac{\langle |x| \rangle_N^2}{\langle x^2 \rangle_N - \langle |x| \rangle_N^2} \quad (51)$$

which asymptotically equals the usual signal-to-noise ratio estimate for the high SNR case (Ref. 5).

VIII. Summary

The main result of this memo is an algorithm for finding upper bounds to the maximum likelihood estimates of signal-to-noise ratio and combiner weights. Further work is needed to determine if these upper bounds equal the maximum likelihood estimates.

Acknowledgment

The authors would like to acknowledge several interesting discussions with V. Vilnrotter, L. Swanson, and J. Yuen.

References

1. Yuen, J. H., Ed., *Deep Space Telecommunications Systems Engineering*, Plenum, New York, N.Y., 1983.
2. Massey, J., "Coding and Modulation in Digital Communications," *1974 Int. Zurich Seminar on Digital Communications*, pp. E2 (1), (2), (3), (4), Zurich, Switzerland, 1974.
3. McEliece, R. J., Pollara, F., and Swanson, L., "Symbol Stream Combining in a Convolutionally Coded System," *TDA Progress Report 42-81*, pp. 47-50, Jet Propulsion Laboratory, Calif., May 15, 1985.
4. Van Trees, H. L., *Detection, Estimation, and Modulation Theory*, McGraw-Hill, New York, N.Y., 1968.
5. Gilchrist, C. E., "Signal-to-Noise Monitoring," in *Supporting Research and Advanced Development*, Space Programs Summary 37-27, Vol. IV, pp. 169-184, Jet Propulsion Laboratory, Pasadena, Calif., June 30, 1964.

Table 1. Properties of $f(m, x)$

$$f(0, x) = 0 \quad (\text{i})$$

$$\lim_{m \rightarrow \sqrt{\langle x^2 \rangle_N}} f(m, x) = \langle |x| \rangle_N \quad (\text{ii})$$

$$\left. \frac{\partial f}{\partial m} \right|_{m=0} = 1 \quad (\text{iii})$$

$$\left. \frac{\partial f}{\partial m} \right|_{m \rightarrow \sqrt{\langle x^2 \rangle_N}} = 0 \quad (\text{iv})$$

$$f(m, x) \text{ is monotonically increasing in } m \quad (\text{v})$$

To third order in m :

$$f(m, x) \sim m + \frac{m^3}{\langle x^2 \rangle_N} \left[1 - \frac{\langle x^4 \rangle_N}{3 \langle x^2 \rangle_N^2} \right] \quad (\text{vi})$$

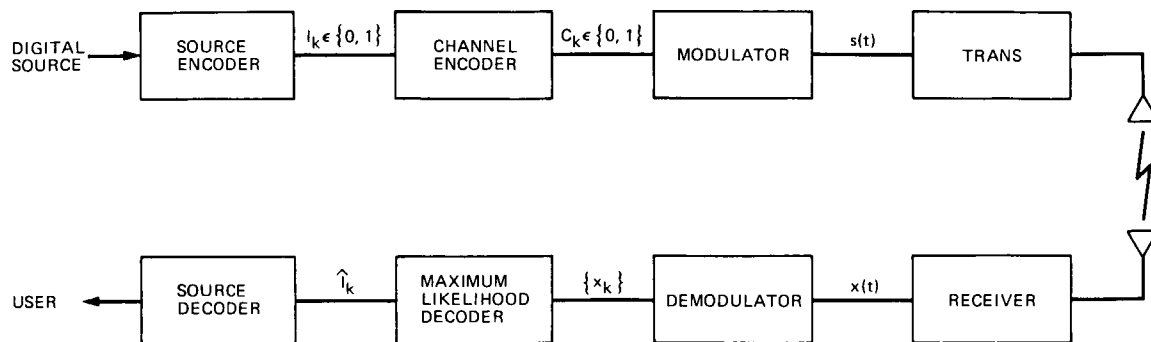


Fig. 1. Model of communication system

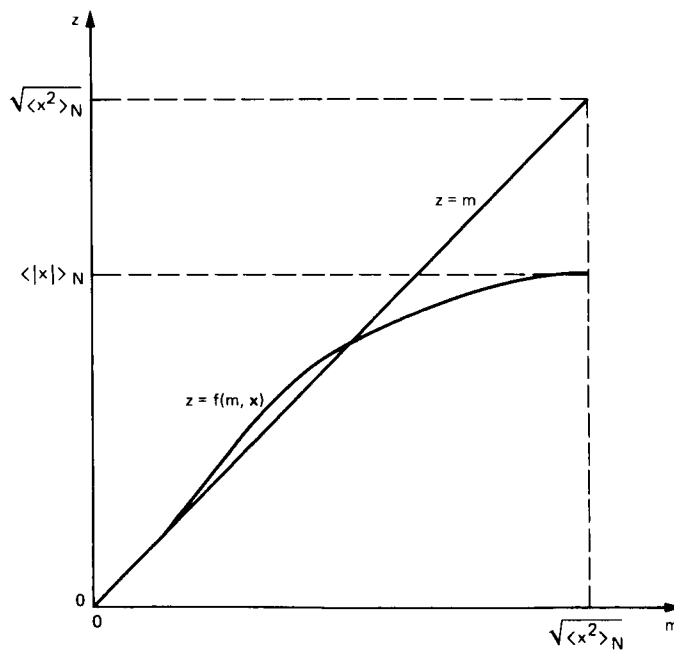


Fig. 2. Sketch of $z = m$ and $z = f(m, x)$

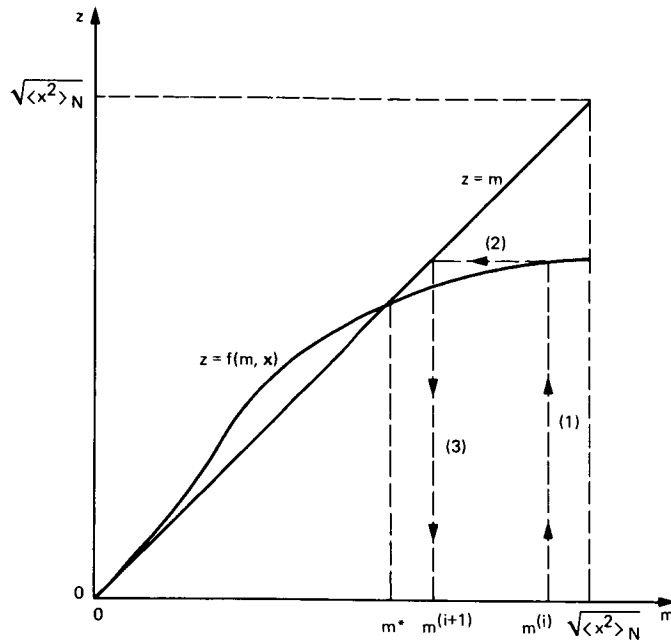


Fig. 3. Graphical representation of an iterative procedure to find m^*

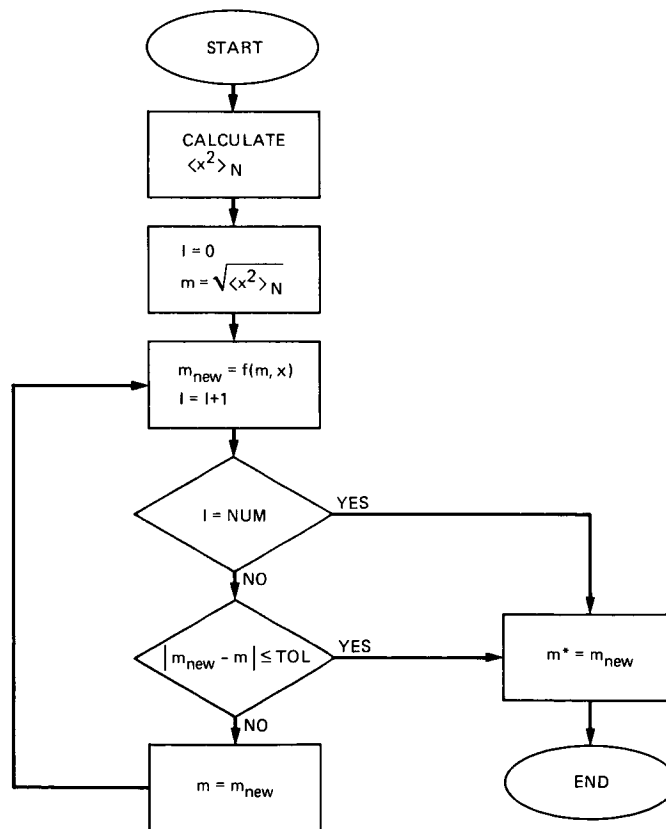


Fig. 4. Algorithm for finding m^*

D5-32

118

N86-28280

13149

A VLSI Pipeline Design of a Fast Prime Factor DFT on a Finite Field

T. K. Truong, I.S. Hsu, and H. M. Shao
Communications Systems Research Section

I.S. Reed and H. C. Shyu
Department of Electrical Engineering
University of Southern California

~~In this article~~, a conventional prime factor discrete Fourier transform (DFT) algorithm is used to realize a discrete Fourier-like transform on the finite field, $GF(q^n)$. A pipeline structure is used to implement this prime factor DFT over $GF(q^n)$. This algorithm is developed to compute cyclic convolutions of complex numbers and to decode Reed-Solomon codes. Such a pipeline fast prime factor DFT algorithm over $GF(q^n)$ is regular, simple, expandable, and naturally suitable for VLSI implementation. An example illustrating the pipeline aspect of a 30-point transform over $GF(q^n)$ is presented.

W. K. S. S. S.

sub n

sub n

I. Introduction

Let $GF(q^n)$ be a finite field, where q is a prime number. A discrete Fourier-like transform over $GF(q^n)$ is defined by

$$A_k = \sum_{n=0}^{d-1} a_n \alpha^{nk} \text{ mod } q, 0 \leq k \leq d-1 \quad (1)$$

where $A_k, a_n \in GF(q^n)$, α is the d th root of unity in $GF(q^n)$ and $d | q^n - 1$.

In some applications of finite field transforms to coding and digital filters, the transform length d is not a power of two. Thus, the usual FFT algorithm cannot be used to calculate transforms of as many as d points.

In this article it will be shown that if $d = d_1 \cdot d_2 \cdot \dots \cdot d_r$, where $(d_i, d_j) = 1$ for $i \neq j$, then the transform in Eq. (1) and

its inverse can be calculated by the fast prime factor DFT algorithm (Refs. 1-3). The prime factor DFT algorithm is based on the use of the Chinese remainder theorem (Ref. 4). In this algorithm, the one-dimensional d -point Fourier transform over $GF(q^n)$ is converted into an r -dimensional, d_i -point, (for $i = 1, 2, \dots, r$) Fourier transforms over $GF(q^n)$. This algorithm is called a prime factor DFT algorithm over $GF(q^n)$.

A primary advantage of the prime factor DFT is that the VLSI processor for computing a d -point transform over $GF(q^n)$ is composed only of $d_1 + d_2 + \dots + d_r$ basic cells. Each basic cell performs a sum and product operation in $GF(q^n)$.

It is well known that the systolic array of a DFT computation requires d basic cells (Ref. 5). Therefore, the number of basic cells of a prime factor DFT algorithm over $GF(q^n)$ are

substantially fewer than the systolic array implementation of the DFT. Of course, this advantage must be weighed against the difficulty of the rearrangement of two input and output sequences of d samples in the VLSI implementation.

In this article, a pipeline structure for rearranging input and output data is developed for a prime factor DFT over $GF(q^n)$. As a consequence, a pipeline fast prime factor DFT over $GF(q^n)$ can be developed. Finally, it is shown that a pipeline fast prime factor DFT over $GF(2^8)$ can be used to decode a (255,223) Reed-Solomon Code (Ref. 6) and that a pipeline fast prime factor DFT over $GF(q^2)$, where $q = 2^p - 1$ is a Mersenne prime, can be used to compute the cyclic convolutions of two sequences of $8 \cdot p$ symbols.

II. A Pipeline Fast Prime Factor DFT Over $GF(q^n)$

In this section a method for computing a d -point DFT over $GF(q^n)$, based on the Chinese remainder theorem, is investigated.

Let $d = d_1 \cdot d_2 \dots d_r$, where $(d_i, d_j) = 1$ for $i \neq j$, and also let k and n in Eq. (1) be represented by the r -tuple (k_1, k_2, \dots, k_r) and (n_1, n_2, \dots, n_r) , respectively, where $k_j \equiv k \pmod{d_j}$ and $n_j \equiv n \pmod{d_j}$ for $1 \leq j \leq r$. By the use of the Chinese remainder theorem, it is shown (Ref. 4) that a d -point DFT over $GF(q^n)$ in Eq. (1) can be decomposed into an r , d_i -point, DFTs ($i = 1, 2, \dots, r$). In other words, the computation of A_k given in Eq. (1) can be written explicitly in terms of the d_i th root of unit in $GF(q^n)$ as

$$A_k = A_{(k_1, k_2, \dots, k_r)} = \sum_{n_1=0}^{d_1-1} \sum_{n_2=0}^{d_2-1} \dots \sum_{n_r=0}^{d_r-1} a_{(n_1, n_2, \dots, n_r)} \alpha_1^{n_1 k_1} \alpha_2^{n_2 k_2} \dots \alpha_r^{n_r k_r} \text{ for } 1 \leq k_j \leq d_j \quad (2)$$

where

$$\alpha_j = \alpha^{(d_1 d_2 \dots d_{j-1} d_{j+1} \dots d_r) d_j^{-1}}$$

with

$$(d_1 d_2 \dots d_{j-1} d_{j+1} \dots d_r) \cdot d_j^{-1} \equiv 1 \pmod{d_j}$$

and $(d_j^{-1}, d_j) = 1$ (for $j = 1, 2, \dots, r$) is a d_j th root of unity in $GF(q^n)$ (Ref. 6).

From Eq. (2), this algorithm consists of the following r stages:

Stage 1

$$A_{(k_1, i_2, \dots, i_r)}^1 = \sum_{n_1=0}^{d_1-1} a_{(n_1, n_2, \dots, n_r)} \alpha_1^{n_1 k_1}, \quad 0 \leq k_1 \leq d_1 - 1 \quad (3)$$

Stage 2

$$A_{(k_1, k_2, \dots, i_r)}^2 = \sum_{i_2=0}^{d_2-1} A_{(k_1, i_2, \dots, i_r)}^1 \alpha_2^{n_1 k_1}, \quad 0 \leq k_2 \leq d_2 - 1$$

Stage r

$$A_j = A_{(k_1, k_2, \dots, k_r)}^r = \sum_{i_r=0}^{d_r-1} A_{(k_1, k_2, \dots, k_{r-1}, i_r)}^{r-1} \alpha_r^{n_r k_r}, \quad 0 \leq k_r \leq d_r - 1$$

Instead of computing Eq. (3) directly, an alternate pipeline technique can be developed to compute Eq. (3). To see this, let $d = d_1 \cdot d_2 \dots d_r = d_1^{(1)} \cdot d_2^{(1)}$, where $d_1^{(1)} = d_1 \cdot d_2 \dots d_{r-1}$, $d_2^{(1)} = d_r$ and $(d_1^{(1)}, d_2^{(1)}) = 1$. Thus, by Eq. (3) a one-dimensional transform of d samples can be converted into a two $d_i^{(1)}$ -point transforms, for $i = 1, 2$. In a similar fashion, the one-dimensional transform for $d_i^{(1)}$ can be converted into two $d_i^{(2)}$ -point transforms, for $i = 1, 2$, where $d_1^{(2)} = d_1 \cdot d_2 \dots d_{r-2}$ and $d_2^{(2)} = d_{r-1}$, and so forth. This algorithm is called a pipeline prime factor DFT algorithm on $GF(q^n)$. It is shown in the next section that this new algorithm can be readily implemented in VLSI technology.

III. VLSI Design for Computing a Pipeline Fast Prime Factor DFT Over $GF(q^n)$

A VLSI processor for computing Eq. (1), composed of d basic cells, is now developed, using the direct approach. Each basic cell performs a sum and product operation in $GF(q^n)$. That is, $a \leftarrow a + b \cdot c$, where " \leftarrow " denotes the operation "is replaced by." The VLSI architecture of the DFT over $GF(q^n)$ using a method similar to the systolic array technique is illustrated in the following example.

Example 1. Architecture of a 6-point DFT using the direct systolic array technique.

A 6-point DFT over $GF(q^n)$ is defined by

$$A_k = \sum_{n=0}^{6-1} a_n \alpha^{nk}$$

where a is a 6th root of unity in $GF(q^n)$. A VLSI architecture structure for computing this transform over $GF(q^n)$ is shown in Fig. 1. This architecture contains six basic cells. The principal function of each basic cell is to perform the operation $a \leftarrow a + b \cdot c$. In this example α^{nk} , which is stored in the registers A_k for $0 \leq k \leq 5$, is assumed to be precomputed.

First, the complex symbol sequence a_n for $0 \leq n \leq 5$ is sent to all of the cells, simultaneously. Assume initially that all registers are set to zero. After the input data are entered, the components of A_k in Eq. (1) are contained in registers B_k for $0 \leq k \leq 5$. The values computed in this manner are shifted sequentially out of register B_0 .

The application of Eq. (3) to the VLSI design of a d -point DFT is illustrated in the following example.

Example 2. Architecture of a 6-point DFT given in Eq. (1) using Eq. (3).

Since $d = d_1 \cdot d_2 = 3 \cdot 2$, by Eq. (3) one obtains a 6-point DFT as

$$A_{(n_1, k_2)}^1 = \sum_{n_2=0}^{2-1} a_{(n_1, n_2)} \alpha_2^{n_2 k_2} \quad (4a)$$

$$A_k = A_{(k_1, k_2)}^2 = \sum_{n_1=0}^{3-1} A_{(n_1, k_2)}^1 \alpha_1^{n_1 k_1} \quad (4b)$$

where $\alpha_2 = \alpha^3$ and $\alpha_1 = \alpha^4$ are the 2nd and 3rd roots of unity in $GF(q^n)$.

To compute Eq. (4a), first, one maps the input index n into a pair of indices n_1 and n_2 , where $n_1 \equiv n \pmod{3}$ and $n_2 \equiv n \pmod{2}$. That is, $a_0 \rightarrow a_{(0,0)}$, $a_1 \rightarrow a_{(1,1)}$, $a_2 \rightarrow a_{(2,0)}$, $a_3 \rightarrow a_{(0,1)}$, $a_4 \rightarrow a_{(1,0)}$, and $a_5 \rightarrow a_{(2,1)}$. The method used to convert a_n to $a_{(n_1, n_2)}$ is described in Example A.1 in the appendix.

The pipeline structure for computing the 6-point DFT given above in Example 2 is shown in Fig. 2. This pipeline architecture makes possible an efficient design with fewer cells and a small loss in throughput rate.

In this figure, the input sequence a_n , first, is shifted sequentially into the memory A , which is composed of six registers A_0, A_1, \dots , and A_5 . Then, each column of memory A is shifted right out of the last column into the unit of the 2-point DFT. Then each column of A is cyclically shifted up by one symbol, except for the first column.

Simultaneously, a 2-point transform of the first column is computed by the direct systolic array method. These operations are continued repeatedly until the first column of memory A is shifted out of the circuit. The components of $A_{(n_1, k_1)}^1$ are obtained in memory B .

Finally, two 3-point transforms of the first and second rows of memory B are calculated by Eq. (4b). The components of $A_{(k_1, k_2)}$ are obtained in memory C (see Fig. 2).

The method used to rearrange the output data from $A_{(k_1, k_2)}$ back to A_k is illustrated for Example A.1 in the appendix. Each column of memory C is shifted up and out of the first row and then into the last stage. After this, each row of C is cyclically shifted right by one symbol except for the third row. These operations are continued repeatedly until the last row of memory C is shifted out of the circuit.

The first three samples, A_0 through A_2 , are obtained by switching them to the output line of memory C . The next three samples are obtained by switching them to the other output line with a three-stage delay element (see Fig. 2).

If a structure similar to that used in Example 2 is used recursively, the general pipeline fast prime factor DFT algorithm over $GF(q^n)$ can be obtained. This is illustrated by the following example.

Example 3. Architecture of a $d = d_1 \cdot d_2 = 5 \times 6$ -point DFT over $GF(q^n)$ using Eq. (3)

To compute this 30-point DFT over $GF(q^n)$, first, one computes the two-dimensional 5×6 DFT over $GF(q^n)$ by

$$A_{(n_2, k_2)}^1 = \sum_{n_2=0}^{5-1} a_{(n_1, n_2)} \alpha_2^{n_2 k_2} \quad (5a)$$

and

$$A_{(k_1, k_2)} = \sum_{n_1=0}^{5-1} A_{(n_1, k_2)}^1 \alpha_1^{n_1 k_1} \quad (5b)$$

where $\alpha_1 = \alpha^6$ and $\alpha_2 = \alpha^{25}$ are the 5th and 6th roots of unity in $GF(q^n)$, respectively.

To compute Eq. (5a), one needs to convert a_n into $a_{(n_1, n_2)}$, where $n_1 \equiv n \pmod{5}$ and $n_2 \equiv n \pmod{6}$. The procedure for rearranging this input sequence is given in Example A.2 in the appendix. Then, the 6-point DFT over $GF(q^n)$ in Eq. (5a) can be decomposed into a two-dimensional 3×2 transform. This 2-D transform can be implemented by Example 2.

A 5-point DFT over $GF(q^n)$ in Eq. (5b) can be computed by the direct systolic array method. Finally, the resulting data $A_{(k_1, k_2)}$ is arranged in the reverse manner back to A_k (see Example A.2 in the appendix). A pipeline architecture for implementing a prime factor 30-point DFT over $GF(q^n)$ is shown in Fig. 3.

In Fig. 3, one observes that one needs to permute the index n_2 of the last column of $d_2 = 6$ symbols in matrix A and the index k_2 of the first row of $d_2 = 6$ symbols in matrix C , where $n_2 \equiv n \pmod{6}$ and $k_2 \equiv k \pmod{6}$. Thus, in order to reduce the number of permutations in the hardware, one should choose $d_2 < d_1$, where $d = d_1 \cdot d_2$. Then, one needs only to permute the index n_2 of the sequence of d_2 symbols.

In Example 3, if one chooses $d = d_1 \cdot d_2 = 6 \cdot 5$, then one does not need to permute the index n_2 of the last column of $d_2 = 5$ symbols in a 6×5 matrix. In general, if $d_1 - d_2 = 1$, then no permutations are needed for index n_2 .

IV. Applications

In this section it is shown that a pipeline fast prime DFT over $GF(q^n)$ has application to future designs of coding and digital signal processors.

A. Coding

It is shown (Ref. 6) that a 255-point transform over $GF(2^8)$ can be used to decode a (255,233) Reed-Solomon Code. Since the transform length of this transform is $d = 255 = 17 \times 5 \times 3 = 17 \times 15 = d_1 \cdot d_2$, the transform can be computed by an algorithm similar to that used in Example 2. Thus, a pipeline fast prime factor DFT algorithm over $GF(2^8)$ can be used to decode a (255,223) Reed-Solomon Code.

The arithmetic needed to compute the 255-point transform over $GF(2^8)$ in RS decoder requires only $3 + 5 + 17 = 25$ basic cells. Each basic cell performs a sum and product operation over $GF(2^8)$.

B. Digital Signal Processor

Recently the authors (Ref. 7) defined transforms over $GF(q^2)$ of the form

$$A_k \equiv \sum_{n=0}^{d-1} a_n \alpha^{nk} \pmod{q}$$

where $q = 2^p - 1$ is a Mersenne prime, α is a d th root of unit in $GF(q^2)$ and $d|q^2 - 1$. They showed that the convolution of two finite sequences of d samples can be obtained as the inverse transform of the product of their transforms.

Nussbaumer in Ref. 8 showed that the complex integer $(1 + i)$ is an $8 \cdot p$ th root of unity in $GF(q^2)$. Multiplications by powers of $(1 + i)$ can be performed by simple bit rotations. As a consequence, the operations needed to compute an $8 \cdot p$ -point transform over $GF(q^2)$ requires only cyclic shifts and additions.

If one uses the direct systolic array method, the VLSI processor needed to compute the above $8 \cdot p$ -point transform over $GF(q^2)$ would require $8 \cdot p$ basic cells. Each basic cell of this transform performs only a sum and cyclic shift in $GF(q^2)$.

Before developing further the pipeline fast prime factor DFT over $GF(q^2)$, consider further some properties of the finite field, $GF(q^n)$.

Theorem 1. Let $GF(q^n)$ be a finite field. Also let $d = d_1^{n_1} \cdot d_2^{n_2} \cdot \dots \cdot d_r^{n_r}$, where $(d_i, d_j) \neq 1$ for $i \neq j$ and $d|q^n - 1$. Then, α is an element of order d in $GF(q^n)$ if and only if $\alpha^{d/d_i} \neq 1 \pmod{q}$ for $i = 1, 2, \dots, r$.

Proof. If α is an element of order d , then d is the smallest integer such that

$$\alpha^d \equiv 1 \pmod{q}$$

This implies $\alpha^{d/d_i} \neq 1 \pmod{q}$.

Assume α is not an element of order d . Then, the order of α is $O(\alpha) \neq d$, where $O(\alpha)$ denotes an order of α . Thus, there exists $h \neq 1$ such that

$$d = d_1^{n_1} \cdot d_2^{n_2} \cdot \dots \cdot d_r^{n_r} = h \cdot O(\alpha) \quad (6)$$

By (Ref. 6), one observes that $d_i|h$ for some i . Therefore,

$$\alpha^{d/d_i} \equiv 1 \pmod{q}$$

Corollary 1. If α is an element of order of d in $GF(q^n)$, then α^j is also an element of order d for $(j, d) = 1$.

Proof. Since $(j, d) = 1$, then $d_i \nmid j$, where d_i is a prime factor of d . Thus,

$$(\alpha^j)^{d/d_i} \equiv (\alpha^{d/d_i})^j \equiv (\alpha_i)^j \pmod{q}$$

where $\alpha_i = \alpha^a$ is an element of order d_i and $a = d/d_i$.

Assume

$$\alpha_i^j \equiv 1 \pmod{q}$$

Then, j must be a multiple of d_i . But $(j, d_i) = 1$. Hence $(\alpha^a)^j \not\equiv 1 \pmod{q}$, i.e., $(\alpha^j)^{d/d_i} \not\equiv 1 \pmod{q}$. By Theorem 1, α^j is an element of order of α for $(j, d) = 1$.

From Corollary 1, one observes that the number of elements of order d in $GF(q^n)$ is $\phi(d)$, where $\phi(d)$ denotes Euler's Function.

Corollary 2. Let $GF(q^2)$ be a Golois field, where $q = 2^p - 1$ is a Mersenne prime, an $8 \cdot p$ th root of unity in $GF(q^2)$ is $(1 + i)$.

Proof. First note the identity

$$(1 + i)^{8p/p} \equiv (1 + i)^8 \equiv 2^4 \not\equiv 1 \pmod{q}$$

and

$$\begin{aligned} (1 + i)^{8p/2} &\equiv (1 + i)^{4p} \equiv (-2^2)^p \equiv -2^{2p} \\ &\equiv -1 \not\equiv 1 \pmod{q} \end{aligned}$$

Thus, by Theorem 1, it follows that $(1 + i)$ is an $8 \cdot p$ th root of unity in $GF(q^2)$.

Corollary 3. Let $GF(q^2)$ be a Golois field, where $q = 2^p - 1$ is a Mersenne prime, 2^j is a p th root of unity in $GF(q^2)$ for $j = 1, 2, \dots, p-1$.

Proof. First note the identity

$$2^{p/p} \equiv 2 \not\equiv 1 \pmod{q}$$

Thus, by Theorem 1, it follows that 2 is a p th root of unity in $GF(q^2)$. Also by Corollary 1, 2^j is also a p th root of unity in $GF(q^2)$ for $(j, p) = 1$, i.e., $j = 1, 2, \dots, p-1$.

Corollary 4. Let $GF(q^2)$ be a Golois field, where $q = 2^p - 1$ is a Mersenne prime. An 8th root of unity in $GF(q^2)$ is in one of forms $\pm 2^{(p-1)/2} (1 \pm i) \pmod{q}$.

Proof. First note the identity

$$2^{(p-1)/2} (1 + i)^4 \equiv 2^{2(p-1)} (1 + i)^4 \equiv 2^{-2} (-2^2) \equiv -1 \pmod{q}$$

Thus, by Theorem 1, it follows that $2^{(p-1)/2} (1 + i)$ is an 8th root of unity in $GF(q^2)$. Also, by Corollary 1, $(2^{(p-1)/2} (1 + i))^j$ for $j = 3, 5, 7$, are 8th roots of unity in $GF(q^2)$. That is,

$$\begin{aligned} \left(2^{(p-1)/2} (1 + i)\right)^3 &\equiv 2^{(p-1)/2} (1 + i) 2^{p-1} (1 + i)^2 \\ &\equiv 2^{(p-1)/2} (-1 + i) \pmod{q} \\ \left(2^{(p-1)/2} (1 + i)\right)^5 &\equiv 2^{(p-1)/2} (1 + i) \left(2^{(p-1)/2} (1 + i)\right)^4 \\ &\equiv -2^{(p-1)/2} (1 + i) \pmod{q} \end{aligned}$$

and

$$\begin{aligned} \left(2^{(p-1)/2} (1 + i)\right)^7 &\equiv 2^{(p-1)/2} (1 + i) \left(2^{(p-1)/2} (1 + i)\right)^6 \\ &\equiv -2^{(p-1)/2} (-1 + i) \end{aligned}$$

Therefore, an 8th root of unity in $GF(q^2)$ is in one of forms $\pm 2^{(p-1)/2} (1 \pm i) \pmod{q}$.

By Corollary 2, for $p = 31$, $(1 + i)$ is a $31 \cdot 8$ th of unity in $GF(q^2)$. If we let $d = d_1 \cdot d_2 = 31 \cdot 8$, then a $31 \cdot 8$ -point transform over $GF(q^2)$ is

$$A_k = \sum_{n=0}^{31 \cdot 8 - 1} a_n \alpha^{nk} \quad (7)$$

where $\alpha = (1 + i)$ is a $8 \cdot p$ th root of unity in $GF(q^2)$.

From Eq. (3), the transform given in Eq. (7) consists of the following two stages:

$$A_{(n_1, k_2)}^1 \equiv \sum_{n_2=0}^{8-1} a_{(n_1, n_2)} \alpha_2^{n_2 k_2} \pmod{q} \quad (8a)$$

and

$$A_k = A_{(k_1, k_2)}^2 \equiv \sum_{n_1=0}^{31-1} A_{(n_1, k_2)}^1 \alpha_1^{n_1 k_1} \pmod{q} \quad (8b)$$

where $\alpha_2 = (1 + i)^{2^{17}} = 2^{15} (1 - i)$ and $\alpha_1 = (1 + i)^{32} = 2^{12}$.

If one uses an algorithm similar to that used in Example 3, a pipeline structure can be used to implement Eqs. (8a) and (8b). For $p = 31$, the VLSI processor for computing an $8 \cdot p$ -point transform over $GF(q^2)$ is only composed of $8 + 31 = 39$ basic cells. Each basic cell in this transform performs only a summation and cyclic shifts.

V. Concluding Remarks

It has been shown that a conventional prime factor discrete Fourier transform (DFT) algorithm can be used to realize a discrete Fourier-like transform on the field $GF(q^n)$.

This algorithm can also be used to compute cyclic convolutions of complex numbers and to decode Reed-Solomon codes. A primary advantage of the prime factor DFT is that the number of VLSI processors needed is substantially fewer than that of the more conventional systolic array implementation. The difficulty of the rearrangement of two input and output sequences of samples in the VLSI implementation was shown to be a soluble problem. As a consequence, a pipeline fast prime factor DFT over $GF(q^n)$ can be developed.

It is possible to use the pipeline fast prime factor DFT over $GF(2^8)$ in decoding a Reed-Solomon code. Furthermore, a pipeline fast prime factor DFT over $GF(q^2)$, where $q = 2^p - 1$ is a Mersenne prime, can be used to compute the cyclic convolutions of two sequences of $8 \cdot p$ symbols.

Acknowledgment

The authors wish to thank Dr. L. J. Deutsch of JPL for his helpful suggestions made during the preparation of this article.

References

1. Good, I. J., "The Interaction Algorithm and Practical Fourier Analysis," *J. Royal Statist. Soc.*, Ser. B, Vol. 20, pp. 361-372, 1958, "Addendum," Vol. 22 (MR 21 1674; MR 23 A4231), pp. 372-375, 1960.
2. Thomas, L. H., "Using A Computer to Solve Problems in Physics," in *Applications of Digital Computers*, Gion and Co., Boston, Mass., 1963.
3. Kolba, D. P., and Parks, T. W., "A Prime Factor FFT Algorithm Using High-Speed Convolution," *IEEE Trans. on Acoustics, Speed, and Signal Processing*, Vol. ASSP-25, No. 4, pp. 281-294, August 1977.
4. McClellan, J., and Rader, C., "Number Theory in Digital Signal Processing," Prentice-Hall, Englewood Cliffs, N.J., 1979.
5. Mead, C., and Conway, L., *Introduction to VLSI Systems*, Chapter 8, Addison-Wesley Publishing Co., Reading, Mass., 1980.
6. Reed, I. S., Troung, T. K., Miller, R. L., and Huang, J. P., "Fast Transforms for Decoding Reed-Solomon Codes," *IEE Proc.*, Vol. 128, Pt. F, No. 1, February 1981.
7. Reed, I. S., and Truong, T. K., "The Use of Finite Fields to Compute Convolutions," *IEEE Trans. on Information Theory*, Vol. IT-21, No. 2, pp. 208-213, March 1975.
8. Nassbaumer, H. J., "Digital Filtering Using Complex Mersenne Transforms," *IBM Journal of Research and Development*, Vol. 20, No. 5, pp. 498-504, September 1976.

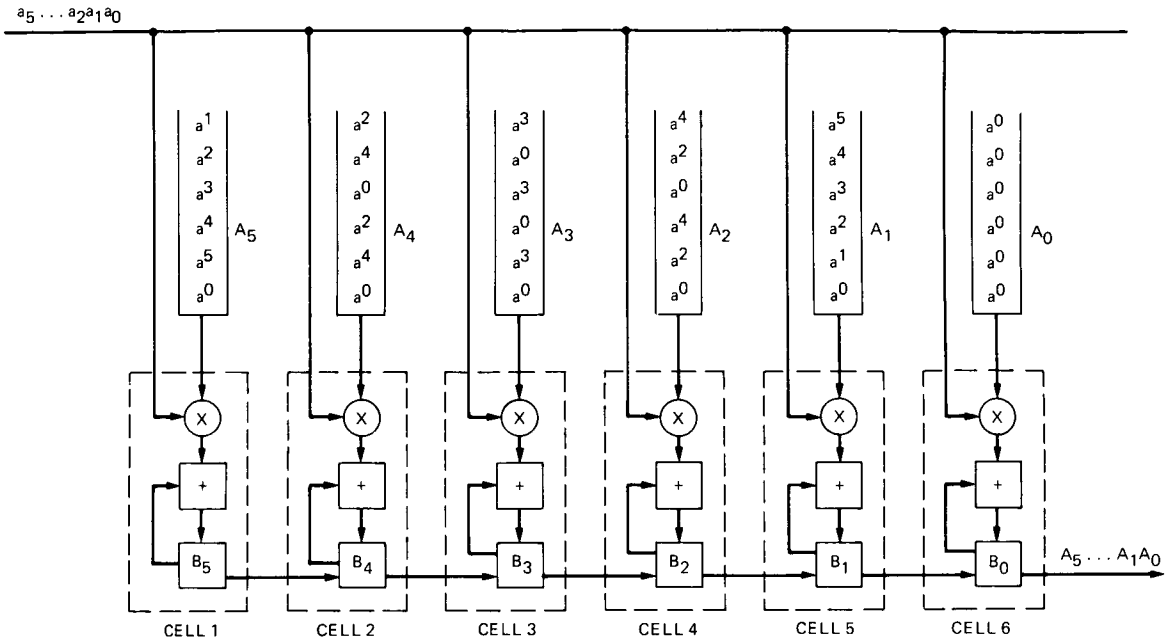


Fig. 1. The systolic array to compute a 6-point DFT using the direct method

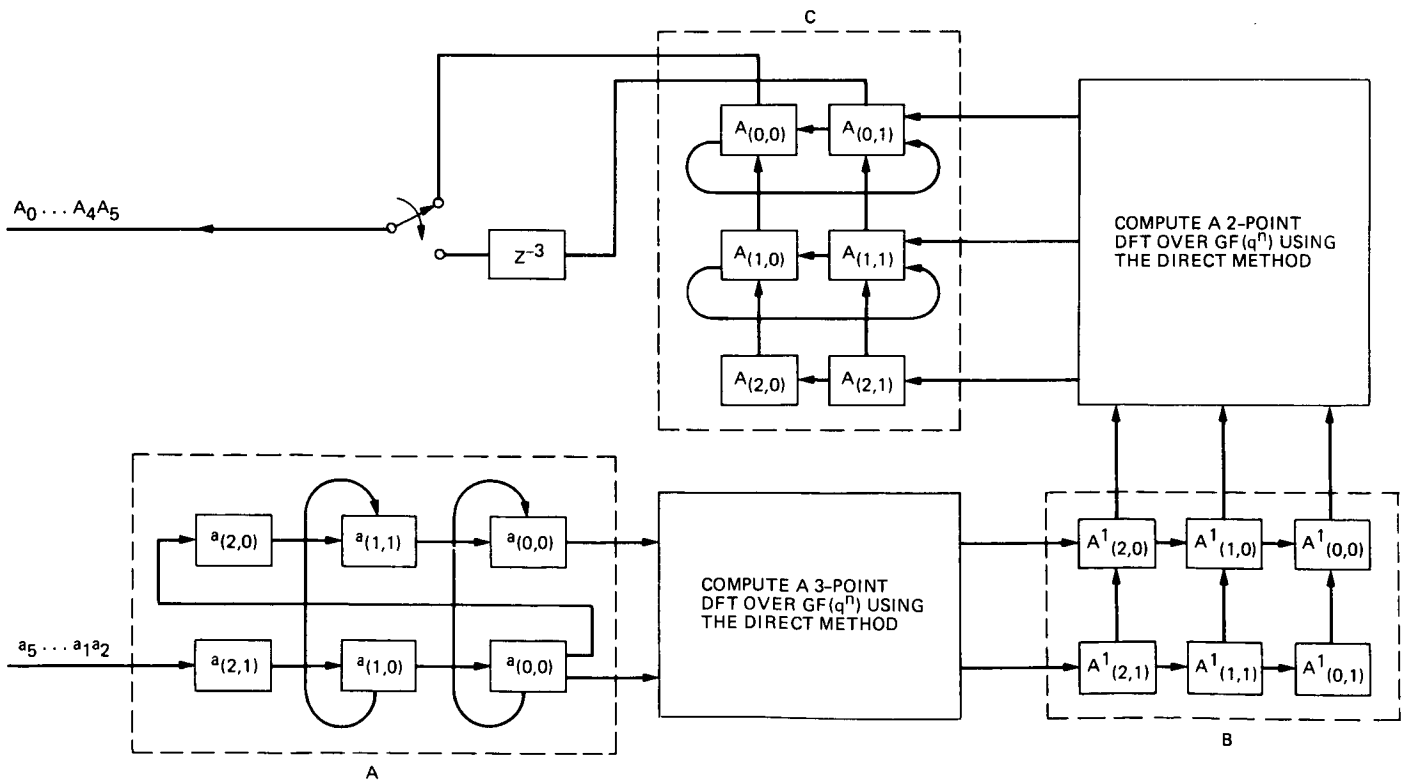


Fig. 2. A pipeline architecture for the implementation of a fast prime factor 6-point DFT over $GF(q^n)$

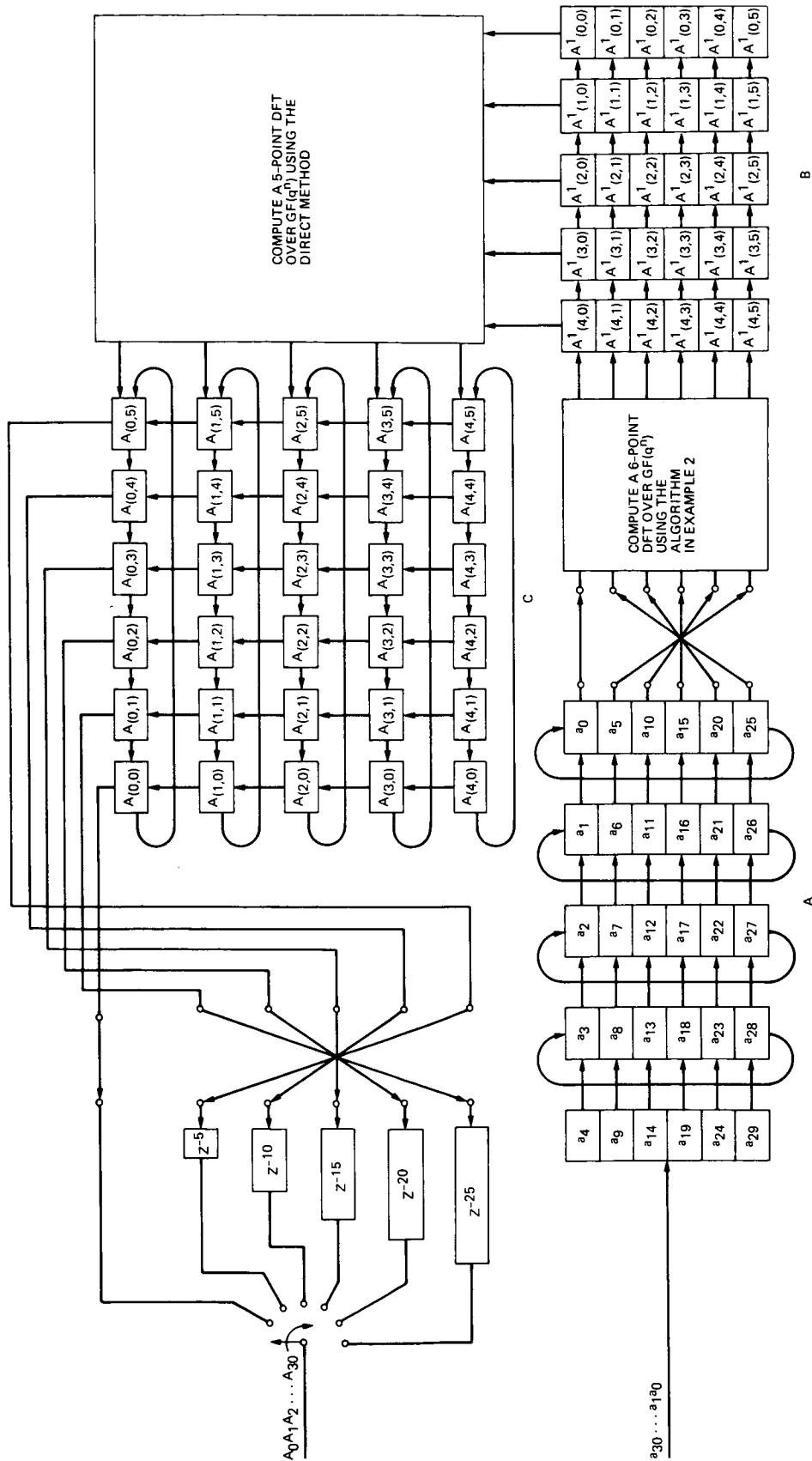


Fig. 3. A pipeline architecture for the implementation of a fast prime factor 30-point DFT over $GF(q^n)$

Appendix

Algorithm for Rearranging the Input and Output Sequences in the Prime Factor DFT Over $GF(q^n)$

To perform Eq. (3), one needs to convert input data from a_n to $a_{(n_1, n_2)}$ and inversely to convert output data from $A_{(k_1, k_2)}$ to A_k , where $0 \leq n, k \leq d = d_1 \cdot d_2 - 1$, $n_i \equiv n \pmod{d_i}$ and $k_i \equiv k \pmod{d_i}$ for $i = 1, 2$. To see this, let the one-dimensional input data of DFT be a_n , where $0 \leq n \leq d = d_1 \cdot d_2 - 1$. This one-dimensional input data can be shifted sequentially into a $d_1 \times d_2$ two-dimensional matrix as follows:

$$\begin{array}{cccc}
 a_{d_1-1} & \cdots, a_2 & a_1 & a_0 \\
 a_{2d_1-1} & \cdots, a_{2d_1+2} & a_{d_1+1} & a_{1d_1} \\
 a_{3d_1-1} & \cdots, a_{3d_1+2} & a_{2d_1+1} & a_{2d_1} \\
 \vdots & \vdots & \vdots & \vdots \\
 a_{d_2 d_1-1} & \cdots, a_{(d_2-1)d_1+2} & a_{(d_2-1)d_1+1} & a_{(d_2-1)d_1}
 \end{array} \tag{A-1}$$

In (A-1) the input index n is mapped into the pair of indices (n_1, n_2) , where $n_1 \equiv n \pmod{d_1}$ and $n_2 \equiv n \pmod{d_2}$. The vector of index n_2 of the last and next to last columns of the matrix in (A-1) are, respectively,

$$\begin{aligned}
 & [0 \cdot d_1 \pmod{d_2}, 1 \cdot d_1 \pmod{d_2}, 2 \cdot d_1 \pmod{d_2}, \dots, (d_2 - 1) \\
 & \cdot d_1 \pmod{d_2}]^T
 \end{aligned} \tag{A-2}$$

and

$$\begin{aligned}
 & [(0 \cdot d_1 + 1) \pmod{d_2}, (1 \cdot d_1 + 1) \pmod{d_2}, (2 \cdot d_1 + 1) \\
 & \pmod{d_2}, \dots, ((d_2 - 1) \cdot d_1 + 1) \pmod{d_2}]^T
 \end{aligned} \tag{A-3}$$

where T denotes matrix transpose.

Then, one can find 1 in (A-3) and some value i in (A-2) such that

$$1 \equiv i \cdot d_1 \pmod{d_2} \tag{A-4}$$

Given d_1 and d_2 , the solution of congruence (A-4) is i . The index n_2 is periodic with period d_2 . If the indices in (A-3) are cyclically shifted up by i or down by $d_2 - i$, the index n_2 of the resulting sequence is equal to the index n_2 of the sequence in (A-2). In a similar fashion, if the data of the k th column of (A-1) is cyclically shifted up or down by i or by $d_2 - i$, then the index n_2 of the resulting data of the k th column is equal to the index n_2 of the data of the $(k + 1)$ th column of the matrix in (A-1). To illustrate this, two examples are presented.

Example A.1. Let the length of input sequence be $d = d_1 \cdot d_2 = 3 \cdot 2$. Convert a_n into $a_{(n_1, n_2)}$ and inversely convert $A_{(n_1, n_2)}$ into A_n , where $0 \leq n \leq 5$, $n_1 \equiv n \pmod{3}$ and $n_2 \equiv n \pmod{2}$. First, the input sequence a_n , $0 \leq n \leq 5$, is shifted sequentially into a 3×2 matrix as follows:

a_2	a_1	a_0
a_5	a_4	a_3

(A-5)

Then, the index of a_n is mapped into two pairs of indices (n_1, n_2) . Thus, the matrix in (A-5) becomes

$a_{(2,0)}$	$a_{(1,1)}$	$a_{(0,0)}$
$a_{(2,1)}$	$a_{(1,0)}$	$a_{(0,1)}$

(A-6)

The index n_2 of the last and next to last columns of (A-5) are

$$[0 \cdot 3 \pmod{2}, 1 \cdot 3 \pmod{2}]^T \tag{A-7}$$

and

$$[(0 \cdot 3 + 1) \pmod{2}, (1 \cdot 3 + 1) \pmod{2}]^T \tag{A-8}$$

respectively.

From (A-4), one obtains the congruence as

$$1 \equiv i \cdot 3 \pmod{2} \quad (\text{A-9})$$

The solution of (A-9) is $i = 1$. Let the data of the first and second columns of the 3×2 matrix in (A-6) be cyclically shifted up by two and by one, respectively. Then, the 2-D matrix is arranged in the same order as the index n_2 of the last column:

$a_{(2,0)}$	$a_{(1,0)}$	$a_{(0,0)}$
$a_{(2,1)}$	$a_{(1,1)}$	$a_{(0,1)}$

(A-10)

This matrix is used to input data for a prime factor DFT algorithm over $GF(q^2)$ after taking three 2-point transforms of the columns and then taking two 3-point transforms of the rows in (A-10); then, (A-10) becomes

$A_{(2,0)}$	$A_{(1,0)}$	$A_{(0,0)}$
$A_{(2,1)}$	$A_{(1,1)}$	$A_{(0,1)}$

(A-11)

To inversely convert 2-D matrix in (A-11) into 1-D A_n for $0 < n \leq 5$, first, the data of the first and second columns of the 3×2 matrix in (A-11) are cyclically shifted down by two and by one, respectively. Then, the matrix in (A-11) becomes

$A_{(2,0)}$	$A_{(1,1)}$	$A_{(0,0)}$
$A_{(2,1)}$	$A_{(1,0)}$	$A_{(0,1)}$

or

A_2	A_1	A_0
A_5	A_4	A_3

Finally, a_n is shifted out sequentially from this matrix.

Example A.2. Let the length of input sequence be $d = d_1 \cdot d_2 = 5 \cdot 6$. Convert a_n into $a_{(n_1, n_2)}$ and inversely convert from output sequence $A_{(k_1, k_2)}$ into A_k , where $0 \leq n, k \leq 30, n_i \equiv n \pmod{5}$, and $k_i \equiv k \pmod{6}$ for $i = 1, 2$.

First, the input sequence $a_n, 0 \leq n \leq 30$ is shifted sequentially into a 5×6 matrix as follows:

a_4	a_3	a_2	a_1	a_0
a_9	a_8	a_7	a_6	a_5
a_{14}	a_{13}	a_{12}	a_{11}	a_{10}
a_{19}	a_{18}	a_{17}	a_{16}	a_{15}
a_{24}	a_{23}	a_{22}	a_{21}	a_{20}
a_{29}	a_{28}	a_{27}	a_{26}	a_{25}

(A-12)

If the index of a_n is mapped into the pair of indices (n_1, n_2) , where $n_1 \equiv n \pmod{5}$ and $n_2 \equiv n \pmod{6}$, then the matrix in (A-12) becomes

$a_{(4,4)}$	$a_{(3,3)}$	$a_{(2,2)}$	$a_{(1,1)}$	$a_{(0,0)}$
$a_{(4,3)}$	$a_{(3,2)}$	$a_{(2,1)}$	$a_{(1,0)}$	$a_{(0,5)}$
$a_{(4,2)}$	$a_{(3,1)}$	$a_{(2,0)}$	$a_{(1,5)}$	$a_{(0,4)}$
$a_{(4,1)}$	$a_{(3,0)}$	$a_{(2,5)}$	$a_{(1,4)}$	$a_{(0,3)}$
$a_{(4,0)}$	$a_{(3,5)}$	$a_{(2,4)}$	$a_{(1,3)}$	$a_{(0,2)}$
$a_{(4,5)}$	$a_{(3,4)}$	$a_{(2,3)}$	$a_{(1,2)}$	$a_{(0,1)}$

(A-13)

In order to arrange the second index of a pair (n_1, n_2) , i.e., n_2 in order, from (A-12), one solves the congruence

$$1 \equiv i \cdot 5 \pmod{6} \quad (\text{A-14})$$

The solution of (A-14) is $i = 5$ or $d_2 - i = 6 - 5 = 1$. If the data of the 1st, 2nd, 3rd, and 4th columns of (A-3) are cyclically shifted down by 4, 3, 2, and 1, the columns of the 5×6 matrix in (A-13) are rearranged in the same order as the last column of (A-13) as follows:

$a_{(4,0)}$	$a_{(3,0)}$	$a_{(2,0)}$	$a_{(1,0)}$	$a_{(0,0)}$
$a_{(4,5)}$	$a_{(3,5)}$	$a_{(2,5)}$	$a_{(1,5)}$	$a_{(0,5)}$
$a_{(4,4)}$	$a_{(3,4)}$	$a_{(2,4)}$	$a_{(1,4)}$	$a_{(0,4)}$
$a_{(4,3)}$	$a_{(3,3)}$	$a_{(2,3)}$	$a_{(1,3)}$	$a_{(0,3)}$
$a_{(4,2)}$	$a_{(3,2)}$	$a_{(2,2)}$	$a_{(1,2)}$	$a_{(0,2)}$
$a_{(4,1)}$	$a_{(3,1)}$	$a_{(2,1)}$	$a_{(1,1)}$	$a_{(0,1)}$

(A-15)

Finally, if one arranges the rows so that the index n_2 is in numerical sequence, (A-15) becomes the desired result, namely,

$a_{(4,0)}$	$a_{(3,0)}$	$a_{(2,0)}$	$a_{(1,0)}$	$a_{(0,0)}$
$a_{(4,1)}$	$a_{(3,1)}$	$a_{(2,1)}$	$a_{(1,1)}$	$a_{(0,1)}$
$a_{(4,2)}$	$a_{(3,2)}$	$a_{(2,2)}$	$a_{(1,2)}$	$a_{(0,2)}$
$a_{(4,3)}$	$a_{(3,3)}$	$a_{(2,3)}$	$a_{(1,3)}$	$a_{(0,3)}$
$a_{(4,4)}$	$a_{(3,4)}$	$a_{(2,4)}$	$a_{(1,4)}$	$a_{(0,4)}$
$a_{(4,5)}$	$a_{(3,5)}$	$a_{(2,5)}$	$a_{(1,5)}$	$a_{(0,5)}$

(A-16)

After taking five 6-point transforms of the columns and then taking six 5-point transforms of the rows in (A-16), (A-16) becomes

$A_{(4,0)}$	$A_{(3,0)}$	$A_{(2,0)}$	$A_{(1,0)}$	$A_{(0,0)}$
$A_{(4,1)}$	$A_{(3,1)}$	$A_{(2,1)}$	$A_{(1,1)}$	$A_{(0,1)}$
$A_{(4,2)}$	$A_{(3,2)}$	$A_{(2,2)}$	$A_{(1,2)}$	$A_{(0,2)}$
$A_{(4,3)}$	$A_{(3,3)}$	$A_{(2,3)}$	$A_{(1,3)}$	$A_{(0,3)}$
$A_{(4,4)}$	$A_{(3,4)}$	$A_{(2,4)}$	$A_{(1,4)}$	$A_{(0,4)}$
$A_{(4,5)}$	$A_{(3,5)}$	$A_{(2,5)}$	$A_{(1,5)}$	$A_{(0,5)}$

(A-17)

To rearrange from $A_{(k_1, k_2)}$ in (A-17) into A_k , first one arranges the rows in (A-17) such that the index n_2 of 5×6 matrix in (A-17) are in the same order as the index in (A-15) as follows:

$A_{(4,0)}$	$A_{(3,0)}$	$A_{(2,0)}$	$A_{(1,0)}$	$A_{(0,0)}$
$A_{(4,5)}$	$A_{(3,5)}$	$A_{(2,5)}$	$A_{(1,5)}$	$A_{(0,5)}$
$A_{(4,4)}$	$A_{(3,4)}$	$A_{(2,4)}$	$A_{(1,4)}$	$A_{(0,4)}$
$A_{(4,3)}$	$A_{(3,3)}$	$A_{(2,3)}$	$A_{(1,3)}$	$A_{(0,3)}$
$A_{(4,2)}$	$A_{(3,2)}$	$A_{(2,2)}$	$A_{(1,2)}$	$A_{(0,2)}$
$A_{(4,1)}$	$A_{(3,1)}$	$A_{(2,1)}$	$A_{(1,1)}$	$A_{(0,1)}$

(A-18)

Then, the 1st, 2nd, 3rd, and 4th columns of the matrix are cyclically shifted up by four, three, two, and one data, respectively. Thus, one obtains

$A_{(4,4)}$	$A_{(3,3)}$	$A_{(2,2)}$	$A_{(1,1)}$	$A_{(0,0)}$
$A_{(4,3)}$	$A_{(3,2)}$	$A_{(2,1)}$	$A_{(1,0)}$	$A_{(0,5)}$
$A_{(4,2)}$	$A_{(3,1)}$	$A_{(2,0)}$	$A_{(1,5)}$	$A_{(0,4)}$
$A_{(4,1)}$	$A_{(3,0)}$	$A_{(2,5)}$	$A_{(1,4)}$	$A_{(0,3)}$
$A_{(4,0)}$	$A_{(3,5)}$	$A_{(2,4)}$	$A_{(1,3)}$	$A_{(0,2)}$
$A_{(4,5)}$	$A_{(3,4)}$	$A_{(2,3)}$	$A_{(1,2)}$	$A_{(0,1)}$

(A-19)

Finally, A_k is shifted sequentially out from this matrix.

13150

Fast Frequency Acquisition via Adaptive Least Squares Algorithm

R. Kumar¹

Communications Systems Research Section

A new least squares algorithm is proposed and investigated for fast frequency and phase acquisition of sinusoids in the presence of noise. This algorithm is a special case of more general, adaptive parameter-estimation techniques. The advantages of the algorithms are their conceptual simplicity, flexibility and applicability to general situations. For example, the frequency to be acquired can be time varying, and the noise can be non-gaussian, non-stationary and colored.

As the proposed algorithm can be made recursive in the number of observations, it is not necessary to have a priori knowledge of the received signal-to-noise ratio or to specify the measurement time. This would be required for batch processing techniques, such as the fast Fourier transform (FFT). The proposed algorithm improves the frequency estimate on a recursive basis as more and more observations are obtained. When the algorithm is applied in real time, it has the extra advantage that the observations need not be stored. The algorithm also yields a real time confidence measure as to the accuracy of the estimator.

I. Introduction

The problem of estimating the parameters of a sinusoidal signal has received considerable attention in the literature, see for example Refs. 1-7 and their references. Such a problem arises in diverse engineering situations such as carrier tracking for communications systems and the measurement of Doppler in position location, navigation and radar systems.

A variety of techniques have been proposed in the literature to solve such problems including, to mention a few, the appli-

cation of the fast Fourier transform (FFT) (as in Refs. 1, 2), one and two dimensional Kalman filters based on a linearized model (Ref. 5), a modified extended Kalman filter that results in a phase locked loop (Ref. 6), or a digital phase locked loop derived on the basis of linear stochastic optimization (Ref. 7).

The fact that there are so many different techniques to solve the problem indicates the importance of the problem. This, however, also implies that there is no single technique superior to all others in all possible situations and/or with respect to different criteria such as computational complexity, statistical efficiency, etc.

¹Also with the faculty of the Electrical Engineering Department at California State University, Long Beach.

In this article we propose the application of the least squares parameter estimation technique to the estimation of an unknown frequency. The least squares algorithm has been extensively studied in the literature in terms of convergence, computational requirements, etc. (Refs. 8, 9), and has found varied applications in a wide variety of communication and signal processing problems. This is due to the relative simplicity of the least squares algorithm and its attractive convergence rates. In Ref. 9 for example, it has been shown that the algorithm exhibits an initial factorial convergence rate followed by exponential convergence. Such a convergence is very desirable in almost all estimation situations including the one under consideration.

When the least squares (LS) algorithm is implemented via the fast algorithm of Ref. 10, the computational requirements of the algorithm compare favorably to the FFT algorithm. The least squares algorithm offers, in addition to the above discussed rapid initial convergence, several other desirable features. First the least squares algorithm provides final estimates of frequency, whereas FFT estimation requires use of a secondary algorithm to interpolate between frequencies. Secondly, using an exponentially weighted least squares algorithm, it is possible to track a time varying frequency. We compare the least squares algorithm to the FFT since the latter is "close" to the optimum in terms of the statistical efficiency (Ref. 1).

In Section II we present the signal model followed by the least squares algorithm in Section III. Section IV analyzes the estimation error of the algorithm. In Section V a few simulation examples are presented. The last section of the article contains some concluding remarks.

II. The Signal Model

Consider the problem of estimating an unknown frequency w_d from the measurements y_k, z_k below

$$\begin{aligned} y_k &= A \sin(w_d t_k + \phi) + n_{ik} \\ z_k &= A \cos(w_d t_k + \phi) + n_{qk}, \quad k = 1, 2, \dots \end{aligned} \quad (1)$$

Here the sequence $\{y_k, z_k\}$ represents the samples of the in-phase and quadrature components of a received signal $s(t)$ obtained by demodulating $s(t)$ by a carrier reference signal $r(t)$ and its 90-deg phase shifted version respectively, i.e.,

$$\begin{aligned} s(t) &= A \sin(w_0 t + \phi_0) + n(t) \\ r(t) &= 2 \sin(w_c t + \phi_c), \quad \phi = \phi_0 - \phi_c, w_d = w_c - w_0 \end{aligned}$$

with n_{ik} and n_{qk} denoting the samples of the quadrature components of white noise $n(t)$. The algorithm can be easily extended to the case where $n(t)$ is a colored noise.

With a power series expansion for the sine and cosine functions, the measurement equations can be written in alternative forms as follows:

$$\begin{aligned} y_k &= A \sin(w_d t_k) \cos \phi + A \cos(w_d t_k) \sin \phi + n_{ik} \\ z_k &= A \cos(w_d t_k) \cos \phi - A \sin(w_d t_k) \sin \phi + n_{qk} \end{aligned}$$

or

$$\begin{bmatrix} y_k \\ z_k \end{bmatrix} = \begin{bmatrix} A \sin \phi & A \cos \phi w_d & -\frac{A \sin \phi}{2!} w_d^2 & -\frac{A \cos \phi}{3!} w_d^3 & \dots & +\frac{A \sin \phi}{(n-1)!} w_d^{n-1} \\ A \cos \phi & -A \sin \phi w_d & -\frac{A \cos \phi}{2!} w_d^2 & +\frac{A \sin \phi}{3!} w_d^3 & \dots & +\frac{A \cos \phi}{(n-1)!} w_d^{n-1} \end{bmatrix} \begin{bmatrix} 1 \\ t_k \\ t_k^2 \\ \vdots \\ t_k^{(n-1)} \end{bmatrix} + \begin{bmatrix} n_{ik} \\ n_{qk} \end{bmatrix} \quad (2)$$

In the above approximation the terms of the order $(w_d t_k)^n/n!$ and smaller order have been ignored (assuming here that $w_d t_k < n$). With obvious definitions, the measurement equation can be written in a form "linear in parameters."

$$Z_k = \theta' x_k + n_k \quad (3)$$

In the above, the prime (') denotes transpose, $Z_k' = [y_k \ z_k]$, $n_k' = [n_{ik} \ n_{qk}]$, x_k' denotes the observable state vector $[1 \ t_k$

$t_k^2 \dots t_k^{n-1}$] and θ' is the unknown parameter matrix. A standard least square algorithm can be applied to estimate the unknown parameter matrix θ' from the sequence of noisy observations $Z_k, k = 1, 2, \dots, N$.

III. Parameter Estimation via Least Squares

The parameter matrix θ' can be estimated by either a recursive or nonrecursive form. We consider in this article the nonrecursive form. The estimate of θ on the basis of measurement $Z_k, k = 1, 2, \dots, N$, denoted $\hat{\theta}_N$, is given by

$$\hat{\theta}_N = \left(\sum_{j=1}^N x_j x_j' \lambda^{N-j} \right)^{-1} \left(\sum_{j=1}^N x_j Z_j' \lambda^{N-j} \right) \quad (4)$$

where $0 < \lambda \leq 1$ is the exponential data weighting factor. One may refer to Refs. 8 and 11, for example, for an equivalent recursive update of $\hat{\theta}_N$. From $\hat{\theta}_N$, the estimates of A , w_d and ϕ can be obtained.

A. Computational Requirements

The algorithm of Eq. (4) requires an inverse of a symmetric ($n \times n$) matrix once, requiring order n^2 computations. It may appear that the computation of each $x_j x_j'$ term requires n^2 computations. However, detailed examination shows that only $2n$ computations are required. Thus, the total computations are equal to $6nN + O(n^2)$. In practice, the matrix inverse can be precomputed, thus reducing the data dependent computations to only $2nN + n^2/2$.

B. Fast Implementation of Least Squares Algorithm

The matrix

$$P^{-1} \triangleq \sum_{j=1}^N x_j x_j' \lambda^{N-j}$$

in Eq. (4) has a very special structure as can be easily seen by explicit computation of the term $x_j x_j'$ of the summand. Thus,

$$x_j x_j' = \begin{bmatrix} 1 & t_j & t_j^2 & \dots & t_j^{n-1} \\ t_j & t_j^2 & t_j^3 & \dots & t_j^{n-1} & t_j^n \\ \vdots & \vdots & \vdots & \ddots & \vdots & \vdots \\ t_j^{n-1} & t_j^n & \dots & \dots & t_j^{2n-2} \end{bmatrix}$$

Each of the matrices $x_j x_j'$ and P^{-1} is a Hankel matrix. That is, all the elements of each cross-diagonal are the same. The structure of a Hankel matrix is very similar to that of a Toeplitz matrix wherein the elements along the various subdiagonals are equal. The fast algorithm of Ref. 10 for the solution of Toeplitz system of equations can be slightly modified so as to become applicable to the present problem. Thus, the computations in Eq. (4) can be made in order $n(\log_2 n)^2$ computations, resulting in considerable reduction in the requirement for large values of n .

If the matrix inverse is precomputed, then with the algorithmic properties of Ref. 10, the solution for $\hat{\theta}_N$ can be obtained in approximately $6n \log_2 n$ operations. In the implementations above, it is sufficient to store only the first row and column of P or P^{-1} .

C. Baseband Sampling

In the case of baseband sampling, only the measurements $\{y_k\}$ are available and the parameter matrix θ' is of dimension $n \times 1$. In such an implementation, however, there may result an ambiguity of π radians in the phase estimate if the sign of w_d is also unknown.

IV. Estimation Error Analysis

Assuming that the model Eq. (3) is exact (the dimension n of the parameter matrix in Eq. (2) is sufficiently high), then the substitution of Eq. (3) in Eq. (4) yields,

$$\hat{\theta}_N = \left(\sum_{j=1}^N x_j x_j' \lambda^{N-j} \right)^{-1} \left\{ \sum_{j=1}^N x_j (x_j' \theta + n_j') \lambda^{N-j} \right\} \quad (5)$$

A simple manipulation of Eq. (5) yields the estimation error $\tilde{\theta}_N \triangleq \theta - \hat{\theta}_N$ as

$$\tilde{\theta}_N = - \left(\sum_{j=1}^N x_j x_j' \lambda^{N-j} \right)^{-1} \sum_{j=1}^N x_j n_j' \lambda^{N-j} \quad (6)$$

As the state vector x_j is deterministic, and n_j is a zero mean process, $\tilde{\theta}_N$ has its mean equal to zero. The error covariance matrix of $\tilde{\theta}_N$ can also be evaluated in a straightforward manner. Post multiplying Eq. (6) by the transpose of $\tilde{\theta}_N$, and taking expected values of both sides,

$$\begin{aligned}
E [\tilde{\theta}_N \tilde{\theta}'_N] &= \left(\sum_{j=1}^N x_j x'_j \lambda^{N-j} \right)^{-1} \\
&\times \left\{ \sum_{j=1}^N \sum_{i=1}^N x_j E [n'_j n_i] x'_i \lambda^{2(N-i)} \right\} \\
&\times \left(\sum_{i=1}^N x_i x'_i \lambda^{N-i} \right)^{-1} \quad (7)
\end{aligned}$$

Considering the case of $\lambda = 1$ and recalling that $\{n_j\}$ is a white noise sequence,

$$E [\tilde{\theta}_N \tilde{\theta}'_N] = \left(\sum_{j=1}^N x_j x'_j \right)^{-1} \sigma^2 \quad (8)$$

$$E [\|n_j\|^2] = E [n_{ij}^2] + E [n_{qj}^2] = \sigma^2$$

A. Frequency Estimation Error

A simple approximate expression can also be obtained for the frequency estimation error when the amplitude A is known and uniform sampling is used. The frequency estimate \hat{w}_d can be obtained as

$$\hat{w}_{d,N} = \left\{ (\hat{\theta}_N^{21})^2 + (\hat{\theta}_N^{22})^2 \right\}^{1/2} A^{-1}$$

When the amplitude A is also unknown, it can be replaced by its estimate given by,

$$\hat{A}_N = \left\{ (\hat{\theta}_N^{11})^2 + (\hat{\theta}_N^{12})^2 \right\}^{1/2}$$

In the above expression, $\hat{\theta}_N^{ij}$ denotes the (i, j) th element of the parameter matrix θ_N . The error variance of these elements of interest is given by

$$E \left[(\hat{\theta}_N^{21})^2 \right] + E \left[(\hat{\theta}_N^{22})^2 \right] \cong K \sigma^2 \left(\sum_{j=1}^N t_j^2 \right)^{-1}$$

where K approaches a constant with the increase in the numbers of observations N .

For relatively small errors, the frequency estimation error $\tilde{w}_{d,N} = w_d - \hat{w}_{d,N}$ has variance of approximately

$$K \frac{\sigma^2}{2} \left(\sum_{j=1}^N t_j^2 \right)^{-1}$$

For the case of uniform sampling $t_j = jT_s$, where T_s is the sampling period. Substituting for t_j and letting $T = NT_s$ denote the observation period,

$$E [\tilde{w}_N^2] = \frac{\sigma^2}{2} K \frac{6}{N(N+1)(2N+1)} \frac{1}{T_s^2} A^2$$

In terms of the unsampled system, if the additive noise process has one-sided noise spectral density N_o , then $\sigma^2 = 2N_o/T_s$. Thus,

$$E [\tilde{w}_N^2] \cong \frac{N_o}{P} \frac{6}{T^3} \frac{K}{4}, \quad T = NT_s \quad (9)$$

where $P = A^2/2$ is the received signal power and K has value approximately equal to 4 for low values of n . This is the same mean square error as for Maximum Likelihood estimation (Ref. 1; Ref. 12, Eq. 8.116).

We note here that in the derivation of Eq. (9), the approximation error in Eq. (3) has been ignored. It is difficult to estimate the error due to such finite approximation. However, from a few computer simulations, it appears that for $n > w_d T = (w_d T_s) N$, such error is small.

B. Examples of Application to the DSN Receiver

To keep the dimension n of the parameter matrix small, the following estimation method is proposed. Dividing both sides of Eq. (9) by $w_{d,\max}^2$, and substituting $T = n/w_{d,\max}$, one obtains

$$\frac{E [\tilde{w}_d^2]}{w_{d,\max}^2} = 6 \frac{N_o}{P} \frac{w_{d,\max}}{n^3}$$

Selecting a value of 1/36 for the left hand side of the above equations allows one to express the maximum frequency uncertainty that can be resolved by the algorithm as a function of n . Thus

$$w_{d,\max} = \frac{n^3}{216} \frac{P}{N_o}$$

The rationale for selecting the value of 1/36 for $E [\tilde{w}_d^2] / w_{d,\max}^2$ is as follows. Since the additive noise has Gaussian distribution, one may assume that the frequency estimation error has Gaussian distribution with its standard deviation denoted by $\sigma_{\tilde{w}_d}$. The above selection thus ensures that $3\sigma_{\tilde{w}_d} < w_{d,\max}/2$.

Example 1. For reception of Voyager 2 signals at DSS 13, a typical carrier power-to-noise spectral density ratio is 24.4 dB-Hz. Let $n = 8$, and $w_{d,\max} = 652$ rad/s. After an initial

estimation period of $T = n w_{d,\max}^{-1}$, the receiver NCO frequency is adjusted by \hat{w}_d . Thus, with an initial adjustment after $T = 12.2$ ms, the frequency offset is reduced to \tilde{w}_d with $\sigma = 108.6$ rad/s (17.4 Hz). Application of the algorithm for a subsequent period of 24.4 ms reduces the standard deviation to 6 Hz. In this manner, four applications of the algorithm bring down the standard deviation of the frequency offset to less than 0.7 Hz in a total time of 183 ms, from an initial frequency offset of 104 Hz.

Example 2. If the initial uncertainty is only 20 Hz, then with a lower value of n equal to 5, after an estimation period of $T = 40$ ms, $\sigma_{\tilde{w}_d} = 18.4$ rad/s (2.94 Hz). A frequency correction at the end of this period and an estimation of the residual frequency offset for a period of 160 ms reduces $\sigma_{\tilde{f}_d}$ to 0.36 Hz ($\tilde{f}_d = \tilde{w}_d/2\pi$). Thus with $n = 5$, the frequency uncertainty is reduced to $\sigma_{\tilde{f}_d} = 0.36$ Hz in a total estimation period of 0.2 s.

In an alternative approach to keep the value of n fixed and small with an increase in the total observation period, instead of resetting the frequency reference (making a correction in the NCO frequency), the time reference is reset to zero. Subsequent observations in Eq. (1) are now with respect to a different phase reference, say $\bar{\phi}$. The application of the least squares algorithm to this set of observations then provides an estimate for $\bar{\phi}$ denoted $\hat{\bar{\phi}}$. At this stage the observations in the second T 's interval are processed to have a phase reference $\hat{\phi}$ and are then combined with the first set of observations. Equivalently, it is required to post multiply the second sum on the right hand side of Eq. (4), obtained for the second sub-interval of T 's, by the following matrix

$$\begin{bmatrix} \cos(\Delta\phi) & -\sin(\Delta\phi) \\ \sin(\Delta\phi) & \cos(\Delta\phi) \end{bmatrix}, \quad \Delta\phi = \phi - \hat{\bar{\phi}}$$

and add the result to the corresponding sum for the first T 's interval. The first sum on the right hand side of Eq. (4) is simply multiplied by a factor of 2. This procedure is extended in an appropriate manner to subsequent intervals, so as to obtain a final estimate for w_d , and ϕ based on the complete set of observations.

V. Simulations

Figures 1 through 5 present the frequency estimates obtained by the least squares algorithm. To avoid singularity of the matrix P^{-1} , it was modified by the addition of a diagonal matrix ϵI with $\epsilon = 0.001$. For convenience, the unknown frequency w_d is taken to be 1 rad/s. From the simulations it is apparent that the frequency estimate comes close to the true frequency in a time equal to a fraction of the time period of

the unknown frequency. To keep the computational burden of the simulations to a minimum, the dimension n was restricted to a small value and the observation period was also restricted to a small value.

For frequencies much higher than one, the least squares algorithm, Eq. (4), was slightly modified. Thus, as $w_{d,\max}$ denotes an upper bound on the magnitude of unknown frequency, we define a normalized parameter matrix $\bar{\theta}$ by $\bar{\theta}^{i,j} = \theta^{i,j}/w_{d,\max}^{(i-1)}$; $i = 1, \dots, n$; $j = 1, 2$. Defining a corresponding state vector \bar{x}_k by

$$\bar{x}_k = \begin{bmatrix} 1 & 0 & \dots & 0 \\ 0 & w_{d,\max} & \dots & 0 \\ 0 & 0 & \dots & w_{d,\max}^{n-1} \end{bmatrix} x_k$$

the measurement Eq. (3) may be rewritten as

$$Z_k = \bar{\theta}^T \bar{x}_k + n_k \quad (10)$$

and the least squares algorithm can now be applied to estimate $\bar{\theta}$. The estimates of the elements of θ are then obtained as

$$\hat{\theta}^{i,j} = w_{d,\max}^{(i-1)} \hat{\bar{\theta}}^{i,j}$$

Such a transformation leaves the previous error analysis invariant. However, for finite dimensional approximation considered here, this makes the algorithm numerically more robust. The simulations for $w_d = 10$ and $w_d = 100$ are precisely the same as in Figs. 1 through 5 with appropriate changes in scaling and are not presented separately.

In Figs. 1 through 5, ψ and ξ represent the first and second row of the parameter matrix respectively. Thus in baseband sampling, only the ψ vector is estimated while in quadrature sampling, the estimates of both ψ and ξ parameter vectors are available. From the figures it is apparent that the dimension n of the state vector \bar{x}_k in the model Eq. (3) is approximately equal to $w_d T$ where T is the sampling interval. Due to over parameterization involved in the problem, there is a considerable amount of flexibility in the estimation of A , w_d , ϕ from the estimates of the elements of θ . Thus whereas in Figs. 1 through 3, the amplitude A is assumed known, Figs. 4 and 5 involve unknown A . A different order of computation can provide an estimate of A when baseband sampling is used. Here, we have reported results only for the frequency estimates; the phase estimates also converge at a fast convergence rate.

VI. Comparison with FFT Techniques

An alternative technique for the fast frequency acquisition is via fast Fourier transform of sampled data. We observe that for the case of infinite observation time, both procedures are optimum and thus are equivalent. However, for finite observation period T , the FFT has the limitation that the frequency estimates are quantized to intervals of $1/T$ Hz. In the finite dimensional approximation of the LS algorithm this is not the case and sufficiently accurate estimates can be obtained by choosing n sufficiently large (finer sampling) even for low values of T .

The price for such an improvement is increased computational requirements which is of order $n \log_2 n$ (though higher than for FFT) if the matrix P is precomputed and is of order $n \log n \log n$ if P must be computed on line. With the application of fast algorithms, the storage requirement of P is only $2n$ (not $n^2/2$).

Also, note that the computational requirements here are dominantly decided by $w_d T$ and not by the number of samples as is the case with FFT.

It may also be mentioned that with the FFT algorithm there also exists a finite probability of the occurrence of an outlier (Ref. 1) and this causes a component of the frequency estimation error with a uniform probability density function over the complete frequency range of the FFT algorithm. As

against this, the frequency estimation error with LS algorithm has a Gaussian distribution.

VII. Conclusion

This article has presented a fast algorithm based on the least squares parameter estimation technique. In Ref. 9 it is shown that the least squares algorithm exhibits a convergence phase wherein the convergence rate is factorial (the estimation error goes to 0 as $1/k!$ where k is the number of observations) followed by an exponential convergence rate. Our simulations also exhibit the same rapid initial convergence rates. Here of course, the estimation error does not approach zero because of a finite and low dimensional truncation of the model. From another viewpoint the algorithm may be perceived as a time domain dual of the FFT algorithm. Whereas the FFT algorithm transforms the data into frequency domain for the estimation/detection purpose, here the estimation is done directly in the time domain. This latter approach has several advantages. First by choosing $\lambda < 1$, it is possible to track the time varying frequency by recursive update techniques (Ref. 8). Moreover unlike the case of the FFT algorithm, the frequency estimates are not quantized to intervals of $1/T$ Hz, which would be large for small observation interval T . The price for these desirable features is in terms of increased computational requirement which in fast implementation of the algorithm could be of order $n \log n$ or $n \log n \log n$ (depending upon the specific implementations), where n is approximately equal to $w_d T$, the product of the frequency uncertainty and the observation period.

References

1. Rife, D. C., Single Tone Parameter Estimation from the Discrete-Time Observations, *IEEE Transactions on Information Theory*, Vol. IT-20, No. 5, pp. 591-598, September 1974.
2. Hurd, W. J., Statman, J. I., and Vlnrotter, V. A., High Dynamic GPS Receiver Validation Demonstration Final Report, *JPL Publication 85-74*, Jet Propulsion Laboratory, California Institute of Technology, Pasadena, Calif., 1985.
3. Tufts, D. W., and Kumaresan, R., Estimation of Frequencies of Multiple Sinusoids: Making Linear Prediction Perform Like Maximum Likelihood, *Proceedings of the IEEE*, Vol. 70, No. 9, pp. 975-987, September 1982.
4. Friedlander, B., On the Cramer-Rao Bound for Time Delay and Doppler Estimation, *IEEE Transactions on Information Theory*, Vol. IT-30, No. 3, pp. 575-580, May 1984.
5. Friedland, B., Optimum Steady-State Positions and Velocity Estimation Using Sampled Position Data, *IEEE Transactions on Aerospace and Electronic Systems*, Vol. 9, pp. 906-911, November 1973.
6. Polak, D. R., and Gupta, S. C., Quasi Optimum Digital Phase-Locked Loops, *IEEE Transactions on Communications*, Vol. 21, pp. 75-82, January 1973.
7. Kumar, R., and Hurd, W. J., A Class of Optimum Digital Phase Locked Loops, *TDA Progress Report 42-83*, Jet Propulsion Laboratory, Pasadena, Calif., pp. 63-80, July 1985; also submitted for publication to *IEEE Transactions on AES*.
8. Kumar, R., Almost Sure Convergence of Adaptive Identification and Prediction Algorithms, accepted for publication in *Recherche di Automatica*.
9. Gitlin, R. D., and Magee, F. R., Jr., Self-Orthogonalizing Adaptive Equalization Algorithm, *IEEE Transactions on Communications*, Vol. COM-25, pp. 666-672, July 1977.
10. Kumar, R., A Fast Algorithm for Solving a Toeplitz System of Equations, *IEEE Transactions on Acoustics, Speech and Signal Processing*, Vol. ASSP-33, No. 1, pp. 254-267, February 1985.
11. Kumar, R., Simultaneous Adaptive Control and Identification via Weighted Least Squares Algorithm, *IEEE Transactions on Automatic Control*, Vol. 29, pp. 259-263, March 1984.
12. Wozencraft, J. M., and Jacobs, I. M., *Principles of Communication Engineering*, New York: Wiley, 1965.

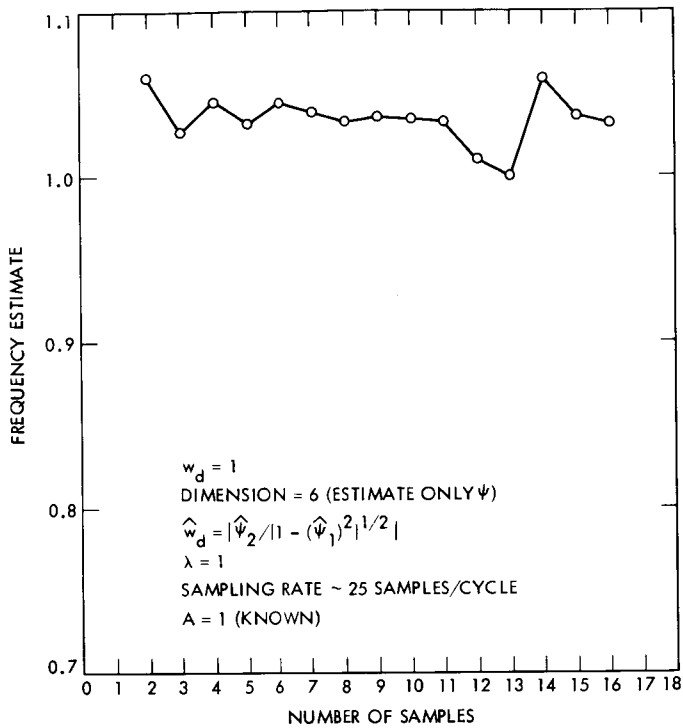


Fig. 1. Least squares algorithm: noise free case and baseband sampling, $n = 6$

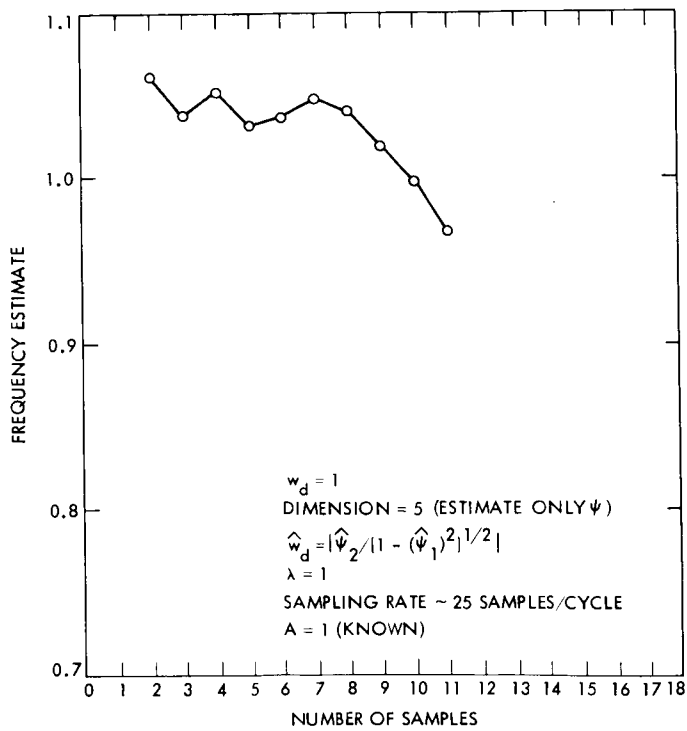


Fig. 2. Least squares algorithm: noise free case and baseband sampling, $n = 5$

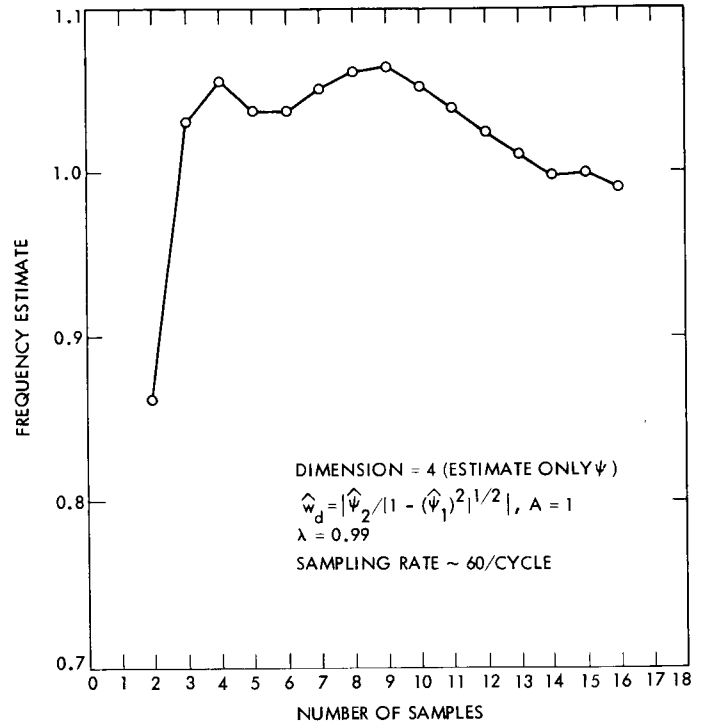


Fig. 3. Least squares algorithm: noise free case and baseband sampling, $n = 4$

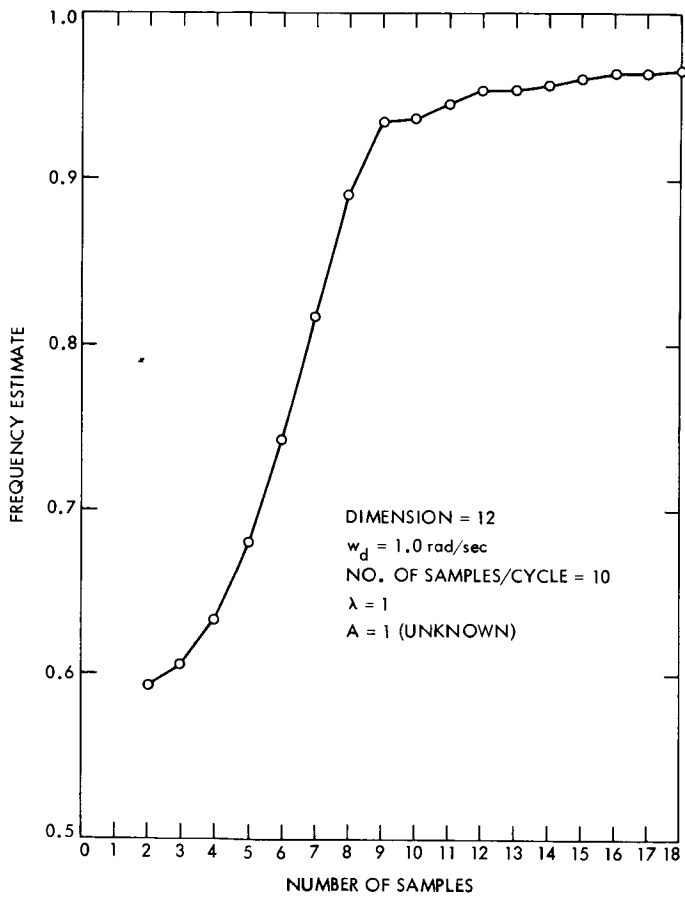


Fig. 4. Least squares algorithm: noise free case and quadrature sampling

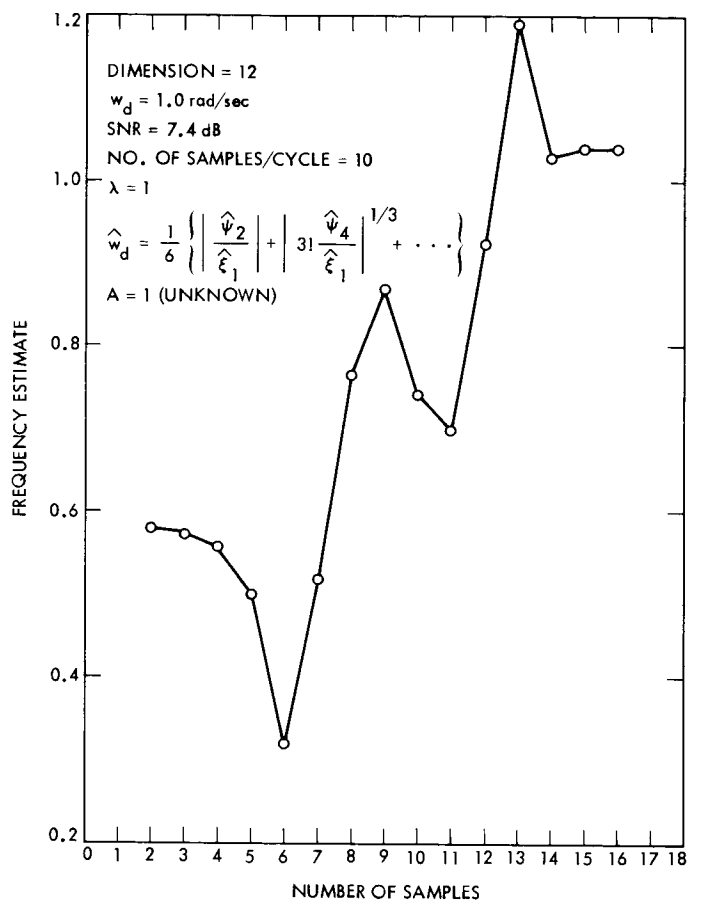


Fig. 5. Least squares algorithm and quadrature sampling

13151

A Systolic Architecture for the Correlation and Accumulation of Digital Sequences

L. J. Deutsch and C. R. Lahmeyer
Communications Systems Research Section

~~This article describes a fully systolic architecture for the implementation of digital sequence correlator/accumulators. These devices consist of a two-dimensional array of processing elements that are conceived for efficient fabrication in Very Large Scale Integrated (VLSI) circuits. A custom VLSI chip that was implemented using these concepts is described. The chip, which contains a four-lag three-level sequence correlator and four bits of accumulation with overflow detection, was designed using the Integrated UNIX-Based Computer Aided Design (CAD) System. Applications of such devices include the synchronization of coded telemetry data, alignment of both real time and non-real time Very Large Baseline Interferometry (VLBI) signals, and the implementation of digital filters and processors of many types.~~

I. Introduction

One of the most common signal processing operations that is used in conjunction with digital signals is correlation. Suppose that a_i and b_i are two sequences of real numbers (where i is an integer $-\infty < i < \infty$). Then the l lag correlation of these two sequences can be defined by

$$C_j [a, b](i) = \sum_{k=-l}^0 a_k b_{k+i} \quad (1)$$

This is not the most general definition of correlation, but it will be sufficient for this article. If the two sequences a and b are identical, then this is called an autocorrelation. If not, it is called a cross-correlation.

The correlation operator, as defined in Eq. (1), is a measure of the amount of agreement between the two sequences as a

function of their relative offset. There are, in fact, many important applications that make use of this observation. In Very Large Baseline Interferometry (VLBI) (Ref. 1), for example, received signals from several antenna sites must be correlated in order to determine the relative time differences between the receivers. In Symbol Stream Combining (Ref. 2), the relative timing is not important, but correlators are used to sum the various signals in a maximum likelihood manner in the presence of noise. Telemetry coding synchronization relies on the detection, using correlators, of fixed binary sequences in encoded data (Ref. 3) or of statistical trends produced by certain error correcting codes (Ref. 4). Finally, Eq. (1) is also the basic equation for a Finite Impulse Response (FIR) digital filter (Ref. 5). This means that a digital correlator may be used in filtering applications as well.

There is some confusion in the digital electronics industry as to exactly what constitutes a correlator. Some parts manu-

facturers produce correlators that only produce the partial products

$$p_j(i) = a_j b_{j+i} \quad (2)$$

A part that also performs the summation in Eq. (1) is sometimes called a correlator/accumulator. In this article, the portion of the system that performs the partial products will sometimes be referred to as a correlator so as not to be confused with the accumulator portion.

Because digital correlator/accumulators in many applications in data acquisition and advanced tracking techniques require large numbers of lags and high speeds, it was decided that an architecture suitable for implementation in Very Large Scale Integrated (VLSI) circuits was needed. This article presents the results of this research effort to date. Indeed, a very efficient architecture has been developed for these devices that takes advantage of the techniques of systolic arrays (Ref. 6). The algorithms are explained in Section II. The implementation of these algorithms in VLSI is described in Section III.

In order to test these algorithms and architectures, a small correlator/accumulator chip was designed, fabricated, and tested. The chip, called SMLCOR, implements a four lag correlator of three-level input sequences. It also contains a fully pipelined set of four bit accumulators with overflow detection circuitry. The chip was fabricated in a 4.0- μ NMOS technology and was found to be fully functional in the initial fabrication run. The design and testing of this chip are described in Section IV.

Finally, a very large VLSI chip using this architecture is currently in fabrication. This chip comprises a 32-lag complex correlator with phase rotation circuitry and 24 bits of accumulation. It is one of the largest chips to be designed at the Jet Propulsion Laboratory (JPL) to this date. It is described in Section IV. This chip will be used as part of the Advanced Decoding System that is currently under development.

II. A Systolic Algorithm for Correlators With Accumulation

The basic architecture for systolic correlators as developed by S. Y. Kung (Ref. 7) is now well known. It is shown in Fig. 1. The basic idea is to take the two digital sequences that are to be correlated and pump them into the circuit from the two sides. As they shift through the single bit delay elements (the boxes labeled "D" in the figure) they are brought into various alignments. The multiplication elements (labeled with a cross in the figure) are then used to form the p results. Because this circuit is fully pipelined, it has the potential for

very high speed applications. It is also modular and therefore suitable for implementation on VLSI chips.

The one drawback of this circuit is that it produces only the even index correlation coefficients, p_{2i} . It is clear that the odd numbered coefficients may be generated using a second circuit with one of the sequences delayed an extra bit time before entering. A slightly different architecture, shown in Fig. 2, could also be used to generate all the coefficients. This architecture is called broadcasting because of the fact that one of the sequences must be broadcast to all the multipliers at once. This has the disadvantage that the broadcast signal must contend with large fan-out and power problems which could result in slower circuit operation.

It was decided that the chips that would be implemented would incorporate both the systolic and broadcast architectures and an external mode switch for selection between them. Some high-speed applications, such as VLBI, do not require all the coefficients and could take advantage of the systolic architecture. Other applications, such as coding synchronization, do require all the coefficients but do not have to run at the very high speeds. These can use the broadcast system. Finally, those applications that require both high speed and high spatial resolution can use two chips to generate the entire set of coefficients.

The architecture for the pipelined accumulators is shown in Fig. 3. The basic idea here is to take the output of a correlator cell (i.e., one of the p 's) and pass it to a first stage that comprises a conventional accumulator. This first stage implements just enough bits of accumulation to generate a single bit output (called the carry) to the rest of the circuit. It can be thought of as a conversion unit that takes an input signal that may be many bits in width and scales it in time to a one-bit signal. It also adds a bias to the signal so that negative numbers in the correlation can be accumulated as positive numbers only.

Following the first stage, the accumulator consists of identical cells that are each single-bit adders. At any time, the result of the accumulation appears in the delay elements with the least significant bit in the uppermost element.

In order to speed up the operation of the accumulators, an additional delay element is added between the stages of accumulations. The results as contained in the delay elements are now skewed in time. This must be taken into account in the use of these circuits in actual applications.

Because of the pipelined nature of the accumulators, the sums should be read out using the following procedure. First, the two data inputs to the correlator should be forced to zero

for a few clock times in order to let the partial sums trickle down the pipe. Then the reset signal should be applied. This will zero the registers in the accumulator while allowing the sums to be shifted out to the right. After all the sums have been read out (this takes four clock cycles in SMLCOR), the reset signal can be removed and new data can be sent to the correlators.

In the next section, the design of a small correlator/accumulator using these concepts is examined in detail.

III. The SMLCOR 4-Lag Correlator/ Accumulator

In order to test some of the above concepts, a small correlator/accumulator circuit was implemented on a VLSI chip. The chip, called SMLCOR (for "Small Correlator"), was designed using the Integrated UNIX-Based Computer Aided Design (CAD) system (Ref. 8). The sequence inputs to SMLCOR are three level. This means that they can assume the values in the set $\{-1, 0, 1\}$ only. This was done for two reasons. First, most applications that are being considered for these chips (such as VLBI and code synchronization) do not require any more accuracy than this. Second, three-level real multipliers are very efficient to implement since the set $\{-1, 0, 1\}$ is closed under multiplication. It takes two bits to represent the three levels. This is a bit inefficient since four levels could be represented with this number of bits as well. However, the added complexity needed to implement four-level multipliers would more than outweigh this waste.

The system of representation for the three-level numbers is as follows:

Number	Representation
-1	10
0	00
1	01

The representation 11 is not allowed, and it can be used for detecting certain failure conditions in the operation of chips using this system.

A block diagram of the correlator portion of SMLCOR is shown in Fig. 4. Notice the addition of the select gates. These are used to determine whether the circuit is in systolic or broadcast mode according to the input signal mode. The multipliers are implemented as Programmable Logic Arrays (PLAs) (Ref. 9). They were generated automatically from a set of Boolean equations in a matter of seconds, thus reducing the design time of SMLCOR considerably. Although PLAs are, in general, not an efficient method of implement-

ing fast logic, in this case, the multipliers are small enough that there would be little difference in performance between the PLA and a full custom design.

The implementation of the accumulators is represented by Fig. 5. Some logic (notably the readout logic) has been omitted for clarity. The first stage accumulation is built from two blocks. The first block, called data converter, takes a three-level input and produces an output according to the following truth table:

Input	Output
10	00
00	10
01	11

In this way, the number of ones that is output reflects the magnitude of the correlation coefficient. This serves the purpose of biasing the number system to take care of negative numbers. These ones need only to be summed in time to produce the desired (biased) result.

The second portion of the first stage accumulation is a full adder and delay that constitute a 0, 1, 2 accumulator. The carry from this circuit is then fed to the remainder of the array.

The rest of the accumulator is identical to that in Fig. 3 with the addition of the overflow detection circuit at the bottom of the figure. This is used to detect when the capacity of the accumulator has been exceeded. Four bits of accumulation were implemented in SMLCOR.

• There is also a method of reading out the results that is not shown in the figures. A reset signal is used to zero the appropriate registers, and the next four clock times are then used to shift the data out of the accumulator delay elements.

A layout of SMLCOR is shown in Fig. 6. SMLCOR was fabricated using a 4- μ NMOS technology. It was tested using the Digital Microcircuit Functionality Tester (DMFT) (Ref. 10) and found to be fully functional with no additional fabrication iterations required.

IV. Ongoing Work: BIGCOR

Since the results obtained from SMLCOR were very encouraging, the decision was made to implement a full version with the new architecture. A much larger correlator/accumulator chip, called BIGCOR, was designed using the same techniques as in SMLCOR. This was particularly easy to accomplish as the basic cells from SMLCOR could be used unaltered in the new design.

In order to make BIGCOR useful to a large variety of applications, it has been designed with 32 lags and 24 bits of accu-

mulation. In addition, BIGCOR can rotate the results of the correlation in the complex plane by using a phase rotation circuit. The same phase correction number is applied to all the lags simultaneously using a broadcast technique. The complex results are then accumulated using two pipeline accumulators for each lag.

Although BIGCOR is conceptually only a little more complex than SMLCOR, it is certainly one of the largest VLSI chips yet designed at JPL. It contains over 60,000 transistors. The design of BIGCOR has been completed. In addition, the design has been checked and simulated. It is now in fabrication. BIGCOR is being implemented in a 3- μ minimum feature size NMOS technology. It should run at 8 MHz in the systolic mode.

V. Conclusions

An efficient architecture has been developed for the VLSI implementation of systolic correlators and accumulators. The architecture is easily extensible in both the number of lags and the number of bits of accumulation. Furthermore, the concepts have been put to practice in the implementation of SMLCOR, a fully functional 4-lag correlator/accumulator chip. The cells that were developed for SMLCOR may be used in the design of similar chips of varying parameters.

The design of a large enough correlator/accumulator chip to be practical in a large number of digital signal processing applications has also been demonstrated. The chip, BIGCOR, is now in fabrication.

References

1. Yuen, J. (ed.), *Deep Space Telecommunications Systems Engineering*, Jet Propulsion Laboratory, Pasadena, Calif., pp. 135-138, July 1982.
2. Hurd, W. J., Reder, L. J., and Russell, M. D., "Symbol-Stream Combiner: Description and Demonstration Plans," *TDA Progress Report 42-78*, Jet Propulsion Laboratory, Pasadena, Calif., pp. 115-121, April-June 1984.
3. Deutsch, L. J., "Reed-Solomon Code Synchronization Revisited," *TDA Progress Report 42-80*, Jet Propulsion Laboratory, Pasadena, Calif., pp. 91-96, October-December 1984.
4. Lordem, G., McEliece, R., and Swanson, L., "Node Synchronization for the Viterbi Decoder," *TDA Progress Report 42-73*, Jet Propulsion Laboratory, Pasadena, Calif., pp. 22-35, January-March 1983.
5. Hamming, R. W., *Digital Filters*, Englewood Cliffs, N.J.: Prentice-Hall Inc., pp. 180-195, 1977.
6. Kung, H. T., "Systolic Arrays (for VLSI)," *Sparse Matrix Proc.*, 1978, SIAM, pp. 256-282, 1979.
7. Kung, S. Y., "VLSI Signal Processing: From Transversal Filtering to Concurrent Array Processing," *VLSI in Modern Signal Processing*, Englewood Cliffs, N.J.: Prentice-Hall Inc., pp. 127-152, 1985.
8. Deutsch, L. J., "An Integrated UNIX-Based CAD System for the Design and Testing of Custom VLSI Chips," *TDA Progress Report 42-81*, Jet Propulsion Laboratory, Pasadena, Calif., pp. 51-62, January-March 1985.
9. Mead, C. and Conway, L., *Introduction to VLSI Systems*, Menlo Park, California: Addison-Wesley Publishing Company, pp. 115-127, 1980.
10. Olson, E. M., and Deutsch, L. J., "A System for the Functional Testing and Simulation of Custom and Semicustom VLSI Chips," *TDA Progress Report*, to appear.

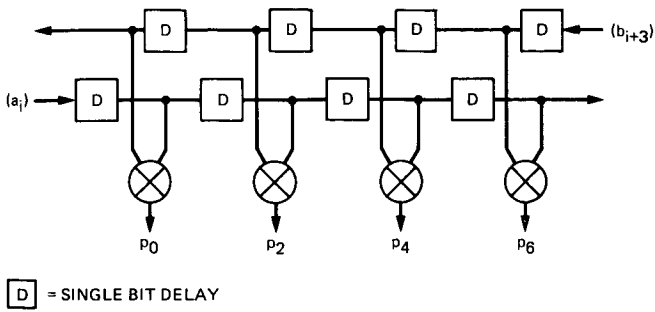


Fig. 1. Systolic architecture for a digital correlator

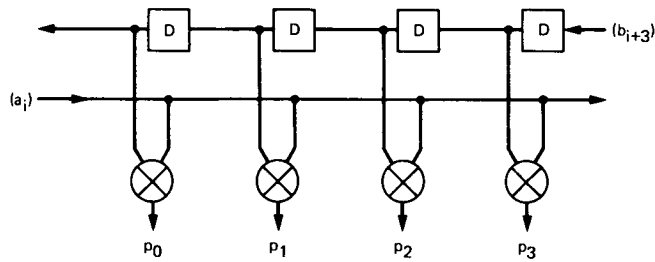


Fig. 2. Broadcast architecture for a digital correlator

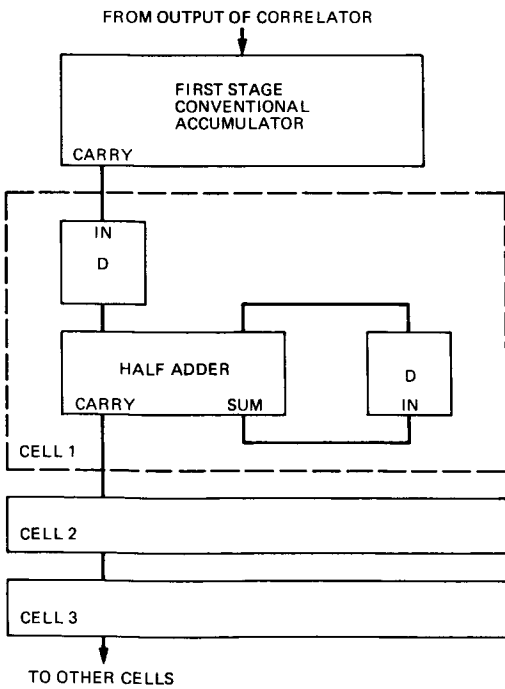


Fig. 3. Design of the pipelined accumulators

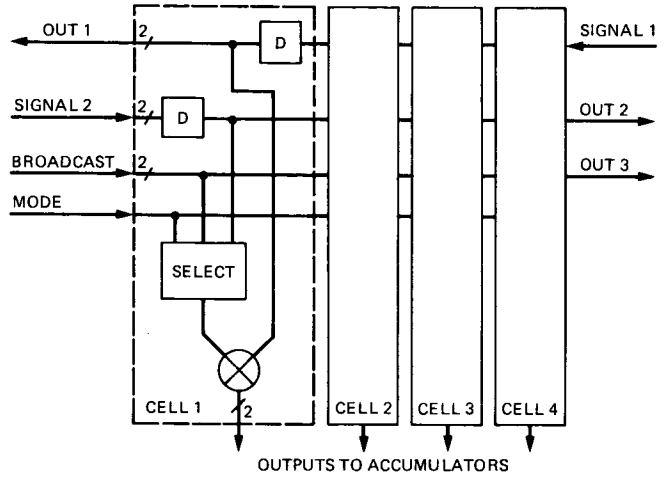


Fig. 4. Correlator design in SMLCOR

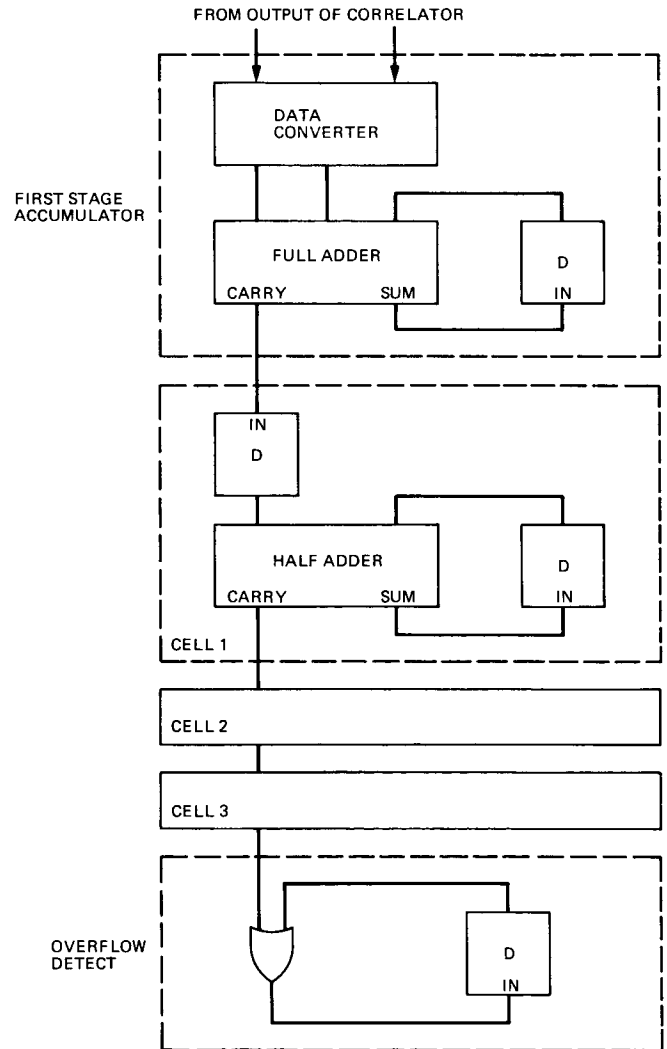


Fig. 5. The pipelined accumulators in SMLCOR

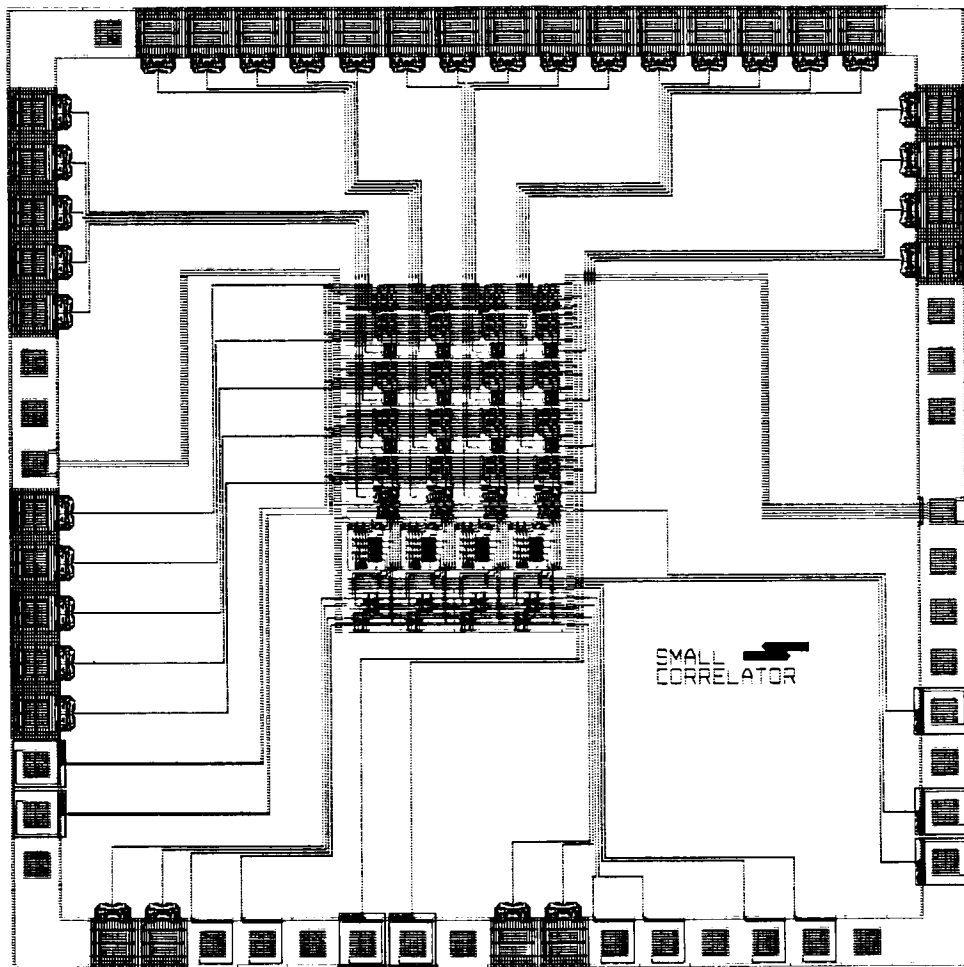


Fig. 6. Layout of the SMLCOR correlator chip

N86 - 28283

D8-93
169

13152

VLBI Observations of 416 Extragalactic Radio Sources

D. D. Morabito, A. E. Niell¹, R. A. Preston,
R. P. Linfield, A. E. Wehrle², and J. Faulkner³

Tracking Systems and Applications Sections

The Deep Space Network is establishing a high-accuracy VLBI celestial reference frame. This article presents VLBI results of observations of 416 radio sources with declinations north of -45 deg which have been conducted at frequencies of 2.3 GHz and 8.4 GHz. At 2.3 GHz, 323 of 391 radio sources observed were detected with a fringe spacing of 3 milliarcsec and a detection limit of ~ 0.1 Jy. At 8.4 GHz, 278 of 416 radio sources were detected with a fringe spacing of 1 milliarcsec and a detection limit of ~ 0.1 Jy. This survey was conducted primarily to determine the strength of compact components at 8.4 GHz for radio sources previously detected with VLBI at 2.3 GHz. Compact extragalactic radio sources with strong correlated flux densities at both frequencies are used to form a high-accuracy reference frame.

I. Introduction

Very Long Baseline Interferometry (VLBI) observations of 416 radio sources have been conducted at frequencies of 2.3 GHz and 8.4 GHz. The observations were performed on two intercontinental baselines composed of antennas of the NASA Deep Space Network (California-Spain and California-Australia). This survey was designed primarily to identify compact radio sources at 8.4 GHz. The observed sample was chosen mainly from sources which had already shown compact structure at 2.3 GHz on similar VLBI baselines. Such compact sources are required for the VLBI reference frame used for planetary spacecraft navigation, geodesy, astrometry, and

remote clock synchronization. With observation at dual frequencies (e.g., 2.3 GHz and 8.4 GHz), charged particle effects can be virtually eliminated in these studies. The investigation of the nature of these compact objects can also be aided by this survey, which complements similar previous surveys at 2.3 GHz (Refs. 1, 2).

II. Observed Sample

A high density of suitable VLBI sources is necessary in the ecliptic region for differential VLBI measurements of spacecraft motion and planetary dynamics. Within ± 10 deg of the ecliptic, all 101 sources from a 2.3 GHz ecliptic VLBI survey (Ref. 2) and a 2.3 GHz full-sky VLBI survey (Ref. 1) with 2.3 GHz correlated flux densities greater than 0.3 Jy were included in our observations.

For other VLBI studies in geodesy, astrometry and clock synchronization, a much broader sky distribution of compact

¹Current employer: Haystack Observatory, Westford, MA, 01886

²Current employer: Dept of Astronomy, UCLA, Los Angeles CA, 90024

³Current employer: Dept of Geophysics, USC, Los Angeles, CA, 90089

radio sources is required. For the region outside of the ± 10 deg band of the ecliptic with declinations of less than -45 deg, 113 out of 135 sources in the 2.3 GHz full-sky survey (Ref. 1) with 2.3 GHz correlated flux densities greater than 0.3 Jy were included in our observations.

Also selected for observation were 202 additional sources, most of which had been previously observed in either the ecliptic or full-sky VLBI surveys but which had correlated flux densities at 2.3 GHz less than 0.3 Jy.

III. Observations and Data Reduction

The station and baseline characteristics are listed in Table 1. Nineteen observing sessions involving VLBI baselines consisting of station pairs listed in Table 1 were conducted from October 1981 to August 1984. Each source was observed for at least 3 minutes. Data were taken at 2.3 GHz and 8.4 GHz on alternating seconds for all experiments except one, which observed at 8.4 GHz only. Typical 8.4 GHz (u, v) points were ($2.3 \times 10^8 \lambda, 2.0 \times 10^8 \lambda$) on the Goldstone-Madrid baseline where generally high declination sources were observed, and ($2.1 \times 10^8 \lambda, 2.1 \times 10^8 \lambda$) on the Goldstone-Tidbinbilla baseline where generally low declination sources were observed, where the spatial frequency in the east-west direction is denoted by u and in the north-south direction is denoted by v . The interferometers were sensitive to compact components smaller than the minimum fringe spacing of ~ 3 milliarcsec at 2.3 GHz and ~ 1 milliarcsec at 8.4 GHz.

The Mark II VLBI recording system (Ref. 3) was used to record the data. Digital sampling and phase stability were controlled by a hydrogen maser or rubidium frequency standard at each station. System temperatures either were measured at both antennas and both frequencies for each observation or were estimated using appropriate temperature versus elevation angle curves along with measured zenith system temperatures and approximate knowledge of the total flux densities of the sources. Standard flux density calibration sources for 2.3 GHz (Ref. 4) and 8.4 GHz (Ref. 5) were observed during most observing sessions to determine antenna sensitivity (efficiency) for use in flux density calibration. When such observations were not performed, nominal antenna sensitivities were used in the calibration. Right circular polarization was used for the observations.

The data tapes were correlated on the California Institute of Technology/Jet Propulsion Laboratory Mark II VLBI processor. Correlated flux densities were calculated in the manner described in a previous report (Ref. 6). The $5\text{-}\sigma$ 2.3 GHz detection limit for most observations (~ 60 sec coherent integrations) was ~ 0.1 Jy, although for longer integrations it reached ~ 0.05 Jy. The $5\text{-}\sigma$ detection limit at 8.4 GHz was

usually about ~ 0.15 Jy, although for longer observations it reached ~ 0.05 Jy. Random noise error was about ~ 0.02 Jy at 2.3 GHz and ~ 0.03 Jy at 8.4 GHz, but systematic errors in calibration of about 10 percent were the major sources of error for most observations. Because most sources have previously been detected at 2.3 GHz, positions accurate to 0.3 arcsec were available for 294 of the sources (Refs. 7-10), thus minimizing the search in delay and delay rate space. For previously unobserved sources, the search window was about ± 30 arcsec at 2.3 GHz.

IV. Results and Discussion

The correlated flux densities at 2.3 GHz and 8.4 GHz for 416 extragalactic radio sources are presented in Fig. 1. Notes concerning the entries in that figure appear below:

<u>Column</u>	<u>Notes</u>
1	Source name
2/3	J2000 position (2000.0 Barycenter Equatorial Coordinate System). Asterisked positions have typical uncertainties of 0.3 arcsec and are from Refs. 7-10. Other positions are from the literature, and in most cases, errors are less than 30 arcsec.
4	Number of 2.3 GHz observations. If blank, there was only one observation.
5	Correlated flux density at 2.3 GHz (13.1 cm). If there was more than one observation, the value given is an average over all observations. If the value is preceded by a "<" sign, the object was not detected and the value given is the $5\text{-}\sigma$ upper limit to the correlated flux density. For sources with multiple observations and no detections, the lowest of the upper limits is given.
6	Lowest value for the 2.3 GHz correlated flux density for sources with multiple observations.
7	Highest value for the 2.3 GHz correlated flux density for sources with multiple observations.
8	Number of 8.4 GHz observations. If blank, there was only one observation.
9	Correlated flux density at 8.4 GHz (3.6 cm). If there was more than one observation, the value given is an average over all observations. If the value is preceded by a "<" sign, the object was not detected and the value given is the $5\text{-}\sigma$ upper limit to the correlated flux density. For sources with multiple observations and no detections, the lowest of the upper limits is given.

<u>Column</u>	<u>Notes</u>
10	Lowest value for the 8.4 GHz correlated flux density for sources with multiple observations.
11	Highest value for the 8.4 GHz correlated flux density for sources with multiple observations.

At 2.3 GHz, 323 of 391 (83%) radio sources observed were detected with a fringe spacing of 3 milliarcsec and a detection limit of ~ 0.1 Jy. At 8.4 GHz, 278 of 416 (67%) radio sources were detected with a fringe spacing of 1 milliarcsec and a detection limit of ~ 0.1 Jy. Readily apparent is the higher percentage of objects detected at 2.3 GHz. The lower fraction of sources detected at 8.4 GHz is primarily due to the fact that the sources were originally selected for observation from low frequency surveys. Figure 2 is a sky plot of all 278 detected objects at 8.4 GHz. Figure 3 displays a histogram of the flux densities at both 2.3 GHz and 8.4 GHz. The

distributions of the flux densities for the two observing frequencies are very similar.

Evident in the large deviations between the low and high values of correlated flux density in Fig. 1 of the multiply observed sources is the high degree of variability. Source variability is due to (1) resolvable source structure observed at different interferometer hour angles and (2) intrinsic changes in source strength. The difference between the high and low correlated flux densities for multiply observed sources compared to the measurement errors discussed in Section III gives a measure of source variability over the available observations.

Only seven of the sources previously detected at 2.3 GHz (Refs. 1, 2) were not detected at either frequency in this survey. Four of these sources (3C 2, 3C 66B, P 1317+019 and P 2145-17) were previously detected at 2.3 GHz with very weak flux densities (~ 0.06 Jy) consistent with the detection threshold (~ 0.1 Jy). The other three sources (P 0122-00, P 0922+005, and P 1143-245) were previously detected at higher flux densities.

Acknowledgments

We would like to thank L. Skjerve and the personnel of the Deep Space Network for performing the observations. We would also like to thank S. Kim, J. Kidder, R. Treuhaft, K. Liewer, J. Gunckel, and A. Louie for assistance in data processing.

References

1. Preston, R. A., Morabito, D. D., Williams, J. G., Faulkner, J., Jauncey, D. L., and Nicolson, G. D., "A VLBI Survey at 2.29 GHz," *Astron. J.* 90, 1599-1641, 1985.
2. Wehrle, A. E., Morabito, D. D., and Preston, R. A., "Very Long Baseline Interferometry Observations of 257 Extragalactic Radio Sources in the Ecliptic Region," *Astron. J.* 89, 336-341, 1984.
3. Clark, B. G., "The NRAO Tape Recorder Interferometer System," *Proc. IEEE* 61, 1242-1248, 1973.
4. Klein, M. J., and Stelzried, C. T., "Calibration Radio Sources for Radio Astronomy: Precision Flux-Density Measurements at 2295 MHz," *Astron. J.* 81, 1078-1083, 1975.

5. Turegano, J. A., and Klein, M. J., "Calibration Radio Sources for Radio Astronomy: Precision Flux-Density Measurements at 8420 MHz," *Astron. Astrophys.* **86**, 46-49, 1980.
6. Preston, R. A., Morabito, D. D., Williams, J. G., Slade, M. A., Harris, A. W., Finley, S. G., Skjerve, L. J., Tanida, L., Spitzmesser, D. J., Johnson, B., Jauncey, D. L., Bailey, A., Denise, R., Dickenson, J., Livermore, R., Papij, A., Robinson, A., Taylor, C., Alcazar, F., Luaces, B., Munox, D., "Establishing a Celestial VLBI Reference Frame, I: Searching for VLBI Sources," *The Deep Space Network Progress Report 42-46*, Jet Propulsion Laboratory, Pasadena, Calif., pp. 46-56, May/June 1978.
7. Morabito, D. D., Preston, R. A., Slade, M. A., and Jauncey, D. L., "Arcsecond Positions for Milliarcsecond VLBI Nuclei of Extragalactic Radio Sources, I: 546 Sources," *Astron. J.* **87**, 517-527, 1982.
8. Morabito, D. D., Preston, R. A., Slade, M. A., Jauncey, D. L., and Nicolson, G. D., "Arcsecond Positions for Milliarcsecond VLBI Nuclei of Extragalactic Radio Sources, II: 207 Sources," *Astron. J.* **88**, 1138-1145, 1983.
9. Morabito, D. D., Wehrle, A. E., Preston, R. A., Linfield, R. P., Slade, M. A., Faulkner, J., and Jauncey, D. L., "Arcsecond Positions for Milliarcsecond VLBI Nuclei of Extragalactic Radio Sources, III: 74 Sources," *Astron. J.* **90**, 590-594, 1985.
10. Morabito, D. D., Preston, R. A., Linfield, R. P., Slade, M. A., and Jauncey, D. L., "Arcsecond Positions for Milliarcsecond VLBI Nuclei of Extragalactic Radio Sources, IV: 17 Sources," *Astron. J.* (in preparation), 1986.

Table 1. Observed stations and baselines

Location	Designation	Diameter, m	Baseline, km	Length, $10^6 \lambda$	
				2.3 GHz	8.4 GHz
Tidbinbilla, Australia	DSS 43	64	10.6×10^3	77	295
Goldstone, California	DSS 14 DSS 13	64 } 26 }			
Madrid, Spain	DSS 63 DSS 61	64 } 34 }	8.4×10^3	61	233

(1) SOURCE NAME	(2) RIGHT ASCENSION (J2000)		(3) DECLINATION (J2000)		(4) NUMBER OF OBS (2.3 GHz)	(5) 2.3 GHz CORRELATED FLUX DENSITY			(6) 2.3 GHz CORRELATED FLUX DENSITY			(7) HIGH (JY)	(8) NUMBER OF OBS (8.4 GHz)	(9) 8.4 GHz CORRELATED FLUX DENSITY			(10) CORRELATED FLUX DENSITY		(11) FLUX DENSITY	
	HR	MIN	SEC	DEG		MIN	SEC	AVERAGE (JY)	LOW (JY)	HIGH (JY)	AVERAGE (JY)			LOW (JY)	HIGH (JY)	AVERAGE (JY)	LOW (JY)	HIGH (JY)	LOW (JY)	HIGH (JY)
NRAO 5	0	6	13.84	-	6	23	34.7	*	3	0.50	0.40	0.55	0.31	0.18	0.41					
3C 2	0	6	22.66	-	0	4	33.1			< 0.07			< 0.14							
GC 0007+17	0	10	33.99	17	24	19.0	*		7	0.32	0.43	0.60	0.25	0.31	0.75					
P 0008-264	0	11	1.22	-26	12	33.2	*			0.49			0.58							
P 0011-046	0	13	54.12	-	4	23	52.0	*		0.23			0.25							
P 0013-00	0	16	11.10	-	0	15	12.5	*		0.33			0.38							
0016+73	0	19	45.73	73	27	30.2		2	0.34	0.32	0.35	0.42	0.41	0.42	0.42	0.23	0.23	0.70	0.70	
P 0019+058	0	22	32.71	6	8	0.0	*	15	0.39	0.28	0.52	0.52	0.23	0.70						
P 0022-423	0	24	42.99	-42	2	4.0	*			0.52			< 0.12							
P 0027+056	0	29	45.97	5	54	39.8	*			0.40			0.15							
P 0030+19	0	32	38.24	19	53	44.7				< 0.09			< 0.14							
0032+276	0	34	43.47	27	54	25.7	*			0.24			< 0.14							
GC 0035+12	0	38	18.04	12	27	30.7	*			0.13			0.22							
P 0035-02	0	38	20.52	-	2	7	40.3	*					0.26		0.31					
P 0038-020	0	40	57.18	-	1	46	14.8			0.38			0.23							
P 0041+001	0	43	35.72	0	24	19.1				< 0.06			< 0.06							
P 0047+023	0	49	43.30	2	37	2.9	*			0.21			0.22							
0047-051	0	50	21.52	-	4	52	20.3	*	3	0.15	0.15	0.16	0.26	0.26	0.27	0.26	0.26	0.87	0.87	
P 0048-09	0	50	40.34	-	9	28	49.9	*	2	0.84	0.77	0.90	0.74	0.60	0.87					
0054-006	0	57	17.01	-	0	24	33.3	*		0.15			0.15							
P 0056-00	0	59	5.59	0	6	1.6	*			0.47			< 0.05							
P 0104-408	1	6	45.11	-40	34	20.1		2	1.78	0.46	0.47	0.47	4.26	0.11	0.51					
0105-008	1	8	27.01	-	0	37	20.6			< 0.07			< 0.14							
P 0106+01	1	8	38.84	1	34	59.2	*	27	2.60	1.99	3.31	3.31	1.07	0.21	1.44					
P 0108-079	1	10	50.04	-	7	41	41.3	*		0.52			0.20							
P 0111+021	1	13	43.18	2	22	16.5	*	15	0.26	0.08	0.44	0.44	0.31	0.11	0.51					
P 0112-017	1	15	17.12	-	1	27	4.8	*		0.55			0.79							
GC 0114+07	1	17	26.18	7	42	17.9	*			0.08			0.12							
P 0115+02	1	18	18.53	2	58	4.9	*			0.06			0.15							
GC 0116+08	1	19	1.23	8	29	50.3	*			0.11			< 0.07							
P 0119+11	1	21	41.65	11	49	49.6	*			0.29			0.46							
GC 0119+04	1	21	56.95	4	22	23.3	*	6	0.31	0.05	1.00	1.00	0.53	0.31	0.66					
P 0122-00	1	25	28.97	-	0	5	58.3	*	2	< 0.08			< 0.14							
0124+189	1	26	54.99	19	12	31.0				< 0.08			< 0.13							
0131-001	1	34	12.64	0	3	45.9				0.20			< 0.12							
DA 55	1	36	58.59	47	51	29.1		11	0.67	0.25	1.03	1.03	0.65	0.16	0.92					
P 0136+176	1	39	41.99	17	53	7.2	*			0.22			0.09							
P 0137+012	1	39	57.33	1	31	46.4	*			0.09			< 0.07							
GC 0144+20	1	46	58.79	21	10	24.1	*			0.46			< 0.13							
GC 079	1	49	22.48	5	55	52.1	*			0.46			0.46							
GC 0147+18	1	49	49.76	18	57	19.5	*			0.12			< 0.12							
P 0149+21	1	52	18.05	22	7	7.6	*			0.39			0.68							
P 0150-334	1	53	10.11	-33	10	25.9	*			0.77			0.73							
P 0158+031	2	0	40.81	3	22	49.7	*			0.27			0.11							
P 0159+034	2	1	51.51	3	43	9.2	*			0.09			0.08							

Fig. 1. VLBI survey results

(1) SOURCE NAME	(2) RIGHT ASCENSION (J2000) HR MN SEC		(3) DECLINATION (J2000) DEG MN SEC		(4) NUMBER OF OBS (2.3 GHz)	(5) 2.3 GHz CORRELATED FLUX DENSITY (JY)			(6) LOW (JY)	(7) HIGH (JY)	(8) NUMBER OF OBS (8.4 GHz)	(9) 8.4 GHz CORRELATED FLUX DENSITY (JY)			(10) LOW (JY)	(11) HIGH (JY)
	AVERAGE	LOW	HIGH	AVERAGE		LOW	HIGH									
P 0201+113	2	3	46.73	11	34	44.4	*	0.90	0.80	1.10	4	0.20	0.11	0.26		
P 0202+14	2	4	50.47	15	14	10.2	*	1.13	0.77	1.40	8	1.18	0.90	1.53		
DW 0202+31	2	5	4.93	32	12	30.0	*	0.77	0.77	0.77	19	0.34	0.19	2.14		
0212+735	2	17	30.83	73	49	32.7	*	0.79	0.25	1.64	19	1.55	0.19	2.14		
3C 66A	2	22	39.63	43	2	7.6	*	0.18	0.18	0.18		0.21				
3C 66B	2	23	11.42	42	59	31.2	*	< 0.08	< 0.08	< 0.08		< 0.08				
GC 0221+06	2	24	28.52	6	59	22.1	*	0.28	0.28	0.28		1.24				
DW 0224+67	2	28	50.03	67	21	2.9		0.92	0.90	0.93	2	< 0.13				
P 0229+13	2	31	45.90	13	22	54.6	*	0.48	0.48	0.48		1.35				
0229+262	2	32	27.62	26	28	38.3	*	0.20	0.20	0.20		< 0.13				
CTD 20	2	37	52.41	28	48	8.9	*	1.32	0.74	1.76	15	2.05	0.94	2.96		
GC 0235+16	2	38	38.95	16	36	58.9	*	1.61	0.90	2.30	14	1.91	1.19	2.55		
GC 0237+04	2	39	51.29	4	16	21.0	*	0.27	0.27	0.27		0.52				
OD 166	2	42	29.19	11	1	0.6	*	0.89	0.75	1.11	10	0.61	0.39	1.00		
0242+238	2	45	16.83	24	5	34.9	*	0.12	0.12	0.12		0.19				
P 0246+064	2	48	58.11	6	41	43.8		< 0.09	< 0.09	< 0.09		< 0.16				
GC 0250+17	2	53	34.90	18	5	42.3	*	0.29	0.29	0.29		0.08				
P 0253+13	2	56	35.00	13	34	35.5	*	0.05	0.05	0.05		0.12				
0254+092	2	56	45.00	9	29	3.6		< 0.10	< 0.10	< 0.10		< 0.17				
OD 094.7	2	59	27.06	7	47	39.9	*	0.48	0.45	0.51	8	0.43	0.16	0.62		
P 0259+07	3	1	49.93	7	25	7.0		< 0.09	< 0.09	< 0.09		< 0.15				
DE 400	3	3	35.24	47	16	16.2	*	1.18	0.43	1.61	9	2.28	1.28	2.89		
0300+162	3	3	15.01	16	26	14.8		< 0.10	< 0.10	< 0.10		< 0.11				
0305+039	3	8	26.32	4	6	37.8		0.18	0.17	0.28	2	< 0.10	0.62	0.68		
DE 110	3	9	3.64	10	29	16.0	*	0.22	0.17	0.28	2	0.65	0.62	0.68		
CTA 21	3	18	57.79	16	28	32.4	*	0.12	0.12	0.12		< 0.07				
3C 84	3	19	48.16	41	30	42.1	*	2.18	1.08	3.75	4	0.97	0.83	1.28		
P 0317+188	3	19	51.27	19	1	31.4	*	0.30	0.30	0.30		0.14				
0322+245	3	25	4.35	24	44	32.0		< 0.24	< 0.24	< 0.24		< 0.14				
GC 0322+22	3	25	35.91	22	24	12.2	*	0.33	0.33	0.33		< 0.07				
P 0332-403	3	34	13.66	-40	8	25.4	*	0.94	0.78	1.13	7	0.88	0.50	1.44		
NRAD 140	3	36	30.11	32	18	29.6	*	0.97	0.37	1.70	12	0.50	0.31	0.94		
P 0335-122	3	37	55.68	-12	4	12.5		< 0.08	< 0.08	< 0.08	2	< 0.13				
P 0336-017	3	39	1.70	-1	33	17.2		< 0.09	< 0.09	< 0.09		< 0.20				
CTA 26	3	39	30.94	-1	46	35.9		1.44	1.44	1.44		0.50				
0338+074	3	40	53.78	7	35	23.9		0.21	0.21	0.21		< 0.10				
P 0338-214	3	40	35.59	-21	19	31.2	*	0.46	0.46	0.46		0.90				
GC 0344+19	3	47	30.56	20	4	38.4	*	0.27	0.27	0.27		< 0.07				
GC 0346+20	3	49	45.25	21	4	45.5		< 0.14	< 0.14	< 0.14		< 0.14				
0357+057	4	0	11.49	5	51	3.4		< 0.09	< 0.09	< 0.09		< 0.12				
CTD 26	4	3	5.58	26	0	1.5	*	0.26	0.21	0.32	2	< 0.14				
P 0400-319	4	2	21.27	-31	47	26.0	*	0.66	0.66	0.66		0.47				
P 0402-362	4	3	53.75	-36	5	2.0		0.52	0.48	0.58	9	1.39	0.59	1.91		
P 0404+177	4	7	28.97	17	50	33.0		< 0.06	< 0.06	< 0.06		< 0.07				
GC 0406+12	4	9	22.00	12	17	39.8	*	0.54	0.34	1.60	14	0.34	0.22	0.45		

Fig. 1 (contd)

(1) SOURCE NAME	(2) RIGHT ASCENSION (J2000)		(3) DECLINATION (J2000)		(4) NUMBER OF OBS (2.3 GHz)	(5) 2.3 GHz CORRELATED FLUX DENSITY		(6) 8.4 GHz CORRELATED FLUX DENSITY		(7) HIGH (JY)	(8) NUMBER OF OBS (8.4 GHz)	(9) 8.4 GHz CORRELATED FLUX DENSITY		(10) CORRELATED FLUX DENSITY		(11) HIGH (JY)
	HR	MN	SEC	DEG		MIN	SEC	AVERAGE (JY)	LOW (JY)			AVERAGE (JY)	LOW (JY)	AVERAGE (JY)	LOW (JY)	
P 0409+22	4	12	43.59	23	4	53.9	0.21	0.11	0.33		2	0.25	0.25	0.26		
3C 109	4	13	40.37	11	12	14.1 *	0.11	0.17	0.17			< 0.15	0.13	0.45		
P 0414-189	4	16	36.51	-18	51	8.1 *	0.44	0.44	0.41		9	0.90	1.03	2.63		
P 0420-01	4	23	15.80	-1	20	33.1	1.79	1.79	1.76	2.00		< 0.07				
GC 0423+23	4	26	34.95	23	27	48.4 *	0.17	0.17	0.07							
P 0423+051	4	26	36.66	5	18	18.9 *	0.52	0.51	0.25	0.53	2	0.25	0.25	0.26		
0426+273	4	29	52.96	27	24	37.4 *	0.21	0.21	0.15			< 0.15	0.25	0.26		
P 0426-380	4	28	40.43	-37	56	19.7 *	0.70	0.70	0.90			< 0.07	0.13	0.45		
P 0428+20	4	31	3.69	20	37	34.1	0.13	0.13	0.26	0.56	7	0.26	0.13	0.45		
3C 120	4	33	11.13	5	21	14.3 *	0.37	0.08	0.07			< 0.15	0.13	0.45		
P 0434-188	4	37	1.46	-18	44	48.5 *	0.74	0.57	0.44	0.80	7	0.44	0.15	0.75		
P 0438-43	4	40	17.18	-43	33	8.6	0.68	0.50	0.77	0.79	6	0.77	0.40	0.92		
P 0446+11	4	49	7.67	11	21	28.3 *	0.31	0.31	0.50	0.31	2	0.50	0.41	0.60		
P 0446+20	4	49	25.76	20	44	34.9	< 0.06	< 0.06	< 0.07			< 0.07				
P 0451-28	4	53	14.60	-28	7	36.7 *	0.59	0.13	0.15			< 0.15	0.21	0.63		
P 0452+23	4	55	22.90	23	10	19.1	< 0.06	< 0.06	< 0.08			< 0.08				
P 0454+06	4	57	7.76	6	49	6.5 *	0.14	0.14	0.42	0.43	2	0.31	0.28	0.34		
0454+844	5	8	42.38	84	32	4.6 *	0.50	0.50	0.38	0.66	17	0.38	0.21	0.63		
P 0456+060	4	58	48.82	6	8	3.2 *	0.16	0.16	0.14	0.17		0.14				
P 0458-02	5	1	12.82	-1	59	14.6 *	1.32	1.32	0.61			0.61				
P 0458+138	5	1	45.26	13	56	7.7 *	0.13	0.13	0.07			< 0.07	0.49	0.51		
GC 0459+06	5	2	15.48	6	9	6.9 *	0.42	0.42	0.31	0.43	2	0.31	0.28	0.34		
3C 133	5	2	58.47	25	16	23.4 *	0.24	0.24	0.16			< 0.16				
0500+060	5	2	40.88	6	9	33.7	< 0.09	< 0.09	< 0.14			< 0.14				
06 003	5	3	21.20	2	3	4.5 *	0.77	0.77	0.55			0.55				
P 0502+049	5	5	23.17	4	59	42.2 *	0.30	0.30	0.50	0.34	2	0.50	0.49	0.51		
P 0504+23	5	7	6.41	23	51	13.7	< 0.06	< 0.06	0.08			< 0.08				
0505+173	5	7	59.87	17	23	41.6	< 0.10	< 0.10	0.16			< 0.16				
0506+056	5	9	25.95	5	41	35.4 *	0.25	0.25	0.13	0.45	3	0.13	0.21	0.81		
P 0507+17	5	10	2.36	18	0	41.5 *	0.33	0.33	0.57			0.57	0.14	0.26		
P 0509+152	5	12	41.01	15	17	23.4 *	0.66	0.66	0.20	0.81	2	0.20	0.14	0.26		
P 0511-220	5	13	49.12	-21	59	16.2 *	0.31	0.31	0.67			0.67				
0514+109	5	16	46.81	10	57	57.8	< 0.10	< 0.10	0.16			< 0.16				
0515+067	5	17	51.14	6	48	11.1	< 0.10	< 0.10	< 0.15			< 0.15				
0516+144	5	19	31.07	14	28	24.2	< 0.10	< 0.10	0.16			< 0.16				
3C 138	5	21	9.88	16	38	22.1 *	0.34	0.34	0.07			< 0.07				
P 0521-36	5	22	57.97	-36	27	30.7 *	0.85	0.85	0.86			0.86				
0528-290	5	30	7.92	-25	3	29.5 *	0.34	0.34	0.13			0.13				
P 0528+134	5	30	56.42	13	31	55.2 *	1.15	1.15	1.06	1.53	6	1.06	0.69	1.66		
P 0537-441	5	38	50.36	-44	5	9.0	0.39	0.39	2.55	0.57	4	2.55	0.88	3.94		
0544+273	5	47	34.12	27	21	57.0 *	0.21	0.21	0.31	0.25	3	0.31	0.29	0.32		
DA 193	5	55	30.81	39	48	49.2	2.03	2.03	2.09	2.33	9	2.09	1.79	2.41		
0554+242	5	57	4.56	24	13	53.7 *	0.23	0.23	0.20	0.34	3	0.20	0.12	0.32		
0556+238	5	59	32.02	23	53	54.0 *	0.24	0.24	0.33	0.25	3	0.33	0.29	0.36		
0600+177	6	3	9.16	17	42	20.9 *	0.34	0.34	0.24	0.35	2	0.24	0.20	0.28		

Fig. 1 (contd)

ORIGINAL PAGE IS
OF POOR QUALITY

(1) SOURCE NAME	(2) RIGHT ASCENSION (J2000) HR MN SEC		(3) DECLINATION (J2000) DEG MN SEC		(4) NUMBER OF OBS (2.3 GHz)	(5) 2.3 GHz CORRELATED FLUX DENSITY (JY)			(6) 2.3 GHz CORRELATED FLUX DENSITY (JY)			(7) HIGH (JY)	(8) NUMBER OF OBS (8.4 GHz)	(9) 8.4 GHz CORRELATED FLUX DENSITY (JY)			(10) 8.4 GHz CORRELATED FLUX DENSITY (JY)		(11) HIGH (JY)
	AVERAGE	LOW	HIGH	AVERAGE		LOW	HIGH	AVERAGE	LOW	HIGH	LOW			HIGH					
P 0601+24	6	4	55.27	24	29	23.2	0.10	0.10	0.10	0.10	0.12	4	< 0.07	0.63	1.13				
P 0607-15	6	9	40.95	-15	42	40.7	0.11	0.10	0.11	0.12	0.11	4	0.91	0.10	0.11	0.63	1.13		
0610+260	6	13	50.12	26	4	36.9 *	0.11	0.10	0.11	0.12	0.11	2	< 0.09	0.10	0.11	0.10	0.11		
0615+82	6	26	3.03	82	2	25.6	0.45	0.45	0.45	0.45	0.45	2	< 0.08						
P 0618+23	6	21	0.34	23	18	43.9	< 0.10												
DH 335	6	24	19.02	38	56	48.6 *	0.47	0.47	0.47	0.48	0.48	2	0.24	0.24	0.25	0.24	0.25		
0629+160	6	32	43.12	15	59	57.7 *	0.29	0.28	0.29	0.31	0.31	2	0.15	0.14	0.16	0.14	0.16		
3C 166	6	45	24.09	21	21	51.1 *	0.49	0.49	0.49	0.49	0.49	2	0.38	0.38	0.38	0.38	0.38		
P 0642-349	6	44	25.25	-34	59	41.8 *	0.49	0.49	0.49	0.49	0.49	2	0.26	0.26	0.26	0.26	0.26		
P 0646-306	6	48	14.07	-30	44	19.5 *	0.56	0.56	0.56	0.56	0.56	2	0.37	0.37	0.37	0.37	0.37		
GC 0650+37	6	53	58.28	37	5	40.6 *	0.82	0.81	0.82	0.83	0.83	2	0.93	0.90	0.95	0.90	0.95		
0657+172	7	0	1.50	17	9	22.0 *	0.72	0.66	0.72	0.78	0.78	2	0.21	0.19	0.24	0.19	0.24		
01 318	7	14	24.85	35	34	39.1 *	0.45	0.43	0.45	0.48	0.48	3	0.36	0.35	0.39	0.35	0.39		
P 0722+145	7	25	17.07	14	25	9.4 *	0.56	0.31	0.56	0.76	0.76	6	0.63	0.34	0.99	0.34	0.99		
DW 0723-00	7	25	50.65	-0	54	56.9 *	0.74	0.56	0.74	0.85	0.85	4	1.61	1.16	1.90	1.16	1.90		
P 0727-11	7	30	19.01	-11	41	11.2 *	0.22	0.21	0.22	0.22	0.22	2	0.26	0.24	0.28	0.24	0.28		
GC 0729+25	7	32	56.28	25	48	38.7 *	0.34	0.32	0.34	0.37	0.37	3	0.32	0.31	0.36	0.31	0.36		
GC 0733+30	7	36	13.65	29	54	22.1 *	0.70	0.54	0.70	0.90	0.90	6	1.18	0.81	1.49	0.81	1.49		
P 0735+17	7	38	7.38	17	42	18.6 *	0.25	0.25	0.25	0.25	0.25	2	0.24	0.24	0.24	0.24	0.24		
P 0736-06	7	38	57.26	-6	26	59.7 *	0.71	0.71	0.71	0.71	0.71	5	0.74	0.74	0.74	0.74	0.74		
P 0736+01	7	39	18.07	1	37	3.8 *	1.33	1.11	1.33	1.51	1.51	5	0.61	0.28	1.03	0.28	1.03		
01 363	7	41	10.73	31	12	0.2 *	0.18	0.10	0.18	0.25	0.25	4	< 0.09	0.24	0.34	0.24	0.34		
B2 0738+27	7	41	25.76	27	6	45.3 *	0.20	0.07	0.20	0.43	0.43	3	0.31	0.30	0.34	0.30	0.34		
B2 0742+31	7	49	41.66	31	42	56.7 *	1.60	0.64	1.60	2.50	2.50	16	0.64	0.30	0.88	0.30	0.88		
DW 0742+10	7	45	33.09	10	11	12.7 *	0.48	0.47	0.48	0.48	0.48	3	0.36	0.33	0.37	0.33	0.37		
GC 0743+25	7	46	25.90	25	49	2.1 *	0.67	0.58	0.67	0.86	0.86	4	1.09	0.74	1.29	0.74	1.29		
B2 0745+24	7	48	36.17	24	0	23.1 *	0.33	0.15	0.33	0.50	0.50	7	0.46	0.26	0.59	0.26	0.59		
P 0748+126	7	50	52.01	12	31	5.0 *	0.33	0.32	0.33	0.35	0.35	3	< 0.09	0.26	0.26	0.26	0.26		
GC 0748+33	7	51	53.66	33	13	19.6 *	0.87	0.87	0.87	0.88	0.88	3	0.66	0.57	0.82	0.57	0.82		
P 0754+100	7	57	6.66	9	56	34.6 *	0.32	0.26	0.32	0.39	0.39	4	0.21	0.18	0.23	0.18	0.23		
GC 0759+18	8	2	48.06	18	9	49.3 *	0.49	0.34	0.49	0.64	0.64	3	< 0.09	0.22	0.22	0.22	0.22		
GC 0802+21	8	5	38.60	21	6	50.6 *	0.11	0.11	0.11	0.11	0.11	8	< 0.13	0.40	0.40	0.40	0.40		
GC 0805+26	8	8	36.78	26	46	36.6 *	0.41	0.41	0.41	0.41	0.41	3	0.27	0.27	0.27	0.27	0.27		
P 0805-07	8	8	15.61	-7	51	11.5 *	< 0.08						< 0.15						
0811+131	8	14	43.68	12	58	4.4	0.94	0.72	0.94	1.11	1.11	8	1.55	1.08	1.89	1.08	1.89		
DJ 425	8	18	16.00	42	22	45.4	0.30	0.30	0.30	0.30	0.30	6	0.28	0.22	0.22	0.22	0.22		
P 0820+22	8	23	24.84	22	23	1.9 *	0.44	0.44	0.44	0.44	0.44	6	1.14	0.22	1.59	0.22	1.59		
P 0823+033	8	25	50.37	3	9	24.2 *	< 0.08						< 0.16	0.40	0.40	0.40	0.40		
0827+235	8	30	21.74	23	23	25.5	0.35	0.35	0.35	0.35	0.35	2	0.25	0.25	0.25	0.25	0.25		
B2 0827+24	8	30	52.09	24	10	59.7 *	0.44	0.44	0.44	0.44	0.44	2	0.14	0.14	0.14	0.14	0.14		
GC 0834+25	8	37	40.23	24	54	23.0 *	0.25	0.25	0.25	0.25	0.25	2	0.25	0.25	0.25	0.25	0.25		
4C 71.07	8	41	24.44	70	53	41.7 *	0.44	0.44	0.44	0.44	0.44	2	0.28	0.28	0.28	0.28	0.28		
GC 0839+18	8	42	5.19	18	35	39.4 *	1.37	1.37	1.37	1.37	1.37	9	3.57	0.99	4.73	0.99	4.73		
DJ 287	8	54	48.93	20	6	29.5 *	< 0.07						< 0.07						
0854+342	8	57	40.26	34	4	39.6													

Fig. 1 (contd)

(1) SOURCE NAME	(2) RIGHT ASCENSION (J2000)		(3) DECLINATION (J2000) DEG MN SEC	(4) NUMBER OF OBS (2.3 GHz)	(5) 2.3 GHz CORRELATED FLUX DENSITY			(6) LOW (JY)	(7) HIGH (JY)	(8) NUMBER OF OBS (8.4 GHz)	(9) 8.4 GHz CORRELATED FLUX DENSITY			(10) LOW (JY)	(11) HIGH (JY)
	HR MN SEC	HR MN SEC			AVERAGE (JY)	AVERAGE (JY)	AVERAGE (JY)				AVERAGE (JY)	AVERAGE (JY)			
P 0912+029	9 14 37.94	2 45 58.5 *			0.18						0.30				
P 0922+005	9 25 10.06	0 20 27.1 *			< 0.08						< 0.10				
4C 39 25	9 27 3.01	39 2 19.7 *		9	1.22		0.63	1.83	9		0.97	0.64		1.43	
P 0925-203	9 27 51.80	-20 34 50.9 *			0.10						0.26				
P 0931-114	9 33 34.46	-11 39 25.9 *			0.38						0.18				
MC 0938+119	9 41 13.55	11 45 32.0 *			0.10						0.10				
AD 0952+17	9 54 56.82	17 43 31.1 *		3	0.13		0.08	0.17	3		0.34	0.29		0.39	
OK 290	9 56 49.86	25 15 16.1		2	0.37		0.36	0.37	2		0.24	0.21		0.26	
GC 1004+14	10 7 41.48	13 56 29.8 *		3	0.26		0.23	0.32	3		0.29	0.28		0.31	
1011+250	10 13 53.45	24 49 16.4 *			0.16						0.37				
P 1012+232	10 14 47.07	23 1 16.4 *			0.56		0.15	0.34	4		0.68	0.27		0.48	
OC 1013+20	10 16 44.28	20 37 48.0 *		4	0.29						< 0.07			0.31	
P 1020+191	10 22 55.13	18 53 34.5 *		3	0.31		0.30	0.31	3		0.28	0.25		0.31	
GC 1022+19	10 24 44.80	19 12 20.4 *			0.45						0.26				
P 1034-374	10 36 53.50	-37 44 15.0 *			0.77		0.61	0.86	3		1.17	0.96		1.47	
P 1034-293	10 37 16.09	-29 34 2.6 *		3	0.29		0.37	0.65	7		0.24	0.31		0.74	
P 1036-154	10 39 6.71	-15 41 6.7 *			0.48						< 0.14				
DL 064.5	10 41 17.19	6 10 17.1 *		7	0.19						0.42				
1039+300	10 42 36.49	29 49 45.0 *													
3C 245	10 42 44.57	12 3 31.6 *													
P 1042+071	10 44 55.91	6 55 38.2 *		4	0.25		0.18	0.32	4		0.24	0.20		0.28	
1044+71	10 48 27.62	71 43 35.8 *			0.75						0.36				
P 1045-18	10 48 6.63	-19 9 35.7 *			0.53						0.84				
P 1045+05C	10 49 32.94	5 5 42.6									< 0.07				
1053+70	10 56 53.62	70 11 45.8 *			0.19						0.43				
P 1055+01	10 58 29.61	1 33 55.7 *		9	0.63		0.49	0.91	9		1.41	1.12		1.59	
GC 1104+16	11 7 15.04	16 28 2.4 *			0.20						0.14				
P 1104-445	11 7 8.70	-44 49 7.4		3	1.40		1.19	1.79	3		0.93	0.75		1.07	
GC 1111+14	11 13 58.68	14 42 27.3 *			0.37						0.11				
P 1118-05	11 21 25.39	-5 53 41.0			< 0.09						< 0.13				
P 1123+26	11 25 53.68	26 10 19.5 *		7	0.58		0.47	0.68	7		0.49	0.42		0.65	
P 1124-186	11 27 4.42	-18 57 17.8 *			1.05						0.61				
P 1127-045	11 29 35.41	-4 47 4.6			< 0.09						< 0.06				
P 1127-14	11 30 7.06	-14 49 27.3		3	0.48		0.36	0.68	3		0.45	0.17		0.73	
GC 1128+38	11 30 53.28	38 15 18.9 *		7	0.83		0.73	0.90	7		1.03	0.65		1.42	
P 1130+10C	11 33 0.42	10 23 30.3 *			0.09						< 0.07				
P 1142+052	11 45 21.24	4 55 27.7 *			0.13						< 0.12				
P 1143-245	11 46 8.10	-24 47 32.7 *			< 0.09						< 0.15				
P 1144-379	11 47 1.47	-38 12 11.2 *		3	0.94		0.87	1.02	3		3.63	2.75		4.31	
1144+352	11 47 22.13	35 1 7.3 *			0.38						< 0.14				
DM-076	11 47 51.40	-7 24 38.6 *			0.69						0.24			0.29	
P 1148-00	11 50 43.97	-0 24 22.8 *		9	0.31		0.19	0.70	9		0.22	0.09			
P 1149-084	11 52 17.20	-8 41 3.3 *			0.24						0.15				
P 1150+09	11 53 13.05	9 14 11.6			0.08						< 0.07				
P 1157-215	11 59 51.92	-21 48 53.7 *			0.38						0.22				

Fig. 1 (contd)

(1) SOURCE NAME	(2) RIGHT ASCENSION (J2000)		(3) DECLINATION (J2000)		(4) NUMBER OF OBS (2.3 GHz)	(5) 2.3 GHz CORRELATED FLUX DENSITY (JY)			(6) 8.4 GHz CORRELATED FLUX DENSITY (JY)			(8) NUMBER OF OBS (8.4 GHz)	(9) 8.4 GHz CORRELATED FLUX DENSITY (JY)			
	HR	MN	SEC	DEG		MIN	SEC	AVERAGE	LOW	HIGH	AVERAGE		LOW	HIGH	AVERAGE	LOW
1215-002	12	17	58.71	-	0	29	45.8	*	0.08	0.43	0.56	4	1.01	0.85	1.16	
P 1217+02	12	20	11.85	2	3	42.8	*	0.08	0.43	0.56	4	1.01	0.85	1.16		
P 1222+037	12	24	52.43	3	30	50.3	*	0.59	0.46	0.89	8	0.89	0.25	0.64		
P 1223-074	12	26	16.33	-	7	41	6.2	<	0.08	0.43	0.56	4	1.01	0.85	1.16	
P 1225-083	12	28	19.84	-	8	38	17.2	<	0.08	0.43	0.56	4	1.01	0.85	1.16	
3C 273	12	29	6.64	2	3	9.8	*	1.94	1.01	4.69	20	4.69	2.94	6.00		
3C 274	12	30	49.43	12	23	28.1	*	0.62	0.43	0.56	4	1.01	0.85	1.16		
P 1228-113	12	30	55.56	-11	39	10.0	*	0.28	0.43	0.56	4	1.01	0.85	1.16		
P 1237-10	12	39	43.06	-10	23	28.7	*	0.08	0.43	0.56	4	1.01	0.85	1.16		
DN-073	12	46	4.23	-	7	30	46.5	*	0.56	0.43	0.56	4	1.01	0.85	1.16	
P 1244-255	12	46	46.81	-25	47	49.5	*	0.48	0.43	0.56	4	1.01	0.85	1.16		
3C 279	12	56	11.17	-	5	47	21.5	*	3.97	1.82	4.88	8	2.12	1.30	3.59	
P 1302-102	13	5	32.62	-10	33	13.1	*	0.42	0.43	0.56	4	1.01	0.85	1.16		
B2 1308+32	13	10	28.74	32	20	41.9	*	0.64	0.30	1.24	11	1.24	0.42	2.21		
P 1310-041	13	12	50.92	-	4	24	50.2	*	0.77	0.47	0.71	2	0.70	0.62	0.78	
OP-322	13	16	8.00	-33	38	58.8	*	0.59	0.47	0.71	2	0.70	0.62	0.78		
P 1317+019	13	20	26.79	1	40	39.7	*	<	0.08	0.43	0.56	4	1.01	0.85	1.16	
P 1333-049	13	35	56.41	-	5	11	40.3	*	0.09	0.43	0.56	4	1.01	0.85	1.16	
P 1333-082	13	36	7.63	-	8	30	48.2	*	0.09	0.43	0.56	4	1.01	0.85	1.16	
DW 1339-12	13	37	39.75	-12	57	24.0	*	0.77	0.51	1.09	5	1.09	0.96	2.02		
P 1340-17	13	43	37.42	-17	47	55.4	*	0.13	0.43	0.56	4	1.01	0.85	1.16		
GC 1342+662	13	43	45.96	66	2	25.6	*	0.25	0.19	0.32	13	0.32	0.18	0.43		
GC 1342+663	13	44	8.67	66	6	11.4	*	0.61	0.53	0.69	26	0.69	0.31	0.71		
P 1349-439	13	52	56.55	-44	12	40.5	*	0.44	0.38	0.50	2	0.50	0.80	1.12		
P 1351-018	13	54	6.98	-	2	6	4.4	*	0.44	0.38	0.50	2	0.50	0.80	1.12	
P 1354-174	13	57	6.03	-17	44	1.3	*	0.22	0.22	0.27	2	0.27	0.27	0.27		
OP-192	13	57	11.20	-15	27	28.3	*	0.93	0.44	0.66	10	0.66	0.53	1.03		
P 1354+19	13	57	4.43	19	19	7.4	*	0.55	0.44	0.66	10	0.66	0.53	1.03		
P 1402-012	14	4	46.00	-	1	30	23.6	*	0.55	0.44	0.66	10	0.66	0.53	1.03	
OG 208	14	7	0.41	28	27	14.6	*	0.55	0.44	0.66	10	0.66	0.53	1.03		
P 1406-076	14	8	56.43	-	7	52	29.9	*	0.24	0.24	0.27	2	0.27	0.27	0.27	
P 1406-230	14	9	10.30	-23	16	48.8	*	<	0.08	0.43	0.56	4	1.01	0.85	1.16	
P 1412-096	14	15	20.66	-	9	56	27.2	*	<	0.08	0.43	0.56	4	1.01	0.85	1.16
GC 1418+54	14	19	46.59	54	23	14.7	*	1.02	0.80	1.31	14	1.31	0.35	1.66		
P 1418-064	14	21	7.80	-	6	43	56.2	*	1.02	0.80	1.31	14	1.31	0.35	1.66	
P 1427+109	14	30	9.73	10	43	29.1	*	0.62	0.58	0.64	3	0.64	0.22	0.29		
OG-151	14	32	57.69	-18	1	35.0	*	0.62	0.58	0.64	3	0.64	0.22	0.29		
P 1430-155	14	33	21.48	-15	48	44.9	*	0.68	0.68	0.70	11	0.70	0.68	0.86		
P 1434+235	14	36	40.98	23	21	3.2	*	0.68	0.68	0.70	11	0.70	0.68	0.86		
P 1443-162	14	45	53.37	-16	29	1.5	*	0.36	0.36	2.19	10	2.19	0.35	1.99		
P 1445-16	14	48	15.05	-16	20	24.5	*	0.35	0.35	2.19	10	2.19	0.35	1.99		
P 1452-167	14	55	3.13	-17	0	9.0	*	<	0.08	0.43	0.56	4	1.01	0.85	1.16	
P 1455+24	14	57	43.45	24	35	7.4	*	<	0.08	0.43	0.56	4	1.01	0.85	1.16	
DR 103	15	4	24.98	10	29	39.2	*	0.62	0.54	0.70	11	0.70	0.68	0.86		
P 1504-167	15	7	4.75	-16	52	29.9	*	1.74	1.33	2.19	10	2.19	0.35	1.99		

Fig. 1 (contd)

(1) SOURCE NAME	(2) RIGHT ASCENSION (J2000)		(3) DECLINATION (J2000)		(4) NUMBER OF OBS (2.3 GHz)	(5) 2.3 GHz CORRELATED FLUX DENSITY			(6) CORRELATED FLUX DENSITY			(7) HIGH (JY)	(8) NUMBER OF OBS (8.4 GHz)	(9) 8.4 GHz CORRELATED FLUX DENSITY		
	HR	MIN	SEC	DEG		MIN	SEC	AVERAGE (JY)	LOW (JY)	HIGH (JY)	AVERAGE (JY)			LOW (JY)	HIGH (JY)	
P 1510-08	15	12	50.53	-9	5	59.8	1.18	1.00	1.31	1.36	0.41	1.93	10	1.36	0.41	1.93
P 1511-100	15	13	44.88	-10	12	0.3 *	0.70	0.43	0.46	0.81			2	< 0.11		
P 1511-210	15	13	56.97	-21	14	57.5 *	0.44	0.12	0.12	< 0.13			2	< 0.13		
1511+238	15	13	40.19	23	38	35.1 *	0.54			0.49						
P 1514-24	15	17	41.83	-24	22	19.4 *										
P 1519-273	15	22	37.73	-27	30	11.0 *	1.09	0.92	1.18	1.65	1.29	1.93	3	1.65	1.29	1.93
1529+337	15	31	26.31	35	34	0.8	< 0.09			< 0.15			2	< 0.15		
P 1532+01	15	34	52.53	1	31	3.1 *				0.76				0.76		
P 1535+004	15	38	15.98	0	19	5.0 *	1.12			< 0.21				< 0.21		
DW 1548+05	15	50	35.29	5	27	10.2 *				1.07				1.07		
P 1550-269	15	54	2.51	-27	4	40.3 *	0.46	0.24	0.47	0.17	0.33	0.48	6	0.17	0.33	0.48
DW 1555+00	15	57	51.43	-0	1	50.4	0.37	0.25	0.27	0.39				0.39		
P 1555-140	15	58	21.92	-14	9	58.9 *	0.26			0.08				0.08		
P 1556-245	15	59	41.42	-24	42	38.7 *	< 0.12			0.10				0.10		
P 1601-222	16	4	1.60	-22	23	47.4				< 0.22				< 0.22		
P 1604-333	16	7	34.74	-33	31	8.8 *	1.17	0.88	1.44	0.38	0.38	1.29	8	0.38	0.38	1.29
DA 406	16	13	41.06	34	12	47.9	< 0.11			< 0.13				< 0.13		
P 1614+26	16	16	38.32	26	47	1.5	0.16	0.15	0.17	0.45	0.24	0.57	3	0.45	0.24	0.57
P 1622-253	16	25	46.91	-25	27	38.3 *				0.89				0.89		
P 1622-29	16	26	6.02	-29	51	26.9 *				0.07				0.07		
P 1625-141	16	28	45.88	-14	15	30.2 *	1.05	0.64	1.45	3.01	2.39	4.49	10	3.01	2.39	4.49
GC 1633+38	16	35	13.50	38	8	4.4 *	0.97	0.78	1.16	0.18				0.18		
GC 1637+57	16	38	13.44	57	20	23.9 *	0.75	0.68	0.80	1.29	0.55	2.41	13	1.29	0.55	2.41
NRAD 512	16	40	29.63	39	46	46.0	0.40	0.34	0.46	< 0.12			2	< 0.12		
OS-268	16	43	33.39	-23	16	7.9 *				0.23				0.23		
1640+254	16	42	40.40	25	23	7.7 *	0.40	0.29	4.05	2.59	0.90	5.92	34	2.59	0.90	5.92
3C 345	16	42	58.84	39	48	36.5 *	1.42			0.62				0.62		
GC 1642+69	16	42	7.85	68	56	39.7 *	0.46	< 0.08		< 0.12				< 0.12		
1642+237	16	44	59.08	25	36	30.1				< 0.07				< 0.07		
P 1643-22	16	46	4.37	-22	27	51.9				0.35				0.35		
P 1647-296	16	50	39.52	-29	43	46.6 *	0.72	0.26	0.50	0.53	0.37	0.70	11	0.53	0.37	0.70
OS 092	16	58	9.02	7	41	27.2 *	0.60	< 0.09		< 0.20				< 0.20		
DW 1654+05	16	58	33.42	5	15	17.9 *	0.48	0.35	0.58	1.28	0.94	1.66	9	1.28	0.94	1.66
P 1657-261	17	0	53.14	-26	10	51.6 *	< 0.10			< 0.17				< 0.17		
P 1657-298	17	1	9.23	-29	54	21.3										
OT-111	17	9	34.36	-17	28	53.5 *	0.37	0.26	0.50	0.53	0.37	0.70	11	0.53	0.37	0.70
1709+303	17	11	19.96	30	19	17.4	< 0.09			< 0.20				< 0.20		
1719+35	17	21	9.36	35	42	11.2	< 0.09			0.29				0.29		
GC 1726+45	17	27	27.64	45	30	39.8 *	2.16	1.47	3.02	2.42	1.43	2.90	16	2.42	1.43	2.90
NRAD 530	17	33	2.70	-13	4	49.5										
OT 465	17	39	57.13	47	37	58.4	0.40	0.27	0.52	0.56	0.31	1.07	12	0.56	0.31	1.07
GC 1739+52	17	40	36.98	52	11	43.4 *	1.89	1.61	2.17	0.54	0.41	0.67	2	0.54	0.41	0.67
P 1741-038	17	43	58.85	-3	50	4.6	1.03	0.80	1.23	1.10	0.60	1.68	11	1.10	0.60	1.68
1749+701	17	48	32.88	70	5	50.6 *	0.40	0.18	0.72	0.31	0.07	0.90	30	0.31	0.07	0.90
OT 081	17	51	32.81	9	39	0.5 *	0.64	0.58	0.70	1.66	1.58	1.74	2	1.66	1.58	1.74

Fig. 1 (contd)

(1) SOURCE NAME	(2) RIGHT ASCENSION (J2000)		(3) DECLINATION (J2000) DEG MN SEC	(4) NUMBER OF OBS (2.3 GHz)	(5) 2.3 GHz CORRELATED FLUX DENSITY (JY)		(6) CORRELATED FLUX DENSITY (JY)	(7) HIGH (JY)		(8) NUMBER OF OBS (8.4 GHz)	(9) 8.4 GHz CORRELATED FLUX DENSITY (JY)		(10) CORRELATED FLUX DENSITY (JY)		(11) HIGH (JY)
	HR	MN			SEC	AVERAGE		LOW	HIGH		AVERAGE	LOW	HIGH	AVERAGE	
1803+78	18	0	45.67	78	28	3.9	0.53	0.30	0.78	16	0.39	0.23	1.22		
3C 371	18	6	50.71	69	49	28.1	0.45	0.30	0.78	16	0.63	0.23	1.22		
GC 1823+56	18	24	7.07	56	51	1.5 *	0.55	0.64	0.67	2	0.55	0.25	0.34		
GC 1842+68	18	42	33.62	68	9	25.4 *	0.65	0.51	0.77	2	0.30	0.60	1.40		
OV-213	19	11	9.79	-20	6	57.0 *	0.62	0.51	0.77	7	1.04	0.60	1.40		
1909+269	19	11	35.08	26	58	13.7 *	0.22	0.22			< 0.13				
OV-235	19	23	32.21	-21	4	33.5 *	0.89	1.75	2.58	10	0.86	4.49	6.95		
OV-236	19	24	51.26	-29	14	32.8 *	2.17	1.12	1.28	2	5.78	0.81	1.35		
1928+73	19	27	48.48	73	58	1.3	1.20	0.28	0.34	5	1.08	0.46	1.10		
P 1936-15	19	39	26.75	-15	25	45.2 *	0.27	0.42	0.49	2	0.85	0.24			
P 1942-313	19	45	59.36	-31	11	38.0 *	0.12	0.28	0.52	4	0.38	0.31	0.46		
P 1946-23	19	49	24.10	-23	27	9.4	< 0.15	0.46	0.52	4	0.37	0.31	0.46		
P 1946-200	19	49	53.15	-19	57	13.3	< 0.15	0.07	0.07	4	< 0.13	0.64	0.91		
OV-198	20	0	57.08	-17	48	57.7	0.32	0.52	0.66	4	0.74	0.64	0.91		
2007+77	20	5	31.00	77	52	43.1 *	0.45	0.40	0.40	4	0.17	0.35			
P 2008-159	20	11	15.70	-15	46	40.4 *	0.28	0.28	0.52	4	0.38	0.31	0.46		
OW 538	20	23	55.84	54	27	35.9 *	0.49	0.46	0.52	4	0.37	0.31	0.46		
P 2024-217	20	27	4.17	-21	36	25.2	< 0.07	0.35	0.66	4	< 0.13	0.64	0.91		
3C 418	20	38	37.10	51	19	13.6 *	0.52	0.35	0.66	4	0.74	0.64	0.91		
P 2037-253	20	40	8.76	-25	7	46.6 *	0.40	0.40	0.40	4	0.17	0.35			
GC 2047+09	20	49	45.87	10	3	14.4 *	0.43	0.43	0.43	4	0.27	0.35	1.20		
P 2047+039	20	50	6.29	4	7	48.1 *	0.32	0.14	0.14	14	< 0.10	0.35	1.20		
2107-109	21	10	0.97	-10	20	57.6 *	0.40	0.65	0.65	14	0.10	0.35	1.20		
P 2111-25	21	14	40.27	-25	41	50.6 *	< 0.07	0.10	0.10	14	< 0.17	0.35	1.20		
2112+283	21	14	58.30	28	32	57.6	< 0.10	0.14	0.14	14	< 0.17	0.35	1.20		
B2 2113+298	21	15	29.42	29	33	38.4	0.56	0.44	0.70	14	0.66	0.35	1.20		
2116-113	21	19	40.17	-11	6	23.0	< 0.14	0.14	0.14	14	< 0.10	0.35	1.20		
OX 036	21	23	44.49	5	35	22.6 *	0.65	0.65	0.65	14	1.46	0.35	1.20		
2121+299	21	23	44.46	30	12	36.3	< 0.10	0.14	0.14	14	< 0.17	0.35	1.20		
P 2124-12	21	27	30.49	-11	51	20.2	< 0.14	0.14	0.14	14	< 0.10	0.35	1.20		
P 2126-185	21	29	21.41	-18	21	22.8 *	0.28	0.28	0.28	14	< 0.09	0.35	1.20		
P 2128-12	21	31	35.29	-12	7	5.1 *	0.50	0.28	0.28	14	0.77	0.35	1.20		
P 2131-021	21	34	10.41	-1	53	18.9 *	0.86	0.28	0.28	14	0.71	0.35	1.20		
P 2134+004	21	36	38.58	0	41	54.1	1.12	0.38	2.07	15	0.91	0.35	1.53		
P 2140-048	21	42	36.91	-4	37	43.4 *	0.25	0.38	2.07	15	0.19	0.35	1.53		
OX-173	21	46	22.96	-15	25	43.7 *	0.27	0.75	1.56	20	0.29	1.58	2.90		
P 2145+06	21	48	5.95	6	57	30.9 *	1.03	0.75	1.56	20	2.33	1.58	2.90		
P 2145-17	21	48	36.32	-17	23	51.3	< 0.09	0.14	0.14	20	< 0.12	1.58	2.90		
2146-133	21	49	28.41	-13	4	23.2	< 0.14	0.14	0.14	20	< 0.14	1.58	2.90		
P 2149-306	21	51	55.55	-30	27	54.4 *	0.92	0.44	0.63	12	0.37	0.24	0.39		
OX 082	21	51	37.83	5	52	13.5 *	0.52	0.44	0.63	12	0.31	0.24	0.39		
2151-152	21	54	7.11	-15	1	34.3	< 0.08	0.08	0.08	12	< 0.10	0.24	0.39		
P 2151-153	21	54	10.04	-15	4	0.2	0.06	0.06	0.06	12	< 0.10	0.24	0.39		
P 2153-204	21	56	35.20	-20	12	18.7	< 0.08	0.08	0.08	5	< 0.14	0.19	0.81		
OX-192	21	58	5.36	-19	0	54.9 *	0.57	0.36	0.78	5	0.54	0.19	0.81		

Fig. 1 (contd)

(1) SOURCE NAME	(2) RIGHT ASCENSION (J2000)		(3) DECLINATION (J2000)		(4) NUMBER OF OBS (2.3 GHz)	(5) 2.3 GHz CORRELATED FLUX DENSITY			(6) 8.4 GHz CORRELATED FLUX DENSITY			(8) NUMBER OF OBS (8.4 GHz)	(9) 8.4 GHz CORRELATED FLUX DENSITY		
	HR	MN	SEC	DEG		MIN	SEC	AVERAGE (JY)	LOW (JY)	HIGH (JY)	AVERAGE (JY)		LOW (JY)	HIGH (JY)	AVERAGE (JY)
2156-203	21	58	50.12	-20	5	25.7	< 0.08	< 0.08	< 0.08	< 0.14	< 0.14	< 0.14	< 0.14	< 0.14	< 0.14
2156-043	21	59	23.31	-4	9	15.3	< 0.08	< 0.08	< 0.08	< 0.14	< 0.14	< 0.14	< 0.14	< 0.14	< 0.14
P 2157-200	22	0	7.78	-19	45	58.8	< 0.08	< 0.08	< 0.08	< 0.14	< 0.14	< 0.14	< 0.14	< 0.14	< 0.14
2158-167	22	0	54.41	-16	32	33.0	< 0.09	< 0.09	< 0.09	< 0.13	< 0.13	< 0.13	< 0.13	< 0.13	< 0.13
2158-177	22	1	59.20	-17	32	59.4	< 0.09	< 0.09	< 0.09	< 0.13	< 0.13	< 0.13	< 0.13	< 0.13	< 0.13
2159-205	22	2	17.13	-20	17	33.1	< 0.09	< 0.09	< 0.09	< 0.13	< 0.13	< 0.13	< 0.13	< 0.13	< 0.13
VR0 42.22.01	22	2	43.32	42	16	40.0	1.51	0.32	2.58	2.38	0.23	4.24	2.38	0.23	4.24
GC 2201+17	22	3	26.90	17	25	48.1	0.54	0.32	0.32	0.32	0.32	0.32	0.32	0.32	0.32
P 2203-18	22	6	10.39	-18	35	38.7	0.07	0.07	0.07	< 0.09	< 0.09	< 0.09	< 0.09	< 0.09	< 0.09
P 2208-137	22	11	24.13	-13	28	10.4	0.26	0.26	0.26	0.26	0.26	0.26	0.26	0.26	0.26
P 2209+236	22	12	5.94	23	55	41.0	0.37	0.37	0.37	0.67	0.67	0.67	0.67	0.67	0.67
P 2216-03	22	18	52.07	-3	35	37.4	1.33	1.11	1.69	2.08	1.23	2.91	2.08	1.23	2.91
P 2220-163	22	23	41.16	-16	7	5.1	0.15	0.15	0.15	0.23	0.10	0.37	0.23	0.10	0.37
P 2223-114	22	25	43.71	-11	13	40.2	0.25	0.25	0.25	0.25	0.25	0.25	0.25	0.25	0.25
3C 446	22	25	47.23	-4	57	1.0	0.61	0.31	0.84	3.11	1.81	4.22	3.11	1.81	4.22
P 2227-08	22	29	40.01	-8	32	53.4	0.48	0.48	0.48	0.75	0.37	0.38	0.75	0.37	0.38
2229+69	22	30	36.45	69	46	28.2	0.72	0.71	0.73	0.38	0.37	0.38	0.38	0.37	0.38
P 2229-17	22	32	22.56	-16	59	2.1	0.27	0.27	0.27	0.19	0.19	0.19	0.19	0.19	0.19
P 2230-149	22	32	42.45	-14	42	27.8	< 0.07	< 0.07	< 0.07	< 0.07	< 0.07	< 0.07	< 0.07	< 0.07	< 0.07
CTA 102	22	32	36.41	11	43	50.9	1.05	0.19	1.69	1.25	0.89	1.94	1.25	0.89	1.94
P 2233-148	22	36	34.11	-14	33	22.7	0.20	0.15	0.26	0.12	0.38	0.32	0.12	0.38	0.32
GC 2234+28	22	36	22.47	28	28	57.4	0.77	0.67	0.87	0.86	0.38	1.32	0.86	0.38	1.32
OY-172.6	22	46	18.23	-12	6	51.3	0.78	0.28	1.26	1.23	0.88	1.40	1.23	0.88	1.40
P 2245-099	22	48	0.52	-5	41	10.6	< 0.05	< 0.05	< 0.05	< 0.07	< 0.07	< 0.07	< 0.07	< 0.07	< 0.07
P 2245-328	22	48	38.68	-32	35	52.2	0.94	0.75	1.09	0.38	0.28	0.50	0.38	0.28	0.50
GC 2246+20	22	49	0.47	21	7	4.4	0.33	0.33	0.33	0.15	0.15	0.15	0.15	0.15	0.15
3C 454.3	22	53	57.75	16	8	53.4	5.65	0.35	6.96	0.77	0.12	2.47	0.77	0.12	2.47
P 2251+006	22	54	7.21	0	55	11.4	< 0.09	< 0.09	< 0.09	< 0.07	< 0.07	< 0.07	< 0.07	< 0.07	< 0.07
GC 2251+24	22	54	9.34	24	45	23.6	0.24	0.24	0.24	0.14	0.14	0.14	0.14	0.14	0.14
P 2252-089	22	55	4.28	-8	44	4.8	0.38	0.38	0.38	0.29	0.29	0.29	0.29	0.29	0.29
GC 2253+41	22	55	36.72	42	2	52.9	0.56	0.17	0.88	0.48	0.28	0.78	0.48	0.28	0.78
P 2254+024	22	57	17.57	2	43	17.2	0.36	0.36	0.36	0.41	0.41	0.41	0.41	0.41	0.41
GC 2254+07	22	57	17.32	7	43	11.7	0.33	0.33	0.33	0.30	0.30	0.30	0.30	0.30	0.30
P 2255-282	22	58	5.96	-27	58	21.4	0.69	0.69	0.69	0.47	0.47	0.47	0.47	0.47	0.47
P 2303-092	23	6	15.32	-4	59	48.6	0.14	0.14	0.14	0.18	0.18	0.18	0.18	0.18	0.18
P 2312-319	23	14	48.48	-31	38	39.6	0.80	0.80	0.80	0.34	0.34	0.34	0.34	0.34	0.34
P 2314-116	23	17	22.31	-11	22	23.0	0.07	0.07	0.07	< 0.07	< 0.07	< 0.07	< 0.07	< 0.07	< 0.07
GC 2318+04	23	20	44.88	5	13	49.4	0.75	0.75	0.75	1.27	1.27	1.27	1.27	1.27	1.27
P 2318-087	23	21	18.63	-8	27	27.1	0.09	0.09	0.09	0.10	0.10	0.10	0.10	0.10	0.10
P 2320-021	23	23	4.51	-1	50	46.7	0.23	0.23	0.23	0.25	0.25	0.25	0.25	0.25	0.25
P 2320-035	23	23	31.81	-3	17	3.3	0.50	0.35	0.65	0.40	0.26	0.50	0.40	0.26	0.50
P 2325-150	23	27	47.96	-14	47	55.8	0.43	0.43	0.43	0.26	0.26	0.26	0.26	0.26	0.26
P 2332-049	23	34	56.92	-4	39	39.4	0.08	0.08	0.08	< 0.07	< 0.07	< 0.07	< 0.07	< 0.07	< 0.07
P 2332-017	23	35	20.41	-1	31	9.7	0.29	0.29	0.29	0.15	0.15	0.15	0.15	0.15	0.15
P 2335-027	23	37	57.17	-2	30	55.5	0.26	0.26	0.26	0.30	0.30	0.30	0.30	0.30	0.30

Fig. 1 (contd)

(1) SOURCE NAME	(2) RIGHT ASCENSION (J2000)		(3) DECLINATION (J2000)		(4) NUMBER OF OBS (2.3 GHz)	(5) 2.3 GHz CORRELATED FLUX DENSITY (JY)			(6) CORRELATED FLUX DENSITY (JY)			(7) HIGH (JY)	(8) NUMBER OF OBS (8.4 GHz)	(9) 8.4 GHz CORRELATED FLUX DENSITY (JY)			(10) LOW (JY)	(11) HIGH (JY)
	HR	MN	SEC	DEG		MN	SEC	AVERAGE	LOW	HIGH	AVERAGE			LOW	HIGH			
P 2340-036	23	42	56.60	-3	22	25.9 *	0.09	2.18	2.32	3	< 0.05	0.66	1.11					
P 2345-16	23	48	2.61	-16	31	12.0	2.25			3	0.92							
P 2349-01	23	51	56.19	-1	9	14.1 *	< 0.09				< 0.07							
2349+280	23	51	57.66	28	20	30.2	0.34				< 0.15							
P 2351-006	23	54	9.17	-0	19	47.7 *					< 0.11							
07-187	23	54	30.03	-15	13	9.1 *	0.60				0.33							
P 2352-04	23	54	51.72	-4	5	3.5 *	0.09				< 0.05							
DA 611	23	55	9.46	49	50	8.1 *	0.22				< 0.13							
P 2354-11	23	57	29.76	-11	25	16.4 *	1.01	0.98	1.04	2	0.23	0.23	0.23					
P 2355-106	23	58	10.91	-10	20	8.8 *	0.53	0.50	0.55	3	0.45	0.36	0.51					
P 2357+00	23	59	58.57	0	42	18.1	< 0.16				< 0.09							

Fig. 1 (contd)

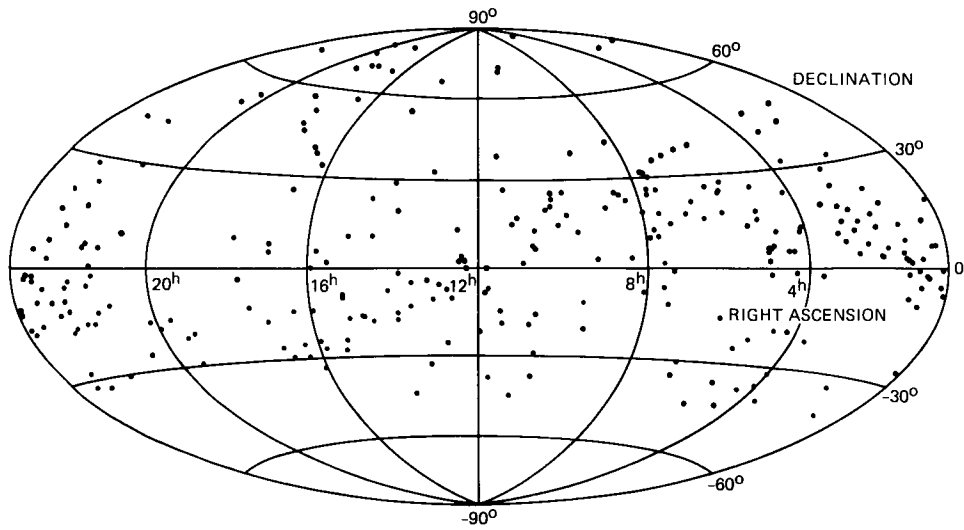


Fig. 2. Sky plot of 278 detected objects at 8.4 GHz

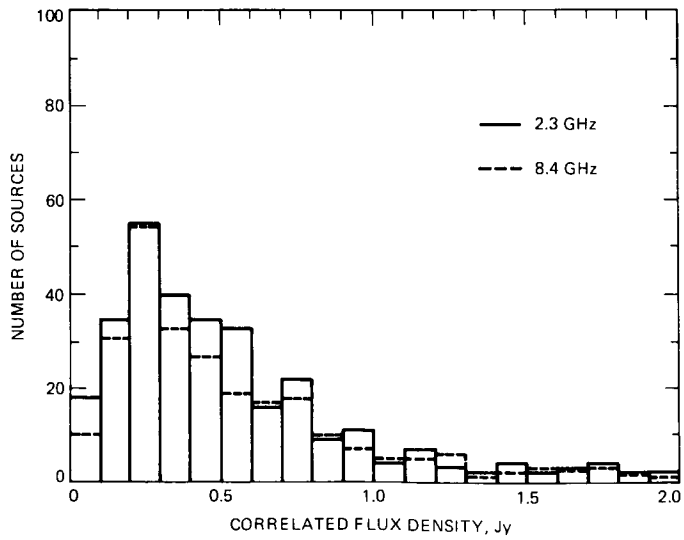


Fig. 3. Correlated flux density histogram for 2.3 GHz and 8.4 GHz observations

C-2

N86-28284

Dg-17
26P

13153

Parkes-CDSCC Telemetry Array: Equipment Design

D. W. Brown
TDA Engineering

H. W. Cooper and J. W. Armstrong
Radio Frequency and Microwave Subsystems Section

S. S. Kent
Telecommunications Systems Section

A unique combination of DSN and non-DSN facilities in Australia provided enhanced data return from the Voyager spacecraft as it encountered the planet Uranus. Many of the key elements are duplicated from Voyager's encounters with Jupiter and Saturn. Some are unique extensions of that technology.

I. Introduction

The Parkes-CDSCC Telemetry Array (PCTA) utilizes the 64-m Australian Parkes Radio Telescope (Fig. 1) to augment the Canberra Deep Space Communication Complex (CDSCC) by some 50% to support the Voyager/Uranus encounter, and, if all goes well, for Neptune. This is based upon a CDSCC complement of one 64-m and two 34-m antennas, as well as a recent reflector surface upgrade at Parkes. This upgrade is part of the X-band preparation recently completed by the Commonwealth Scientific and Industrial Research Organization (CSIRO) and the European Space Agency (ESA) for the support of the Giotto mission. Arrangements have been made to share the common front-end electronics, such that the DSN implementation at Parkes does not impact the focal point equipment area. A dedicated two-way intersite link between Parkes and the CDSCC has been completed by Telecom Australia, under contract with the Australian Department of Science.

Together, these facilities provide the critical elements of a real-time combining system as utilized for past encounters

with Goldstone's DSS-12 and DSS-14. To achieve this capability, a short-loop receiver, operating from a fixed frequency downconverter, is required at Parkes to extract the Voyager baseband signal. In addition, a third-generation baseband combiner is required at the CDSCC to accommodate the longer baseline. To complete the real-time system, a dedicated monitor and control capability offers improvements in operational reliability and convenience as compared to the combining systems in use for recent planetary encounters.

Because the Voyager Project has based its data return strategy upon the Parkes contribution, the real-time system is backed-up with baseband recordings at both sites, such that the tapes can be brought together for playback through the combiner (when and as required) within six hours of the end of pass. This near-real-time capability has been developed as a temporary modification to the Mark III Very Long Baseline Interferometry Data Acquisition Terminals scheduled in the near future for all DSN complexes. This recording capability creates redundancy for the intersite link and portions of the CDSCC electronics equipment.

II. System Description

Figure 2 is a functional block diagram of the system with its interfaces with ESA, CSIRO, Telecom, and the Mark IVA DSN at CDSCC. Mark IVA is the designated configuration of the DSN complexes in the latter half of this decade.

At the Parkes antenna, now in service for over 20 years, CSIRO has just completed a major upgrade in facilities, servo, pointing, and data processing computers and master equatorial. In addition, the reflector surface improvements on the antenna were designed for X-band performance approaching that of DSS-43 at high elevation angles, as is required for Voyager support.

A corrugated wide-illumination-angle focal point feedhorn (Fig. 3) has been designed and fabricated at CSIRO's Division of Radiophysics at Epping, New South Wales. This couples to the JPL-supplied microwave assembly (Fig. 4), a direct copy of the DSN 64-m design. This unit provides simultaneous right-hand circular polarization (RCP) and left-hand circular polarization (LCP) outputs to the following dual traveling wave masers (TWM) in such a manner that by rotating the polarizer, redundant TWM capability is available to the Giotto and Voyager RCP signals, as well as to the Voyager back-up LCP mode. The ESA-provided, U.S.-manufactured TWMs are of JPL Block II design. The international flavor of the front-end equipment is rounded out with the dual downconverter of French origin, all integrated at ESA's European Space Operations Center (ESOC) at Darmstadt, West Germany. The remaining non-JPL-provided equipment is the Telecom supplied video grade link of Japanese manufacture. In addition, a controller interface data link at 4800 baud is provided, along with several voice circuits for overall monitor, control, and coordination of the array.

The remaining dedicated equipment is subdivided as follows and is the subject of this report.

- (1) The Receiver Subsystem is a single channel telemetry demodulator, accepting an approximate 315-MHz signal at the ESA interface and providing baseband outputs for recording and intersite link transport to CDSCC.
- (2) The Recording Subsystem consists of duplicate sets of equipment (at Parkes and at CDSCC) which accept a single channel of baseband telemetry and format it for recording on one or both of two transports. Each transport is fitted with a deformatting channel, such that the Parkes tape and the CDSCC tape can be played back simultaneously for near-real-time processing. The Parkes equipment further provides for radio science

input and downconversion, prior to processing through the baseband channel.

- (3) The Combining Subsystem provides not only the actual combining at CDSCC, but the interconnect, monitor, and control of the entire system. This includes test signal facilities, link calibration devices, array controllers at both sites for configuration control and tape coordination, and a dedicated array operator position at CDSCC. An additional operator is required intermittently at each site for tape changing and back-up modes of operation.

Performance specifications are provided elsewhere.¹ Such detail will be included herein only as pertinent to the equipment descriptions to follow.

A detailed description of the recording equipment is not available at this writing. Hence, the remainder of this article is devoted to the elements of the real-time implementation.

III. The Receiver

A. General Description

The PCTA receiver is a phase tracking receiver that demodulates telemetry data and provides a telemetry baseband signal for data processing. The receiver has been designed to function at a 64-meter site as an array receiver on missions to the outer planets. The receiver operates in the 300-MHz band. It will accept a signal on any DSN X-band channel that has been translated to the 300-MHz band in a downconverter using a fixed frequency local oscillator signal of 8100 MHz.

A block diagram of the receiver is shown in Fig. 5. The basis for the design is the Block III receiver. In fact, surplus Block III modules are used from the 10-MHz intermediate frequency (IF) amplifier through the carrier tracking loop. To interface with the Block III 10-MHz IF amplifier, a dual conversion module has been added (preamplifier/mixer/IF amplifier). This module converts the incoming 300-MHz band signal to a first IF of 70 MHz and then to the second IF of 10 MHz. Since the carrier tracking loop is composed of Block III modules, the loop characteristics of the receiver are identical to those of the Block III receiver. Further detail may be found in Ref. 1.

B. Unique Features

During routine operations, the receiver is under the control of the receiver microprocessor controller. Instructions to estab-

¹PCTA System Requirements and Design, JPL internal document 1200-2, Jet Propulsion Laboratory, Pasadena, Calif., April 15, 1984.

lish the receiver configuration, initialization, and tracking routines are generated in the array controller (Combining Subsystem) and transmitted to the receiver controller for execution. The receiver also has the capability of being controlled from a local terminal, using the same I/O port that is normally used for communicating with the Combining Subsystem controller. The receiver is also capable of being switched to a fully manual mode of operation.

The controller provides both control and monitor capability. Control functions include configuration, acquisition of the carrier signal, and tracking of signal dynamics. Some major performance parameters, such as receiver status and signal level, are monitored. Frequency programming allows the local oscillator to provide phase-continuous tracking over a full pass.

A narrowband receiver output provides capabilities of measuring carrier signal-to-noise ratios using both fast Fourier transform (FFT) and Y-factor techniques in real time. Further descriptions follow in Section III.C.

C. Functional Description

1. Telemetry channel. Telemetry detection is performed at the first IF of 70 MHz. Since the second mixer reference frequency obtained from the Block III design is 60 MHz, the first IF could have been either 50 MHz or 70 MHz to obtain a second IF of 10 MHz. Seventy MHz was selected to provide the capability of wider telemetry-channel bandwidth.

At outer planet distances, the telemetry channel is dominated by noise. This is true over the dynamic range of the input signal level. Consequently, it is not necessary to have carrier signal automatic-gain control. However, to operate the telemetry detector most efficiently, at the maximum allowable detector input signal level, it is necessary to provide total power gain control of the telemetry channel in the predetection 70-MHz IF amplifier. This will compensate for any gain changes in the low-noise amplifier and downconverter and for any noise temperature variations due to antenna orientation.

To minimize the effect of phase offsets in the telemetry detector reference signal, which are created in the receiver loop and caused by tracking signal dynamics resulting from Doppler, a phase-error correcting loop operates around the detector. At outer planet distances with planetary fly-by Doppler dynamics, the phase correcting loop reduces the telemetry detector phase error sufficiently to cause no telemetry baseband data degradation.

2. Narrowband channel. A narrowband channel is included in the receiver to provide the capability of making signal-to-

noise measurements and to aid in acquisition. To support these two functions, two separate output bandwidths are used: 125 Hz for signal-to-noise measurements and 1250 Hz for acquisition aid. In each case the carrier appears at midband when the receiver is in-lock. One synthesizer is used for the final local oscillator signal for both bandwidths. Consequently, these two outputs cannot be used simultaneously.

When using the 125-Hz output, the final mixer, local oscillator signal is set to 10.0000625 MHz. When the receiver is in-lock, the carrier signal is at 62.5 Hz. This output is used to calculate carrier-to-noise, spectral-density power ratios using Y-factor techniques, both in the computer mode and the manual mode.

When using the 1250-Hz output, the final mixer, local oscillator signal is set at 10.000625 MHz. When the receiver is in-lock, the carrier signal is at 625 Hz. During acquisition in the computer mode, the frequency offset of the carrier from 625 Hz is automatically measured using FFT techniques. A correction is then made to the receiver local oscillator to reduce this frequency offset to less than 10 Hz. The receiver will then automatically acquire the carrier signal. In the manual mode, the same technique is used, using an auxiliary spectrum analyzer. In addition, the frequency offset can be observed by monitoring the dynamic phase error as the signal-to-noise ratio (SNR) in the predetection bandwidth is near unity. The receiver local oscillator can then be adjusted manually until the observed frequency offset is less than 10 Hz, at which time the receiver will automatically acquire the carrier signal.

3. Controller. A simplified block diagram of the Receiver Controller is shown in Fig. 6. The Receiver Controller design is implemented using an Intel SBC 86/14A single-board computer (5-MHz 8086/8087 based), an SBX 488 General Purpose Interface Bus (GPIB) interface controller, an SBX 311 A/D (12 bit) analog-to-digital converter, and an SBC 464 PROM board. The Controller is configured around a standard multi-bus (IEEE-796) chassis using $\pm 5V$ and $\pm 12V$ power.

Upon power-up and after a self-test, the Controller software enters the main loop of the program, which monitors input and processes timer queued tasks. The tasks that are queued by an onboard timer are update and correct system status (once every 3 sec), update sweep frequency, and update auto-track frequency (each once every second). The monitoring of user input is always active.

The main features of the Receiver Controller are the automation of carrier acquisition and signal-to-noise calculations. The Receiver Controller performs a 256-point, real-to-imaginary

FFT calculation on the carrier during the automatic acquisition and during SNR calculations. For additional SNR accuracy, the Y-factor measurement technique is used. The carrier signal level is then calculated from the measured SNR, assuming a 20-Kelvin (or operator updated value) system-noise temperature.

During carrier acquisition, the Controller calculates the expected X-band frequency from the text predict values. These values are entered by the operator during the tracking procedure or prior to tracking. Using these predict values, the Controller calculates and sets the synthesizer frequency based on algorithms similar to those used in the manual mode. The receiver loop is then disabled and 256 samples of the wideband output of the receiver are taken. The predict values will set synthesizer frequency within ± 625 Hz of the desired in-lock value, so that the carrier appears in the receiver 1250-Hz output. With 256 samples of the receiver wideband output, the result is an FFT calculation with a 10-Hz bandwidth resolution. An amplitude spectrum is then generated and the assumption is made that the strongest signal in the spectrum is the carrier. The carrier-frequency offset from 625 Hz is calculated, the synthesizer frequency is then corrected for the offset, and the receiver loop enabled. The receiver then acquires the carrier signal and the controller polls the receiver up to 10 seconds for an in-lock indication.

During operation, when the receiver is in the Controller mode, the Controller monitors the status of the receiver. If any error occurs, the Controller will inform the operator via an error message to the terminal. In some instances, the Controller will correct the error and then inform the operator of its occurrence. To aid in the operation of the receiver, a "HELP" menu is available to the operator upon request (Fig. 7).

Spectral displays are available for both the 125-Hz and the 1250-Hz receiver outputs using the same FFT algorithm used in the acquisition procedure. In addition, signal-to-noise, spectral-density calculations are also made using the FFT algorithms.

In addition to the FFT algorithm, a more precise signal-to-noise, spectral-density calculation is available at the receiver 125-Hz output using a Y-factor algorithm. The output is sampled (with the carrier in the spectrum) 256×10 times at 4 msec intervals. Using the synthesizer to move the carrier out of the receiver narrowband output spectrum, the output (without carrier in the spectrum) is sampled 256×30 times at 4 msec intervals. Using the same type of Y-factor algorithm that is used in the manual mode, the carrier signal-to-noise spectral density is then calculated and displayed.

IV. The Combiner

A. General Description

The function of the Long Baseline Combiner (LBC) is to accept baseband signals from Parkes and CDSCC, to align them properly in time, weight the signals appropriately according to their respective SNRs, and then to sum and output the results. The block diagram in Fig. 8 shows how this is accomplished.

The LBC is similar to the Baseband Assembly (BBA) Real-Time Combiner. The latter consists of two 4-channel combiners, which are cascaded to produce an eight-channel combiner. Since the LBC requires only two channels, and must compensate for larger static and dynamic delays, the internal configuration is different. Due to the similarity of the devices, some of the BBA modules are used in the LBC. These include the analog-to-digital converters (ADC), the clock phase shift (CPS) board, the multiplier-adder board (MAB), the correlator board (CB), and the digital-to-analog converter (DAC). The digital delay board (DDB) is similar to the one in the BBA, but is designed to provide four times the static and dynamic delay capability for a given clock rate.

Requirements for the LBC consist of being able to compensate for 2.4 msec of round-trip transport delay between Parkes and CDSCC (2.4 for testing, only 1.2 for operating), a dynamic delay in excess of ± 200 μ sec, and a delay rate of 40 nsec/sec. Meeting these requirements, and still maintaining a SNR loss of less than 0.1 dB, required a higher loop-update rate than that used in the BBA. The higher rate was achieved by using a higher speed Intel 86/14 single-board computer utilizing the 8086 microprocessor, with 8087 coprocessor, rather than the Intel 80/204 single-board computer utilizing the 8080 microprocessor, which is used in the BBA.

The signals from Parkes and CDSCC are first low-pass filtered at 4 MHz before being applied to the ADC. This choice of bandwidth is bounded by the need to pass the harmonics of the 360-kHz subcarrier signal and by noise-squaring effects in the correlator (see Section IV.B. below).² The 8-bit digitized signals are passed through the DDBs and then to the MAB. The MAB multiplies each signal by a weighting factor based on its SNR, and then adds the signals. The summed signal is then converted back to analog form by the DAC. All modules are under control of the 8086 microprocessor.

²This limitation is also related to dynamic range characteristics of the ADC. Had the noise-squaring and attendant signal-suppression effects been more severe, additional (digital) filtering might have been employed in the correlator path.

The feedback loop, which maintains the time alignment of the signals, consists of the DDBs, the CB, a loop filter equation implemented by the microprocessor, the CPS board, and the ADC. Loop design is described in the next section.

B. Combiner Loop Design

1. **A delay tracking loop.** Having established the memory capacity to satisfy the static delay requirements for the Parkes-CDS-CC application (Section IV.A.), the next step was to model the BBA combiner loop hardware. Figure 9a is a hybrid s/z -transform block diagram, developed with the aid of Ref. 2 and personal communication with the author. A significant change from the Mariner-Venus-Mercury (MVM) design [Ref. 2] is that the dynamic delay device and clock provide a delay hold in the interval between loop updates, rather than a frequency (or phase ramp) hold as with a voltage-controlled oscillator. As a direct consequence, the alignment error, τ_e , is a replica of the change in input over the interval T . The sinusoidal geometric delay, $\tau_{IN}(t)$, has a maximum rate of change for the Parkes-CDS-CC baseline of 40 nsec/sec. As will be noted later, alignment errors of approximately 10 nsec were budgeted for the 360-kHz square-wave subcarrier application. These factors dictated that the loop update interval and/or the aiding interval, T_{aid} , must be less than one second, the value used for telemetry combiners to date. As will be discussed in Section IV.C., the delay aiding is provided to minimize the tracking requirements upon the loop. A convenient value was found to be $T_{aid} = 0.025$ sec resulting in a negligible, one nanosecond peak-to-peak sawtooth of ramp error, superimposed upon the loop. Thus, the aiding will not be explicitly treated below, except as it mitigates the dynamics of the input.

Another factor, computation time, was considered negligible for engineering purposes, estimated at 10-to-20 msec, given a loop update interval of $T = 0.20$ sec (see Section IV.B.2.) and the insensitivity of performance characteristics established in Ref. 3.

Referring now to Fig. 9b, the open-loop transfer function may be written as

$$G_{OL}(z) = K_c F(z) \frac{z-1}{Tz} \left[\frac{z-1}{zs} \frac{1}{s} \right]^*$$

where $z = e^{Ts}$ and $[\]^*$ denotes the z -transform of the bracketed expression.

This yields

$$G_{OL}(z) = K_c \frac{F(z)}{z}$$

where K_c is the (dimensionless) correlator gain and all other gains are lumped in $F(z)$. This simple expression illustrates that the loop type (I or II) will be exactly that of the $F(z)$ employed and that the dominant effect of the remainder of the loop is a transport lag of T sec. It is the latter that gives rise to the gain margin limitation as derived in Appendix A.

A strawman loop filter was postulated (Appendix A) with three generalized parameters A , B , and C as

$$F(z) = \frac{A z^2 + C(z-1)z}{(z-1)(z-B)}$$

resulting in

$$G_{OL}(z) = K \frac{z + \frac{C}{A}(z-1)}{(z-1)(z-B)} \quad (1)$$

where $K = AK_c$. The closed-loop portion of Fig. 9b has the transfer function:

$$G_{CL}(z) \triangleq \frac{\tau_{OUT}(z)}{\left[\frac{\tau_{IN}(s)}{s} \right]^*}$$

$$G_{CL}(z) = \frac{K_c F(z) \frac{z-1}{Tz} \left[\frac{z-1}{zs} \right]^*}{1 + G_{OL}(z)}$$

$$G_{CL}(z) = \frac{K}{T} \frac{(z-1)z + \frac{C}{A}(z-1)^2}{(z-1)[(z-1) + 1 - B] + Kz + \frac{C}{A}K(z-1)} \quad (2)$$

Appendix A derives expressions for gain margin, damping, and loop bandwidth as presented in Fig. 10. Note that $G_{CL}(z)$ is not the transfer function relating τ_{OUT} to τ_{IN} .

General solutions for steady-state errors are obtained through

$$\begin{aligned} \tau_e(z) &= \tau_{IN}(z) - \tau_{OUT}(z) \\ &= [\tau_{IN}(s)]^* - \left[\frac{\tau_{IN}(s)}{s} \right]^* G_{CL}(z) \end{aligned}$$

and application of the final value theorem. Appendix A derives for all values of filter parameters A , B , and C

$$\left. \begin{aligned} \frac{\tau_{\epsilon}(ss)}{\Delta\tau} &= 0 && \text{(Delay step)} \\ \frac{\tau_{\epsilon}(ss)}{\dot{\tau}} &= \frac{T}{K}(1-B) - \frac{T}{2} && \text{(Delay ramp)} \\ \frac{\tau_{\epsilon}(ss)}{\ddot{\tau}} &= \frac{T^2}{K} - \frac{T^2}{K^2}(1-B) - \frac{T^2}{6} && \text{(Delay accel.)} \end{aligned} \right\} \quad (3)$$

Due to the sinusoidal nature of the delay input to the loop, each order of error maximizes when the adjacent order is zero; hence, the expression for delay acceleration does not include the unbounded, integrated ramp error for the type I loop where $B < 1$ (see Appendix A.4). Note that the final term in each case is independent of loop type and gain, K ; it represents the value at the update instant and is a consequence of the replica "ripple" discussed above.

2. Choice of loop type. Equation (1) most easily illustrates how the choice of design values for parameters A , B , and C in the filter can yield loops of type I (single integrator) and II (double integrator) with a variety of operational characteristics as illustrated in Eq. (3) and Fig. 10. Over the ranges plotted in this Figure, the straight line asymptotes are valid for engineering purposes. For example, in the (worst-case) region labelled MVM, Eq. (A-4) deviates from the asymptote by 5%.

An initial estimate of the desired loop bandwidth, $2B_L = 0.1$ Hz, was considered as a compromise between expected jitter losses and transient response at acquisition. Figure 10 and Eq. (3) reveal that the average ramp error for a type I loop ($B = 0$) at this bandwidth and at $T = 1$ sec is *five times* the input rate. For example, a two nsec/sec aiding residual (5% of 40 nsec/sec) would yield a 10-nsec steady-state error. This value is on the threshold of acceptable loss for a 360-kHz square wave. While 5% is a rather loose requirement on the ephemeris aiding, a more robust loop was sought to allow for unmodelled errors.

Type II design requires B to be identically one with the C/A ratio establishing the appropriate damping. With the average steady-state ramp error now zero, Fig. 10 points up the need to reduce T in order to obtain adequate gain margin for variations in operating point versus input SNR (adaptive gain and bandwidth) and to allow for unmodelled effects such as computation time discussed above. As noted earlier, a value of $T = 0.20$ sec was chosen, yielding the upper curve for $B = 1$ (Fig. 10).

The unaided delay acceleration steady-state error, Eq. (3), is negligible (< 3 nsec) on the Parkes-CDSCC baseline (0.003 nsec/sec²) for bandwidths greater than about 0.03 Hz, and thus no problem for this design.³

Lacking an explicit loss model for loop jitter, several test bandwidths in the range $0.04 \leq 2B_L \leq 0.50$ were evaluated under design point conditions for degradation of telemetry SNR. Incremental loss for the widest value was within the resolution of the test set-up, 0.1 dB. Hence, a nominal design point bandwidth of $2B_{L_o} = 0.25$ Hz at a damping of $\zeta = 1.0$ was established as the baseline design for further test and analysis. Figure 11 illustrates this design point and the adaptive range of operability.

The independent variable $SNR_1 SNR_2$ characterizes the correlator input. The input filters were selected as $B_N = 4$ MHz as a compromise between jitter performance, Appendix A.5, and data spectrum fidelity for the harmonics of 360 kHz. Upstream bandwidths, including that of the microwave link, were specified as 5 to 6 MHz minimum, except the recording equipment which was specified at 3 MHz.

The clear, dry weather SNRs for Voyager/Uranus encounter were nominally +45 and +48 dB-Hz for Parkes and CDSCC respectively, yielding

$$SNR_1 SNR_2 = +45 + 48 - 20 \log 4 \times 10^6 = -39 \text{ dB}^2$$

rounded off to the combiner loop design point value of -40 dB^2 as identified in Fig. 11. The parameter K_{SNR} , also discussed in Appendix A.5, is analogous to the signal suppression factor, α , in continuous loop design, with the significant difference of twice the logarithmic slope due to the squaring effect of two noisy signals in the correlator.

Figure 11 illustrates the adaptive region of operation for design point values of A , B , and C

$$A = 0.0125$$

$$B = 1.00$$

$$C = 0.625$$

$$K_c = 20 K_{SNR}$$

³For the Goldstone and Very Long Array (VLA) baselines, bandwidths are ~ 0.01 Hz and ~ 0.1 Hz, respectively.

The upper value of $2B_L = 0.45$ Hz could conceivably be approached as follows

Nominal SNR_1, SNR_2	-39 (as above)
If Parkes equals DSS-43	+1
Recording bandwidth Δ	+2.5 (1.25 dB each)
Voyager signal uncertainty	+1 (0.5 dB each)
	-34.5 dB ²

Similarly, values of $2B_L$ as low as 0.15 Hz could be obtained near the horizon with rain at one or both sites. Values as low as 0.10 Hz ($\zeta = 0.5$) could be approached only upon degradation of the Voyager signal, but these illustrate loop characteristics in the extreme. The gain margin notation on Fig. 11 illustrates why it is necessary to reduce K by a factor of 10 or more during strong signal testing ($K_{SNR} \rightarrow 1$).

Before turning to a summary of performance for the Parkes-CDSCC long baseline combiner loop, consider the intermediate design (between types I and II) as illustrated in Fig. 10 (dashed lines). This approach sets $C = 0$ and $0 < B < 1$ to satisfy stability criteria, yielding the digital equivalent of an analog "imperfect" second-order loop whose gain is so low as to not require lead compensation. Because selection of B is doubly constrained (ramp error and damping), this configuration is more difficult to optimize than the type II loop.

3. Second-order loop performance. Two significant characteristics remain to be considered for the nominal loop design illustrated in Figs. 10 and 11. First, as a by-product of the steady-state error analysis in Appendix A, the transient responses to a delay step and a delay ramp were obtained by computing the power series in z^{-n} for each pulse response function, $\tau_e(z)$, where the coefficients represent the magnitudes of the time response inverted from the z -domain [Ref. 4, p. 60].

The results are presented in Figs. 12 and 13 and indicate that for loop gain changes of $\pm 2:1$ ($\Delta SNR_1, SNR_2$ of ± 6 dB) the loop is well behaved and essentially stabilized at 30 sec. Figure 12 points up the importance of initializing the loop with the best available delay estimate. For example, the $\zeta = 0.7$ response would yield stabilization to 10 nsec in something less than 40 sec for an offset of one μ sec and 5 sec for a 0.05 μ sec offset. The magnified portion of Fig. 13 illustrates the "ripple" effect and the vanishing average error predicted by Eq. (3) for a delay ramp input.

The remaining performance consideration is loop jitter as a function of K_{SNR} and $2B_L$. From Ref. 3 and Appendix A

$$\sigma_T^2 = \frac{2B_L}{256 B_N f_{sc}^2 K_{SNR}^2}$$

and with $B_N = 4$ MHz and $f_{sc} = 360$ kHz

$$\sigma_T = \frac{\sqrt{2B_L}}{11.52 K_{SNR}} \text{ nsec} \quad (4)$$

yielding

	-6 dB SNR_1, SNR_2	Design Point	+6 dB SNR_1, SNR_2
$2B_L$, Hz	0.15	0.25	0.45
K_{SNR}	0.0032	0.0064	0.0128
σ_T , nsec	10.5	6.8	4.5

which are consistent with design goals and test results.

The design thus results in steady-state losses limited to the effects of σ_T and input sampling/filtering losses, which should readily meet the design objective of less than 0.2 dB. The transient responses are seen to be tolerable for rather modest accuracies in initialization and ephemeris aiding and to readily meet the 10-sec design goal under expected conditions.

C. Combiner Firmware

The firmware in the LBC controls the high-speed signal processing boards and also does some of the low-speed signal processing (e.g., some of the tracking loop is in the software). This section describes the choice of computer and compiler and some of the features of the control program that relate to the time alignment of the two input baseband signals and the weighting of those signals to produce the combined output.

Because of the relatively long Parkes-CDSCC baseline, the PCTA geometrical delay can change by as much as 40 nsec/sec. Following the BBA Real-Time Combiner design, it was planned to correct for the known (geometric) delay variations via ephemeris-aiding. This would reduce the dynamics of the signals at the input to the tracking loop and minimize the loop's performance requirements. To assure that the ephemeris-aiding was done sufficiently smoothly so that the dynamics would, in fact, be accurately removed, the LBC firmware had to correct for the geometric delay fairly often, about 10 to 100 times/sec. This put some constraints on the microcomputer speed and on the compiler used. For compatibility with other PCTA controllers, it was also desired that the LBC firmware be written in Pascal MT+86 on an 8086 host computer. (This

presented a conflict since it was also desired to maximize use of BBA code, which was written in FORTRAN. This was resolved by simply translating the relevant procedures into Pascal, guided by an analysis of the combiner signal processing done in the BBA).⁴

Early timing tests showed that the calculations and input/output required for the loop and ephemeris-aiding could not be done from MT+86 alone. An 8087 numerical coprocessor was added to speed up floating-point operations and input/output code segments were rewritten in assembly language to get around these problems. After some experimentation, it was determined that ephemeris-update rates of 100/sec were feasible with this compiler-computer combination, if the machine was not being interrupted with other tasks. The actual rate was then reduced to 40/sec, which was satisfactory for smoothly tracking out the known geometrical delay variations. Since the rate of change of the geometrical delay is sensibly constant over 10 sec, the actual update rate was not recomputed every 0.025 sec, but rather once every 10 sec from the known station and spacecraft positions and the time.

Once it was determined that the 8086/8087/MT+86 combination could support the loop and ephemeris speed requirements, the general structure of the program was patterned after the other PCTA controllers. In the case of the LBC, the program has three interrupt-driven tasks: 1 pps for time, 40 pps for ephemeris aiding (and loop timing), and an asynchronous interrupt for communications input from the PCTA controller. Tasks that were not time critical were then scheduled. The general control flow is an infinite loop which waits for commands from the PCTA control computer. Valid commands then cause procedure calls which execute the commands in *background* to the interrupt procedures.

A useful feature of the LBC firmware is that it allows the combiner to time-share the correlator board between loop operations (i.e., delay tracking) and operations useful for verifying proper symbol alignment, correct combining weights, and ADC adjustments. In the usual situation, the correlator is being used to produce an error signal proportional to the time alignment error of the CDS and Parkes signals. This signal is then processed by the loop filter (in firmware) to produce a correction which is applied to the delay boards. This error signal allows the LBC to properly align the signals with respect to the subcarrier; it does not guarantee that the data symbols are correctly aligned. For example, at acquisition, the Parkes data stream might be advanced by one subcarrier period with respect to the CDS data due, say, to a slightly incorrect station location entry. The LBC would appear to lock correctly, but

the symbols would be misaligned by one subcarrier period and the resulting combined signal would be suboptimum.

The LBC firmware allows a check for this condition. The command "CMAP" suspends loop operations, but maintains the relative alignment of the time series with ephemeris-aiding. During about the next 20 sec (actual integration time is under operator control), the correlator board is reprogrammed to map out the cross-correlation function of the two inputs as a function of relative time lag out to about $\pm 7 \mu\text{sec}$. The resulting cross-correlation function CMAP is then plotted on the operator's console, the loop tracking is enabled, and the observed cross-correlation is compared with the expected cross-correlation function under various hypotheses regarding the symbol alignment. These hypotheses are "alignment correct," "one input inverted," "signals misaligned by one subcarrier period," "one signal inverted and signals misaligned by one subcarrier period," "signals misaligned by two subcarrier periods," etc. The choice which best describes the observed cross-correlation function is then printed on the operator's console along with a recommendation for the sequence of commands required to bring the inputs into proper alignment. Figure 14 shows the plot of the temporal correlation function produced by CMAP. Prominent features are the triangle-wave auto-correlation of the square-wave subcarrier, and the decrease in the overall level of correlation at large time lags due to symbol misalignment.

Another feature of the LBC is that it allows independent measurement of the SNRs of its two inputs using the correlator board. Once every 20 sec, the LBC firmware temporarily suspends loop operations and tracks on the ephemeris alone. The correlator board is then reprogrammed to look at the correlation function with an offset of 1.5 subcarrier periods. The difference between the correlation readings at 1 and 1.5 subcarrier periods is proportional to the SNR for that input. This measurement has the advantage that it is independent of some sources of systematic error (notably, DC offset of the ADCs). Of course, this is a measurement of the SNR in whatever the input bandwidth of the data is (e.g., for typical PCTA operating conditions these SNR estimates are on the order of 1%). The LBC firmware allows the operator to specify the differences, if any, in the input bandwidths of the two signals. Using these measured input SNRs (smoothed over any time scale greater than 20 sec and corrected for input bandwidth differences), the LBC can then calculate the optimum weighting factor for the two signals independently of any external instrumentation.

The operator has the option of using the LBC-estimated weighting factor or a weighting factor derived from manually input *a priori* SNRs for the actual combining weights. However, in any case, the LBC-estimated weighting factor is

⁴L. D. Howard, unpublished notes on BBA Real-Time Combiner, 1983.

included in various operator displays and can serve as a check that the relative SNRs of the inputs are near nominal. (Additionally, the LBC is continuously measuring the correlated power – the value of the cross-correlation function at the alignment point. If enabled, an alarm is sounded should this value drop by more than 2 dB. This is a test for catastrophes such as a loss of input, a large reduction in one or both of the input signal's SNRs, a failure of one of the LBC signal processing boards, etc.)

To use the correlator board for the two tasks discussed above, the delay tracking loop must be temporarily suspended. Relative alignment of the signals is maintained via ephemeris-only tracking during these suspensions. The symbol alignment test (CMAP) suspends closed-loop tracking for about 20 sec and is typically called once or twice per pass just after initial acquisition. The SNR-estimating routine is scheduled once every 20 sec and suspends the tracking loop for about 3 sec. Additionally, once every 50 sec the tracking loop is suspended for about 2 sec while the DC offsets in the ADC are measured and the appropriate adjustments are made.

Finally, the LBC firmware allows the operator to call up graphs of the recent correlator error signal versus time (i.e., the input to the tracking loop filter) and the recent delay board corrections versus time (i.e., the output of the tracking loop). These plots proved useful in the design and debugging of the loop filter and in choosing appropriate loop parameters. These plots are also useful in observing the transient response of the loop during acquisition and in determining the extent of (short time-scale) stress on the loop during operations. Included with the plots is also the cumulative closed-loop delay. In the ideal situation, this number is less than one-half of a subcarrier period (i.e., the worst-case delay that had to be added to the ephemeris delay to align the subcarriers). In practice, this is larger due to various inaccurately modeled delays (for example, due to small errors in effective station or spacecraft locations). This number is useful in determining the slowly varying, systematic delay changes that the loop has to track out.

V. Instrumentation and Control

A. General Description

In the PCTA system, the primary signal-processing elements are the telemetry receiver and the LBC. Once the system is operating, these devices essentially do all of the work.

In order to make these devices easier to use, they are surrounded by monitoring, controlling, and testing equipment. This equipment was designed so as to make the PCTA real-time equipment independent as far as pre-pass system

testing and operational monitor and control are concerned, thereby not requiring the use of external resources.

(See Ref. 5 for a more detailed overview. Following is a description of each element and the function it performs.)

B. Array Controller

Overall monitor and control of the PCTA equipment is achieved by using a CPM-86 based multibus microcomputer at each site (Fig. 15). Each device, such as the receiver, combiner, test signal generator, etc., is connected and controlled by the monitor and control computer, or the Array Controller (AC) via an RS-232 interface.

Monitor and control functions reside in all assemblies. Each assembly contains software which makes it stand alone as far as operation is concerned. All assemblies are controlled using the same form of command. They all have self-test capability, command parameter checking, status displays of various parameters as appropriate, and "HELP" menus (Fig. 7).

Residing in the AC is the software which gives it its power. The software has been designed to provide as much power as possible, a user friendly interface, and also a few unique features described below.

The AC at each site is connected to the other via a 4800-baud modem. Using this data link, an operator at Parkes or CDSCC can control all the PCTA real-time equipment from one location. This feature is especially useful when an operator at one site desires the status of assemblies at the other site.

Since the AC is actually a CPM-86-based microcomputer, the operator may generate configuration or command files similar to the familiar submit files used in CPM systems. These configuration files are generated using a standard editor prior to the pass, which the software will execute on command. This capability allows pre-canning of error-prone commands, such as spacecraft and station location used by the LBC, receiver tuning predicts, and switch positions (thereby greatly reducing operator type ins and errors). Standard self-test configuration files are used for system pre-pass testing. An example of a configuration file is shown in Fig. 16. The configuration file capability also includes programmable pauses and looping, which allows operator prompting and periodic automatic status logging.

C. Test Signal Generator

The test signal generator (TSG) (Fig. 17), provides four test signals. One of these is an RF signal which is used by the telemetry receiver. Two are baseband signals used by the Recording Subsystem and also by the combiner. The other

signal is a calibration signal used to assist in the measurement of the transport delay between Parkes and CDSCC. The TSG located at Parkes is the same as at CDSCC; however, not all of the signals are used at a given location.

The TSG uses a 316.8-MHz oscillator which provides the carrier test signal for the receiver. The oscillator drives a phase modulator which, when modulated by a baseband signal, produces a carrier (C) × subcarrier (SC) × data (D) signal. The TSG also contains a RF-noise generator. Summers and front panel attenuators are provided so as to be able to adjust the signal to simulate actual predicted signal levels both in total power and SNR.

The two baseband signal generators each generate a SC × D + noise signal. The subcarrier is generated by dividing down the 316.8-MHz oscillator signal. The data signal is generated in a like manner. The noise generators consist of a 27- or 28-stage digital pseudo-random sequence (PN) generator. The PN generator's long sequence length and high clock rate (16 MHz) produce a noise signal sufficiently flat and free of spectral lines. The two baseband signal generators are identical except that the noise generators are of different length, thereby producing independent noise. Data modulation is selectable between alternating ones and zeros, a PN sequence (length 2048, the same as used in the DSN Test Support Assembly), or none. Like the RF generator, the total power level, as well as the SNR of each baseband generator, is adjustable from the front panel.

The clock to each baseband signal generator comes from a clock deletion circuit. When a clock pulse is deleted, the time difference between the SC × D signals from the two generators is changed. Using this deletion scheme, the TSG can simulate fixed as well as dynamic signal delays. Under control of the built-in microprocessor, the TSG can simulate static and dynamic signals from which the algorithms of the long baseline combiner can be verified. One of the SC × D signals (without the noise) is used to modulate the RF modulator described above.

The TSG also generates a 250-Hz pulse signal, synchronized with the station 1 pps which can be used to measure the microwave link polarity, and transport delay.

Subcarrier rates, data rates, static delay, dynamic delay, etc. are all user controllable via an RS-232 interface from the AC.

D. Subcarrier SNR Estimator

Keeping in line with the philosophy of a stand-alone system, a method of determining the presence and level of a signal in the baseband bandwidth is needed. The Subcarrier SNR Estimator (SSE) (Fig. 18) performs two functions: to determine

the frequency of the modulated subcarrier, if present; and to measure the subcarrier-to-noise density ratio.

The SSE operates on a modulated subcarrier with a frequency of 360 kHz and symbol rates up to 60 Ksps. Since it is expected that a randomly modulated subcarrier at the noise level cannot be seen on a standard spectrum analyzer due to the spreading of the subcarrier power, the SSE is necessary.

The input signal is first bandpass filtered at 360 ± 30 kHz and gain controlled using a microprocessor-controlled digital attenuator and amplifier. The signal is then input to a squaring circuit consisting of a four-quadrant multiplier which removes the data modulation, and doubles the subcarrier frequency to 720 kHz. The doubled subcarrier frequency is then downconverted to 62 Hz using another four-quadrant multiplier and a microprocessor-controlled frequency synthesizer. The downconverted signal is then passed through a 125-Hz low-pass filter, digitized at 250 sps, and the samples are sent to the microprocessor for processing.

The SSE performs two functions on the digital samples. The first is an FFT on the samples. The FFT is displayed on the cathode ray tube (CRT), thereby showing the spectrum about the subcarrier. The display shows the presence of the signal, the approximate SNR, and the subcarrier frequency offset from 360 kHz. This computation will determine the subcarrier frequency to better than 0.5 Hz, and the absolute SNR to about 2 dB if the SSE is set to the exact subcarrier frequency.

If the signal is approximately centered in the display, the second function, a Y-factor SNR measurement, can be made. The familiar Y-factor method computes SNR by knowing that $S/N = (S + N)/N - 1$. The $S + N$ measurement is made by squaring an ensemble of samples, computing their average, and taking the square root of that average. The N measurement is performed in a like manner, with the exception that the frequency synthesizer is changed so that the signal does not appear in the passband of the low-pass filter. For greater accuracy, the user can control how many averages are taken. The accuracy of this measurement is about 0.5 dB with a subcarrier SNR of 48 dB-Hz.

The SSE is primarily used to verify that proper signals are present at the LBC inputs prior to attempting combining, and to verify combining gain independently of the LBC itself.

E. Switching Assembly

Signal routing between various components of the PCTA system is performed by the switching assembly. The switching assembly contains coax relays, a power splitter, and ampli-

fiers required to maintain the proper signal flow, impedance, and signal levels throughout the system. The coax relays may be controlled manually from front panel switches, but are normally automatically controlled by the AC. Engraved on

the switching assembly front panel is a PCTA-system block diagram. The manual control switches and light-emitting diodes (LEDs) are positioned to provide a convenient indication of the signal flow.

References

1. Operations and Maintenance, PCTA Receiver, JPL Technical Manual 03110, Jet Propulsion Laboratory, Pasadena, Calif., July 1, 1984.
2. Winkelstein, R. A., "Analysis of the Signal Combiner for Multiple Antenna Arraying," *DSN Progress Report 42-26*, Jet Propulsion Laboratory, Pasadena, Calif., pp. 102-118, April 15, 1975.
3. Simon, M. K., and Mileant, A., "Performance Analysis of the DSN Baseband Assembly (BBA) Real-Time Combiner (RTC)," JPL Publication 84-94, Jet Propulsion Laboratory, Pasadena, Calif., May 1, 1985.
4. Ragazzi, J. R., and Franklin, G. F., *Sampled-Data Control Systems*, McGraw-Hill, New York, 1958.
5. Parkes-CDSCC Telemetry Array, Users' Guide, JPL Technical Manual 513957, Jet Propulsion Laboratory, Pasadena, Calif.

ORIGINAL PAGE IS
OF POOR QUALITY



Fig. 1. Parkes Radio Telescope

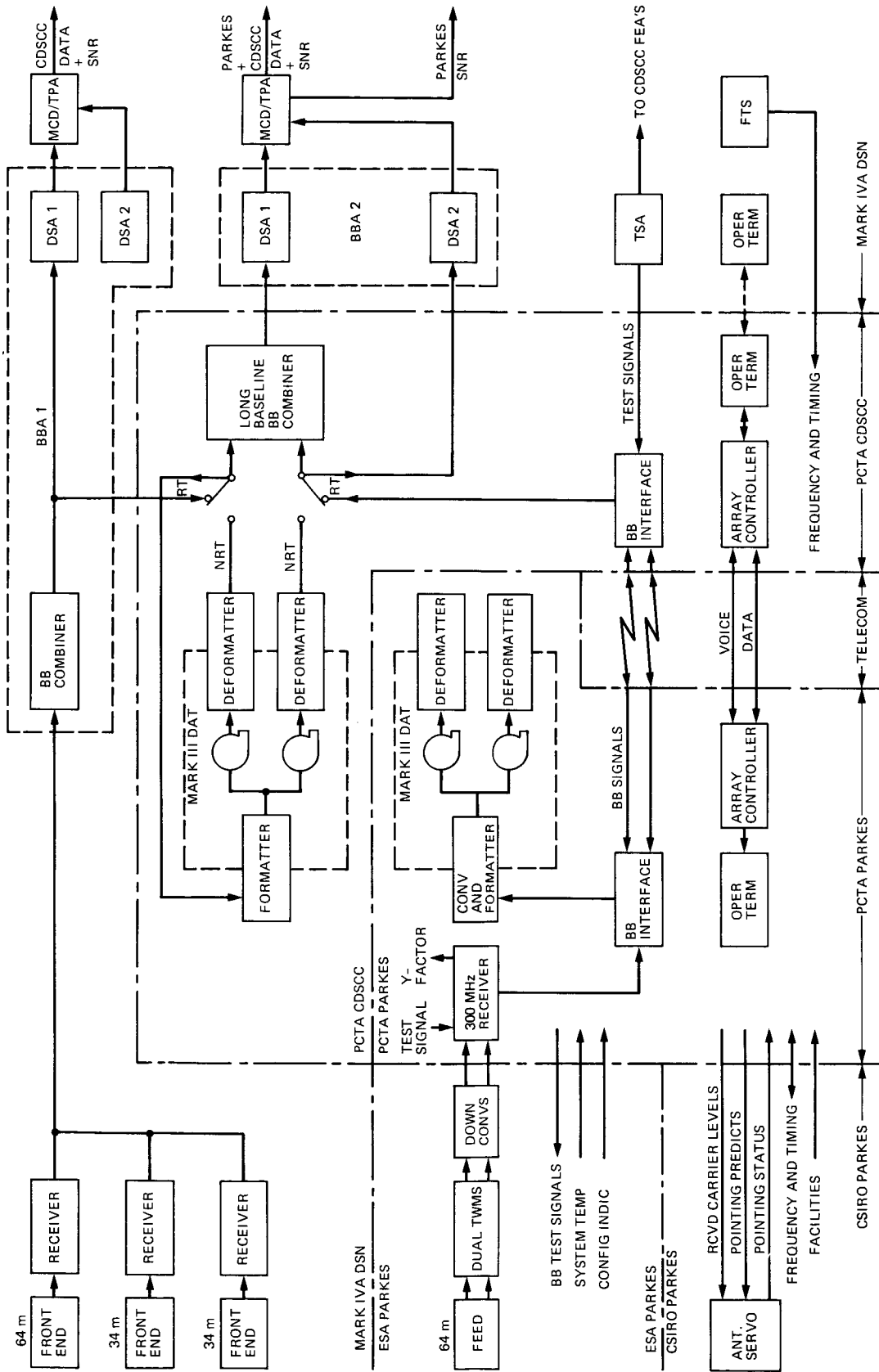


Fig. 2. Parkes-CDSCC Telemetry Array, functional block diagram

ORIGINAL PAGE IS
OF POOR QUALITY



Fig. 3. Parkes X-band feedhorn

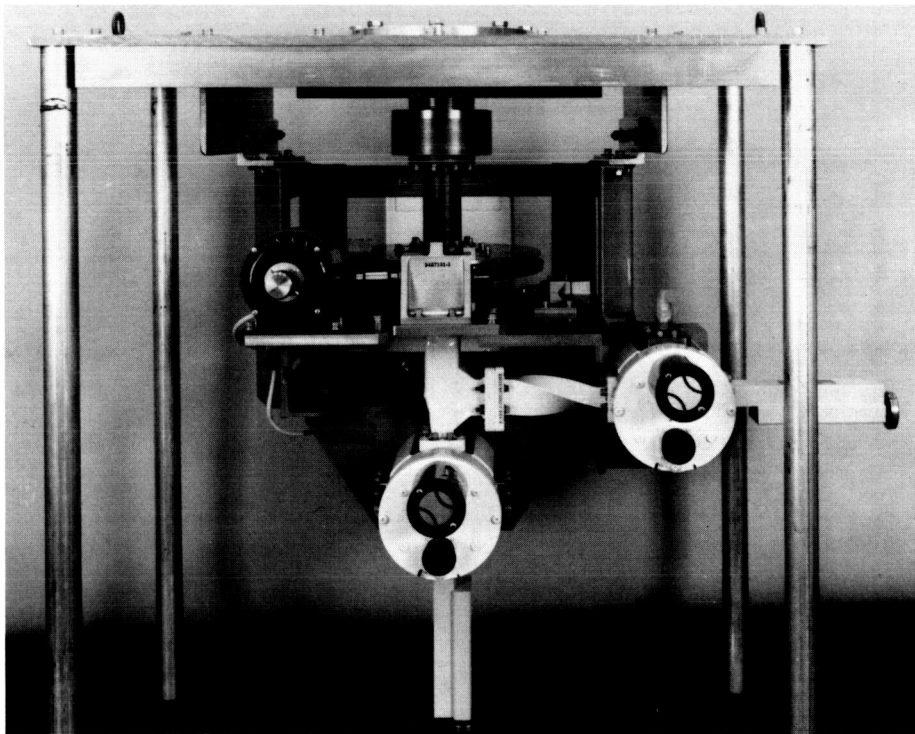


Fig. 4. X-band microwave assembly

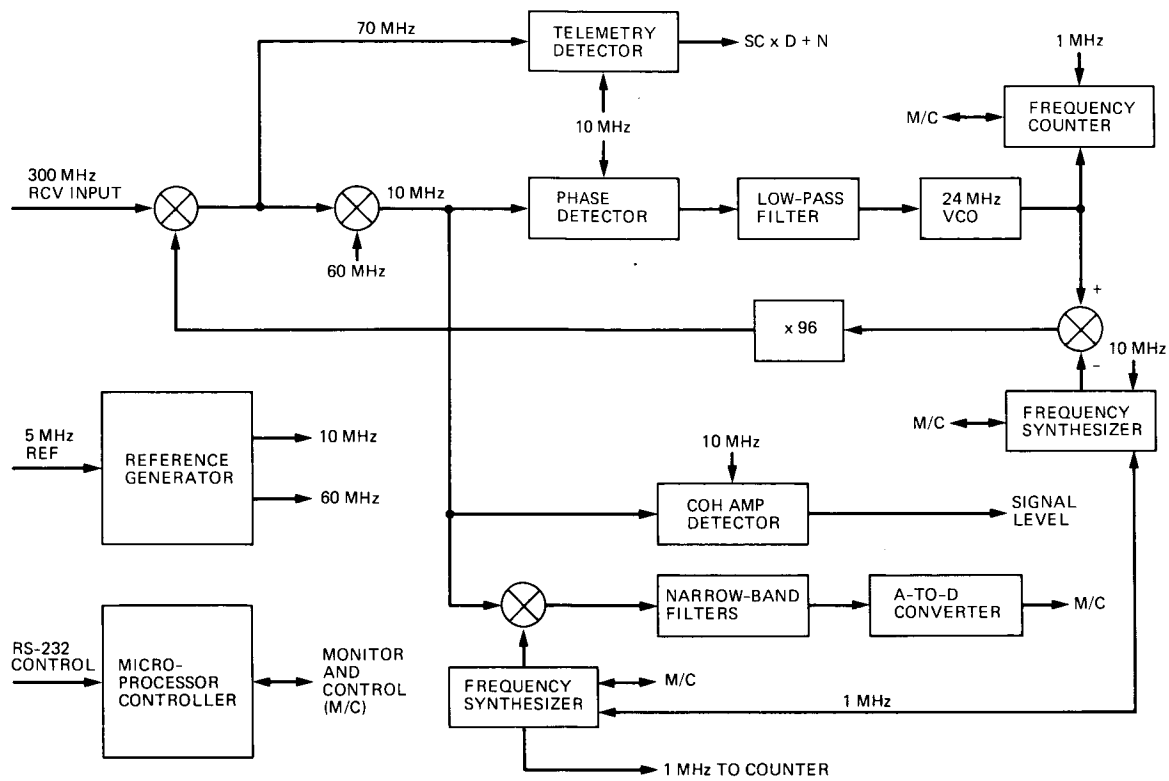


Fig. 5. Receiver block diagram

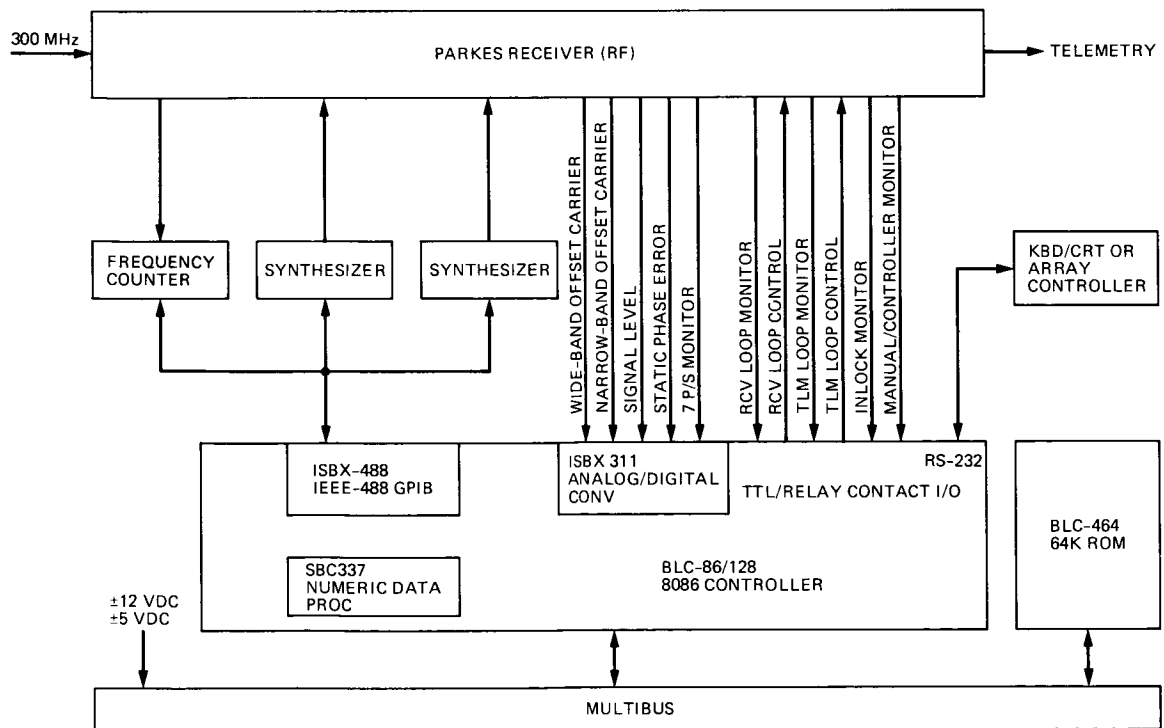


Fig. 6. Receiver controller block diagram

PRCV help . . .
 The format for user input is: <COMMAND>:<DATA OR OPTION>

THE COMMANDS ARE:

INIT : < Init Rcvr subsystem. Options NONE or S (self-test) or H (HPIB)>
 TSFR : < Enter predix track freq in HZ, KHZ or MHZ or >
 < TEST option (use test valves for TSF & doppler)>
 DOPP : < Enter predix doppler freq in HZ, KHZ or MHZ. Options NONE>
 SFSR : < Enter sweep rate. Options NONE>
 SPEC : < Display carrier spectrum & SNR. Options are >
 < N (nb), W (wb) or P (wideband using predix)>
 STAT : < Options V (volt), P (phase), M (mode), 0
 < 1 (synth 1 freq), C (carrier signal level) & D (predix/VCO)>
 ECHO : < Options ON or OFF>
 RLEN : < Rcvr loop ENABLE or DISABLE>
 ACQR : < Initiate automatic carrier acquisition.>
 < Option P (acquire using last entered predix valves)>
 ATRK : < Initiate auto-tracking. Options ON or OFF>
 TLEN : < Telemetry loop ENABLE or DISABLE>
 YSNR : < Calculate Y-factor SNR and power of carrier. Options NONE>
 STMP : < Enter system temperature (assumed to be in degrees Kelvin)>
 MLEV : < Enter SNR monitor threshold level (assumed to be in dB)>
 HELP : < Display help menu. Options NONE>

Fig. 7. Help menu, Parkes receiver

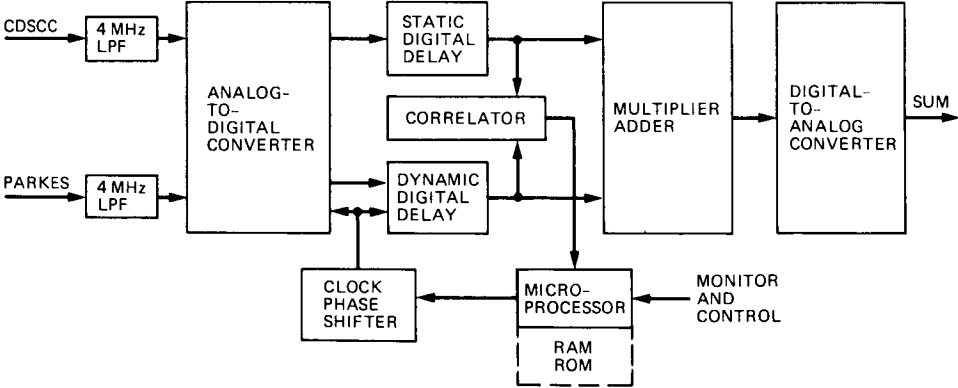


Fig. 8. Combiner block diagram

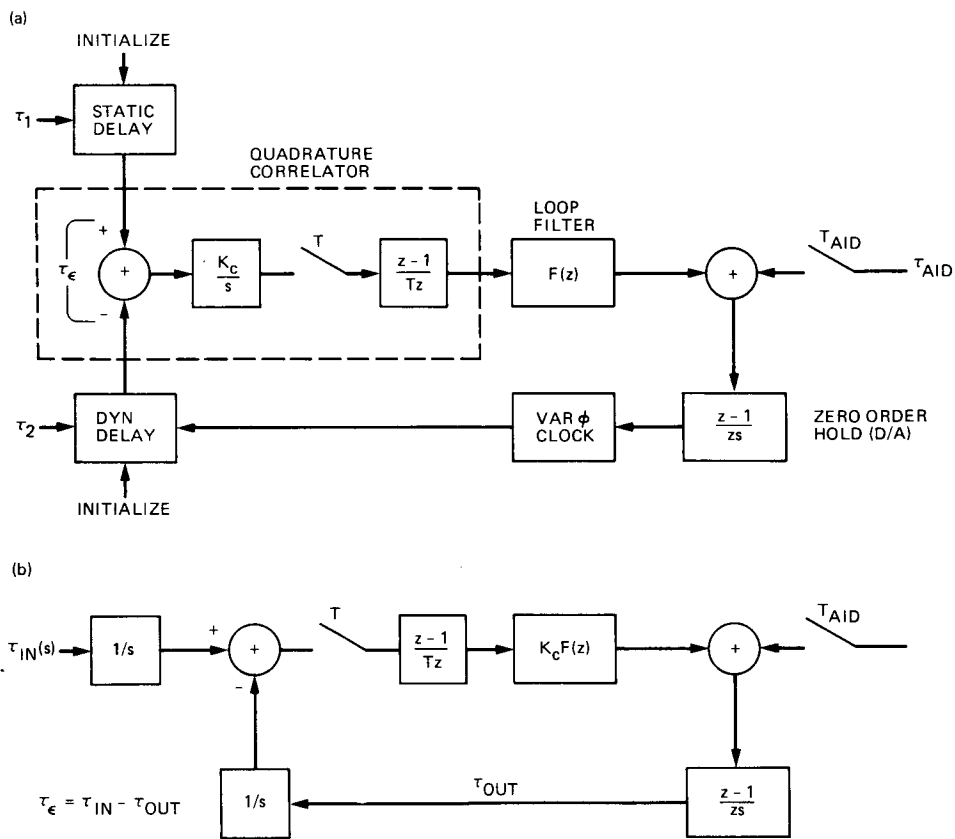


Fig. 9. Loop diagrams (a) hybrid and (b) equivalent error sampled

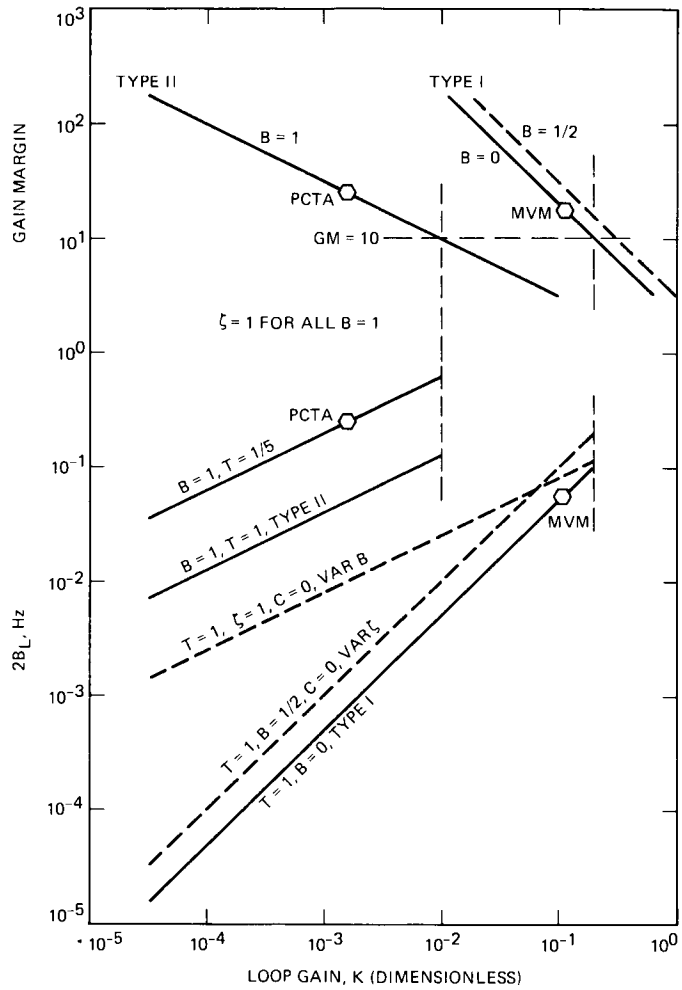


Fig. 10. Loop bandwidth and gain margin

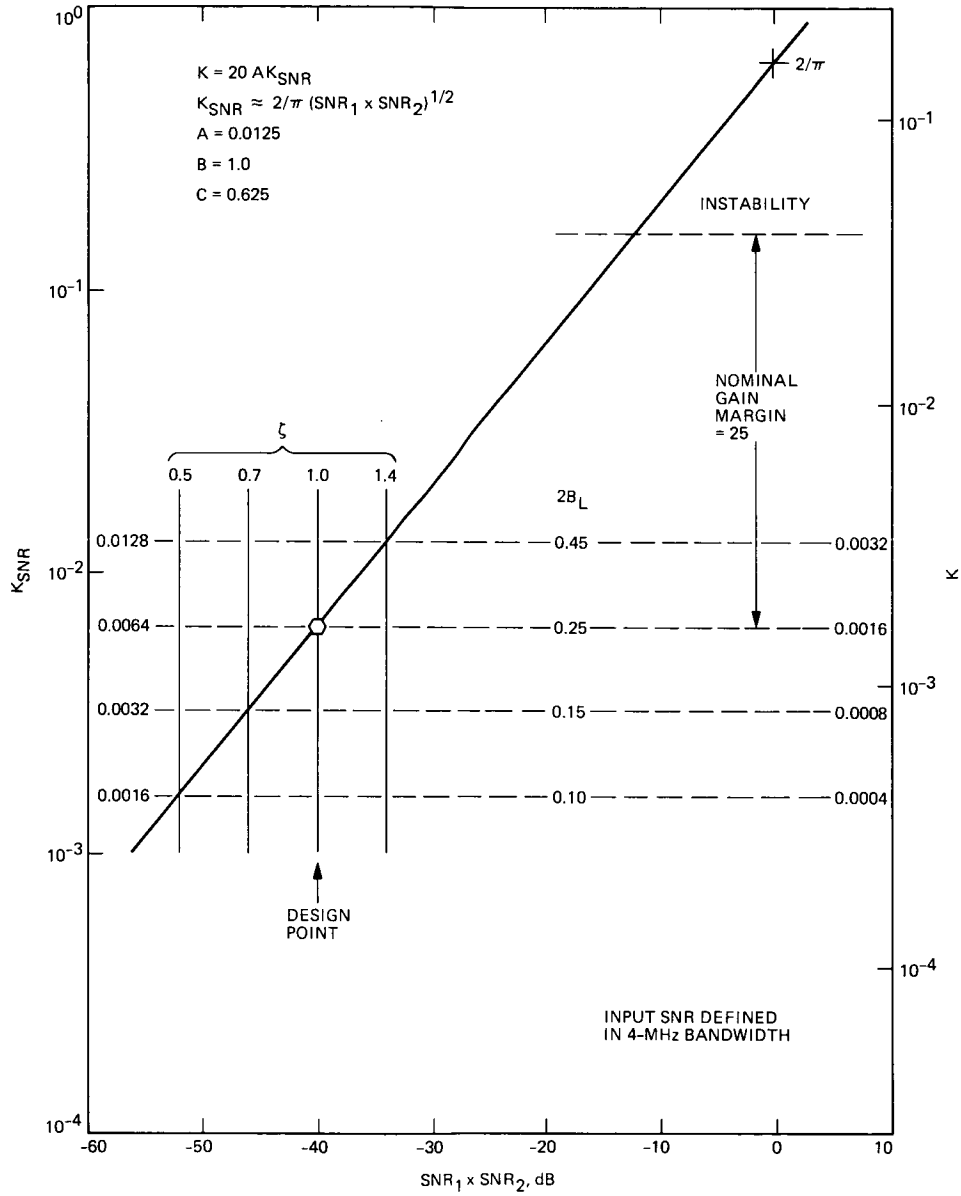


Fig. 11. Loop gain versus input SNR

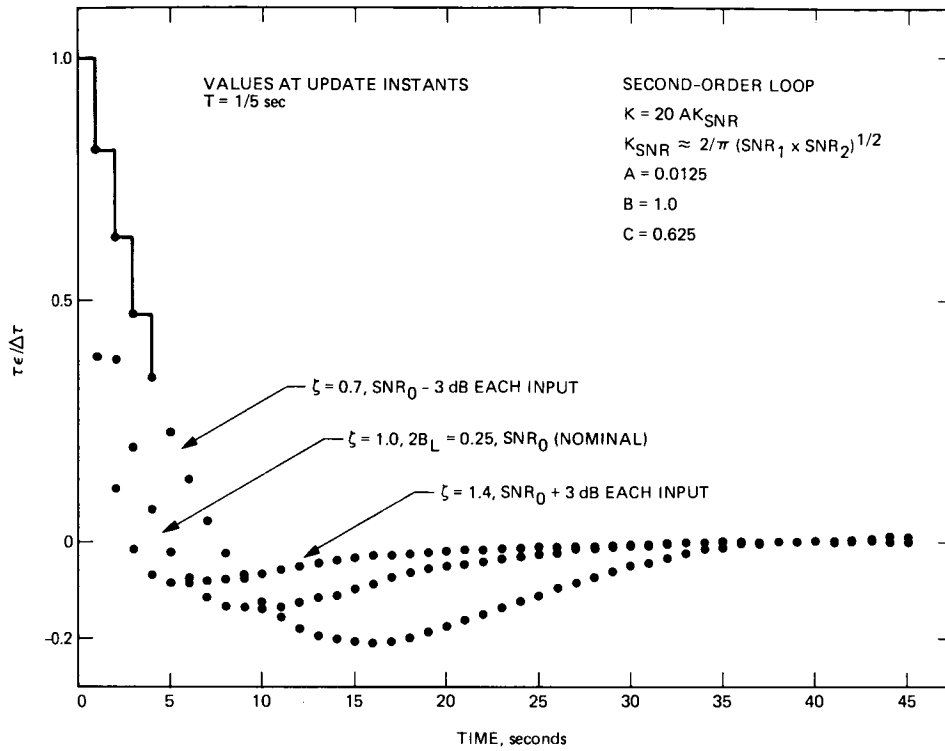


Fig. 12. Transient step response versus input SNR

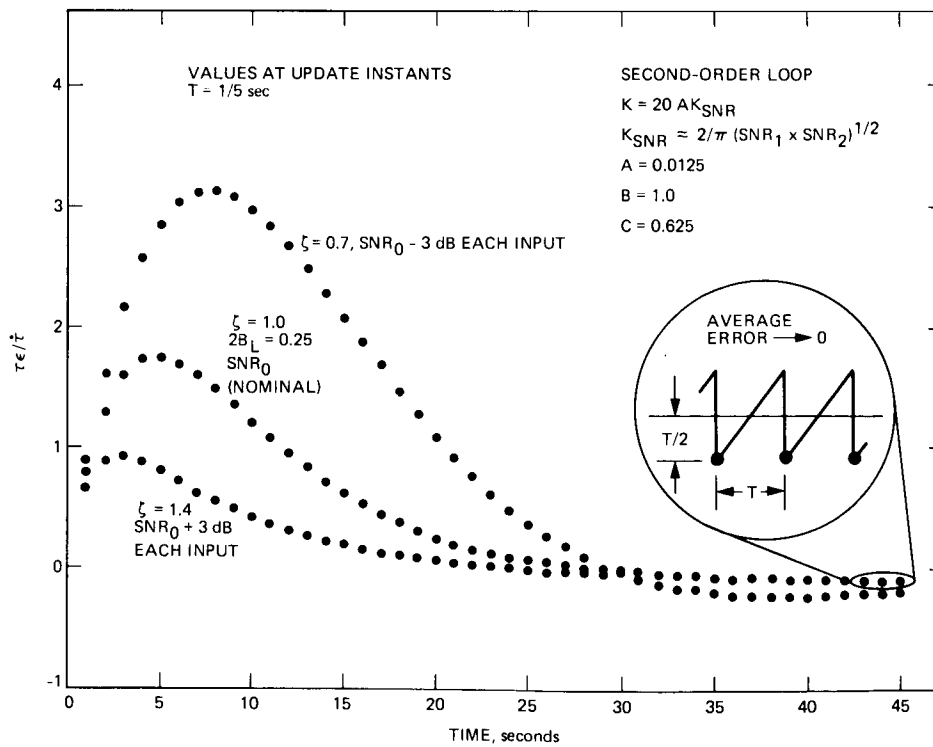
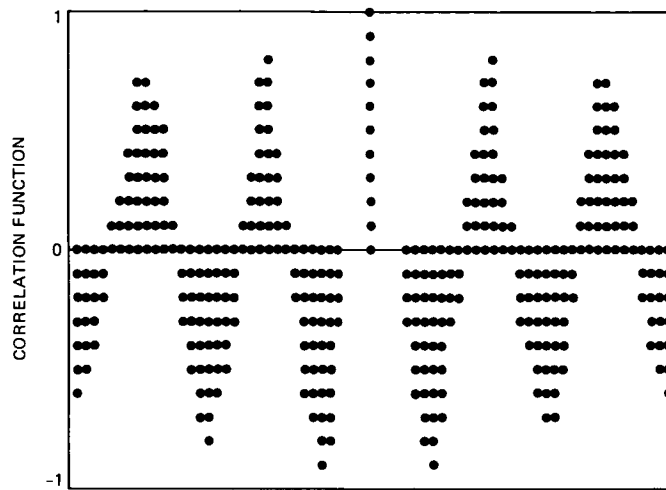


Fig. 13. Transient ramp response versus input SNR

ORIGINAL PAGE IS
OF POOR QUALITY



POLARITY AND SUBCARRIER PROBABLY CORRECT
RECOMMEND: NO ACTION

Fig. 14. CMAP display

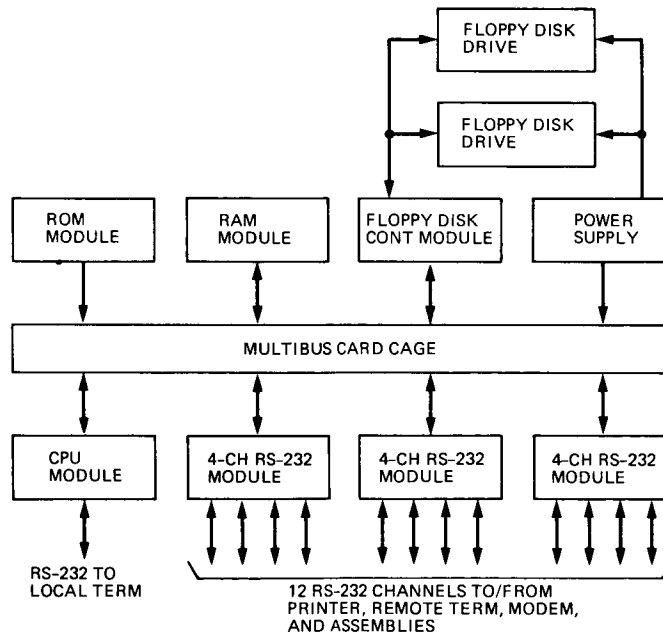


Fig. 15. Array controller block diagram

```

-----
OPERATIONAL MODE
LIVE SIGNAL COMBINING AND RECORDING - OPRMOD.CNF
LAST UPDATE 01/16/85
-----

```

OPERATIONAL MODE COMMAND CONFIGURATION FILE (LIVE SIGNAL COMBINING AND RECORDING) FOR SWITCHING ASSEMBLY SIGNAL ROUTING, TEST SIGNAL GENERATOR CONTROL COMMANDS, PCTA COMBINER CONTROL COMMANDS AND RECEIVER CONTROL COMMANDS.

***** CDSCC SIGNAL ROUTING CONFIGURATION - [CSAM] COMMANDS *****

CDSCC COMBINER INPUT SELECT <1 | 2 | 3 | 4 | 5>
CSAM:S1:4

LINK INPUT SELECT <1 | 2 | 3>
CSAM:S2:3

PARKES COMBINER INPUT SELECT <1 | 2 | 3>
CSAM:S3:2

PARKES SIGNAL POLARITY SELECT <1 | 2>
CSAM:S4:2

LINK OUTPUT SELECT <1 | 2 | 3 | 4 | 5 | 6>
CSAM:S8:6

***** PARKES SIGNAL ROUTING CONFIGURATION - [PSAM] COMMANDS *****

LINK OUTPUT SELECT <1 | 2 | 3 | 4>
PSAM:S1:4

RECORDER INPUT SELECT <1 | 2>
PSAM:S2:2

RECEIVER INPUT SELECT <1 | 2 | 3>
PSAM:S3:3

***** CDSCC TEST SIGNAL GENERATOR CONFIGURATION - [CTSG] COMMANDS*****

SET HIGH FREQUENCY NOISE <ON | OFF>
CTSG:RFNS:OFF

SET HIGH FREQUENCY CARRIER <ON | OFF>
CTSG:RFCR:OFF

***** PARKES RECEIVER - [PRCV] COMMANDS *****

SET BLOCK IN RECEIVE FREQUENCY PREDICT <41.8 - 44.0 MHz | TEST>
PRCV:REFR:TEST

SET AUTO TRACK MODE <ON | OFF>
PRCV:ATRK:OFF

SET LINEAR SWEEP <0 TO 9 Hz>
PRCV:SFBR:0

SET ISS LOOP SHORT <ENABLE | DISABLE>
PRCV:RLEN:DISABLE

***** CANBERRA LONG BASELINE COMBINER CONFIGURATION - [CLBC] COMMANDS *****

SET LINK DELAY <MICROSECONDS>
CLBC:LDLY:0.0

SET BBA THROUGHPUT DELAY <MICROSECONDS>
CLBC:SDLY:0.0

SET CLOCK OFFSETS <+ OR - NUMBER MICROSECONDS>
CLBC:SDLY:0.0

SET YEAR OF OBSERVATIONS <YYYY>
CLBC:YEAR:1982

Fig. 16. Sample configuration file

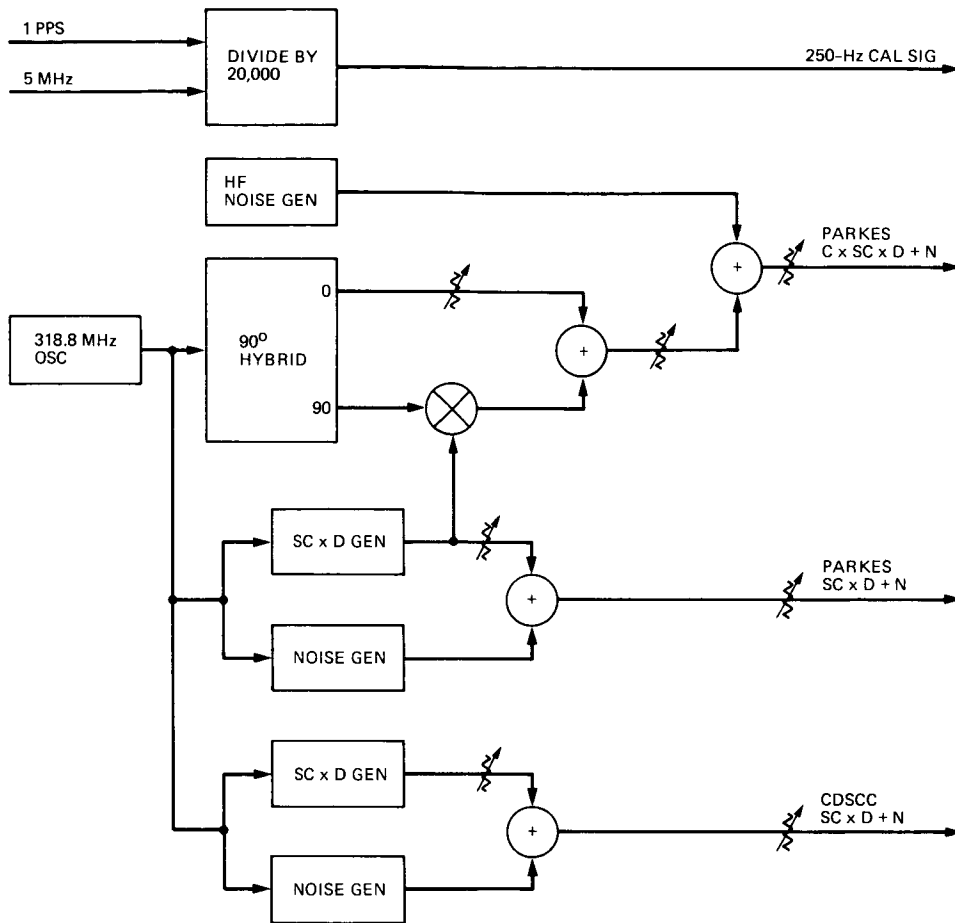


Fig. 17. Test signal generator block diagram

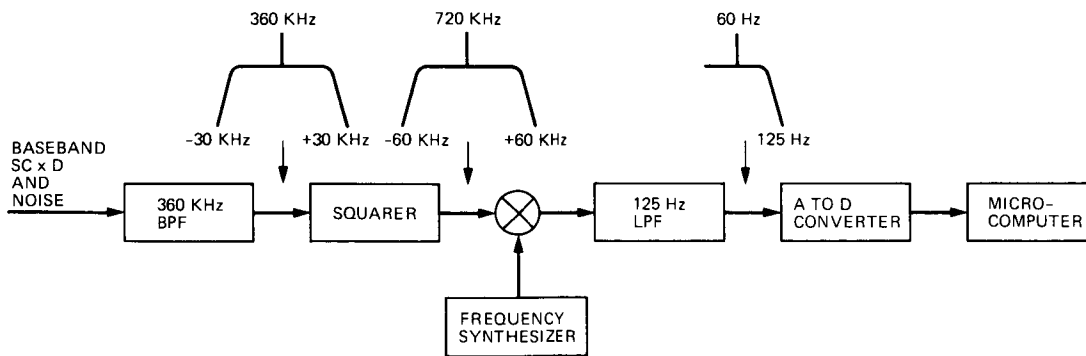


Fig. 18. Subcarrier SNR estimator block diagram

Appendix A

Combiner Loop Analysis

I. Generalized Loop Filter

Consider a sampled-data loop filter. If the output delay τ_i at the i th instant is formed by updating the previous value

$$\tau_i = \tau_{i-1} + \Delta\tau_i$$

and if the update is formed from the input τ_x as follows

$$\Delta\tau_i = A \tau_{x_i} + B \Delta\tau_{i-1} + C(\tau_{x_i} - \tau_{x_{i-1}})$$

the filter output is

$$\tau_i = \tau_{i-1} + A \tau_{x_i} + B(\tau_{i-1} - \tau_{i-2}) + C(\tau_{x_i} - \tau_{x_{i-1}})$$

Converting this difference equation to z -transform notation

$$\tau = \tau z^{-1} + A \tau_x + B \tau(z^{-1} - z^{-2}) + C \tau_x(1 - z^{-1})$$

yields

$$F(z) = \frac{\tau}{\tau_x} = \frac{Az^2 + C(z-1)z}{(z-1)(z-B)} \quad (\text{A-1})$$

Note that the parameter C of Ref. 3 is unrelated to the parameter C herein.

II. Stability Criteria and Gain Margin

Setting to zero the denominator of Eq. (2) yields the characteristic equation

$$D(z) = z^2 - \left[1 + B - K \left(1 + \frac{C}{A}\right)\right]z + B - \frac{C}{A}K = 0$$

for which stability criteria are

$$D(1) > 0: K \left(1 + \frac{C}{A}\right) > K \frac{C}{A}$$

or $K > 0$ (negative feedback)

$$D(-1) > 0: 1 + B > \frac{K}{2} \left(1 + 2 \frac{C}{A}\right)$$

$$\text{Gain Margin} \triangleq \frac{2(1+B)}{K \left(1 + 2 \frac{C}{A}\right)} \quad (\text{A-2})$$

$$D(0) < 1: K \frac{C}{A} > B - 1$$

or, by Eq. (A-3), $\zeta > 0$ (damping).

III. Continuous Equivalent Loop Parameters

Given the closed loop transfer function, Eq. (2)

$$G_{CL}(z) = \frac{K}{T} \frac{(z-1)z + \frac{C}{A}(z-1)^2}{(z-1)[(z-1) + 1 - B] + Kz + \frac{C}{A}K(z-1)}$$

and letting

$$1 - z^{-1} = 1 - e^{-Ts} \rightarrow Ts \quad \text{and } z \rightarrow 1$$

the continuous equivalent loop is defined for the update rate ($1/T$), which is large compared with the frequencies of interest

$$G_{CL}(s) \approx \frac{s \left(1 + \frac{C}{A}Ts\right)}{1 + \frac{T}{K} \left(1 - B + \frac{C}{A}K\right) s + \frac{T^2}{K} s^2}, B > 0$$

and from Fig. 9b

$$H(s) = \frac{\tau_{OUT}(s)}{\tau_{IN}(s)} = \frac{1}{s} G_{CL}(s)$$

$$H(s) \approx \frac{1 + \frac{C}{A}Ts}{1 + \frac{T}{K} \left(1 - B + \frac{C}{A}K\right) s + \frac{T^2}{K} s^2}, B > 0$$

By direct analogy with continuous loop analysis, ω_N^2 , ζ , and $2B_L$ are defined

$$\left. \begin{aligned} \omega_N^2 &\triangleq \frac{K}{T^2} \\ \zeta &\triangleq \frac{1-B+\frac{C}{A}K}{2\sqrt{K}} \end{aligned} \right\} B > 0 \quad (A-3)$$

$$2B_L \triangleq \left(\zeta + \frac{1}{4\zeta} \right) \sqrt{\frac{K}{T^2}} = \frac{K}{2T} \left(\frac{C}{A} + \frac{1}{\frac{C}{A}K} \right), \quad B = 1$$

For $B = C = 0$ (Type I)⁵

$$2B_L = \frac{K}{2T} \left(\frac{1}{1-\frac{K}{2}} \right) \quad (A-4)$$

Finally, for $0 < B < 1, C = 0$ [Ref. 3]

$$2B_L = \frac{K}{2T} \left(\frac{1}{1-B} \right) \text{ for } \frac{T_{comp}}{T} \ll 1 \text{ and } K \ll 1 \quad (A-5)$$

IV. Steady-State and Transient Errors

Owing to the configuration of Fig. 9b, overall $H(z)$ cannot be specified without defining the input $\tau_{IN}(s)$. Accordingly, the loop error is written as

$$\begin{aligned} \tau_e(z) &= \tau_{IN}(z) - \tau_{OUT}(z) \\ &= [\tau_{IN}(s)]^* - \left[\frac{\tau_{IN}(s)}{s} \right]^* G_{CL}(z) \end{aligned}$$

A. Step Response

For $\tau_{IN}(t) = \Delta\tau$

$$\begin{aligned} \frac{\tau_e(z)}{\Delta\tau} &= \left[\frac{1}{s} \right]^* - \left[\frac{1}{s^2} \right]^* G_{CL}(z) \\ \frac{\tau_e(z)}{\Delta\tau} &= \frac{(z-B)z}{(z-1)(z-B) + Kz + \frac{C}{A}K(z-1)} \quad (A-6) \end{aligned}$$

The steady-state error

$$\frac{\tau_e(ss)}{\Delta\tau} = \lim_{z \rightarrow 1} \left\{ \frac{z-1}{z} \frac{\tau_e(z)}{\Delta\tau} \right\} = 0$$

for all filter forms, due to the $z/(z-1)$ integration factor in Eq. (A-1) above.

B. Ramp Response

For $\tau_{IN}(t) = \dot{\tau}t$

$$\frac{\tau_e(z)}{\dot{\tau}} = \left[\frac{1}{s^2} \right]^* - \left[\frac{1}{s^3} \right]^* G_{CL}(z)$$

$$\frac{\tau_e(z)}{\dot{\tau}} = \frac{Tz}{(z-1)^2}$$

$$- \frac{KT}{2} \frac{(z+1)z^2 + \frac{C}{A}(z+1)(z-1)z}{(z-1)^3(z-B) + K(z-1)^2z + \frac{C}{A}K(z-1)^3} \quad (A-7)$$

The steady-state error

$$\frac{\tau_e(ss)}{\dot{\tau}} = \lim_{z \rightarrow 1} \left\{ \frac{z-1}{z} \frac{\tau_e(z)}{\dot{\tau}} \right\}$$

$$\frac{\tau_e(ss)}{\dot{\tau}} = \frac{T}{K}(1-B) - \frac{T}{2} \quad (A-8)$$

C. Acceleration Response

For $\tau_{IN}(t) = \frac{1}{2}\ddot{\tau}t^2$ and proceeding as above

$$\frac{\tau_e(z)}{\ddot{\tau}} = \left[\frac{1}{s^3} \right]^* - \left[\frac{1}{s^4} \right]^* G_{CL}(z)$$

except setting $C = 0$ for simplicity

$$\frac{\tau_e(z)}{\ddot{\tau}} = \frac{T^2}{6} \frac{3(z+1)z[(z-1)(z-B) + Kz] - K(z^2 + 4z + 1)z^2}{(z-1)^4(z-B) + K(z-1)^3z} \quad (A-9)$$

⁵Winkelstein, R. A., "Long Baseline Combiner Type I Loop Analysis," JPL internal document, IOM 331-84-272A, July 31, 1984.

This restriction will not affect the steady-state result below (by the continuous analogy).

To obtain the steady-state acceleration error, the limit ($z \rightarrow 1$) of Eq. (A-9) above will not suffice, since it is unbounded due to the integrated ramp error of the $B < 1$ loop configurations. Employing the artifice of subtracting out this ramp error prior to taking the limit, the *instantaneous* steady-state acceleration error is obtained for the general case

$$\frac{\tau_{\epsilon}(ss)}{\ddot{\tau}} \triangleq \lim_{z \rightarrow 1} \left\{ \frac{z-1}{z} \left[\frac{\tau_{\epsilon}(z)}{\ddot{\tau}} - \frac{\tau_{\epsilon}(ss)}{\dot{\tau}} [t] * \right] \right\}$$

After substitution, cancellation, and differentiation, Eq. (A-10) is finally obtained

$$\frac{\tau_{\epsilon}(ss)}{\ddot{\tau}} = \frac{T^2}{K} - \frac{T^2}{K^2} (1-B) - \frac{T^2}{6} \quad (\text{A-10})$$

The total *growing* steady-state error as a function of time can be synthesized as

$$\frac{\tau_{\epsilon}(ss)}{\ddot{\tau}}(t) = \left[\frac{T^2}{K} - \frac{T^2}{K^2} (1-B) - \frac{T^2}{6} \right] + \left[\frac{T}{K} (1-B) - \frac{T}{2} \right] t$$

which must be interpreted with care. The "real world" separates the components of this error by virtue of the sinusoidal delay variation in which the maxima are separated by six hours.

V. Loop Jitter

From Ref. 3, Eq. (53)

$$\sigma_N^2 = \frac{B_L T_L N_s}{K f_p^2} \left\{ [\text{erf} \sqrt{\text{SNR}_1} \text{erf} \sqrt{\text{SNR}_2}]^{-2} - 1 \right\}$$

where N_s is the number of Nyquist samples per symbol and K is the number of symbols per update period T_L , such that

$$\frac{N_s}{K} = \frac{2B_N T_s}{T_L/T_s} = 2B_N T_s^2/T_L$$

where B_N = noise bandwidth of the correlator input.

Also

$$f_p^2 \approx 16 \left(\frac{N_s}{N_{sc}} \right)$$

for low symbol-rate-to-subcarrier ratio and/or low data-transition probability [Ref. 3, Eq. (22)], where N_{sc} = number of Nyquist samples per subcarrier period, such that

$$\frac{N_s}{N_{sc}} = \frac{T_s}{T_{sc}}$$

Substituting all of the above in Eq. (53) of Ref. 3

$$\sigma_N^2 = \frac{B_L B_N}{8 f_{sc}^2} \left(\frac{1}{4 K_{SNR}^2} - 1 \right) \approx \frac{B_L B_N}{32 f_{sc}^2 K_{SNR}^2}$$

for low SNRs (defined in correlator input bandwidth) and

$$K_{SNR} \triangleq \frac{1}{2} \text{erf} \sqrt{\text{SNR}_1} \text{erf} \sqrt{\text{SNR}_2} \quad (\text{A-11})$$

K_{SNR} may be considered as the noise-dependent factor of K_c , the correlator gain. For all cases of interest, i.e., low SNR

$$K_{SNR}^2 \approx \frac{4}{\pi^2} \text{SNR}_1 \text{SNR}_2 \quad (\text{A-12})$$

and

$$\sigma_N^2 \approx \frac{\pi^2}{128} \frac{B_L B_N}{f_{sc}^2 \text{SNR}_1 \text{SNR}_2}$$

Converting from Nyquist variance to time

$$\sigma_T^2 = \left(\frac{\sigma_N}{2B_N} \right)^2 \text{sec}^2$$

$$\sigma_T^2 \approx \frac{2B_L}{256 B_N f_{sc}^2 K_{SNR}^2}$$

$$\approx \frac{\pi^2}{1028} \frac{2B_L}{B_N f_{sc}^2 \text{SNR}_1 \text{SNR}_2} \text{sec}^2 \quad (\text{A-13})$$

DSA's Subcarrier Demodulation Losses

M. Simon and A. Mileant
Telecommunications Systems Section

The degradation in bit error rate performance due to imperfect subcarrier tracking by the Demodulation Synchronization Assembly (DSA) is investigated. Results apply to any type of digital loop and received signal dynamics. A type four loop causes the least amount of loss, because it tracks phase jerk with zero steady-state error. However, when \dot{f} and \ddot{f} are as large as in the extended Magellan mission, it will be necessary to decrease the loop update time in order to minimize the losses. Figures 2 through 8 illustrate numerical results of this analysis.

I. Introduction

Figure 1 depicts, in block diagram form, the overall process of demodulating, synchronizing, and decoding a stream of binary data. Subcarrier demodulation and symbol synchronization are performed in the DSA of the Baseband Assembly (BBA). From there, the convolutionally encoded data go to the Maximum Likelihood Convolutional Decoder (MCD) for decoding. Phase jitter and phase error due to Doppler in both the subcarrier and the symbol synchronization loops decrease the energy-per-bit to noise spectral density ratio (E_b/N_0) at the input to the MCD. This decrease in E_b/N_0 increases the bit-error rate (BER) at the decoder's output. Given a desired BER, the increase in dB of the E_b/N_0 necessary to compensate for this degradation is denoted as *demodulation loss*.

The degradation in BER due to the effects of phase jitter and Doppler in the subcarrier tracking loop is estimated. The analysis applies to any digital loop with an integrate-and-dump circuit. The numerical results, which are applicable to the existing and potentially useful BBA's loops, are summarized in Figs. 2 through 8. The subcarrier demodulation losses were estimated at a nominal BER of 5×10^{-3} .

II. Discussion

First, it is necessary to express the variance of the phase error as a function of the input signal-to-noise ratio. The variance of the open-loop error signal at the output of the integrate-and-dump is given by [Ref. 1]

$$\sigma_\epsilon^2 = \frac{K}{2} (K_1 K_2 K_3 N_s)^2 \sigma_n^4 \left[1 + \left(\frac{S}{\sigma_n^2} \right) \frac{N_s}{2} \right] \quad (1)$$

where

S = the signal power

K = the number of symbols per update

$K_1, K_2,$ and K_3 = gains defined in Ref. 1

Also, the number of Nyquist samples per symbol is given by

$$N_s = \frac{2B_n}{r} \quad (2)$$

where

B_n = the baseband noise-equivalent bandwidth

r = the symbol rate

Finally, the thermal noise power is shown as

$$\sigma_n^2 = N_o B_n \quad (3)$$

Assuming that the spectrum of the error process (Fig. 3 of Ref. 1) is wide in relation to the loop bandwidth, then the variance of the steady-state error signal will be

$$\sigma_{\epsilon_{ss}}^2 = \sigma_{\epsilon}^2 \frac{1}{2\pi j} \oint H(z)H(z^{-1}) \frac{dz}{z} \quad (4)$$

Here $H(z)$ is the closed-loop transfer function. Using Eq. (82) of Ref. 1, Eq. (4) can be written as

$$\sigma_{\epsilon_{ss}}^2 = \sigma_{\epsilon}^2 2T B_L \quad (5)$$

where

T = the loop update time

B_L = the one-sided noise-equivalent loop bandwidth (see Table 1 of Ref. 1 for various values of B_L)

Given $\sigma_{\epsilon_{ss}}^2$, the variance of the phase error (σ_{ϕ}^2) at update instants is obtained from the relation

$$\sigma_{\phi}^2 = \frac{1}{(G_Q T)^2} \sigma_{\epsilon_{ss}}^2 \quad (6)$$

where G_Q is the "gain" of the integrate-and-dump device and is given by [Ref. 1]

$$G_Q = \frac{K K_1 K_2 K_3 N_s^2 S}{T\pi} \quad (7)$$

It can be shown that

$$\frac{S}{\sigma_n^2} = \frac{1}{2} \frac{E_b}{N_o} \frac{r}{B_n} \quad (8)$$

where E_b/N_o is the ratio of the energy-per-bit to noise spectral density. The factor of 2 comes because the rate 1/2 convolutional code has two symbols per bit. Inserting Eqs. (1), (2),

(3), (5), (7), and (8) into Eq. (6) and simplifying, the variance of the phase error becomes

$$\sigma_{\phi}^2 = \frac{B_L \pi^2}{r} \frac{1}{\left(\frac{E_b}{N_o}\right)^2} \left[1 + \frac{1}{2} \left(\frac{E_b}{N_o}\right)\right] \quad (9)$$

With no phase error in the carrier, subcarrier, or symbol synchronization loops, the bit error probability for the convolutional code can be expressed by the equation

$$P_B = C_1 \exp\left(C_2 \frac{E_b}{N_o}\right) \quad (10)$$

where C_1 and C_2 are constants which depend on the rate and constraint length of the code. The presence of an instantaneous phase error $\phi(t)$ in the subcarrier loop degrades E_b/N_o by the factor

$$\eta = \left(1 - \frac{|\phi(t)|}{\pi/2}\right)^2 \quad (11)$$

Assume that $\phi(t)$ is of the form

$$\phi(t) = \phi_r + \phi_d(t) \quad (12)$$

where

ϕ_r = the random component of $\phi(t)$ and is modeled as a Gaussian random variable with zero mean and variance σ_{ϕ}^2 given by Eq. (9)

$\phi_d(t)$ = the deterministic component of $\phi(t)$ which is of the form

$$\phi_d(t) = \phi_{ss} + \dot{\phi}_q t + \pi \dot{f} t^2 + \pi \ddot{f} t^3/3 \quad (13)$$

where

ϕ_{ss} = the steady-state phase error at loop update instants

$\dot{\phi}_q$ = the DCO's phase rate quantization error

\dot{f}, \ddot{f} = the frequency rate and frequency acceleration of the received subcarrier which appear because of the Doppler effect

It is assumed that \ddot{f} and higher derivatives are negligibly small.

Let f_T be the frequency of the transmitted subcarrier, $v(t)$ the instantaneous radial velocity of the spacecraft relative to the receiving station, and c the speed of light. Then, the instantaneous frequency of the received subcarrier will be

$$f \triangleq f_r(t) = f_T \left[\frac{1 - \frac{v(t)}{c}}{\sqrt{1 - \left(\frac{v(t)}{c}\right)^2}} \right]$$

$$= f_T \left\{ 1 - \frac{v(t)}{c} + \frac{1}{2} \left(\frac{v(t)}{c}\right)^2 - \frac{1}{2} \left(\frac{v(t)}{c}\right)^3 + \dots \right\} \quad (14)$$

Meanwhile, \dot{f} and \ddot{f} will be the first and second derivatives of Eq. (14)

$$\dot{f} \triangleq \frac{df_r(t)}{dt} = f_T \frac{\dot{v}(t)}{c} \left(-1 + \frac{v(t)}{c} - \frac{3v^2(t)}{2c^2} + \dots \right) \quad (15)$$

and

$$\ddot{f} \triangleq \frac{d^2 f_r(t)}{dt^2} = \frac{f_T}{c} \left[\ddot{v}(t) \left(-1 + \frac{v(t)}{c} - \frac{3v^2(t)}{2c^2} \right) + \frac{\dot{v}^2(t)}{c} \left(1 - \frac{3v(t)}{c} \right) + \dots \right] \quad (16)$$

which, for $v(t) \ll c$, reduces to

$$\dot{f} \cong -f_T \frac{\dot{v}(t)}{c}$$

and

$$\ddot{f} \cong -f_T \frac{\ddot{v}(t)}{c}$$

The steady-state phase error ϕ_{ss} depends on the number of integrators present in the subcarrier tracking loop. Using Table 2 and Eq. (30) of Ref. 2, Table 1 is obtained. In this table,

$$F_c = \frac{\pi(1-g)^2}{G} \frac{\prod_{i=1}^n (1-p_i)}{\prod_{i=1}^m (1-z_i)} \quad (17)$$

where

p_j and z_i = the poles and zeros of the loop filter ($p_j \neq 1$)

g = normalized computation time

G = effective loop gain defined by Eq. (9) in Ref. 2

Assuming that $3\sigma_\phi \ll \pi/2$, the bit-error rate [Eq. (10)] together with the degradation factor [Eq. (11)], averaged over one update interval, will be

$$\bar{P}_B = \frac{C_1}{T} \frac{1}{(2\pi)^{0.5} \sigma_\phi}$$

$$\times \int_0^T \int_{-\infty}^{\infty} \exp \left[C_2 \frac{E_b}{N_0} \left(1 - \frac{|\phi(t)|}{\pi/2} \right)^2 + \frac{\phi_r^2}{2\sigma_\phi^2} \right] d\phi_r dt \quad (18)$$

$$= \frac{C_1}{2T(d)^{0.5}} \int_0^T \left\{ \exp \left[a \left(1 - \frac{\phi_d(t)}{\pi/2} \right)^2 \right] \operatorname{erfc} \left(b - \frac{\phi_d(t)}{(2d)^{0.5} \sigma_\phi} \right) \right.$$

$$\left. + \exp \left[a \left(1 + \frac{\phi_d(t)}{\pi/2} \right)^2 \right] \operatorname{erfc} \left(b + \frac{\phi_d(t)}{(2d)^{0.5} \sigma_\phi} \right) \right\} dt \quad (19)$$

where

$$a = \frac{C_2 E_b}{d N_0}$$

$$b = \left(\frac{8}{d} \right)^{0.5} C_2 \frac{E_b}{N_0} \frac{\sigma_\phi}{\pi}$$

$$d = 1 - 8 C_2 \frac{E_b}{N_0} \frac{\sigma_\phi^2}{\pi^2}$$

and $\phi_d(t)$ is defined by Eq. (13).

For the (1/2, 7) convolutional code, $C_1 = 85.7469$ and $C_2 = -5.7230$. The second integration over the time variable t must be performed numerically. By measuring the horizontal distance at a given value of \bar{P}_B , the corresponding loss of the subcarrier loop is obtained.

III. Numerical Results

The average bit-error rate (\bar{P}_B), expressed by Eq. (19), was calculated for several loops of types 2, 3, and 4. The corresponding loss was estimated at $\bar{P}_B = 5 \times 10^{-3}$.

Curves of subcarrier demodulation loss versus \dot{f} are shown on Figs. 2 through 8. It was assumed that, for the Voyager encounter, \dot{f} would be less than 1.0 mHz/s, and \ddot{f} less than 1×10^{-7} Hz/s². For the Magellan mission, it was assumed that \dot{f} would be less than 25 mHz/s, and \ddot{f} less than 3×10^{-5} Hz/s².

The loss for a type 2 loop is quite significant, due to a high steady-state error even with a small \dot{f} . The loss can be reduced by decreasing the update time (Fig. 2).

If a type 3 loop is selected, the loop is degraded only when \ddot{f} is significant, which increases the steady-state error.

In a type 4 loop, the steady-state phase error is insensitive to either \dot{f} or \ddot{f} . However, when \dot{f} and \ddot{f} are high, as in the Magellan mission, $\phi_d(t)$ can be quite large at the end of the

loop update instant. This produces a large demodulation loss (Fig. 8). In this case, the loss can be reduced only by decreasing the loop update time.

In the numerical calculations, it was noticed that the contribution to the demodulation loss due to thermal noise was insignificant for $E_b/N_0 > 2.0$ dB and $B_L < 1.0$ Hz. For this reason, Figs. 2 through 8 apply to data rates between 10 and 500 kilosymbols per second.

IV. Conclusion

An equation for the average bit error rate versus E_b/N_0 and spacecraft dynamics was derived. A type 2 loop is very sensitive to \dot{f} and \ddot{f} . A type 4 loop has a zero steady-state error even with high values of \dot{f} . However, with high \dot{f} and \ddot{f} , the degradation due to phase error in the subcarrier loop could be quite significant if the loop update time is large. Reduction of loop update time will be necessary for the Magellan mission. Figures 2 through 8 numerically illustrate the above conclusions.

References

1. Simon, M. K., and A. Mileant, "Performance of the DSA's Subcarrier Demodulation Digital Loop," *TDA Progress Report 42-80*, pp. 180-194, Jet Propulsion Laboratory, Pasadena, California.
2. Simon, M. K., and A. Mileant, "Digital Filters for the Digital Phase-Locked Loops," *TDA Progress Report 42-81*, pp. 81-93, Jet Propulsion Laboratory, Pasadena, California.

Table 1. Steady-state phase error (at loop update instants)

Loop Type	Number of Integrators in the Filter	Steady-State Phase-Error, ϕ_{ss}		
		f Hz	\dot{f} Hz/sec	\ddot{f} Hz/sec ²
1	0	$1!fTF_c$	∞	∞
2	1	0	$2!\dot{f}T^2F_c$	∞
3	2	0	0	$3!\ddot{f}T^3F_c$
4	3	0	0	0

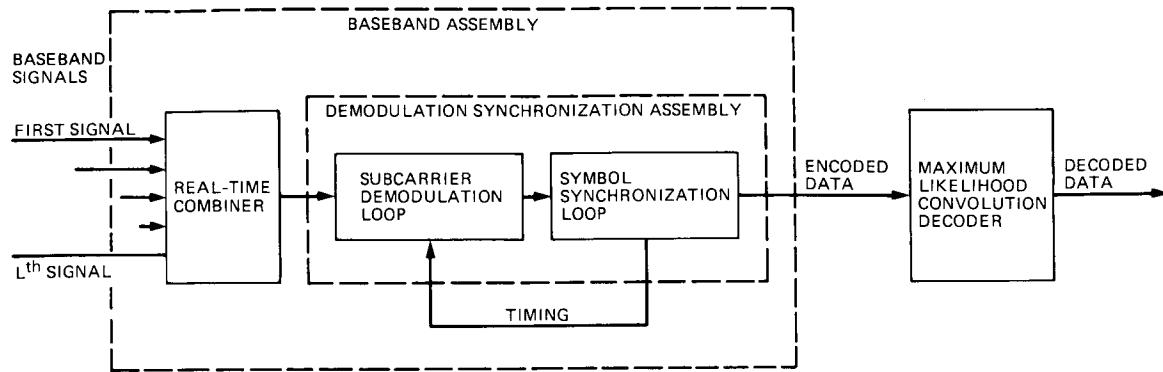


Fig. 1. Demodulation and decoding process

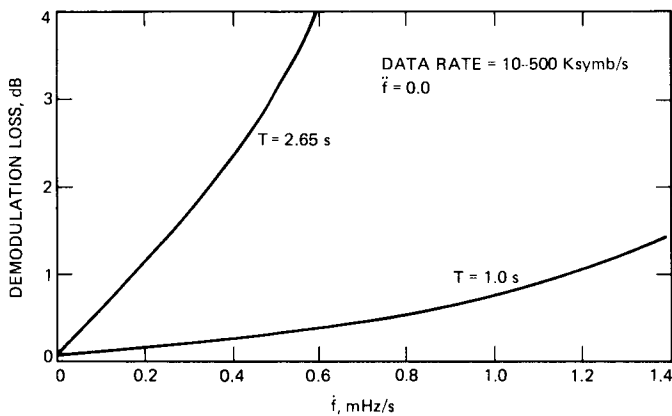


Fig. 2. Subcarrier demodulation loss versus \hat{f} for loop type 2 at: $B_L = 0.38$, $T = 2.65$ and 1.0 , $p_1 = -0.176$, $p_2 = -0.68$, $z_1 = 0.828$, $z_2 = 0.00$, $z_3 = 0.0$, $z_4 = 0.0$, $G = 0.188$, $\dot{\hat{f}} = 0.0$

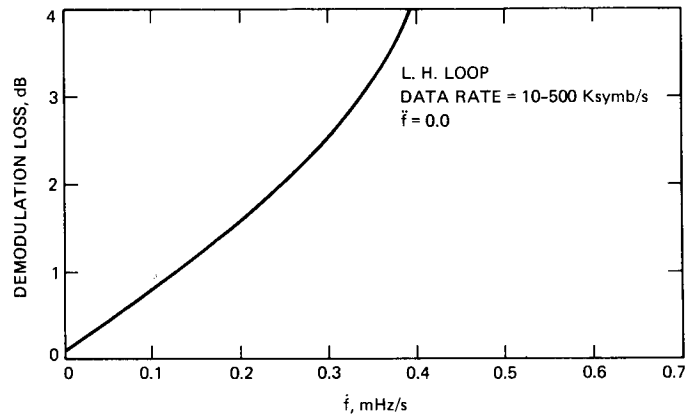


Fig. 3. Subcarrier demodulation loss versus \hat{f} for loop type 2 at: $B_L = 0.19$, $T = 2.65$, $p_1 = 0.0$, $p_2 = 0.0$, $z_1 = 0.895$, $z_2 = 0.1048$, $z_3 = 0.0$, $z_4 = 0.0$, $G = 0.1248$

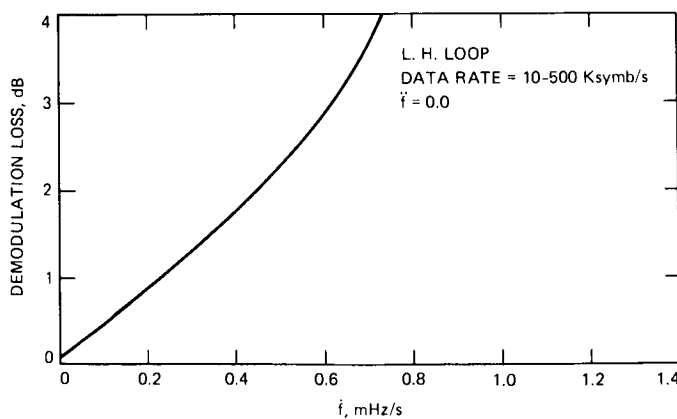


Fig. 4. Subcarrier demodulation versus \hat{f} for loop type 2 at: $B_L = 0.41$, $T = 2.65$, $p_1 = 0.0$, $p_2 = 0.0$, $z_1 = 0.853$, $z_2 = 0.1464$, $z_3 = 0.0$, $z_4 = 0.0$, $G = 0.1665$

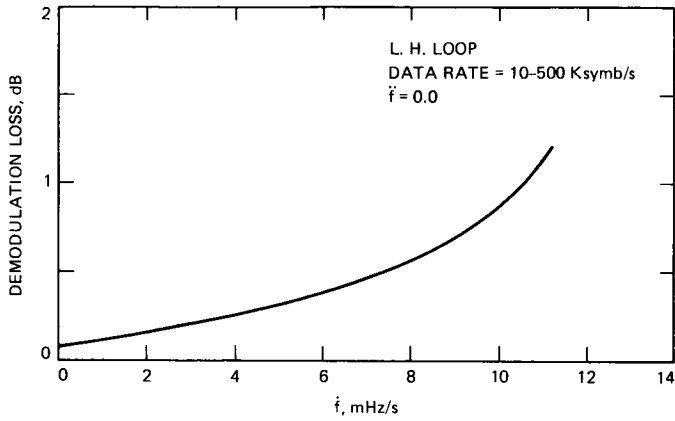


Fig. 5. Subcarrier demodulation versus \dot{f} for loop type 3 at: $B_L = 0.51$, $T = 2.65$, $p_1 = 0.0$, $p_2 = 0.0$, $z_1 = 0.217$, $z_2 = 0.007$, $z_3, z_4 = 0.883 \pm j 0.104$, $G = 0.1873$

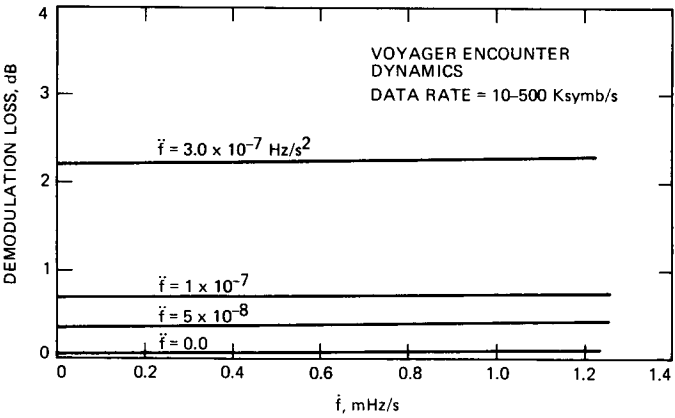


Fig. 6. Subcarrier demodulation versus \dot{f} for loop type 3 at: $B_L = 0.5/T$, $T = 2.65$, $p_1 = -0.173$, $p_2 = -0.999$, $z_1 = 0.960$, $z_2 = 0.960$, $z_3 = 0.0$, $z_4 = 0.0$, $G = 0.15$

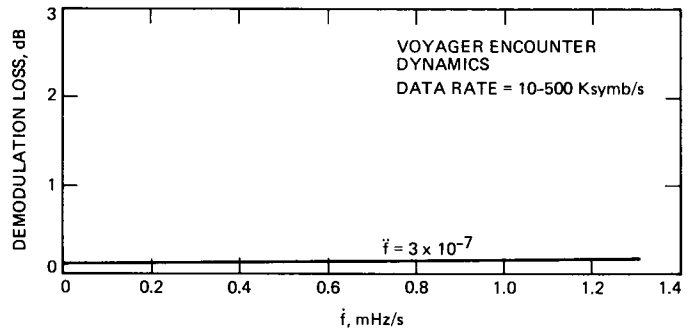


Fig. 7. Subcarrier demodulation versus \dot{f} for loop type 3 at: $B_L = 0.5/T$, $T = 1.0$, $p_1 = -0.173$, $p_2 = -0.999$, $z_1 = 0.960$, $z_2 = 0.960$, $z_3 = 0.0$, $z_4 = 0.0$, $G = 0.15$

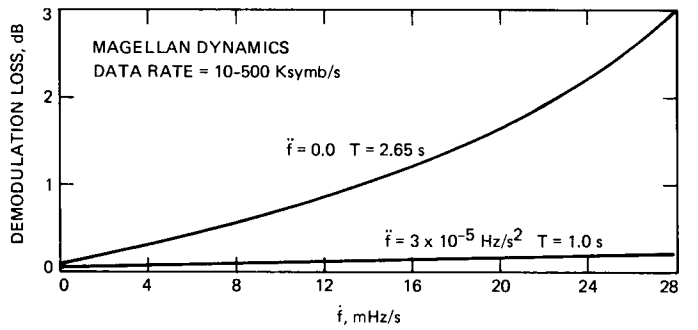


Fig. 8. Subcarrier demodulation versus \dot{f} for loop type 4 at: $B_L = 0.5/T$, $T = 2.65$ and 1.0 , $p_1 = -0.173$, $p_2 = -0.999$, $z_1 = 0.960$, $z_2 = 0.930$, $z_3 = 0.930$, $z_4 = 0.0$, $G = 0.15$

011-32
98.

13155

SNR Estimation for the Baseband Assembly

M. K. Simon and A. Mileant
Telecommunications Systems Section

The expected value and the variance of the Baseband Assembly symbol signal-to-noise ratio (SNR) estimation algorithm are derived. The SNR algorithm treated here is designated as the Split Symbol Moments Estimator (SSME). It consists of averaging the first two moments of the integrated half symbols. The SSME is a biased, consistent estimator. The SNR degradation factor due to the jitter in the subcarrier demodulation and symbol synchronization loops is taken into account. Curves of the expected value of the SNR estimator versus the actual SNR are shown.

I. Introduction

The Baseband Assembly¹ uses a Split Symbol Moments Estimator (SSME) algorithm to estimate the symbol signal-to-noise ratio (SNR) of the input signal. Here we describe the SSME algorithm and give the expected value and the variance of the SNR estimator. Two numerical examples corresponding to the Voyager and the Pioneer missions are included to illustrate its performance. As in previous Baseband Assembly analyses (Refs. 1 and 2), Nyquist sampling rate is assumed.

II. Statistics of the SNR Estimator

Figure 1 is a flow chart representation of the SSME algorithm. Referring to this figure, the input to the SNR estimator is a string of signal samples modeled as

$$y_{ij} = s_{ij} + n_{ij} \quad (1)$$

where

s_{ij} = unitless random variable whose amplitude is proportional to the information signal voltage

n_{ij} = unitless random variable whose amplitude is proportional to the rms noise voltage

The first two moments of y_{ij} are

$$E\{y_{ij}\} = \sqrt{S} \quad (2)$$

$$E\{(y_{ij})^2\} = S + \sigma_n^2 \quad (3)$$

It is assumed that $E\{n_{ij}\} = 0$

$i = 1, 2, \dots, N_s$ Nyquist samples per symbol

$j = 1, 2, \dots, n$ symbols

The variance of the noise process is assumed to be

$$\sigma_n^2 = N_0 B_n \quad (4)$$

¹Deep Space Network/Flight Project Interface Design Handbook, JPL internal document 810-5, Rev. D, 1981.

where N_0 is the one-sided noise spectral density, and B_n is the one-sided baseband noise-equivalent bandwidth.

As shown in Fig. 1, in the upper "arm" the samples from the first half of a symbol are summed to produce $Y_{\alpha j}$. In the lower "arm" the samples of the second half of a symbol are summed to produce $Y_{\beta j}$. In this analysis, it will be assumed that the number of samples in both summers are equal at the instants when $Y_{\alpha j}$ and $Y_{\beta j}$ are sampled. For this reason, $Y_{\alpha j}$ and $Y_{\beta j}$ have identical statistics. Making $Y_{\alpha j} = Y_{\beta j} = Y_j$, the mean value and the variance of Y_j will be, assuming that the samples are independent,

$$\bar{Y}_j \triangleq E\{Y_{\alpha j}\} = E\{Y_{\beta j}\} = \frac{N_s}{2} \sqrt{S} \sqrt{d_j} \quad (5)$$

$$\sigma_j^2 \triangleq E\{(Y_{\alpha j} - \bar{Y}_{\alpha j})^2\} = E\{(Y_{\beta j} - \bar{Y}_{\beta j})^2\} = \frac{N_s}{2} \sigma_n^2 \quad (6)$$

The factor d_j , designated as the SNR degradation factor, is due to the phase jitter and timing jitter in the subcarrier demodulation and symbol synchronization loops, respectively. In general,

$$0 < d_j < 1 \quad (7)$$

It can be shown that

$$d_j = \left(1 - \frac{|\phi_j|}{\pi/2}\right)^2 \left(1 - 2p_T \frac{|\tau_j|}{T_s}\right)^2 \quad (8)$$

where

ϕ_j = phase error in the subcarrier demodulation loop during the j th symbol

τ_j = timing error in the symbol synchronization loop during the j th symbol

p_T = probability of symbol transition

T_s = symbol time

In this preliminary analysis, it will be assumed that there is no doppler stress in the tracking loops and that ϕ_j and τ_j are functions of the phase and timing jitter only. With this assumption, ϕ_j and τ_j will be constant during one update interval, and the subscript j can be dropped, i.e., we will assume that during the estimation interval

$$d_j = d_{j+1} = d \quad (9)$$

and, consequently, the statistics of Y_j will be equal to those of Y_{j+1} .

In the SSME algorithm, the random variables Y_α and Y_β are combined to create two new random variables X_p and X_{ss} in the following way:

$$X_p = Y_\alpha Y_\beta \quad (10)$$

and

$$X_{ss} = (Y_\alpha + Y_\beta)^2 \quad (11)$$

Then, as shown in Fig. 1, n samples of X_p and X_{ss} are averaged in the second pair of summers to produce m'_p and m'_{ss} . Finally, m'_p and m'_{ss} are scaled and combined to produce the random variable R^* , which is the SNR estimator of the SSME algorithm, namely,

$$R^* = \frac{m'_p}{2 \left(\frac{1}{4} m'_{ss} - m'_p \right)} \quad (12)$$

The statistics of R^* can be determined from the statistics of the random variables along the two paths in Fig. 1. These statistics are obtained in what follows.

Using Eqs. (6) and (7) and the fact that Y_α and Y_β are independent, the first two moments of their product defined in Eq. (10) will be

$$\bar{X}_p = N_s^2 S d / 4 \quad (13)$$

$$\bar{X}_p^2 = (N_s^2 S d / 4 + N_s \sigma_n^2 / 2)^2 \quad (14)$$

The first two moments of X_{ss} defined by Eq. (11) are obtained using Eq. (A-2) of Appendix A with $\mu = N_s \sqrt{S d}$ and $\sigma^2 = N_s \sigma_n^2$, namely,

$$\begin{aligned} \bar{X}_{ss} &= E(X_{ss}^2) \\ &= N_s^2 S d + N_s \sigma_n^2 \end{aligned} \quad (15)$$

$$\begin{aligned} \bar{X}_{ss}^2 &= E(X_{ss}^4) \\ &= 3N_s^2 \sigma_n^4 + 6N_s^3 S d \sigma_n^2 + N_s^4 S^2 d^2 \end{aligned} \quad (16)$$

Referring to Fig. 1, and using Eq. (A-5), the first and second moments at the outputs of the second pair of summers will be

$$\bar{m}'_p = \bar{X}_p \quad (17)$$

$$\overline{(m'_p)^2} = \overline{X_p^2} \quad (18)$$

$$\overline{m'_{ss}} = \overline{X_{ss}} \quad (19)$$

$$\overline{(m'_{ss})^2} = \overline{X_{ss}^2} \quad (20)$$

The variances of m'_p and m'_{ss} are obtained using Eq. (A-6) with the moments obtained in Eqs. (13) through (16), namely,

$$\begin{aligned} \text{var}(m'_p) &= \frac{1}{n} (\overline{X_p^2} - (\overline{X_p})^2) \\ &= \frac{N_s^2 \sigma_n^2}{4n} (N_s S_d + \sigma_n^2) \end{aligned} \quad (21)$$

$$\begin{aligned} \text{var}(m'_{ss}) &= \frac{1}{n} [\overline{X_{ss}^2} - (\overline{X_{ss}})^2] \\ &= \frac{2N_s^2 \sigma_n^2}{n} (2N_s S_d + \sigma_n^2) \end{aligned} \quad (22)$$

The covariance of X_{ss} and X_p is, by definition,

$$\begin{aligned} \text{cov}(X_{ss}, X_p) &\triangleq E\{(X_{ss} - \overline{X_{ss}})(X_p - \overline{X_p})\} \\ &= E\{[(Y_\alpha + Y_\beta)^2 - (\overline{Y_\alpha} + \overline{Y_\beta})] [Y_\alpha Y_\beta - \overline{Y_\alpha} \overline{Y_\beta}]\} \\ &= E\{[Y_\alpha^2 - \overline{Y_\alpha}^2] + (Y_\beta^2 - \overline{Y_\beta}^2) \\ &\quad + 2(Y_\alpha Y_\beta - \overline{Y_\alpha} \overline{Y_\beta}) [Y_\alpha Y_\beta - \overline{Y_\alpha} \overline{Y_\beta}]\} \\ &= \overline{Y_\beta} (\overline{Y_\alpha^3} - \overline{Y_\alpha} \overline{Y_\alpha^2}) + \overline{Y_\alpha} (\overline{Y_\beta^3} - \overline{Y_\beta} \overline{Y_\beta^2}) \\ &\quad + 2(\overline{Y_\alpha^2} \overline{Y_\beta^2} - (\overline{Y_\alpha})^2 (\overline{Y_\beta})^2) \end{aligned} \quad (24)$$

Using Eqs. (6) and (7) in Eq. (A-2), the third moment of Y_α and Y_β is

$$\overline{Y_\alpha^3} = \overline{Y_\beta^3} = \frac{3}{4} N_s^2 \sqrt{S_d} \sigma_n^2 + \frac{1}{8} N_s^3 (S_d)^{3/2} \quad (25)$$

Inserting Eqs. (6), (7), and (25) in Eq. (24) and dividing by n , we obtain the covariance of m'_p and m'_{ss} , namely,

$$\text{cov}(m'_p, m'_{ss}) = \frac{N_s^2 \sigma_n^2}{2n} (2N_s S_d + \sigma_n^2) \quad (26)$$

Having obtained the moments of m'_p and m'_{ss} , we now are ready to determine the statistics of the estimator R^* . Using Eq. (A-9), the expected value of R^* defined by Eq. (12) is

$$\begin{aligned} \overline{R^*} &= R^* \left| \begin{array}{c} \overline{m'_p} \\ \overline{m'_{ss}} \end{array} \right| + \frac{1}{2} \left[\frac{\partial^2 R^*}{\partial m_p'^2} \text{var}(m'_p) + \frac{\partial^2 R^*}{\partial m_{ss}'^2} \text{var}(m'_{ss}) \right] \left| \begin{array}{c} \overline{m'_p} \\ \overline{m'_{ss}} \end{array} \right| \\ &\quad + \frac{\partial^2 R^*}{\partial m_p' \partial m_{ss}'} \text{cov}(m'_p, m'_{ss}) \left| \begin{array}{c} \overline{m'_p} \\ \overline{m'_{ss}} \end{array} \right| + \dots \end{aligned} \quad (27)$$

Inserting Eqs. (A-16), (A-18), (A-19), (21), (22), and (26) in Eq. (27) and ignoring higher order terms, we obtain

$$\overline{R^*} = \hat{R} + \frac{1}{n} (2\hat{R} + 1) \quad (28)$$

where

$$\hat{R} \triangleq \frac{\overline{m'_p}}{2 \left(\frac{1}{4} \overline{m'_{ss}} - \overline{m'_p} \right)} = \frac{N_s S_d}{2\sigma_n^2} = R d \quad (29)$$

is the degraded symbol SNR at the input to the SNR estimator. From Eq. (28) we observe that R^* is a biased but consistent estimator (i.e., the bias goes to zero when n goes to infinity).

The variance of R^* is obtained using Eq. (A-10), namely,

$$\begin{aligned} \text{var}(R^*) &= \left(\frac{\partial R^*}{\partial m_p'} \right)^2 \left| \begin{array}{c} \text{var}(m'_p) \\ \overline{m'_p} \end{array} \right| + \left(\frac{\partial R^*}{\partial m_{ss}'} \right)^2 \left| \begin{array}{c} \text{var}(m'_{ss}) \\ \overline{m'_{ss}} \end{array} \right| \\ &\quad + 2 \frac{\partial R^* \partial R^*}{\partial m_p' \partial m_{ss}'} \text{cov}(m'_p, m'_{ss}) \left| \begin{array}{c} \overline{m'_p} \\ \overline{m'_{ss}} \end{array} \right| \end{aligned} \quad (30)$$

Inserting Eqs. (A-15), (A-17), (A-19), (15), (16), and (26) in Eq. (30), we obtain

$$\text{var}(R^*) = \frac{1}{n} (1 + 4\hat{R} + 2\hat{R}^2) \quad (31)$$

By defining the SNR of our estimator as the ratio

$$\text{SNR}(R^*) = \frac{(\overline{R^*})^2}{\text{var}(R^*)} \quad (32)$$

we see that

$$\lim_{R \rightarrow 0} \text{SNR}(R^*) = \frac{1}{n} \quad (33)$$

$$\lim_{R \rightarrow \infty} \text{SNR}(R^*) \cong \frac{n}{2} + 2 \quad (34)$$

III. Evaluation of d

Assuming that there are no doppler or quantization errors, the SNR degradation factor defined in Eq. (8) is a function of the phase jitter in the subcarrier demodulation loop and the timing jitter in the symbol synchronization loop. Both jitter processes, ϕ and τ , are modeled as Gaussian random variables having zero mean and variance σ_ϕ^2 and σ_τ^2 , respectively.

According to Ref. 2, the variance of the phase error in the subcarrier demodulation loop at update instants is

$$\sigma_\phi^2 = \left(\frac{T_L B_{L1}}{4K} \right) \frac{\pi^2}{\left(\frac{E_s}{N_0} \right)^2} \left(1 + \frac{E_s}{N_0} \right) \quad (35)$$

Repeating the steps of Ref. 2, it can be shown that the variance of the timing error in the symbol synchronization loop at update instants is

$$\sigma_\tau^2 = \left(\frac{T_L B_{L2} a_2}{8 K a_1} \right) \frac{T_s^2}{\left(\frac{E_s}{N_0} \right)^2} \left[1 + 2 \left(\frac{E_s}{N_0} \right) (a_1 + a_2) \right] \quad (36)$$

where

B_{Lj} = one sided noise-equivalent bandwidth, $j = 1$ for subcarrier loop, $j = 2$ symbol synch loop

T_L = loop update time, assumed to be identical for both loops

K = number of symbols between updates

T_s = symbol time = $1/r$

E_s/N_0 = ratio of energy per symbol to noise spectral density

$$\triangleq R = \frac{N_s S}{2\sigma_n^2} \quad (37)$$

$a_1 = M/N_s$ = ratio of the width of the middle portion of a symbol to the total symbol length (typically 1/2)

$a_2 = L/N_s$ = ratio of the width of the transition portion of a symbol to the total symbol length (typically 1/4)

The expected value of d in Eq. (8) will be

$$\begin{aligned} d &= \frac{1}{\sqrt{2\pi} \sigma_\phi} \int_{-\infty}^{\infty} \left(1 - \frac{|\phi|}{\pi/2} \right)^2 \exp\left(-\frac{1}{2} \frac{\phi^2}{\sigma_\phi^2}\right) d\phi \\ &\times \frac{1}{\sqrt{2\pi} \sigma_\tau} \int_{-\infty}^{\infty} \left(1 - 2p_T \frac{|\tau|}{T_s} \right)^2 \exp\left(-\frac{1}{2} \frac{\tau^2}{\sigma_\tau^2}\right) d\tau \quad (38) \\ &= \left[1 - 4 \sqrt{\frac{2}{\pi}} \left(\frac{\sigma_\phi}{\pi} \right) + 4 \left(\frac{\sigma_\phi}{\pi} \right)^2 \right] \left[1 - 4 \sqrt{\frac{2}{\pi}} p_T \left(\frac{\sigma_\tau}{T_s} \right) \right. \\ &\quad \left. + 4p_T^2 \left(\frac{\sigma_\tau}{T_s} \right)^2 \right] \quad (39) \end{aligned}$$

In Appendix B two numerical examples are given for parameter values typical of the Voyager and Pioneer missions.

In general, the bias in $\overline{R^*}$ can be reduced by increasing n (number of symbols in the estimator). Of course, we can

improve our knowledge of R if we compensate for the effects of the bias and the degradation factor in Eq. (28), i.e., we may assume that the actual input SNR is

$$\tilde{R} = \frac{\langle R^* \rangle}{\tilde{d} \left(1 + \frac{2}{n} \right) + \frac{1}{n}} \quad (40)$$

where $\langle R^* \rangle$ is the average value of many R_i^* and \tilde{d} is our estimate of d .

IV. Conclusions

In this article the expected value and the variance of the SSME SNR estimator was derived. This estimator was shown to be biased and consistent.

Figures 2 and 3 illustrate the numerical results for the Voyager and Pioneer missions. At high signal SNR, the positive bias of the estimator dominates over the degradation effect due to phase jitter in the tracking loops. At low SNR, it is the other way around. Figure 4 is for the ideal case when there is no jitter in the tracking loops ($d = 1$).

Acknowledgment

The authors wish to acknowledge Larry D. Howard of the Radio Frequency and Microwave Subsystem Section for his suggestion of the split-symbol correlator SNR detector configuration and an analysis that laid the groundwork for our analysis. (Howard, L., "Split-Symbol Correlator Signal-to-Noise Ratio Detector" JPL internal document, Feb 22, 1982.)

References

1. Simon, M. K., and Mileant, A., *Performance Analysis of the DSN Baseband Assembly (BBA) Real-Time Combiner (RTC)*, JPL Publication 84-94, Rev. 1, Jet Propulsion Laboratory, Pasadena, Calif., May 1, 1985.
2. "Performance of the DSA's Subcarrier Demodulation Digital Loop," *TDA Progress Report 42-80*, pp. 180-194, Jet Propulsion Laboratory, Pasadena, Calif., Feb. 15, 1985.
3. Kindal, M. G., and Stuart, A., *The Advanced Theory of Statistics*, Vol. I, Hafner Publishing Co., N.Y., 1973.

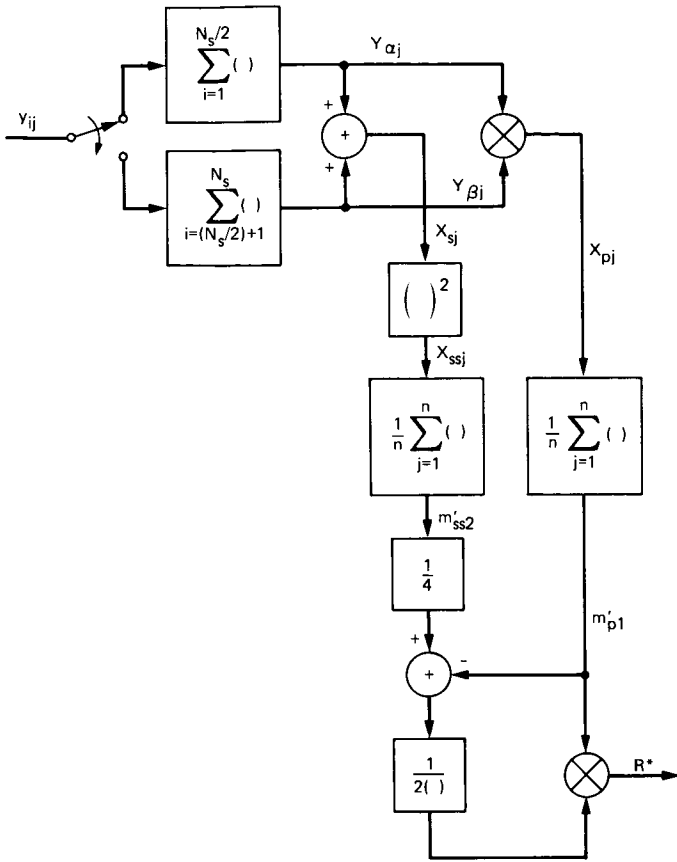


Fig. 1. Split symbol SNR estimator algorithm

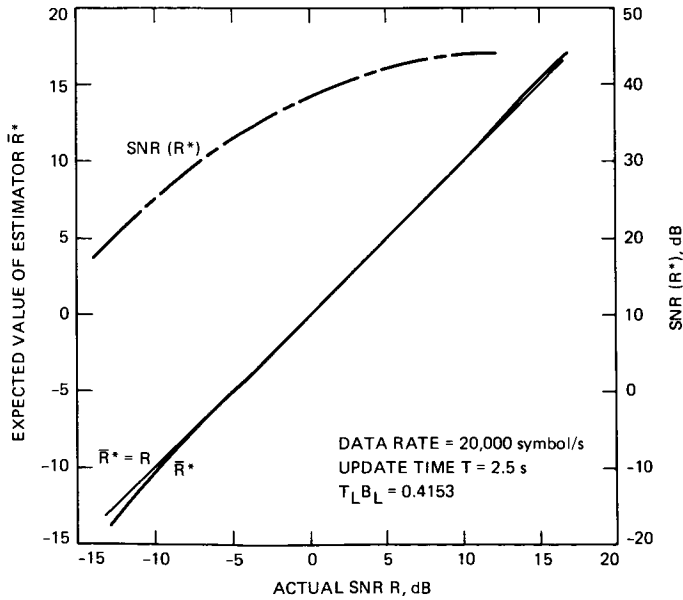


Fig. 2. Mean value and SNR of SNR estimator vs actual SNR: Voyager mission

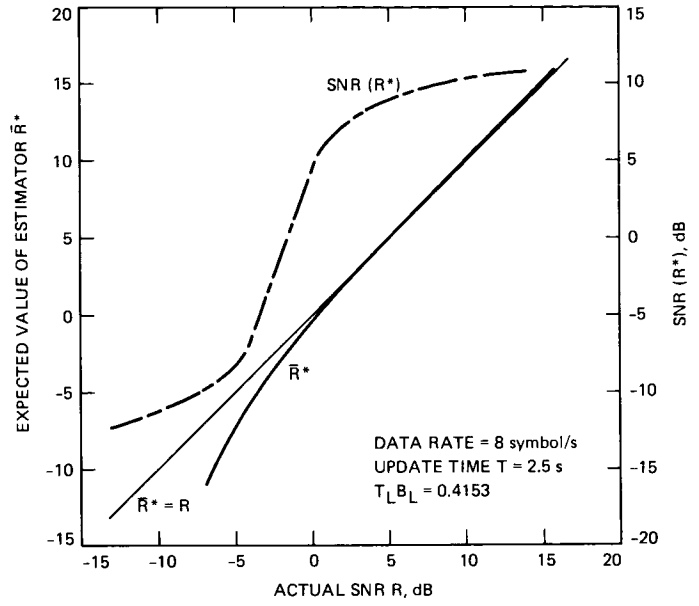


Fig. 3. Mean value and SNR of SNR estimator vs actual SNR: Pioneer mission

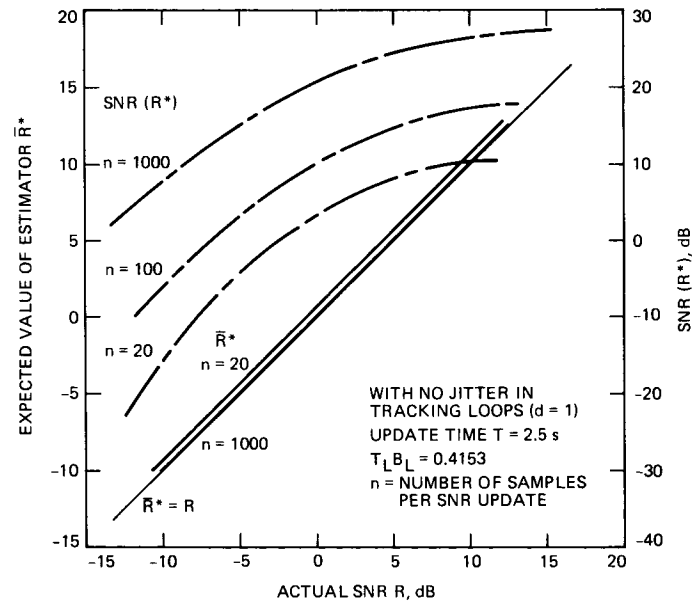


Fig. 4. Mean value and SNR of SNR estimator vs actual SNR: general

Appendix A

Gaussian Moments

1. Relation Between Statistical and Probabilistic Moments

Given a random variable x with Gaussian pdf $G(\mu, \sigma^2)$ and defining the r th moment as

$$\mu'_r = E \{x^r\} \quad (\text{A-1})$$

the first four *probabilistic* moments of x will be

$$\begin{aligned} \mu'_1 &= \mu \\ \mu'_2 &= \mu^2 + \sigma^2 \\ \mu'_3 &= 3\sigma^2\mu + \mu^3 \\ \mu'_4 &= 3\sigma^4 + 6\sigma^2\mu^2 + \mu^4 \end{aligned} \quad (\text{A-2})$$

Defining m'_r as the r th *statistical* moment of a random variable

$$m'_r = \frac{1}{n} \sum_{j=1}^n (x_j)^r \quad (\text{A-3})$$

and the variance of m'_r as

$$\text{var} (m'_r) = E \left\{ \frac{1}{n} \sum_{j=1}^n (x_j)^r - \mu'_r \right\}^2 \quad (\text{A-4})$$

Chapter 10 of Ref. 3 shows that

$$E \{m'_r\} = \mu'_r \quad (\text{A-5})$$

and

$$\text{var} (m'_r) = \frac{1}{n} [\mu'_{2r} - (\mu'_r)^2] \quad (\text{A-6})$$

This is an exact result.

Given a function g of K random variables x_k ,

$$g(x) = g(x_1, x_2, \dots, x_K) \quad (\text{A-7})$$

with means

$$\begin{aligned} E \{x_K\} &= \theta_K \\ \theta &\triangleq \theta_1, \theta_2, \dots, \theta_K \end{aligned} \quad (\text{A-8})$$

it can be shown (Prob 10.17, Ref. 3) that

$$\begin{aligned} E \{g(x)\} &= g(\theta) + \frac{1}{2} \sum_{k=1}^K \frac{\partial^2 g(x)}{\partial x_k^2} \bigg|_{x=\theta} \text{var} (x_k) \\ &+ \frac{1}{2} \sum_{i=1}^K \sum_{j=1}^K \frac{\partial g(x)}{\partial x_i} \frac{\partial g(x)}{\partial x_j} \bigg|_{x=\theta} \text{cov} (x_i, x_j) + \dots \end{aligned} \quad (\text{A-9})$$

The variance of $g(x)$ will be (Eq. (10.12) of Ref. 3)

$$\begin{aligned} \text{var} \{g(x)\} &= \sum_{k=1}^K \left[\frac{\partial g(x)}{\partial x_k} \right]^2 \bigg|_{x=\theta} \text{var} (x_k) \\ &+ \sum_{i=1}^K \sum_{j=1}^K \frac{\partial g(x)}{\partial x_i} \frac{\partial g(x)}{\partial x_j} \bigg|_{x=\theta} \text{cov} (x_i, x_j) + \dots \end{aligned} \quad (\text{A-10})$$

2. Evaluation of the Derivatives of the Estimator

In the SSME algorithm R^* is computed from m'_p and m'_{ss} , namely,

$$R^* = \frac{m'_p}{2 \left(\frac{1}{4} m'_{ss} - m'_p \right)} \quad (\text{A-11})$$

It can be shown that

$$E \{m'_p\} = \overline{m'_p} = \frac{1}{4} N_s^2 S_d \quad (\text{A-12})$$

and

$$E \{m'_{ss}\} = \overline{m'_{ss}} = N_s^2 S_d + N_s \sigma_n^2 \quad (\text{A-13})$$

Let

$$\hat{R} \triangleq \frac{E \{m'_p\}}{2 E \left\{ \frac{1}{4} m'_{ss} - m'_p \right\}} = \frac{N_s Sd}{2\sigma_n^2} \quad (\text{A-14})$$

$$\left. \frac{\partial R^*}{\partial m'_{ss}} \right|_{\overline{m'_p}, \overline{m'_{ss}}} = - \frac{1}{\sigma_n^2 N_s} \hat{R} \quad (\text{A-17})$$

The following derivatives of the estimator R^* are evaluated:

$$\left. \frac{\partial R^*}{\partial m'_p} \right|_{\overline{m'_p}, \overline{m'_{ss}}} = \frac{2}{\sigma_n^2 N_s} (1 + 2\hat{R}) \quad (\text{A-15})$$

$$\left. \frac{\partial^2 R^*}{\partial m'^2_{ss}} \right|_{\overline{m'_p}, \overline{m'_{ss}}} = 2 \left(\frac{1}{\sigma_n^2 N_s} \right)^2 \hat{R} \quad (\text{A-18})$$

$$\left. \frac{\partial^2 R^*}{\partial m'^2_p} \right|_{\overline{m'_p}, \overline{m'_{ss}}} = \left(\frac{4}{\sigma_n^2 N_s} \right)^2 (1 + 2\hat{R}) \quad (\text{A-16})$$

$$\left. \frac{\partial^2 R^*}{\partial m'_p \partial m'_{ss}} \right|_{\overline{m'_p}, \overline{m'_{ss}}} = -2 \left(\frac{1}{\sigma_n^2 N_s} \right)^2 (1 + 4\hat{R}) \quad (\text{A-19})$$

Appendix B

Constants Used to Derive Figs. 2-4

In order to illustrate the performance of the SSME estimator, two cases are considered.

(1) Voyager

$$\text{Data rate } r = 20,000 \text{ symbols/second}$$

$$\text{Update time } T_L = 2.5 \text{ seconds}$$

$$K = n = 2.5 \times 20,000 \text{ symbols/loop update}$$

$$T_L B_L = 0.4153 \text{ (from Table 1, Ref. 1 for both tracking loops)}$$

$$\text{Noise bandwidth } B_n = 3.75 \text{ MHz}$$

(2) Pioneer

$$r = 8 \text{ symbols/second}$$

$$T_L = 2.5 \text{ seconds}$$

$$K = n = 2.5 \times 8 \text{ symbols/loop update}$$

$$T_L B_L = 0.4153 \text{ for both tracking loops}$$

$$B_n = 135 \text{ kHz}$$

The performance of R^* for the Magellan mission will be better than for Voyager.

Using Eqs. (35), (36), (39), (28), (29), (31), and (32), Figs. 2 and 3 are obtained.

N86 - 28287 ↓

D12-32
129

13156

The New 34-Meter Antenna

M. F. Pompa
TDA Engineering

is described.

This article describes the new 34-m high efficiency Azimuth - Elevation antenna configuration, including its features, dynamic characteristics and performance at 8.4-GHz frequencies. The current-technology features of this antenna produce a highly reliable configuration by incorporation of a main wheel and track azimuth support, central pintle pivot bearing, close tolerance surface panels and all-welded construction. Also described are basic drive controls that, as slaved to three automatic microprocessors, provide accurate and safe control of the antenna's steering tasks.

At this time antenna installations have been completed at Goldstone and Canberra and have operationally supported the Voyager - Uranus encounter. A third installation is being constructed currently in Madrid and is scheduled for completion in late 1986.

I. Introduction

The addition of the 34-m Azimuth - Elevation high efficiency antennas was undertaken as a result of early Mark IVA Project studies directed at providing increased DSN aperture capacity to support the Voyager - Uranus encounter. Furthermore, the presence of these antennas - one each at the Deep Space Communications Complexes (DSCCs) located at Goldstone, Canberra and Madrid - would provide support for the increased quantity of high priority missions in the late 1980's to early 1990's period. Imaging data, 8.4-GHz telemetry and science data are the primary data yields sought at the Voyager - Uranus encounter and beyond, and can be expected only with the 34-m Az - El antennas addition, when arrayed with the existing 64-m antenna.

A principal contending option for providing the netwide added aperture was the collocation of existing 26-m STDN antennas, including their enlargement to 34 m, a project similar to the earlier S - X (26-m to 34-m) upgrade project. Final cost and performance comparisons favored the new 34-m Az - El antenna, and implementation of this configuration was initiated in April 1982.

II. General Features and Performance Capacities

The 34-m diameter, Az - El configuration is a quasiparaboloid surface of revolution whose RF reflective surface has a focal length-to-diameter ratio of approximately 0.325, and a

cassegrain RF optics path consisting of a quadripod structure, adjustable subreflector, and an interchangeable feedcone similar to those used on other DSN antennas. The antenna is steerable in azimuth and elevation with intersecting axes. These highly recognizable features are shown in Fig. 1.

The antenna structure is designed to maximize stiffness, minimize surface distortions and provide accessibility for maintenance. In order to maximize traction and to minimize wheel loadings, a four wheel azimuth turntable with a square platform is used. This azimuth turntable has self-aligning wheels and a machined track to minimize stress concentrations.

The reflector structure is a triangulated truss system constructed of standard angles and tubes. In order to minimize load induced surface distortions, the reflector is attached to the pedestal via a trussed elevation wheel structure which provides eight equally still mounting points to the reflector and isolates the counterweight loads from the reflector.

Table 1 is a summary of the antenna specifications and characteristics of the 34-m AZ - El configuration.

III. Physical Description

A. Azimuth—Elevation Structure and Drive Equipment

1. Foundation and alidade structure.

a. Basic Support. The fundamental support for the entire antenna is the azimuth rail and ring resting on an earth and concrete foundation with spread footings. (See Figs. 2 and 3.) Radial rigidity for the ring structure is provided by four (4) radial beams tied in at the center pintle bearing support. Minimum compressive strength of the concrete in the ring beam is 34,475 kPa (5000 psi).

b. Alidade structure. The alidade structure illustrated in Fig. 4 supports all components above the four (4) azimuth wheels. It is a triangulated structure with a square base interfacing with the azimuth wheels over the track and the center pintle bearing. The square base and lateral plane of the alidade are braced for structural stabilization.

The bracing in the base frame includes radial members framed into the center pintle bearing so that the alidade transfers all loads to the four azimuth wheels and pintle bearing. A plane of bracing is also included near the elevation drives (top plane) to stabilize the working points of the alidade side frames.

The alidade is constructed of standard wide flange structural beams. Standard bolted field flange splices are used at

installation, after which the field joints are welded to prevent any joint slippage. Wide flange sections are used to provide a good stiffness to weight ratio for bending loads, which is extremely important in the base frame that interfaces with the four azimuth wheels and pintle bearing. Wide flange sections also are not susceptible to the internal corrosion problem encountered in the tubular sections.

The top plane of the alidade structure serves to mount the two elevation bearings, elevation wheel and drive motors. These bearings support and actuate the entire tipping structure, i.e., main reflector, quadripod, subreflector, counterweights, etc. These are discussed further in Section III.A.2.

c. Azimuth radial bearing. The azimuth radial pintle bearing, illustrated in Fig. 5, is a single-row ball, four point contact bearing equipped with replaceable split grease seals and lubrication ports for greasing the rolling elements. It is the main stabilizing point of the antenna's rotational motion.

The inner ring of the radial pintle bearing is bolted to an adapter ring plate which is securely fastened to the concrete center pedestal. The outer ring of the pintle bearing has six flexure plate assemblies bolted to it which are also bolted to the diagonal members of the alidade base frame. The flexure plate assemblies transmit lateral forces from the alidade base frame to the radial bearing, since the flexure plates are relatively stiff when loaded radially. Small vertical thrust loads are transmitted to the radial bearing by virtue of the flexibility of the flexure plate assemblies. The azimuth radial bearing has sufficient capacity to carry radial loads induced by misaligned azimuth wheels in addition to radial loads induced by winds.

The azimuth radial bearing has an outside diameter of 240 cm (94.50 in.) and an inside diameter of 200 cm (78.88 in.).

d. Azimuth bearing track. Vertical or thrust loading is carried by the azimuth bearing which consists of a self aligning wheel and track configuration.

The mean radius of the azimuth bearing track is 982 ± 0.635 cm (386.7 ± 0.25 in.). The annular ring segments are 12.2 cm (4.80 in.) thick and 36.6 cm (14.40 in.) wide.

The azimuth bearing track shown in Fig. 6 consists of an annular ring made of low carbon steel and formed by 16 segments leveled, grouted into place, and capped with hardened wear strips with mitered ends.

After the ring segments are aligned and held in position, drypack grout is placed between the ring elements and foundation. The wear strips are 3.05 cm (1.20 in.) thick and 27.94 cm

(11.0 in.) wide, and the edges and ends of the wear strips and ring segments are sealed with RTV silicone for corrosion protection.

e. Azimuth bearing wheel assembly. Each of the four corners of the alidade base structure is supported by a wheel assembly. The two wheel assemblies nearest the reflector (when the reflector is in its near-horizon position) are the powered (driving) assemblies, as shown in Fig. 7. Each wheel assembly consists of a wheel and shaft supported by two spherical roller bearings contained within a wheel housing.

The wheels are 60 cm (23.62 in.) in diameter and 14.4 cm (5.67 in.) wide with a tapered wheel rim in order to roll true on the circular track. The wheel is shrunk fit on a wheel axle and mounted in a housing which is supported by two pairs of flexure links, thus allowing full width alignment of the wheel on the track.

Provision is made for jacking each corner of the alidade base frame for relieving the loads on the wheel assembly attachment bolts for wheel alignment.

f. Azimuth drive assemblies. Each of the two powered wheel assemblies is driven by two 3.2 kW (5 hp) direct current (DC) drive motors, also shown in Fig. 7. The drive axle ends are mounted to the output shaft of a 649:1 ratio speed reducer which is flange mounted to the wheel assembly housing.

A double C-face disc brake coupler is mounted to each DC drive motor and to the input shaft of each speed reducer. Each DC drive motor is equipped with a tachometer.

The total ratio from the DC drive motor output shaft to the antenna axis is 21,250:1, resulting in an antenna azimuth speed of 0.49 deg/s when the DC drive motor is operating at 1750 rpm.

2. Elevated and tipping structure assemblies.

a. Elevation bearing assembly. The elevation axis bearings consist of two spherical roller bearings which are mounted in housings bolted to the top of the alidade structure. The elevation shafts are fixed to the reflector back-up structure and the bearings are mounted on the shafts as shown in Fig. 8.

Split grease seals with seal retainers are mounted in the bearing housing on each side of the bearing. The seals can be removed and replaced while the bearing and housing are in place by using standard hydraulic pumps and gear pullers. At the outer end of each elevation shaft, flexible coupling connects the angle encoders in such a way that the encoder

mount stiffness is consistent with the encoder accuracy requirements.

b. Elevation wheel and counterweights. The elevation wheel structure is a welded plate girder braced by a trussed framework as shown in Fig. 8. It is especially configured to provide uniform support for the reflector at all orientations. The elevation wheel structure is a steel space frame that supports the primary reflector structure, the elevation counterweights, the drive bullgear, and the elevation drive. It is supported by the elevation bearing assembly. The back rim of the elevation wheel consists of a steel flange for supporting the elevation bull gear. This gear is shimmed against the wheel to adjust for radial run-out and for lateral position. The bull gear is bolted to the wheel to prevent tangential slippage during operation.

c. Elevation drive carriage. The elevation drive carriage consists of a housing which supports two drive pinions arranged with their axes parallel and spaced circumferentially apart, meshing with the elevation bullgear. The drive carriage is supported by two tangent links connected to alidade joints. Each pinion is driven by a Sumitomo Cyclo Drive Model 19045, whose speed reducer ratio is 385:1 and whose output shaft is keyed to the pinion. The two reducers are mounted on opposite sides of the bullgear to provide a balanced elevation drive carriage. A fail-safe brake is mounted on the input side of each reducer and two 6.4-kW (10-hp) DC drive motors with tachometers are mounted to each brake. Air blowers are provided so that cooling air is ducted over each drive motor. The total ratio of the elevation drives is 21,988:1, which corresponds to a slewing speed of 0.48 deg/s.

d. Elevation gear. The elevation bullgear is composed of gear segments which are mounted on the elevation wheel structure. The elevation gear is formed to provide a surface for back-up rollers which is concentric to the pitch diameter of the gear teeth, insuring proper mesh of the gear and pinions. The elevation gear has a pitch radius of 653 cm (257 in.) and a diametral pitch of 2.

e. Primary reflector structure. The reflector structure supports the aluminum reflector panels' quadripod and sub-reflector. The reflector is supported from the elevation axis by the elevation wheel structure. This structure consists of twenty-four radial trusses extending out from a welded center hub. The reflector trusses and interconnecting chords are fabricated of welded square steel tube sections. The resulting space frame acts to distribute asymmetric wind pressure loads and provide torsional resistance; it is illustrated atop the alidade structure in Figs. 9 and 10.

The primary reflector with its total support structure and mechanical systems has a natural frequency of 1.5 Hz (locked

rotor system), while the quadripod subreflector subset has a natural frequency of 1.0 Hz.

f. Reflector panels and assembly. The main reflector, as configured by the contiguous positioning of individual panels, presents a homologous paraboloid for improved microwave efficiency. The individual panels are manufactured from 6061-T6 aluminum and have a skin thickness of 1.78 mm (0.070 in.). All surface panels inside the 26-m (85-ft) diameter are solid surfaces; the panels outside this diameter have a perforated surface with a porosity of 40% provided by 3.175-mm (0.125-in.) holes in a diamond pattern. The solid surface panels can support a 137-kg (300-lb) shoe load with no permanent deformation; similarly, the perforated panels can support a 91-kg (200-lb) shoe load on any point of the surface. The panels are manufactured with a ± 0.305 mm (± 0.012 in.) surface tolerance. Details of the assembled panel array are shown in Fig. 11, and a typical panel sector is shown in Fig. 12.

g. Quadripod - apex structure. The quadripod - apex structure serves to support the 381 cm (150 in.) diameter subreflector, and its 3-axis drive system with its associated support structure. Aperture blockage is 5%. The quadripod legs have a trapezoidal cross-section, consisting of square tubing in the corners with square tubing or plate webbing as shown in Fig. 13. Two legs enclose a 12.7-cm (5-in.) diameter conduit pipe that houses the control cables to the subreflector drive system at the apex.

h. Subreflector. The aluminum subreflector is fabricated out of six individual panels, each being supported from a trussed backup structure in the assembled configuration. All surface gaps between individual panels and between the panels and the center tooling plug are covered with one layer of Kapton adhesive tape, overlaid by one layer of aluminum adhesive tape to form a continuous conducting surface. A center hub is provided for mounting a rotating sweep template to verify the surface accuracy of 0.305 mm (0.012 in.) RMS.

The assembled and mounted subreflector assembly is shown in Fig. 1, atop the quadripod structure.

i. Subreflection positioning mechanism. The subreflector position mechanism serves to compensate and minimize systematic loss of gain due to gravity deformation of the antenna primary structure, quadripod structure and primary reflector surface when operating at the various elevation positions. The subreflector positioner coordinate system is as shown below:

+Z axis, away from primary reflector

+X axis, to right (when looking in +Z axis direction)

+Y axis, up (when looking in +Z axis direction and primary reflector is at zenith)

The positioner can adjust the central coordinator points of the subreflector from 0 to ± 7.1 cm (± 2.8 in.) along each of the 3 orthogonal axes mentioned above.

IV. Antenna Drive Control Command and Monitoring

The antenna control as required to meet the Mark IVA reconfiguration is accomplished through the use of a system of interconnecting microprocessor computers. At one end of the controls network are the Antenna Drive Assembly (ADA) microprocessors located on the antenna to provide antenna drive actuator signals (through servo control loops), monitor equipment status, and provide limit and fault energization. At the other end are two Modcomp computers comprising prime and backup Antenna Pointing Assembly (APA) processors located in the Signal Processing Center (SPC). The APA stores data for the pointing process, e.g., it stores trajectory prediction points profiles, systematic error correction tables, transformation of coordinates, and monitor data back to the Area Routing Assembly (ARA), MDA, and NTK. One primary computer connection exists between the APA and ADA which is embodied in the Antenna Control Subassembly (ACS). In effect the ACS, located on the antenna, is an extension of the APA, and operates to store predict tables, perform interpolation between predict points, combine position commands to obtain a final pointing position, and provide antenna and subreflector positions feedback.

A detailed treatment of the APA and ACS will be covered in a future paper. In this current article the discussion will be on the drive and control assemblies and microprocessors. Figure 14 shows a block diagram of the major control assemblies' microprocessors, including simplified interconnecting routes and locations. These assemblies are required for complete antenna control and pointing. To the left are the pointing process computers and to the right are the front end area (FEA-Antenna) microprocessors and drive controls. The FEA mounted assemblies, incorporating the Antenna Servo Controller (ASC), the Antenna Control and Monitor (ACM), Subreflector Controller (SRC) and servo control chassis, will be discussed further as to purpose, function and performance.

A. Basic Drive Controls and Chassis

As previously described, electric motors and actuators, acting through appropriate gearing, provide the basic motion to the antenna about the azimuth and elevation axis and to the subreflector. These prime movers are augmented and modulated by the use of limit switches, relays, brakes, field modu-

lators, wave shapers, sensors, etc. which may be manually energized to provide the desired torque and counter torque. The switching and interfacing for all these devices takes place at the Drive Control Cabinet, Subreflector Drive Cabinet and Field Interface Module (FIM). From these modules commands and status are intercommunicated with the ASC, ACM and SRC microprocessors which provide the signal processing for automated servo control of the antenna. Therefore signal voltages are generated from the various input error signals, or manual slew commands, which flow to the ASC and return to the Drive Cabinet for amplification and gain processing and thence to the drive motors.

The current (drive motor armature) and velocity servo loops are closed in the Drive Control Cabinet.

B. ASC

The ASC accepts position commands from the ACS and closes the position servo loop for the main driving assemblies. It also issues rate and limit commands, and provides antenna monitoring functions for status determination as required for appropriate operation and personnel safety.

The ASC chassis contains an Intel MULTIBUS based microprocessor and the custom interface electronics required to interface the chassis to the antenna mounted devices. The microprocessor consists of four standard MULTIBUS compatible microprocessor boards together with the card cage and the motherboard.

A large-error algorithm and a small-error one are used for rate command calculation. The large-error algorithm is utilized when the calculated rate command error is greater than 0.05 deg/s and the position error is greater than 0.03 deg (nominal values); the small-error algorithm is used at values less than those given for the large-error one. After the rate command is calculated by one of these algorithms, it is then processed by the rate and acceleration limiter section.

Whichever algorithm is currently being used, the current antenna position is always monitored by strobing the encoder of an axis every 50 ms. Validity of the data is verified by the status provided by the encoder board itself. Under normal circumstances, the converted encoder position is reported to the ACS controller and used as input to the position loop.

Commanded positions are received by the ASC controller in one of the following forms: MOVE commands from the ACS assembly, STOW, or STOP. The primary purpose of the commands is to generate a new commanded position. In the case of the MOVE commands from the ACS assembly which are used only during tracking conditions, the commanded posi-

tion dictated by the ACS is interpolated over twenty 50-ms periods.

C. Antenna Subreflector Controller (SRC)

The subreflector is positioned in its three orthogonal axes by a system of motor driven ballscrew jacks and linkages. In normal operation the motors are energized to correct the subreflector position or magnetically detented to hold the subreflector against gravity or wind loads. The SRC operates to achieve the necessary motion and position control of the subreflector.

The SRC accepts position commands from the ASC and closes the position loop for the drive assembly. The ASC also provides antenna position data to the SRC. Limit switches, brakes and a self-diagnostic function are also monitored in the SRC.

The SRC controller is located in a single chassis assembly designated 3763/ANT-310 and containing the following four circuit boards:

- (1) 16-bit CPU board (A1A1)
- (2) 4-channel intelligent communication board (A1A3)
- (3) PROM board (A1A4)
- (4) Digital input/output board (A2A1)

Each of these circuit boards communicates with the others through the Intel Multibus.

D. Antenna Control and Monitoring (ACM)

The ACM program has three major functions:

- (1) Configuration and Control
- (2) Monitoring and Alarm Reporting
- (3) Data Collection

On the 34-m Az – El antennas, there are no operator-selectable configuration parameters except enabling/disabling of alarm condition reporting and entering the criticality of a track. The ACM starts up or shuts down the drive cabinet electronics, motor controllers, and power supplies on command. Such startup and shutdown commands can be entered from the local terminal, or from a terminal connected to any upstream computer. They are also generated automatically by the APA.

Whenever the antenna is up and running, the ACM monitors various sensors to determine whether the antenna is operating properly. If any discrepancies are detected, the ACM will

generate appropriate event messages designed to ensure the safety and integrity of the antenna and personnel.

The ACM constantly collects analog and digital data from the Field Interface Module (FIM) and periodically sends this information upstream for analysis or logging. In addition, monitor point values may be requested by name.

The ACM physical makeup consists of the following equipment:

- (1) A standard chassis with cardcage and power supply
- (2) iSBC-86/14 master CPU card
- (3) iSBC-337 Floating Point Arithmetic piggyback module
- (4) Two (2) iSBC-464 PROM expansion cards
- (5) MCM-8086 core card

V. Microwave Testing and Performance

Gain values were measured during dedicated engineering tests by scanning of various radio sources. Antenna focusing was also determined while stepping the subreflector through the range of its excursions. Operating temperatures at 8.4 GHz were measured as a function of elevation angle and considering the effects of atmospheric loss, spill-over and stellar body contributions.

A system temperature of 18.7 deg K at 90 deg was measured. The antenna beamwidth at half-power points was found

to be 0.067 deg by the drift curve method. In combination with the improved main reflector and subreflector surfaces, the microwave performance of these antennas ranges from 68% to 70% efficiency (67.9 and 68.2 dB gain, respectively). This is a clear increase over the 34-m HA – Dec standard antennas with indicated efficiencies of 49% to 53% (66 to 67.2 dB gain, respectively).

VI. Epilogue

At this time the 34-m Az – El antennas are fully operational at Goldstone and Canberra, and participated in tracking assignments of the highly significant Voyager – Uranus encounter.

They are presently operating in a receive-only mode, at 2 or 8.4 GHz frequencies. At Madrid, the erection and installation of the 34-m Az – El configuration is nearing the mid-point of construction completion. During the remaining installation activity, the configuration will receive a new 8.4-GHz exciter and 20 kW transmitter, and be ready for operational use by April 1987, to support the Galileo and Magellan missions. This added transmit capability is planned for subsequent installation at Canberra and Goldstone in 1987 and 1988.

These highly efficient, highly reliable antennas represent full use of current technology and add significantly to the expected successful deep space encounters during the ensuing decades.

Table 1. Antenna specifications and characteristics

Item	Performance
Antenna Size and Type	34-m, Azimuth – Elevation, Wheel Track
Antenna Weight on Az Axis	345,455 kg (760,000 lb)
Antenna Weight on El Axis	181,818 kg (400,000 lb)
RSS Pointing Error:	
Gravity Plus 30 mph Winds	0.017 deg
Compensated Plus 10 mph	0.004 deg
Compensated Plus 30 mph	0.010 deg
RMS Surface Accuracy:	
Gravity	0.6604 mm (0.026 in.)
Gravity Plus 10 mph Winds	0.635 mm (0.025 in.)
Gravity Plus 30 mph Winds	0.764 mm (0.030 in.)
Locked Rotor Frequency	1.8 Hz
Stability Ratio	1.7 Against Overturning
Balance Structure	Within 6929 m • kg (50,000 ft • lb)
Quadripod Frequency	1.0 Hz
Panel Accuracy	252 0.3049-mm (0.012-in.) RMS Solid Surface Panels to 26-m Diameter. 96 Porous (40% Porosity) Panels to 34-m Diameter.
Panel Strength	136 kg (300 lb) Shoe – Solid Panels 91 kg (200 lb) Shoe – Porous Panels
Aperture Blockage	Maximum of 5%
Subreflector Positioner	2-Axis Automatic Plus 3-Axis Mechanized
Subreflector	Surface Axes Coincide With Mirror Within 10 s Accuracy to Be Within 0.1274 mm (0.005 in.) RMS
Axis Rates	Slew – 0.8 deg/s Track – 0.4 deg/s
Environment	Operational – To 72 kmph (45 mph) Drive to Stow – 80 kmph (50 mph) Hold Any Position – 112 kmph (70 mph) Survive Stowed – 160 kmph (100 mph)
Encoders	Resolution – 0.000343 deg Static Accuracy – 0.00275 deg Repeatability – 0.000343 deg Stability – 0.000343 deg
Loop Closure	0.000343 deg
Overshoot	Zero deg for Step Commands of ± 0.00417 deg
Position Loop Bandwidth	0.25 Hz
Antenna Frequency	8.4 GHz
Antenna Gain	67.9 dB to 68.2 dB
Antenna Temperature	18 deg K at Zenith, 23 deg K at Horizon
Cost	About \$4,800,000 (1986 US Dollars)
Fire Protection	Automatic Halon Suppression System on Antenna Building and Feed Cone. Dry Standpipe on Antenna. Sprinklers in Cable Wrap Up.
Heating, Ventilation and Air Conditioning	Automatic Controlled System with Economizer, Can Be Remotely Controlled. Energy Efficient Motors Used.

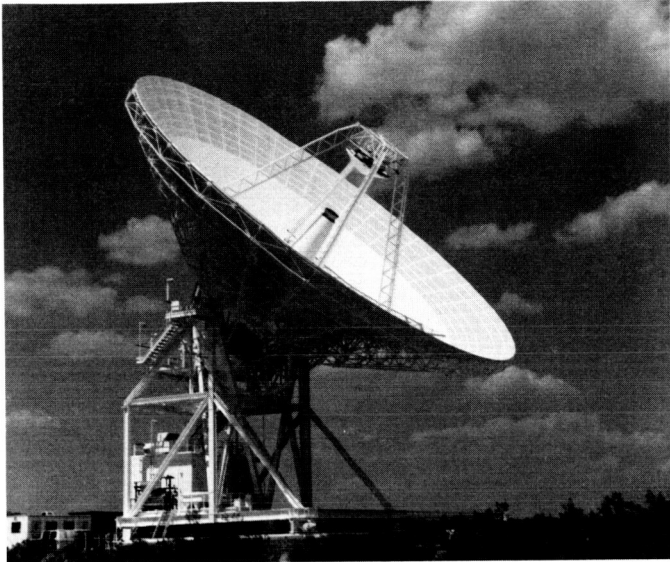


Fig. 1. 34-m Az—El antenna, DSS 15



Fig. 3. Track foundation and runner support

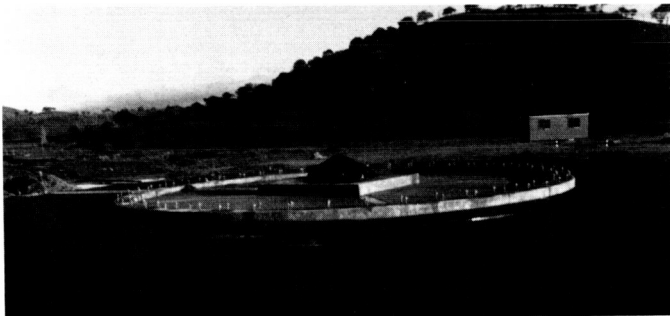


Fig. 2. Foundation, 34-m Az—El antenna, DSS 45

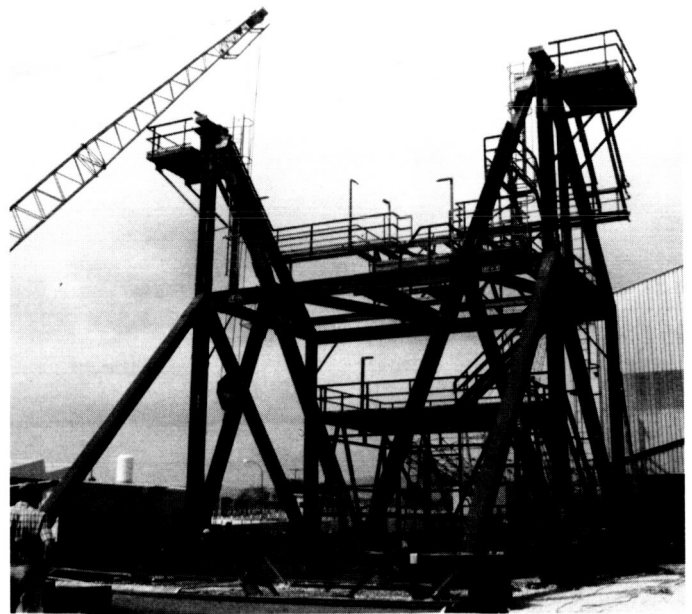


Fig. 4. Alidade structure assembly fit-check, DSS 65

ORIGINAL PAGE IS
OF POOR QUALITY

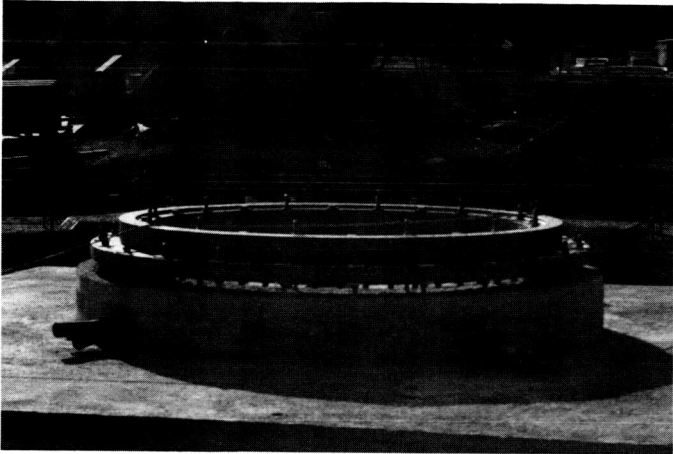


Fig. 5. Pintle bearing and support, DSS 65

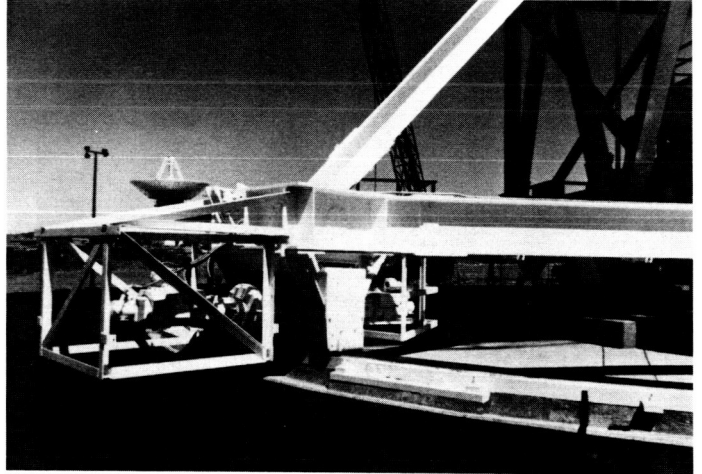


Fig. 7. Azimuth wheel and drive motors, DSS 15



Fig. 6. Track and support runner, DSS 15



Fig. 8. Tipping structure support and elevation bearing

ORIGINAL PAGE IS
OF POOR QUALITY

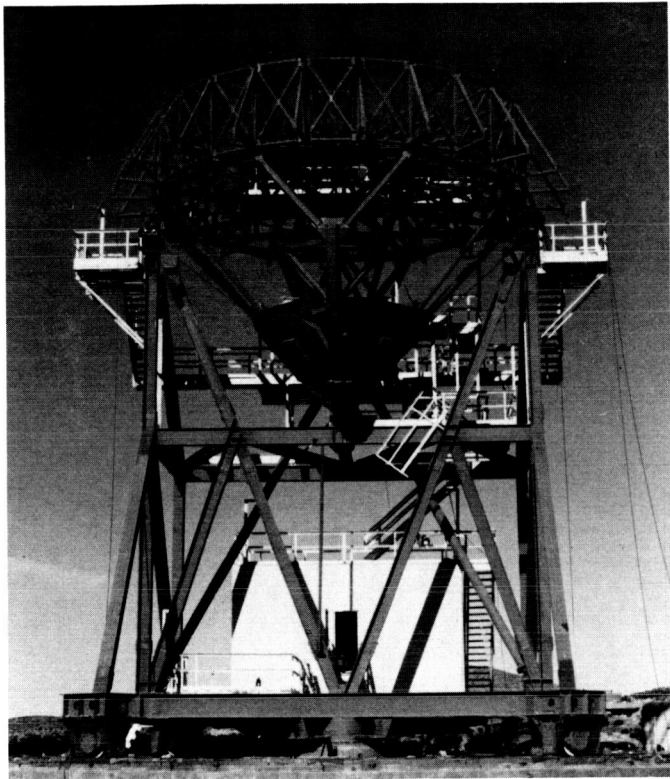


Fig. 9. Main reflector support structure, DSS 15

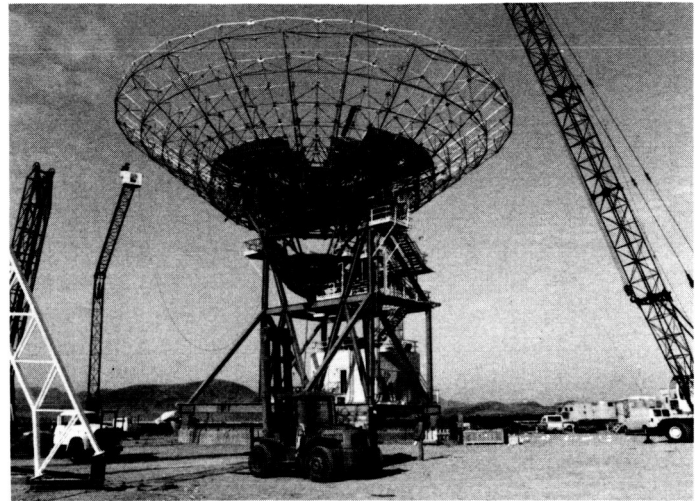


Fig. 10. Reflector and panel support, DSS 15

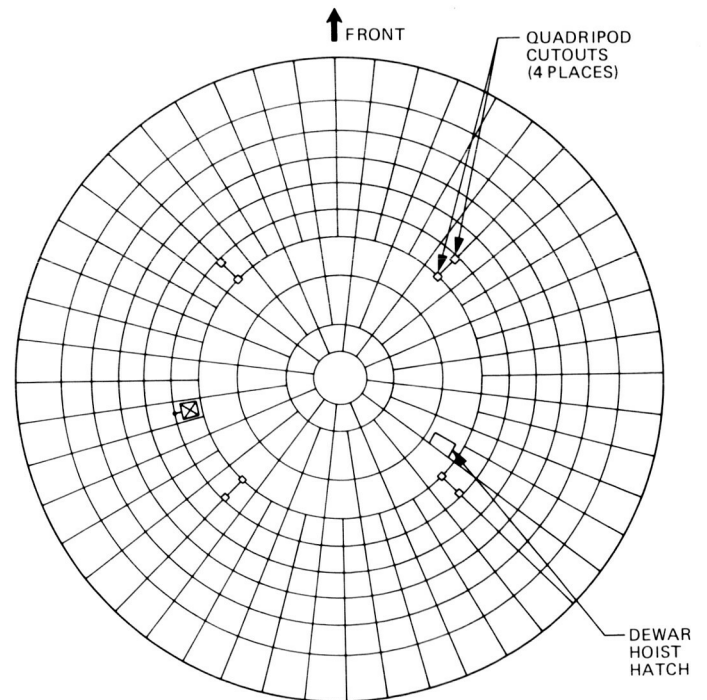


Fig. 11. Reflector panel assembly, from zenith down, DSS 15

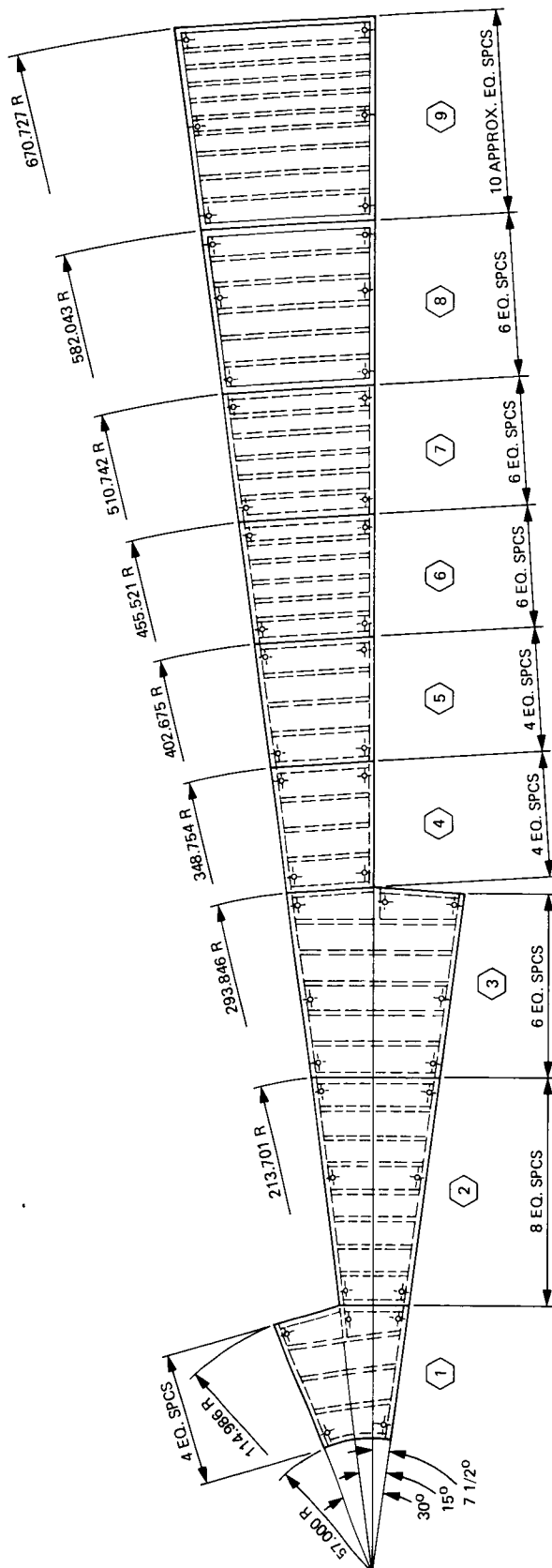


Fig. 12. Typical reflector panel sector, DSS 15

ORIGINAL PAGE IS
OF POOR QUALITY



Fig. 13. Quadripod structure, DSS 15

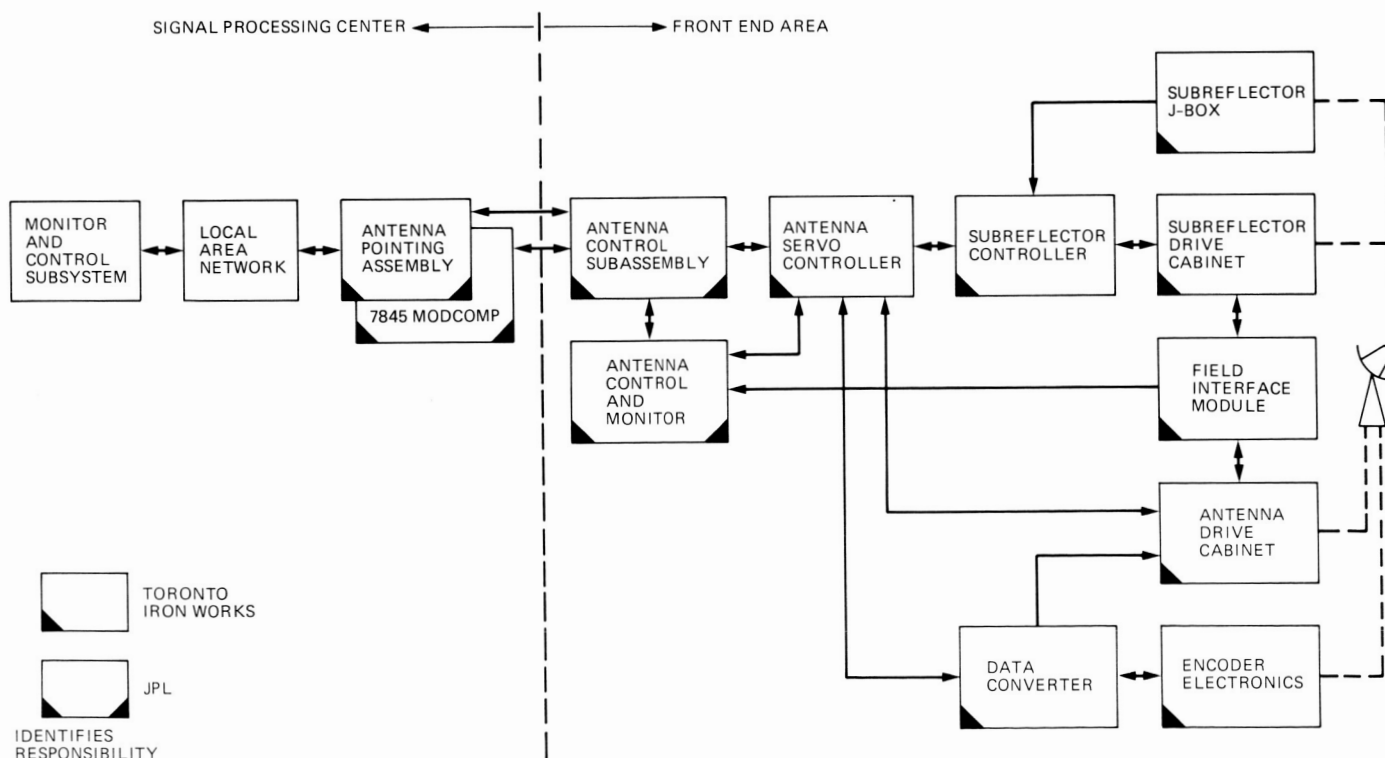


Fig. 14. Block diagram of the antenna control assembly

N86 - 28288

D13-17
78

13157

The Deep Space Network Tracking System, Mark IV-A, 1986

J. A. Wackley

Telecommunications and Data Acquisition Engineering

The DSN Tracking System provides highly precise measurements of spacecraft Doppler and range. It was recently extensively modified as part of the Mark IV-A implementation. ~~This article describes the DSN Tracking System as currently implemented, its performance in support of Voyager 2, and plans for new implementation, etc.~~

I. Introduction

The Deep Space Network (DSN) Tracking System is composed of the hardware, software, personnel and procedures required to perform the following primary functions:

- (1) Acquire and maintain the communications link with the spacecraft;
- (2) Generate radio metric data (consisting of doppler, range and angle measurements) at each Deep Space Station (DSS);
- (3) Format and transmit radio metric data;
- (4) Validate the radio metric data to assure that performance requirements are being met.

The data generated by the Tracking System are used for spacecraft orbit determination, gravity wave studies, and relativity experiments, among other usages.

This article describes the current Mark IV-A configuration of the Tracking System, discusses system performance and problem areas during the recent Voyager Uranus encounter, outlines modifications scheduled for delivery in the current fiscal year (FY 86) and describes several major implementations planned for the near future.

II. Functional Description

The subsystems and major assemblies that comprise the Tracking System and the data flow between them are illustrated in Figs. 1 and 2.

Using cesium and hydrogen maser standards, the Deep Space Communications Complex (DSCC) Frequency and Tuning Subsystem (FTS) distributes highly stable timing pulses and reference frequencies to elements of the Tracking System.

The generation of doppler and range measurements utilizes a closed loop between the DSS and the spacecraft. To provide this link, the Exciter Assembly (EXC) of the DSCC Receiver-Exciter Subsystem (RCV) generates a 2.1 GHz (S-Band) signal. The frequency of this signal is controlled by the DSCC Tracking Subsystem (DTK). When ranging, the uplink signal is modulated by a ranging signal generated by the Planetary Ranging Assembly (PRA).

The uplink signal is amplified by the DSCC Transmitter Subsystem (TXR) to power levels of 20 kW (34-m STD DSS) or up to 400 kW (64-m DSSs). As part of Mark IV-A, a high power transmitter controller was installed at each 64-m DSS to allow the Signal Processing Center (SPC) to control and monitor the transmitter.

The amplified signal is provided to the DSCC Antenna Microwave Subsystem (UWV) which directs the signal to the antenna for radiation to the spacecraft.

Tracking of the apparent motion of the spacecraft is accomplished by the DSCC Antenna Mechanical Subsystem (ANT). This subsystem was extensively redesigned as part of the Mark IV-A implementation. All antennas at the DSCC are under control of a single Antenna Pointing Assembly (APA), while antenna dependent activities are controlled and monitored by the Angle Data Assembly (ADA) which interfaces with the APA. Antenna pointing is accomplished using predictions generated by the NOCC Support Subsystem (NSS) corrected by conical scanning, angle correction tables, and manual offsets.

Received 2.3 GHz (S-Band), 8.4 GHz (X-Band), and 1.5 GHz (L-Band) signals are focused by the antenna and amplified by the UWV. These signals, appropriately up-converted (for 1.5 GHz) or down-converted (for 8.4 GHz at the 34-m DSSs), are provided to the RCV where they are tracked using phase-locked loop receivers. Doppler is extracted and provided to the Metric Data Assembly (MDA) for counting. Received ranging modulation is provided to the PRA which generates the range measurements.

The MDA formats the doppler and range measurements and provides them to the Ground Communications Facility (GCF) for transmission to the Network Operations Control Center (NOCC). Also at each DSCC, the Meteorological Monitor Assembly (MMA) continuously accumulates local weather data and Faraday Rotation angle measurements from geostationary spacecraft tracking. These data are also provided to the GCF which transmits them to the NOCC.

The DSCC Monitor and Control Subsystem (DMC) provides control and configuration data for all elements of the TRK located at the DSCC. It also generates displays of status, configuration and performance data received from the subsystems. The DMC was the centerpiece of the Mark IV-A implementation, providing a new, centralized method for controlling subsystems and receiving and distributing monitor data required by each subsystem.

At the NOCC, the NOCC Tracking Subsystem (NTK) receives radio metric and MMA data and provides displays of data and warning messages to allow real-time validation of the data. The NOCC Support Subsystem (NSS) generates prediction data using input received from the NOCC Navigation Subsystem (NAV) and the flight project navigation teams and transmits them to the DMC for dissemination and archiving.

Orbit data files and state vectors received from NAV are transmitted by NSS to external users such as the European Space Operations Center, located in Darmstadt, Germany; the German Space Operations Center, located at Oberpfaffenhofen, Germany; and the Tracking and Control Center, located at Tsukuba, Japan.

The NAV uses radio metric data to compute the orbits of those certain deep space missions and earth orbiters supported on a reimbursable basis. NAV was newly implemented with Mark IV-A to provide this capability. Additionally, NAV preprocesses radio metric data to generate orbit data files for delivery to the flight project navigation teams.

III. Tracking System Performance

Immediately following the Mark IV-A implementation at each DSCC, the quality and quantity of radio metric data being delivered to the flight projects, especially Voyager, took a significant downturn. By March 1985, concern about the poor performance was serious enough that a team was formed at JPL to monitor data quality and recommend changes to hardware, software and procedures (at both the DSCCs and JPL) to improve the data return. In parallel, work continued in the Mark IV-A project to improve the operability of the Mark IV-A configuration.

Figure 3 illustrates the percentage of usable doppler and range data provided to Voyager from April 1985 through February 1986. As can be seen, the percentage of usable data was unstable prior to December 1985.

It should be noted that the scheduled tracking passes rarely provided the level of support required by the Support Instrument Requirements Document (SIRD). Thus, minor problems were typically magnified by the lack of tracking time.

Encountered problems that had significant impact on data quantity and quality were:

- (1) Procedural – including incorrect entry of range parameters, frequently incorrect configuration of the doppler reference frequencies and incorrect flagging of doppler mode;
- (2) Software – including halts of the Metric Data Assembly, Area Routing Assembly, Antenna Pointing Assembly, frequent occurrences of the antenna driving off point, missing data blocks (especially the uplink tuning data) and erroneous transmitter status flags in the data;
- (3) Hardware – including transmitter failures and PRA failures.

These problems all were given special attention by the Mark IV-A implementers. By the beginning of the encounter period the majority of the problems had been resolved.

The Performance Analysis Group of the DSN Control Center Operations Section and the Multimission Navigation Support Team of the Navigation Systems Section worked closely to identify causes of problems and to recover data through special processing.

The excellent quality of data during the encounter period was, according to the Voyager Navigation Team chief, a strong contributor to the successful flyby of the Uranian moon, Miranda, and to the Uranus encounter.

The team established to monitor the data will continue this activity at a reduced level to attempt to ensure that data quality levels remain high.

IV. Planned FY 86 Implementations

During the current fiscal year, a multitude of changes have been planned which will continue to improve the operability of the Mark IV-A Tracking System. These modifications include (by subsystem):

- (1) Antenna Mechanical – improvements in CONSCAN signal tracking, improved angle data and predicts displays, and high-level control of the Angle Data Assembly.
- (2) DSCC Tracking Subsystem – redesign of the MDA-DCO (Digitally Controlled Oscillator) interface and displays, new interface with the Transmitter subsystem; and a doppler reference frequency monitor;
- (3) NOCC Tracking Subsystem – addition of data monitoring for 26-m DSS radio metric data;
- (4) DSCC Monitor and Control Subsystem – improved display handling, transmission of logs to JPL, and text file handling capability;
- (5) Transmitter Subsystem – automation of the 20 kW transmitter and new MDA interface.

Transfer of the upgraded software and firmware is planned to be completed by September 30, 1986.

V. Future Major Implementations

Current planning calls for several major capabilities to be implemented during the next four years. These capabilities include X-Band uplink, the Media Calibration Subsystem, a

real-time navigation interface, and the Sequential Ranging Assembly.

A. X-Band Uplink

This project is well underway towards a January 1988, operational date at DSS-45. A key feature of this implementation is the installation of a complete Tracking System at the 34-m High Efficiency (HEF) Antennas. This capability will provide coherent 7.2 GHz/8.4 GHz doppler and ranging capability for use during the upcoming Galileo, Magellan, and Mars Observer missions.

B. DSCC Media Calibration Subsystem (DMD)

The DMD will replace the existing MMA and Faraday Rotation equipment with a new MMA and receivers for tracking the Global Positioning System (GPS) satellites. Local weather data of improved quality and measurements of the differential phase and group delay from the dual frequency GPS downlinks will be generated by the DMD for use in computing ionosphere and troposphere calibration data. Implementation of the DMD is scheduled to begin in late 1988.

C. Real-time Navigation Interface

The current method for providing radio metric data to the flight project navigation teams requires that the data be logged in the Data Records Subsystem (GDR) and periodically written to tape as intermediate data records (IDRs). These IDRs are provided to the navigation teams for reformatting, preprocessing, and calibrating prior to their use in the orbit determination process. In October 1987, a dedicated NOCC Navigation Subsystem (NAV) computer with a real-time interface to the GCF for receipt of radio metric data will become operational. At that time, the IDRs will be replaced and the DSN will assume responsibility for providing preprocessed data to the flight projects. This implementation should improve the current radio metric data flow.

D. Sequential Ranging Assembly

The Sequential Ranging Assembly (SRA) will replace the current Planetary Ranging Assembly. The SRA will provide for coherent 7.2 GHz/8.4 GHz (X-Band) ranging as well as for the usual 2.3 GHz (S-Band) ranging. Key features of the SRA are automation of the Ranging Demodulator Assembly (RDA) configuration and calibration, automation of the pre-track DSS calibration, capability to change ranging parameters without loss of data and a capability to go eventually to higher ranging frequencies. The SRA is currently planned to be installed at DSS-14 in March 1987 for testing and evaluation with the first operational units planned for installation in October 1987.

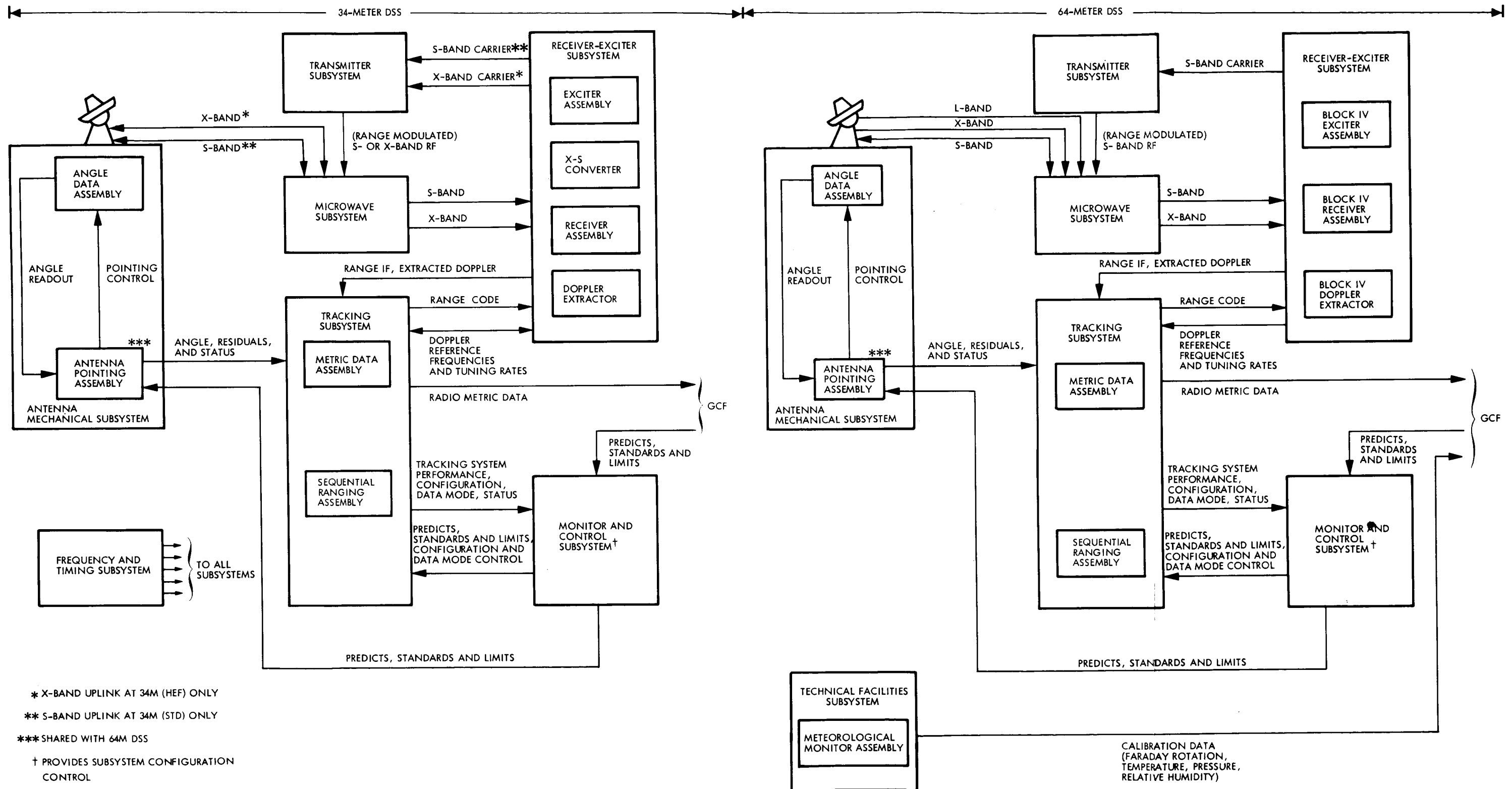
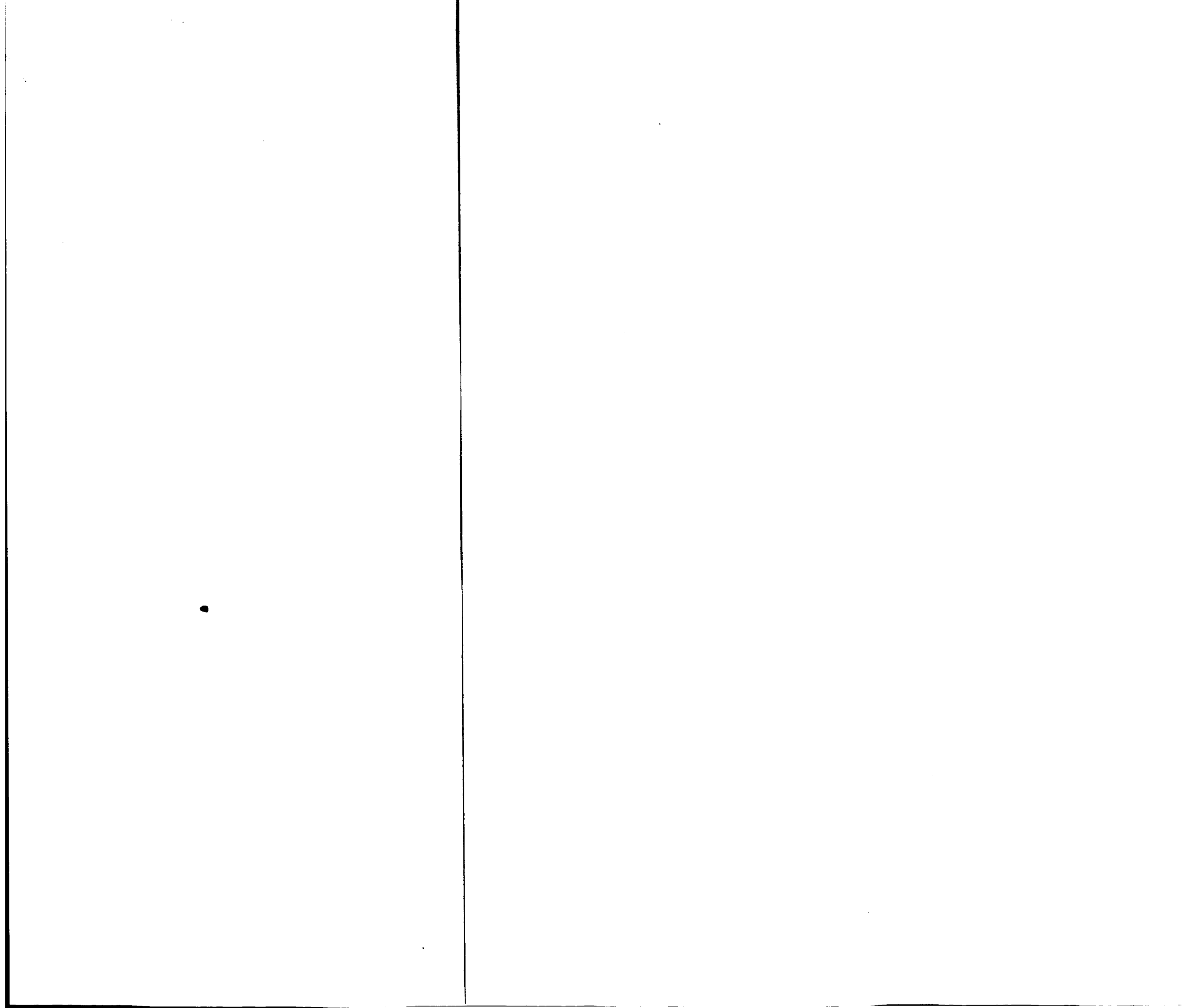


Fig. 1. Detailed block diagram of the DSN Tracking System at the 34- and 64-m DSSs

PRECEDING PAGE BLANK NOT FILMED

FOLDOUT FRAME

2. FOLDOUT FRAME



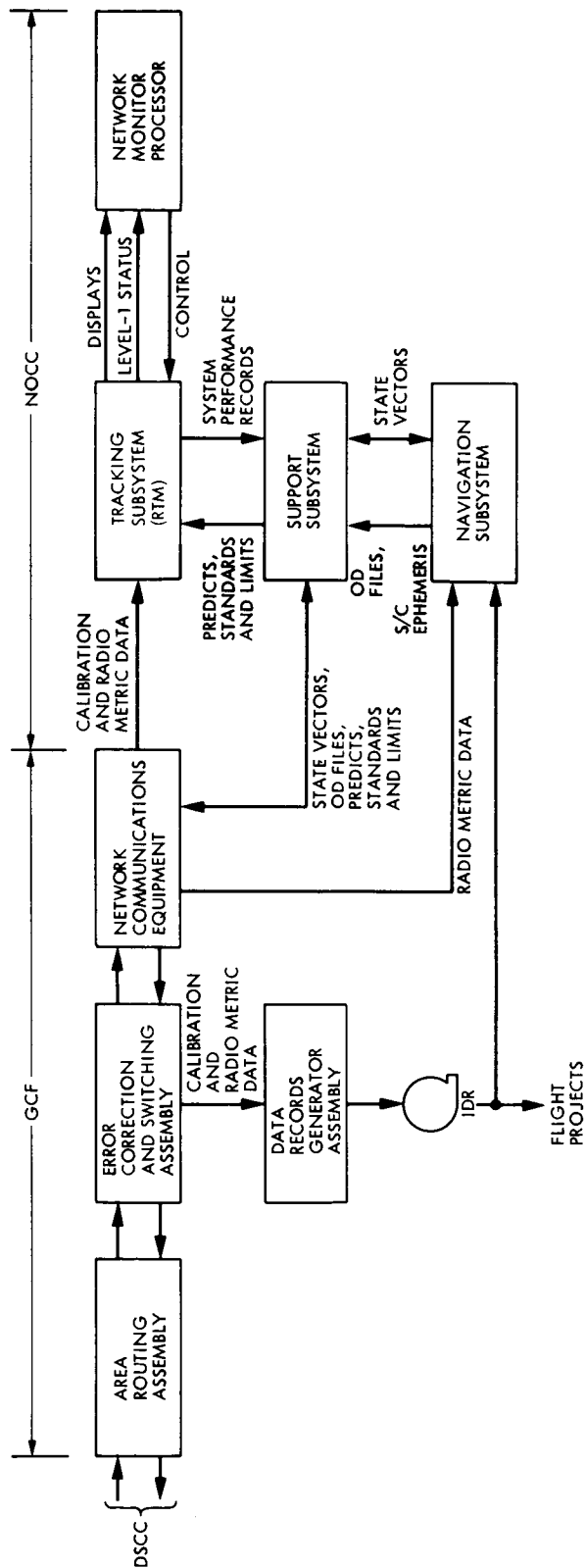


Fig. 2. GCF/NOCC functions and data flow within the DSN Tracking System

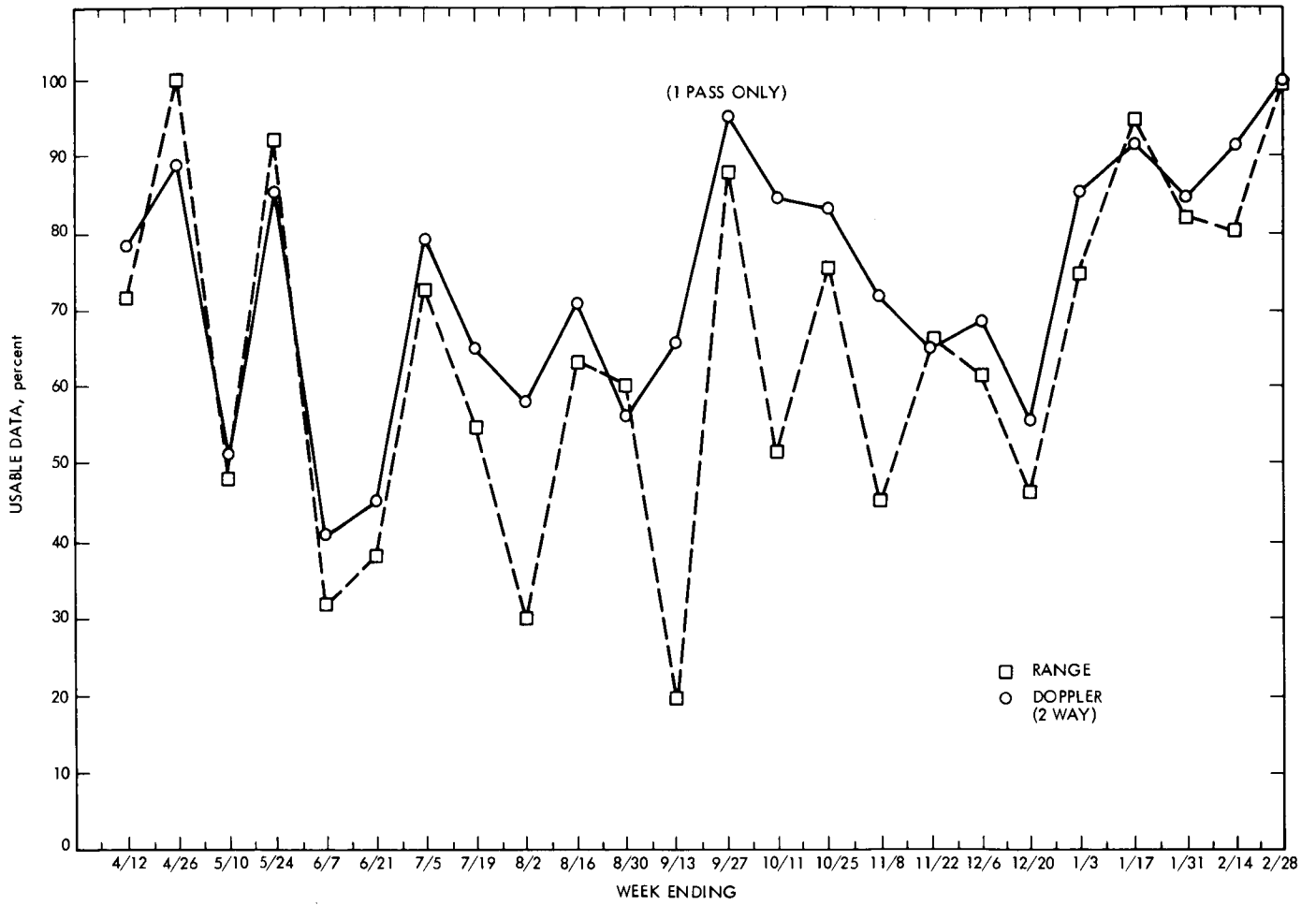


Fig. 3. Tracking System performance

13158

Mark IVA DSN Receiver-Exciter and Transmitter Subsystems

M. R. Wick
TDA Engineering Office

This article describes the present configuration of the Mark IVA DSN Receiver-Exciter and Transmitter Subsystems. Functional requirements and key characteristics are given to show the differences in the capabilities required by the Networks Consolidation task for combined High Earth Orbiter and Deep Space Network tracking support.

I. Introduction

The purpose of this article is to describe the Receiver-Exciter and Transmitter Subsystems in the Mark IVA configuration as recently implemented at the Goldstone, Canberra, and Madrid Deep Space Tracking Stations. Mission requirements contributing to the changing configuration include Voyager, Magellan (Venus Radar Mapper), Venus-Balloon/Pathfinder support of High Earth Orbiters (HEO) including ICE, AMPTE, Shuttle, and Ulysses.

The Receiver-Exciter Subsystem and Transmitter Subsystem at the 64-meter and 34-meter standard (STD) receive-transmit antennas have been modified for central control. Venus-Balloon and Pathfinder required the addition of an L-band (1 GHz) downlink capability at the 64-meter antennas. A high power 400-kW Transmit capability was also added to the 64-meter antennas to support Voyager Uranus and ICE missions, and the 34-meter standard (STD) subnet was modified to provide S-band (2 GHz) uplink and downlink coverage of the HEO frequency band. A Block III Receive channel was installed in the new 34-meter High Efficiency Antennas.

II. Functional Description

A. Receiver-Exciter Subsystem

The Receiver-Exciter Subsystem is composed of three groups of equipment: the Closed Loop Group, the Open Loop Group, and the RF Monitor Group.

The Closed Loop phase tracking reception of spacecraft microwave signals provides telemetry and radiometrics. Table 1 gives the present Closed Loop configuration set at each station in the DSN. The received signals are demodulated for telemetry processing; spacecraft doppler residuals are extracted; and Intermediate Frequency (IF) signals containing ranging code are separated for further processing of tracking information.

The Open Loop Group provides radio path effects on the spacecraft signal and observations of extra-galactic radio source noise spectra for Radio Science and Very Long Baseline Interferometry purposes.

The RF Monitor Group provides spectral measurements, measurements of the receive channel system temperature, and spacecraft signal level. Key characteristics of the Receiver-Exciter Subsystem are as follows:

- (1) L-band (1 GHz), S-band (2 GHz), and X-band (8.5 GHz) reception of deep space spacecraft signals.
- (2) S-band reception of high Earth orbiter spacecraft signals.
- (3) S-band (2 GHz) and X-band (7 GHz) uplink with command and range modulations.
- (4) Coherent two-way doppler and range, S-band and X-band.
- (5) Baseband telemetry demodulation.
- (6) Generation of X-band and S-band microwave test signals.
- (7) Open-loop down conversion of X-band and S-band radio science occultation signals.
- (8) Open-loop down conversion of X-band and S-band VLBI signals.
- (9) High-resolution spectral signal indication.
- (10) Precision measurement of system temperature and carrier signal power.
- (11) Centralized monitor and control.
- (12) Predicts-driven automatic tuning of receiver and exciter frequencies (deferred to 1988).

The Mark IVA configuration of the Receiver-Exciter Groups is described below.

1. Closed Loop Receiver Group. The Block IV Receiver-Exciter (Fig. 1) in the 64-meter antenna contains two receive channels each capable of L-band (1 GHz), S-band (2 GHz) or X-band (8.5 GHz) reception and an S-band exciter which generates the uplink carrier for transmission to the spacecraft after being amplified by either a low-power 20-kW or high power 400-kW transmitter. The uplink frequency is computer controlled, for phase-continuous frequency tuning. The Block IV Receiver-Exciter has been modified for central control from the Signal Processing Center (SPC) at Goldstone, Canberra, and Madrid. An L-band to S-band upconverter was also installed in the 64-meter antennas as part of the Block IV Receiver-Exciter to support the Venus-Balloon/Pathfinder experiment. An L-band horn and low noise amplifier (FET) was added to the microwave equipment (Ref. 1), and an L-band noise diode added to the Precision Power Monitor for L-band System Temperature Measurements (Fig. 8).

The Block III Receiver-Exciter at the 34-meter STD antennas (Fig. 2) contains two receive channels each capable of S-band or X-band reception and generates an S-band uplink carrier which drives a 20-kW low-power transmitter. The uplink frequency is computer-controlled for phase-continuous tuning. This 34-meter STD antenna Block III Receiver-Exciter has been modified to cover both the DSN and HEO uplink and downlink frequency bands (Table 2), and is capable of reception over the DSN X-band frequency range. It has also been modified for central control from the SPC.

One channel of a Block III Receiver has been installed at the new 34-meter HEF antennas at DSS 15 and DSS 45 (Fig. 3). The modification is similar to that at the 34-meter STD antenna except that the tuning range is limited to the DSN frequencies at both S-band and X-band (see Table 2). At present, these stations are single channel downlink, receive only.

2. Open Loop Receiver Group. The Open Loop Receiver Group performs open loop frequency down conversion for DSN Radio Science and Very Long Baseline Interferometry (VLBI) purposes. Four channels of S-band (2 GHz) and X-band (8.5 GHz) signals are received (2-channel S-band, LCP and RCP, and 2-channel X-band, LCP and RCP) at the 64-meter antennas. These signals are down-converted to video frequencies for processing by the Radio Science/VLBI Spectrum Processing Subsystem.

The Radio Science/VLBI Open Loop Receiver Group (Fig. 4) uses a different type of down conversion and data processing methodology than that of the Closed Loop Receivers. Down conversion is accomplished so as to preserve the amplitude and phase variations for analysis of the effects of both the radio source and radio path. Within this Open Loop Receiver Group are two similar yet quite different receivers: the Radio Science Receiver and VLBI Receiver. The Radio Science Receiver is used to observe radio source and path effects of a spacecraft generated "line spectra" carrier, whereas the VLBI Receiver is used to observe both the characteristics of "line spectra" and Extra Galactic Radio Sources noise spectra for Radio Science, spacecraft navigation, and Time Sync of the DSN tracking network.

The Radio Science Open Loop Receiver (Fig. 5) has a different type of IF to video down conversion than the VLBI Open Loop Receiver; however, it is similar in that the image-noise spectrum is rejected, thus preserving the input signal SNR. Figure 5 shows the present configuration implemented at the 64-meter antennas for the Voyager-Uranus encounter. The IF-VF converter uses crystal bandpass filters with selectable BWs to reject image noise. A programmable local oscillator is used to correct for the doppler shift effect of the

received carrier signal to maintain centering of the received signal within the narrow, fixed bandwidth of the crystal filter. This signal is then further down-converted to the video band for recording.

Table 2 lists the open loop frequency tuning ranges. Frequency tuning, filter selection, and signal attenuation of the receiver are planned to be remotely controllable from the Radio Science/VLBI Spectrum Processor Subsystem. Presently, only the frequency is remotely controlled.

The VLBI IF to video converters use single-sideband (SSB) methodology for image-noise rejection. Tunable oscillators provide frequency flexibility in the channel selection. This permits variable data channel bandwidths by selectable low-pass filtering of the video band, i.e., the capability of down converting a segment of the BW at any frequency over a broad RF spectrum.

The VLBI IF to video down converters are of two types: a Narrowband Channel Bandwidth (NCB) type (BLK I) (Fig. 6) with channel BW in the kHz range, and a Wide Channel Bandwidth (WCB) type (BLK 0 and BLK II) (Fig. 7) with BW in the MHz range.

NCB IF to video down conversion is used for Universal Time 1 (UT1), Polar Motion (PM), Clock Sync, and DOR (Differential Downlink One Way Range) applications. The WCB IF to video down conversion is used for Radio Source Catalog Maintenance by observing the continuous noise spectrum of Extra Galactic Radio Sources (EGRS) using extremely large spanned BW (100 to 400 MHz at X-band).

The VLBI receiver furnishes two video signals in quadrature, 0 and -90 degrees, to the Spectrum Processor (DSP). The DSP uses digital techniques to generate a second -90-degree phase lag and summation needed to accomplish the image rejection (Ref. 3). Within the span bandwidth of 100 MHz, eight X-band and four S-band channels, each generated by one of 12 digitally controlled local oscillators, are used in the down conversion. These oscillators are operated continuously uninterrupted to preserve the reference phase.

3. RF Monitor Group. The RF Monitor Group consists of a Precision Power Monitor (PPM) for system temperature and signal level measurement and a Spectral Signal Indicator (SSI) which generates digital spectral data for display.

The PPM measures antenna system noise temperature using a Noise Adding Radiometer (NAR) and measures received carrier-signal power level with a Signal Level Estimator (SLE). Figure 8 shows the Goldstone and Canberra 64-meter antenna installation of the PPM. The PPM input is from the Closed

Loop Receiver 2nd IF frequency (50-MHz Block III Receiver, 55-MHz Block IV Receivers) prior to the gain control (AGC). The Canberra installation differs slightly because of the collocation of DSS 42; however, both the Goldstone and the Canberra antennas have a full complement of noise diodes for all input channels.

Signal level measurement is based on the results of the system temperature measurement conducted simultaneously on the same antenna for the same signal stream. Measured noise power from a radio star is used for antenna pointing calibrations. The measured carrier signal level is also a radio science data type and is a reference for calibrating test signals, command modulation indices, receiver AGC curves, and an indicator of telemetry system performance. PPM capability has been implemented at the Goldstone and Canberra 64-meter and 34-meter stations for Voyager-Uranus Encounter; a PPM will be installed at Madrid to support the Galileo and Magellan missions. The PPM is centrally controlled from the Monitor and Control Subsystem at the SPC.

Signal-spectrum measurements are performed by a Spectral Signal Indicator (SSI) which translates a video band signal into a frequency spectrum and generates digital spectral data for display at the Signal Processing Center and also for transmission to JPL. Principal uses of the SSI include detection and monitoring of spacecraft frequency variations during a radio science experiment, and an indication of signal presence and spectral properties during a test. The SSI has not been modified for centralized control.

4. Transmitter Subsystem. The Transmitter Subsystem is composed of three groups of equipment (Fig. 9). A low-power 20-kW S-band transmitter and a high-power 400-kW S-band (2 GHz) transmitter at each 64-meter antenna, and a low-power 20-kW S-band transmitter at each 34-meter standard antenna. Key characteristics of the Transmitter Subsystem are as follows:

- (1) S-band 20-kW transmit capability at the 34-meter HEF antennas covering the DSN and HEO tuning range.
- (2) S-band 20-kW transmit capability at the 64-meter antennas covering the DSN tuning range.
- (3) S-band 400-kW transmit capability at the 64-meter antennas covering the DSN tuning range and 2090.6 MHz at reduced power for the ICE mission.
- (4) Centralized monitor and control.
- (5) Interlock protection circuits for equipment and personnel.

The Transmitter Subsystem amplifies drive signals from the Block III or Block IV Receiver-Exciter Subsystem exciter and illuminates the antenna via the Microwave Subsystem feed. The 20-kW and 400-kW transmitters at the 64-meter antenna are operated simultaneously.

The high-power transmitters are installed at all three 64-meter antennas to provide emergency commanding of a deep space mission, such as Voyager, in case the spacecraft must use its low-gain antenna for communications with Earth. The Canberra high-power transmitter was operated at 60 kW to ensure low-noise telemetry performance at the Voyager mission Uranus encounter, operating in a two-way communications mode. The high-power transmitter was designed and used for coverage of the ICE uplink frequency (2090.6 MHz) for similar purposes.

The 2110 to 2120-MHz transmit range is used by the deep space missions, whereas the High Earth Orbiter (HEO) missions use the 2025 to 2120-MHz range. As such, the 34-meter standard antennas can support all HEO and DSN frequencies up to 20 kW. The 64-meter antenna supports DSN frequencies only in S-band with the exception of the ICE frequency.

Both the low-power and high-power transmitters received modifications for increased reliability including the capability for centralized control for reduced manual operations. The high-power transmitter central control modifications have been completed; the low-power transmitters have been modified for monitor capability with control capability deferred until 1986. Figure 10 shows the functional elements of each transmitter.

III. Modifications Planned (1986–1988)

At the Madrid complex, a 34-meter HEF antenna will be built to support Galileo and Magellan; construction is to be completed in mid-1986. The Canberra and Madrid HEF antennas, DSS 45 and DSS 65, will receive the new X-band exciter and X-band 20-kW transmitter (Ref. 2) planned for operational use in 1987.

Initially, these stations will be capable of X-band telemetry, Radio Science, and VLBI. Radiometric capability is to be added for the Magellan mission. The new X-band transmitter will be phase-stabilized with a phase control loop implemented in the exciter. A sample of the transmitter output is fed back to the exciter phase correction loop to minimize the uplink transmitted signal phase variations to less than 5 parts in 10^{15} as it leaves the transmitter.

Also, as part of the X-band uplink modification, the Radio Science Open Loop Receiver will be modified for tuning at the second local oscillator frequency, which improves stability and significantly reduces the noise present with the higher local oscillator frequency. The new Radio Science/ VLBI fixed first local oscillator down converter provides an output IF in the range 200 MHz to 400 MHz. Both the 64-meter and 34-meter HEF antennas will have the new down converter. The IF selector switch selects either antennas as the signal source.

The PPM will be installed at the Madrid complex for DSS 61, 63, and 65 antennas.

It is planned to incorporate a predict controlled digitally controlled oscillator and an automatic signal acquisition capability early in 1988 to support the high doppler rates of Magellan at Venus orbit.

References

1. Parsons, P., "Antenna Microwave Subsystem," *TDA Progress Report 42-79*, pp. 165-171, Jet Propulsion Laboratory, Pasadena, CA, Nov. 15, 1984.
2. Cormier, R., and Tesarek, T., "Development and Testing of a 20-kW X-Band Transmitter With High Phase Stability," *TDA Progress Report 42-79*, pp. 47-61, Jet Propulsion Laboratory, Pasadena, CA, Nov. 12, 1984.
3. Sosa, E. N., Sato, T., and Tyner, D. A., "Narrow Channel Bandwidth Receiver for VLBI," *TDA Progress Report 42-64*, pp. 18-29, Jet Propulsion Laboratory, Pasadena, CA, Aug. 15, 1981.

Table 1. Closed loop configuration set at DSN stations

Antenna ^a	Goldstone	Australia	Madrid
64-meter Transmit S-band Receive L, S, X-band	DSS 14	DSS 43	DSS 63
34-meter STD Transmit S-band Receive S, X-band	DSS 12	DSS 42	DSS 61
34-meter HEF Transmit X-band Receive S, X-band	DSS 15 ^b	DSS 45 ^c	DSS 65 ^c

^aS-band: 2 GHz; L-band: 1 GHz; X-band: 7 GHz uplink, 8.5 GHz downlink.
^bX-band transmit capability 1990.
^cX-band transmit capability 1987.

Table 2. Frequency tuning ranges

Antenna	Uplink, MHz	"Closed loop" downlink, MHz
64-m DSSs 14, 43, 63	(LO PWR) 2110 - 2120 (HI PWR) 2090 - 2120	(L-band) 1663 - 1673 (S-band) 2200 - 2300 (X-band) 8400 - 8440
34-m STD DSSs 12, 42, 61	(LO PWR) 2024 - 2120	(S-band) 2200 - 2300 (X-band) 8400 - 8440
34-m HEF DSSs 15, 45, 65	(LO PWR) 7145 - 7190	(S-band) 2270 - 2300 (X-band) 8400 - 8440

Antenna	"Open loop-radio science/VLBI" downlink
64-m DSSs 14, 43, 64	2-channel RCP, LCP 2-channel RCP, LCP (S-band) 2265 - 2305 (X-band) 8400 - 8500
34-m DSSs 45, 65	1-channel 1-channel (S-band) 2200 - 2300 (X-band) 8200 - 8600

LO PWR = 5 to 20 kW, HI PWR = 40 to 400 kW.
RCP, LCP = Right/Left Circular Polarization.

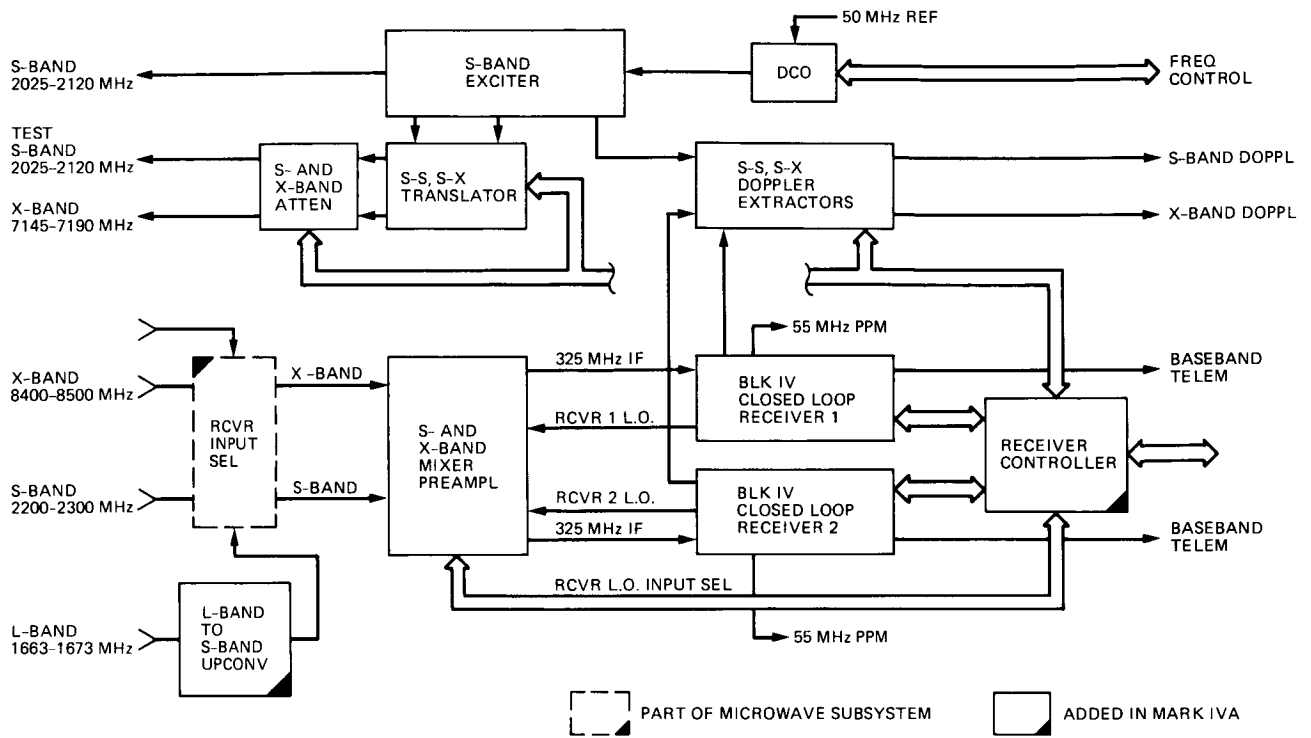


Fig. 1. Closed loop receiver group: 64-m block IV receiver-exciter

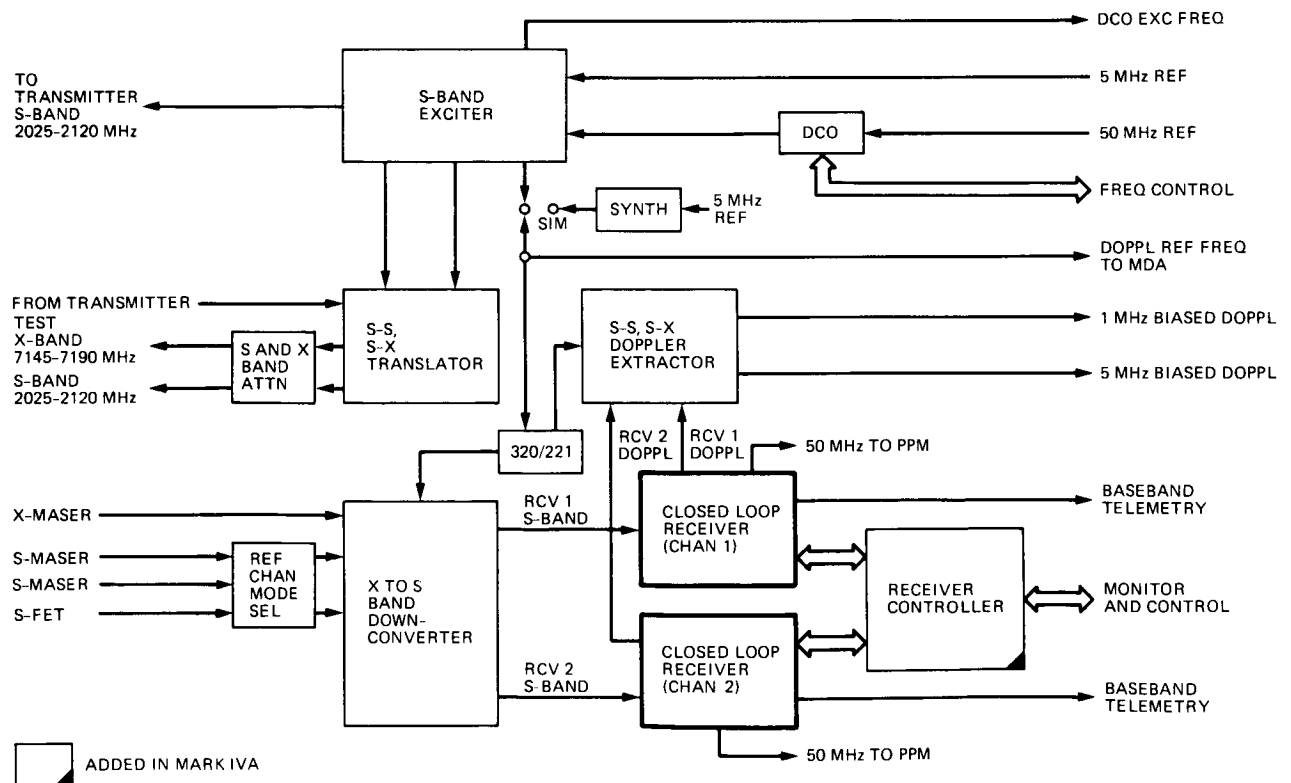


Fig. 2. Closed loop receiver group: 34-m standard block III receiver-exciter

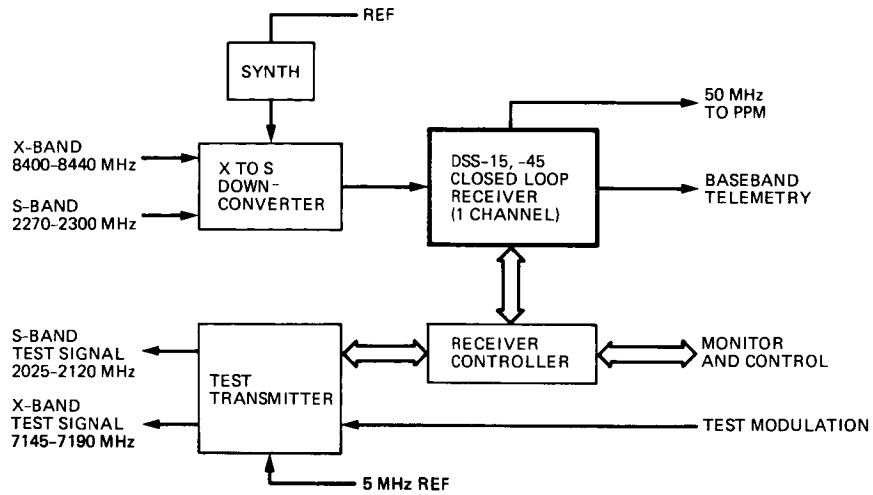


Fig. 3. Closed loop receiver group: 34-m HEF block III receiver

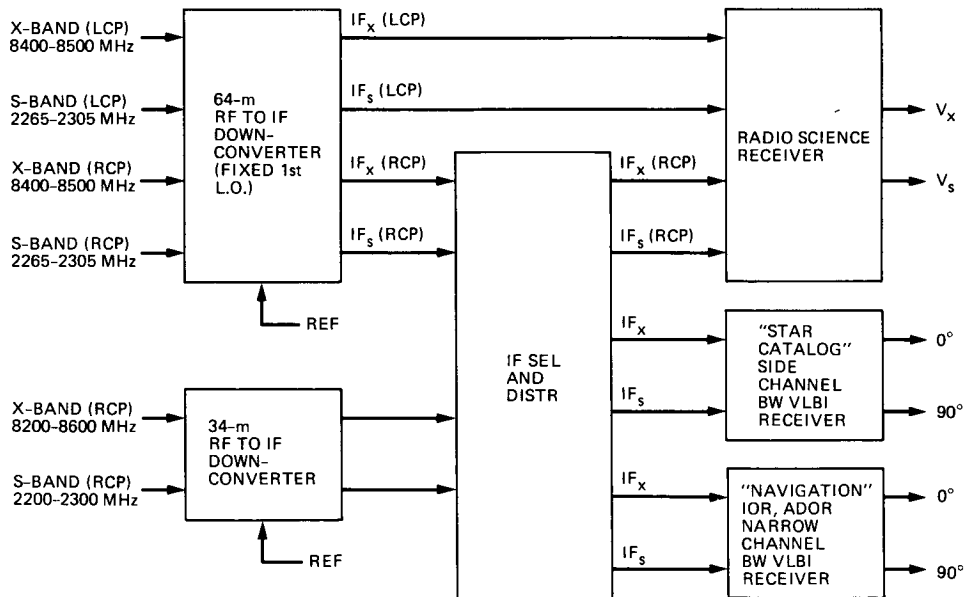


Fig. 4. Open loop receiver group

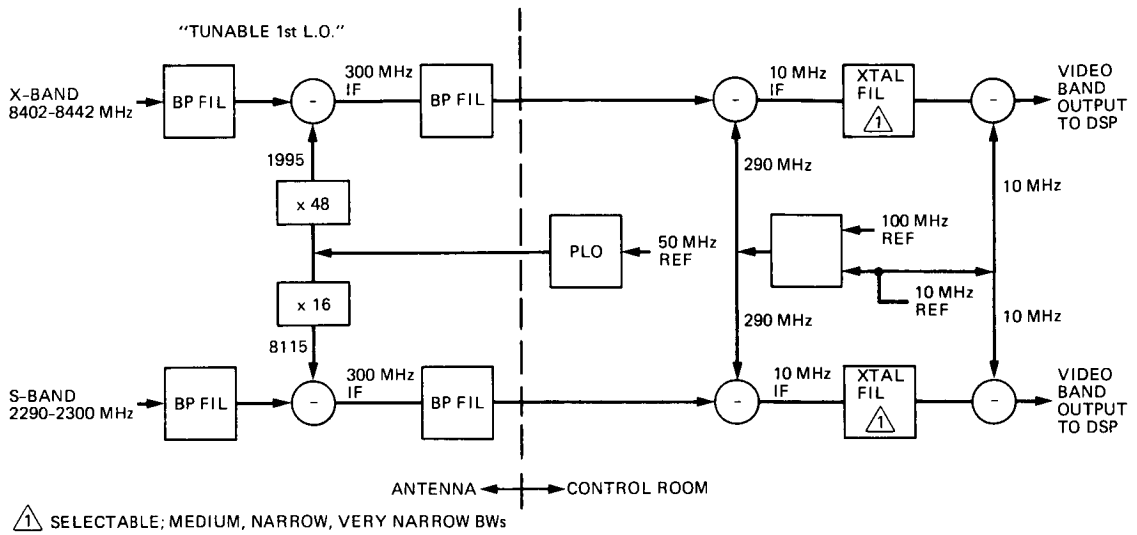


Fig. 5. Radio science receiver

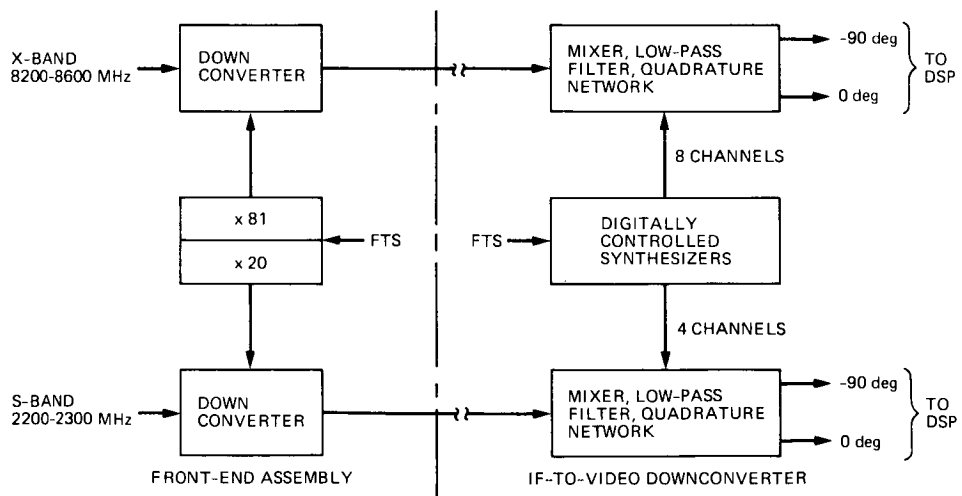


Fig. 6. Narrow channel BW VLBI receiver

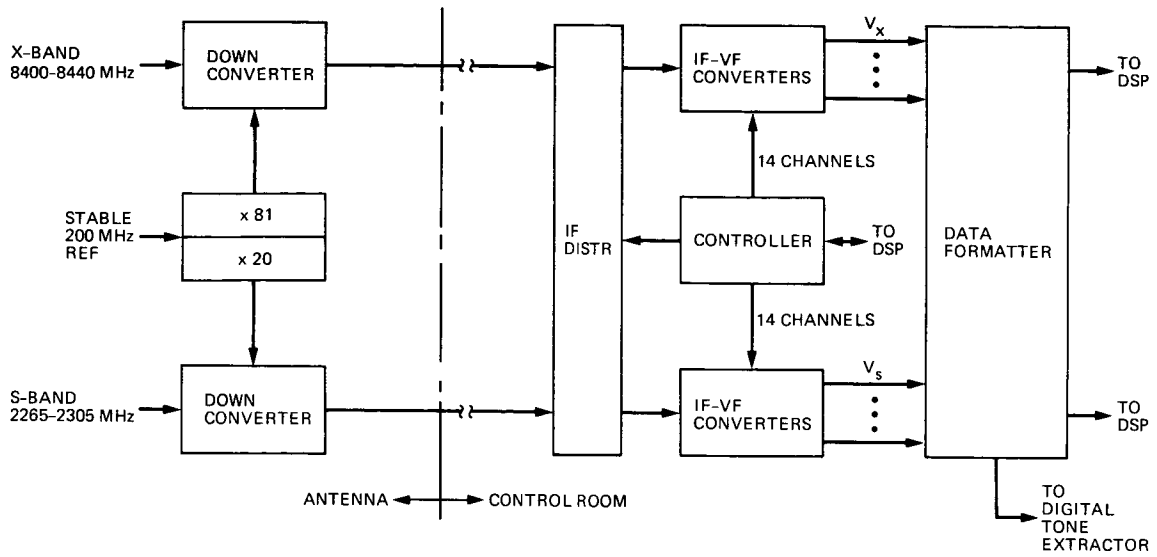


Fig. 7. Wide channel BW VLBI receiver

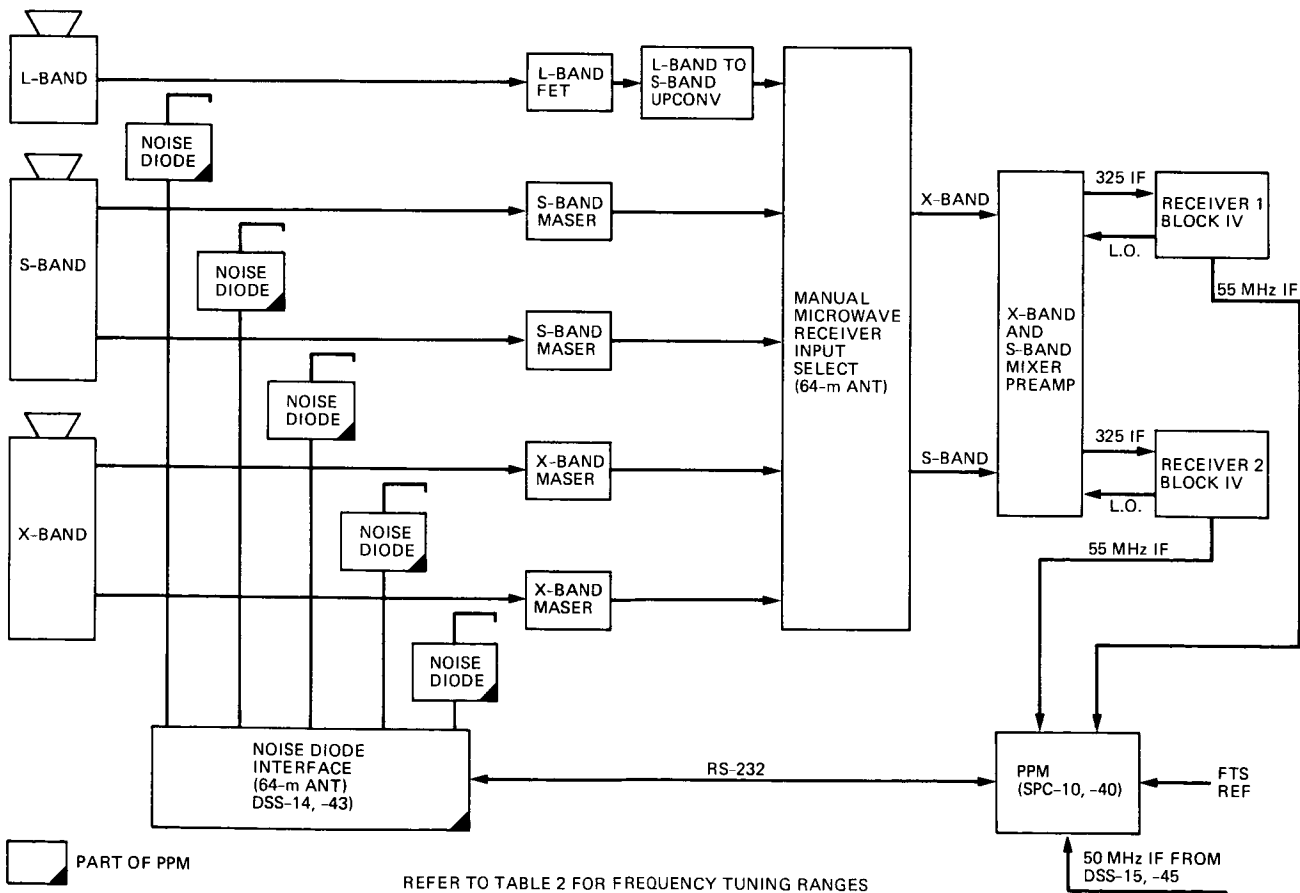


Fig. 8. RF monitor group: PPM

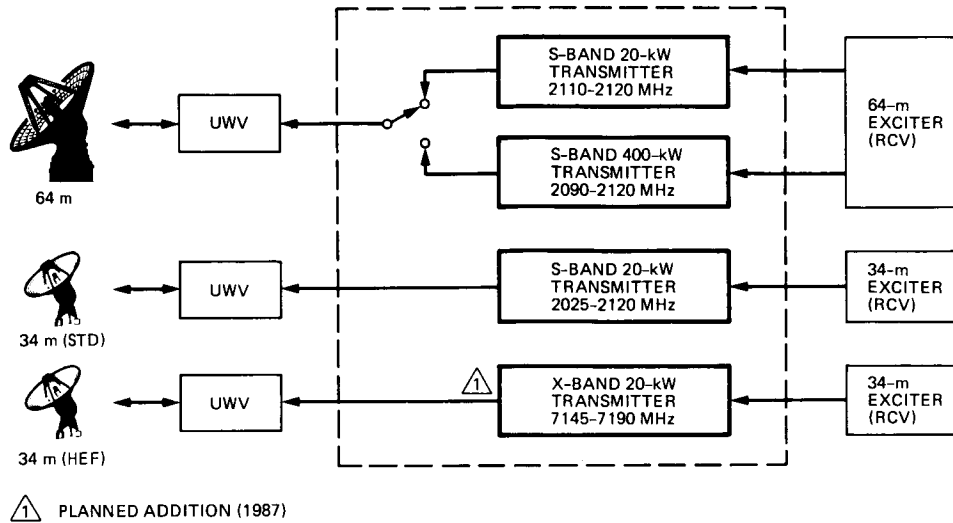


Fig. 9. Transmitter subsystem

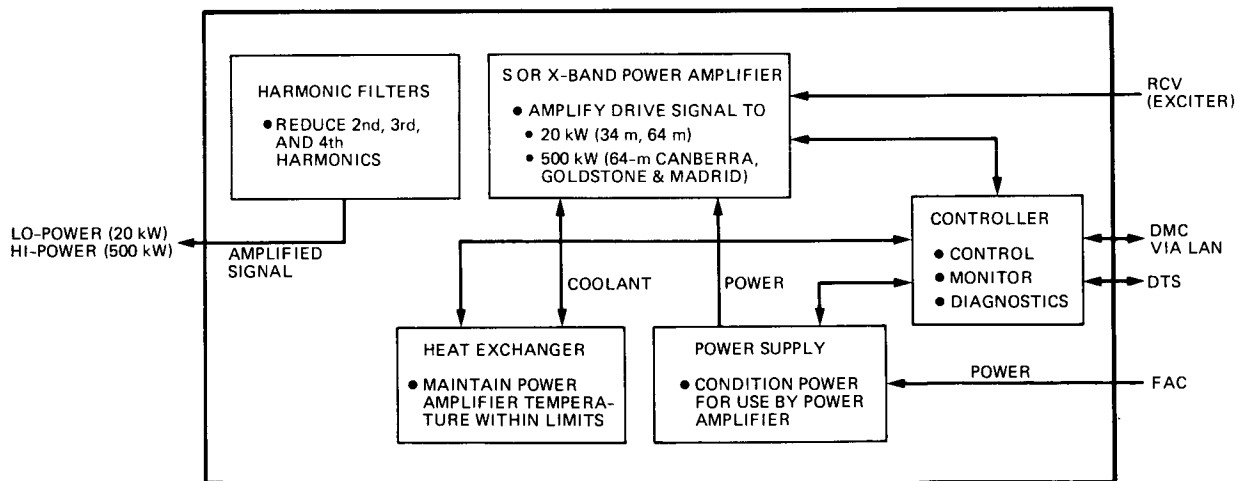


Fig. 10. Transmitter functional elements

3159

HVAC Modifications and Computerized Energy Analysis for the Operations Support Building at the Mars Deep Space Station at Goldstone

A. Halperin and P. Stelzmuller

Ground Antenna and Facilities Engineering Section

are described.

This article describes the key heating, ventilation, and air-conditioning (HVAC) modifications implemented at the Mars Deep Space Station's Operation Support Building at Jet Propulsion Laboratories (JPL) in order to reduce energy consumption and decrease operating costs. An energy analysis comparison between the computer-simulated model for the building and the actual meter data was presented. The measurement performance data showed that the cumulative energy savings was about 21% for the period 1979-1981. The deviation from simulated data to measurement performance data was only about 3%.

I. Introduction

This article describes the HVAC modifications implemented and the energy and cost analysis provided by the computer simulation for the Operations Support Building (G-86), one of the major energy consumers of the Deep Space Complex, located at the Mars Deep Space Station (DSS-14) at Goldstone, California.

Reduction of energy consumption, as well as operation costs, at all NASA-JPL Deep Space Network Facilities has been a NASA directive since 1974. Under an intensive energy conservation program, the goal was to reduce by the end of FY85 both the fossil fuel consumption and purchased energy by 50%. Consumption levels at FY73 were to be considered the "baseline."

To that effect, a two-approach method was followed. The first approach was to implement a technical program of energy consumption surveys (audits) to identify and analyze the areas of major consumption. A computer program called Energy Consumption Program (ECP) was developed in-house. It provided a model of the building by simulating the hourly, daily, monthly, and yearly behavior of the heating and cooling loads. Simulation comparisons of both existing and modified conditions resulted in the net energy savings and net energy cost savings.

Two consulting engineering companies were contracted to assist in the studies. In 1975, Keller and Gannon Consulting Engineers used a commercial computer program (E³) developed by the Southern California Gas Co. The Keller and Gannon Study determined the energy profile and the possible

energy savings due to a set of HVAC modifications. In 1976, Burns and Roe, Consulting Engineers, provided another energy study, which included additional proposed modifications.

The second approach was for personnel awareness and motivation under the Energy Conservation Awareness and Recognition Program (ECARP). This program was initiated for the purpose of motivating energy conservation actions within the organization. Energy Conservation Representatives (ECR) for each building were appointed to monitor the initial conservation actions implemented at that time, especially in the area of lighting level reduction, thermostat settings, etc.

The energy conservation program instituted at the Deep Space Communication Complex at Goldstone, California, has been successful. In FY84, one year before the deadline, the goals to reduce 50% of the fossil fuel consumption and purchased energy were accomplished.

II. Building and Original HVAC Equipment Configuration

The Operations Support Building is a two-story structure which houses all remote servo controls and data acquisition equipment for the entire Mars station. Figures 1 and 2 illustrate the floor plan for each story.

The building was originally divided into seven air-conditioned zones (Table 1). Figure 3 provides a schematic diagram of the original HVAC configuration air side. Figure 4 provides a schematic diagram of the original cooling and heating equipment configuration.

The building was originally air-conditioned by three active Air Handling Units (AH1, AH2, and AH4) and one standby unit (AH3); AH1 is a multi-zone blow-thru unit, and the other three are single-zone draw-thru units. Unit AH1 supplied conditioned air to Zones Z1 to Z6, satisfying the temperature of the zones by mixing hot and cold airstreams. If the offices at Zone Z5 and the women's restrooms were too cold, Electric Duct Heaters EH4 and EH3 were energized by thermostats located in the respective areas.

Unit AH2 (and/or standby unit AH3) supplied conditioned air to the control and communication plenums (Zone Z1) by providing air at 50°F, modulated to 55°F using EH1 (or standby EH2) to satisfy the requirements of 70°F at 50% RH at the control and communication rooms located on the second floor. Unit AH4 supplied conditioned air to the hydrogen maser room (Zone Z7) by drawing air from the plenum (Zone Z1), and returning it back to Unit AH4, or relieving it to Zone Z1.

On the refrigerant side, direct expansion cooling coils (DX) at Units AH1, AH2 (and/or AH3 standby), and AH4 cooled the air to the required temperatures. Unit AH1 was served by two compressors (C1 and C2) and one standby Compressor (C3). Compressors C1, C2, and C3 are connected to two Air-Cooled Condenser Units (ACCU1 and ACCU2). Unit AH2 was served by Compressor C4, connected to Air-Cooled Condenser Unit ACCU3. Unit AH3 was served by Compressor C5 (standby), connected to the Air-Cooled Condenser Unit ACCU4. Unit AH4 is served by Compressor C6, a part of Air-Cooled Condensing Unit CU1. On the heating side, Electric Boiler B1 provides heating hot water through a heat exchanger for the heating coil at Unit AH1, and steam for the steam injector at the same unit (Humidifier HU1).

In 1977, loads and capacities were simulated with the JPL-ECP program on the basis of a new energy consumption survey (Ref. 1). In 1979, some electronic and lighting loads had changed. Therefore, this analysis is divided into two phases: Phase I, describing the original building loads in the period 1979-1981, and Phase II, describing the modified building loads that were caused by the Network Consolidation Program (NCP) Mark IVA changes.

III. Phase I of HVAC Modifications

Phase I consisted of a simulation of the original building as of 1979, and all modifications using ECP, with an updated electronic load of 85.5 kW.

The 7 air-conditioned zones of Table 1 were modeled by ECP into 6 macro-zones. Table 2, Mod-0, gives the results of the original equipment configuration without any HVAC modifications. Figure 5 reflects the original HVAC configuration as modeled by ECP. Table 2, Mod-0, provides the monthly and yearly energy consumption and energy cost. The energy cost was based on a fixed energy rate of 0.05 dollars/kWh(e).

All HVAC modifications were examined in light of initial conservation measures and new energy costs, and the selected list for Phase I is as follows:

Mod-1 – Change the inside design temperature: from 72°F (22°C) all year to 68°F (20°C) in winter and 78°F (25°C) in summer. Install “dead band” thermostat controls.

Mod-2 – Provide variable air-volume (VAV) control at Zone Z3 only. Install a by-pass air flow at Unit AH1 (Table 3).

Mod-3 – Arrange HVAC system components and change the cooling system from DX to chilled water. In this modification, Compressor C2 is disconnected and Compressor C1,

with the addition of a liquid cooler (LC1), will provide chilled water to Units AH1, AH2, and AH3. AH4 (maser unit) will continue to be served by Compressor C3. Modified cooling and heating equipment configuration is shown in Fig. 6.

Mod-4 – Add outside air (OSA) economizers and automatic temperature reset setpoints to Units AH2 and AH3. This modification required that Units AH2 and AH3 were operating with the economizer. In this case, Unit AH1 supplies 0 CFM to Zone Z2, and it is operating in low speed (minimum CFM). If the *economizer is not operating* due to outside weather conditions, Unit AH3 becomes a standby unit and AH-1 supplies 20,000 CFM (9,440 l/s) to Zone Z2, operating in high speed.

Mod-5 – Add chilled water storage tank to provide: (1) reduction of partial load losses, (2) leveling of cooling loads, and (3) uniform supply chilled water temperatures. Based on the calculated loads generated by Mod-4, Table 3 provides the energy consumption and energy cost *without storage tank, with storage tank* option and the total annual savings.

The results of the computer simulation are presented in Tables 2 and 3. A summary of all modifications, based on the original building conditions, is provided in Table 4.

IV. New HVAC Configuration — Phase II

In 1983, the total electronic loads at the operation support building were increased from an original load of 85.5 kW to an ultimate load of 255 kW. This proposed increase was due to the JPL Network Consolidation Program Mark IVA, and it is the basis for the computer simulation under Phase II.

The building configuration changed slightly from the one shown in Figs. 1 and 2. The new configuration is shown in Figs. 7 and 8. Figure 9 is the new view of the actual Control Room 201. The zones remain the same as shown in Table 1, except for changes in the Zone air flow which are shown in Table 6. Table 5 also provides the updated ECP zone identification.

Table 6 provides the results of Mod-6 for the basic DX design, with additional units AH5 and AH6, and the required C4 and C5 compressors to accommodate the increased load of 255 kW.

The three HVAC modifications for Phase II were based on Mod-6 data and are listed below.

Mod-7 – Change the inside design temperature: from 72°F (22°C) all year to 68°F (20°C) in winter and 78°F (25°C) in

summer. Install “dead band” thermostats. Change the DX system to a chilled water system. Add setpoints to units AH5 and AH6.

Mod-8 – Add OSA economizers and automatic reset setpoints for Units AH5 and AH6.

Mod-9 – For existing chilled water storage tank, and based on the new calculated loads generated by Mod-8, Table 8 provided energy consumption and energy cost *without storage tank, with storage tank* option and the total annual savings.

The actual HVAC configuration, which includes Units AH5 and AH6 and Chiller CH2, is reflected in Fig. 10.

The results of the computer simulation are presented in Tables 6 and 7.

A summary of all Phase II modifications, based on Mod-6, is given in Table 8.

V. HVAC System Design Controls and Operation

The original HVAC design used American Society of Heating, Refrigeration and Air-Conditioning Engineering (ASHRAE) standard air discharge temperature setpoints compatible with the operating parameters of the installed refrigeration and heating equipment. Temperature control was achieved by reheating the air to the desired setpoint in the zone. Capacity control was performed manually and was limited to adjusting the mechanical unloaders in the refrigeration compressors. The design of the system was constrained in such a way that a reduction in the cooling load below 50% of the original design capacity would damage the refrigeration equipment. This problem was avoided by maintaining a sufficiently high artificial load to prevent a drop below the 50% point.

A. Design Criteria

The data obtained from the analysis of the original building operation and the proposed modifications were the basis for the selection of the mechanical design. The new control design was to meet stringent requirements for unattended HVAC system operation and easy maintainability.

In addition, the new system configuration was to permit an expansion in load capacity up to 300% of its base design, as well as to accommodate load changes from 20% to 100% of the base capacity with only minor adjustments.

B. HVAC Design Modifications

The existing air distribution network was revised and the required air flow capacity increased. The function of each air handler was defined and allocated to meet the imposed demand at maximum obtainable efficiency. The new HVAC functional block diagram is shown in Fig. 11.

To best utilize the existing refrigeration equipment, and to consolidate it with the added cooling capacity, a load decoupled chilled water system with thermal storage was selected as the prime mechanical cooling system. Sections of the existing DX systems were modified and retained for redundancy and backup.

The existing manual controls were removed and replaced with fully automated temperature and humidity controls, which are able to select the most economical mode of operation available to meet the demand. The required equipment can start and stop without operator assistance, and the status of each major component is displayed on the HVAC status panel.

C. HVAC Operation Logic

Since the electronic equipment installed is the major load, all HVAC parameters were adjusted to provide, with the least amount of energy expenditure, both an optimum inlet temperature to the electronic racks and a rack discharge temperature most suitable for human comfort. The new HVAC achieves this by operating and controlling the equipment as outlined below.

1. Plenum Air Distribution. Four air handlers, with a total supply of 82,000 CFM (38,695 l/s), hold the air pressure differential between the main plenum and the control room at $0.04 \text{ in H}_2\text{O} \pm 0.01 \text{ in H}_2\text{O}$ ($1 \text{ mm H}_2\text{O} + 0.25 \text{ mm H}_2\text{O}$) and maintain an airflow of 475 CFM (225 l/s) per kW of installed electronic load. With the mass of air flowing through an equipment rack adjusted to 475 CFM ± 20 CFM (225 l/s ± 9.5 l/s) per kW of heat to be dissipated, a rise of 8°F (4.5°C) in the air temperature is produced. And with the plenum (rack inlet) temperature maintained at 64°F (18°C), the air will exit from the racks at an average temperature of 72°F (22.2°C). All other loads such as lights, roof, etc., are added to the air-stream after it leaves the control room. This load changes the return air temperature from 72°F (22.2°C) to 75°F (24°C) before it is cooled again. If the enthalpy of the outside air (OSA) is less than the enthalpy of the return air (RA), the enthalpy controller will release the economizer lockout and the system will operate with 100% outside air. The chilled water cools the air until the temperature drops below the

plenum setpoint. With the OSA temperature below the plenum setpoint (64°F/17.8°C), the controls close the chilled water valves and limit the amount of OSA to the level needed to maintain the plenum setpoint.

2. Comfort and Plenum Backup Air Distribution. One two-speed air handler (Unit AH1) supplies the comfort load via a double duct system. At low speed, the unit delivers 11,000 CFM (5,190 l/s) of either heating or cooling air to the system. Zone control is achieved by mixing either heating or cooling air with return air.

If one of the plenum supply units fails, the unit switches to high speed, delivering 27,000 CFM (12740 l/s) and diverts 20,000 CFM (9440 l/s) to the main plenum (Fig. 12).

3. Chilled Water System. The chilled water system is a load decoupled system which consists of four closed loop flow circuits: two constant flow charge circuits of 180 GPM (11.4 l/s) each, and two variable flow demand circuits of 0-160 GPM (0-10 l/s) each. All circuits are connected to a 10,000 gallon (37,854 l) storage tank which acts as a pressure differential equalizer, a load buffer, and a thermal mass storage. The cooling capacity for Charge Circuit No. 1 is provided by Chiller No. 1, a 60 ton (211 kW) split system with two compressors; and for Charge Circuit No. 2 by Chiller No. 2, a 90 ton (316 kW) package unit with four compressors. Figure 13 shows the Chilled Water System Functional Block Diagram, and Fig. 14 shows the liquid cooler LC1, Pumps P3, P3A, P4, and P4A assembly.

The mode of operation depends on the demand. The controls select the appropriate lead-lag and start-stop sequence for each of the four circuits. On a rise in demand, the chilled water control valves open and the demand pumps start. The pumps draw chilled water from the thermal storage tank until the temperature of the water entering the supply headers connecting the demand pumps and the storage tank rises to the "High" setpoint. The signal that the stored cooling capacity is used up starts the charge pumps and initiates the chiller start sequence. Once operating, the chillers adjust their cooling capacity to maintain a preset temperature in the supply header.

During a period of low demand, with the control valves only partially open, the excess cooling capacity of the charge circuit is supplied to the thermal storage tank and displaces the warm water until the temperature of the water leaving the tank drops to the "Low" setpoint. This signal that the storage is fully charged stops the charge pumps and initiates the chillers pump down and stop sequence.

As the demand increases, more water is diverted into the demand circuits and less goes into the storage tank. This increases the amount of time the charge circuits have to operate until a new equilibrium is reached. When the demand approaches the charging capacity, all circuits operate continuously. On a drop in demand, the control valves begin to throttle the flow through the demand circuits again. This increases the back pressure at the inlet to the demand pumps, and more water from the charge circuits is diverted back to the storage until the storage is charged again and the cycle is repeated.

4. Control Groups. The control system selected is hierarchical in nature and has three levels of control function arranged in three control groups as follows:

- (1) **Primary Controls:** The primary control group encompasses all sensors, switches, and protective devices which allow an operator to control the system manually.
- (2) **Secondary Controls:** The secondary control group encompasses all sensors (temperature, humidity, power, etc.), amplifiers, logic functions, and indicating displays needed to automatically control the mechanical equipment. The controls continuously monitor the operation of the primary controls and the HVAC system performance, and display the current status on the HVAC status panel. If a component failure is detected, the controls will select and start a backup, give an alarm and indicate the type of failure and the equipment affected. If a power failure occurs, the controls reset all systems to "off," and restart the equipment in a preselected sequence once power is restored.
- (3) **Technical Facility Controller (TFC):** The secondary controls also act as an interface for the remote commands from the third level of controls: the Technical Facilities Controller. The remote commands are accepted and evaluated, and if they are within the selected safety limits of performance, they will be passed on to the primary controls. The new status is then displayed on the HVAC status panel and sent back to the Facilities Controller for evaluation. If the commands of the Facilities Controller violate the safety limits, or if no commands are generated, the secondary controls automatically revert back to autonomous operation (Fig. 15). The actual HVAC status panel is shown in Fig. 16.

VI. Verification of Computer Simulation vs Measurement Performance

A. Phase I

This study provided the computer simulation for the original HVAC system as shown in Table 2. The following two outputs are important for energy consumption verification:

- (1) Total electrical consumption for one year,
- (2) Total electronic equipment load for one year.

In Table 2, the original HVAC equipment simulation gave the total electric consumption as 1,856,944 kWh(e)/yr, and the total electronic equipment load as 749,000 kWh(e)/yr.

The actual electric meters data were used for verification. The meters' locations are shown in Fig. 17. The Mod-0 computer simulation was based on survey data for the year 1979, and the corresponding actual electric meter readings (Meter No. 42 and Meter No. 43) for that year were as follows:

Meter No. 42: 2,360,000 kWh(e)/yr (Building Meter)

Meter No. 43: 953,600 kWh(e)/yr
(Electronic Equipment Load Meter)

By comparing the actual meter data vs the simulation from Table 2, we observe that the meter readings seem to exceed the computer simulation results by 21%. In order to obtain the realistic difference, the following points are noted:

- (1) The electronic equipment load at the actual meter reading is 953,600 kWh(e)/yr, which is equivalent to 109 kW(e). This is compared against the electronic equipment load provided for the computer simulation of 749,000 kWh(e)/yr, or its equivalent 85.5 kW(e). This difference represents a 204,600 kWh(e)/yr (953,600 - 749,000) that should be accounted for in the ECP input.

This load reduction, or its equivalent, was purposely done in 1979 because of expected ongoing consolidation of electronic equipment at the time of the study. In fact, in 1984 the electronic load was 794,200 kW(e)/yr, which is equivalent to 91 kW(e), i.e., close to the electronic equipment computer-simulated load of 85.5 kW(e).

- (2) Excluding the additional loads for Building G-84, UPS and MDU panels (as shown in Fig. 17), which is approximately equal to:

30 kW(e) or 262,800 kWh(e)/yr

- (3) The total unaccounted loads in Items 1 and 2 above is 467,400 kWh(e)/yr (204,600 + 262,800).

Deducting that amount from the building electric meter gives:

$$1,892,600 \text{ kWh(e)/yr (2,360,000 - 467,400).}$$

The true deviation between the meter reading and the computer simulation would be:

$$(1,892,600 - 1,856,944) / 1,892,600 = 2\%$$

which is below the allowed margin ($\pm 10\%$) in this computer simulation.

The energy consumption for Meter No. 42 for the year 1981, after all the modifications of Phase I were completed, read 1,591,200 kWh(e)/yr. Beginning in 1980, Building G-84 was out of commission, and the deduction for UPS and MDU panel was about 12 kW(e) or 105,100 kWh(e)/yr. Deducting this amount from the meter reading gives 1,486,100 kWh(e)/yr, which, if compared with the computer simulation output of 1,524,400 kWh(e)/yr, gives a 2% deviation of the simulated load.

Actual electronic loads have not decreased as much as originally scheduled, but lighting and other accessory loads have decreased. The net effect was that the total building energy consumption in 1981 showed a net decrease of

$$(1,892,600 - 1,486,100) / 1,892,600 = 21\%$$

as compared to the 1979 level.

The net decrease in energy costs in 1981 (relative to 1979) was about

$$(1,892,600 - 1,486,100) \times 0.0633 \text{ or } \$25,731.$$

The 0.0633 dollars/kWh was the actual cost of prorated utility (Southern California Edison) purchased and JPL generated electricity for 1981.

The simulated values in Table 5 give the cumulative energy savings (Mod-1 through Mod-5) as 18%, which, if compared with the 21% figure, indicates that the computer simulation and the meter performance data are in good agreement.

B. Phase II

The actual electric meter readings were found to be below the computer simulated results listed in Table 8. Note that the electronic equipment load in 1985 has gone up slightly to 97 kW(e), and the computer simulation input was for 255 kW. The control room was only partially loaded.

Another verification made for the computer simulation inputs was to compare it against the Test Performance Data. These tests were performed in June 1985 and are given in Table 9. The ECP input data and test performance data values verify their agreement.

Another parameter to be verified is the chilled water storage tank discharge capacity, which is shown as Mod-5 in the computer simulation. The input data for Mod-5 was a 10°F differential for the chilled water, giving a charging capacity of 69.4 tons of refrigeration (or 244 kW). The temperature difference between discharge cycle start and finish was found to have a 9°F differential temperature, giving the tank discharge capacity as 62.55 tons (220 kW), which is within the conditions imposed to the storage tank charging/discharging cycle.

Under Phase II, the actual HVAC system is partially loaded. And according to Table 8, the projected energy savings will be $(4,610 - 3,935) / 4,610 = 15\%$, and the projected cost-savings \$47,305.

VII. Summary

Several HVAC modifications were implemented to the Operations Support Building (G-86) at the Mars Deep Space Station DSS-14 to reduce the required peak-load capacity, and decrease energy and costs. The introduction of the chilled water storage tank provided the sink for the excess cooling capacity available during nighttime operation and allowed a controlled shift of that capacity to the peak demand time. In addition, the chilled water storage acted as a margin of safety for unexpected changes in load or cooling equipment failure.

Automatic controls were optimally designed to operate with the optimum combination of mechanical equipment required to meet the HVAC demand, and provided the basis for the lowest operating and maintenance cost obtainable.

Computer simulations were performed using the ECP program and the simulation results were compared against the actual meter reading. The results agreed to within 3%.

Acknowledgments

The authors are indebted to Floyd W. Stoller (Ground Antennas and Facilities Engineering Section) for his direction, leadership, and invaluable contribution to energy conservation projects. To Fikry L. Lansing (Ground Antennas and Facilities Engineering Section) for his coordinating effort in completing this article. To G. Walls and Chris Yung (Ground Antennas and Facilities Engineering Section) for helping with the ECP program runs. And to A. Cantu (Ground Antennas and Facilities Engineering Section) for his support throughout the phases of the project.

Reference

1. Yung, C. S., "Computerized Energy Analysis for the Mars Operations Support Building," *TDA Progress Report 42-64*, pp 247-256, Jet Propulsion Laboratory, Pasadena, California, May/June 1981.

List of Symbols

ACCU	Air-cooling condenser unit	kW(e)	Kilowatt (electrical)
AH	Air handler	kWh(e)	Kilowatt-hour (electrical)
ASHRAE	American Society of Heating, Refrigeration and Air-Conditioning Engineering	kWh(t)	Kilowatt-hour (thermal)
B	Boiler	kWh(e)/yr	Kilowatt-hour (electrical) per year
BD	Barometric or backdraft damper	l	Liter
Btu	British thermal units	LC	Liquid cooler
C	Compressor	l/s	Liters per second
°C	Degree centigrade	MD	Motorized damper
CFM	Cubic feet per minute	MDU	Main distribution—utility
CH	Chiller	mm H ₂ O	Millimeters of water
CU	Air-cooled condensing unit	Mod	Modification
E _C	Economizer	MWh(3)	Megawatt-hour (electrical)
ECARP	Energy Conservation Awareness and Recognition Program	MWh(t)	Megawatt-hour (thermal)
ECP	Energy Consumption Program	NCP	Network Consolidation Program
ECR	Energy Conservation Representative	OSA	Outside air
EH	Electric duct heater	P	Pump
°F	Degrees fahrenheit	RA	Return air
FY	Fiscal year	RH	Relative humidity
GPM	Gallons per minute	SCE	Southern California Edison
HP	Horsepower	ST	Storage tank
HVAC	Heating, ventilating and air-conditioning	TFC	Technical facilities controller
HU	Humidifier or steam injector	ton	Ton of refrigeration
in H ₂ O	Inches of water	UPS	Uninterrupted power supply
kW	Kilowatt	VAV	Variable air volume
		Z	Zone

Table 1. Original configuration and ECP zone identification (Phase I)

Zone No.	Room		Floor	Zone Air Flow CFM (l/s)	ECP Zone No.
	No.	Name			
1	101	Control room, plenum	1	40,000 (18,000)	2
	102	Communications room, plenum			
2	201	Control room comfort	2	4,480 (2,115)	3
3	202	Communication room comfort	2	2,000 (945)	3
4	206, 207 208, 209	Offices	2	2,350 (1,100)	1
	202	Corridor			
5	210, 211	Offices	2	400 (190)	4
6	105	Frequency Standard Control Room (Hydrogen maser room)	1	2,000 (945)	6
7	205	Women's rest room	2	125 (60)	5

Table 2. Yearly energy consumption and costs – Mod-0, Mod-1, Mod-2, Mod-3, and Mod-4

Mod	Accessories		Lights			Equipment		Thermal Meter kWh(t)	Electric Meter kWh(e)	Cost, Dollars
	Thermal Btu	Electrical 10 ⁶ kWh(e)	Incandescent 10 ³ kWh(e)	Fluorescent 10 ⁶ kWh(e)	Electric 10 ⁶ kWh(e)	Mechanical kWh(e)	Thermal tons			
Mod-0	0	0.438	0.365	0.211	0.749	0	0	0	1,856,944	92,847
Mod-1	0	0.438	0.365	0.211	0.749	0	0	0	1,851,731	92,587
Mod-2	0	0.438	0.365	0.211	0.749	0	0	0	1,849,902	92,495
Mod-3	0	0.370	0.365	0.211	0.749	0	0	0	1,757,267	87,863
Mod-4	0	0.402	0.365	0.211	0.749	0	0	0	1,558,538	77,927

Table 3. Chilled water storage tank energy consumption and costs – Mod-5

Parameter	Without Storage Tank	With Storage Tank	Annual Savings
Yearly energy consumption, kWh(e)	206,950	172,810	34,137
Yearly energy costs, dollars	14,893	12,469	2,423

Table 4. Summary of all modifications (Phase I)

Mod No.	Description	Annual Energy Consumption		Estimated Construction Costs, Dollars	Annual Costs, Dollars	Annual Costs Saving, Dollars	Payback Period, Years
		Thermal MWh(t)	Electrical MWh(e)				
Mod-0	Original condition	0	1,856.9	--	92,847 ^a 130,914 ^b	--	--
Mod-1	Addition of dead controls	0	1,851.7	2,000	92,587 ^a 130,548 ^b	260 ^a 366 ^b	5.46
Mod-2	Addition of VAV control to Zone Z-3	0	1,849.9	1,500	92,495 ^a 130,418 ^b	92 ^a 130 ^b	11.54
Mod-3	Rearranging HVAC system addition of CHW system	0	1,757.3	80,000	87,863 ^a 123,887 ^b	4,632 ^a 6,531 ^b	12.25
Mod-4	Addition of HVAC status panel and econ. and auto reset for AH2 and AH3	0	1,558.5	90,000	77,927 109,877	9,936 ^a 4,010 ^b	6.42
Mod-5	Addition of chilled water storage tank (10,000 gal.)	0	1,525.4	25,000	76,029 ^a 10,754 ^b	1,718 ^a 2,423 ^c	10.30
Total All Mods		0	1,524.4	198,500	76,209 ^a 107,454 ^b	16,638 ^a 23,460 ^b	8.46

^aAnnual cost and annual cost savings on a fixed rate of 0.05 dollars/kWh(e).

^bAnnual cost and annual cost savings adjusted for variable rate (0.07/0.05).

^cAnnual cost savings was calculated on a variable rate.

Table 5. ECP zone identification (Phase II)

Zone No.	Room		Zone Air Flow CFM, l/s	ECP Zone No.
	No.	Name		
1	101	Control room, plenum	82,000	2
	102		(38,695)	
2	200	Control room, comfort	3,800	3
	201		(1,795)	
3	206	Lounge room	2,850	1
	207	New monitor room	(1,345)	
4	208	New communications room	2,200 (1,040)	4
5	204	Women's rest room	150 (70)	5
6	105	Frequency Standard Control Room (Hydrogen maser room)	5,000 (2,360)	6
-	-	-	2,000 (945)	7*

*Bypass air flow at Unit AH-1.

Table 6. Yearly energy consumption and costs – Mod-6, Mod-7 and Mod-8

Mod	Accessories		Lights			Equipment		Thermal Meter kWh(t)	Electric Meter kWh(e)	Cost, Dollars
	Thermal Btu	Electrical 10 ⁷ kWh(e)	Incandescent 10 ³ kWh(e)	Fluorescent 10 ⁶ kWh(e)	Electric 10 ⁶ kWh(e)	Mechanical kWh(e)	Thermal tons			
Mod-6	0	0.1363	0.365	0.255	0.2234	0	0	0	4,610,038	322,703
Mod-7	0	0.1111	0.365	0.255	0.2234	0	0	0	4,132,582	289,281
Mod-8	0	0.1111	0.365	0.255	0.2234	0	0	0	3,991,366	279,396

Table 7. Chilled water storage tank energy consumption and costs – Mod-9

Parameter	Without Storage Tank	With Storage Tank	Annual Savings
Yearly energy consumption, kWh(e)	495,680	439,350	56,332
Yearly energy costs, dollars	35,321	31,223	4,098

Table 8. Summary of all modifications (Phase II)

Mod No.	Description	Annual Energy Consumption		Estimated Construction Costs, Dollars ^b	Annual Costs, Dollars ^c	Annual Costs Saving, Dollars	Payback Period, Years
		Thermal MWh(t)	Electrical MWh(e)				
Mod-6	Original condition and addition of AH5 and AH6 ^a	0	4,610		322,703	–	
Mod-7	Addition of dead band controls	0	4,133	26,000	289,281	33,422	0.8
Mod-8	Addition of Chilled Water System No. 2						
Mod-8	Addition of HVAC status panel. Economizer and automatic reset for AH5 and AH6	0	3,991	40,000	279,396	9,785	4.1
Mod-9	Connection of Chilled Water System No. 2 to existing chilled water storage	0	3,935	4,000	275,298	4,098	1.0
Total All Mods		0	3,935	70,000	275,298	47,305	1.5

^aThe hypothetical Mod-6 is based on the original air handling and DX systems, in addition to Units AH5 and AH6 with their corresponding DX systems.

^bEstimated construction costs shown are the additional costs for the chilled water system, economizer, and automatic controls, above the cost required for a DX system of identical capacity.

^cAll annual costs were calculated on a fixed rate of 0.07 dollars/kWh(e), except Mod-9, which was calculated on a variable rate.

Table 9. ECP input data and test performance data

Location	Input Data	Test Data
Plenum	64° F	63° F (at 50% RH) 64° F (at 80% RH)
Control room	72° F	72° F – 73° F (at 50% RH) 71° F – 75° F (at 80% RH)

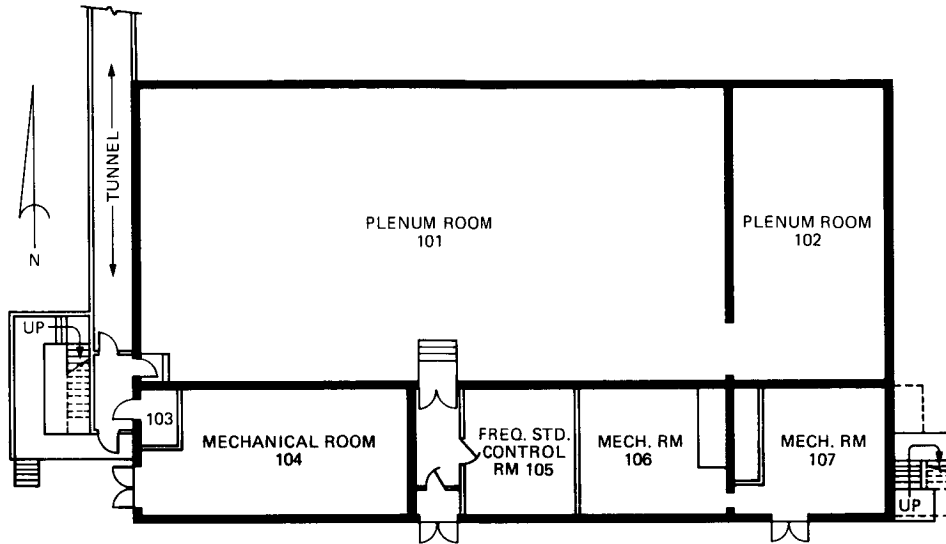


Fig. 1. Operations Support Building, first floor plan

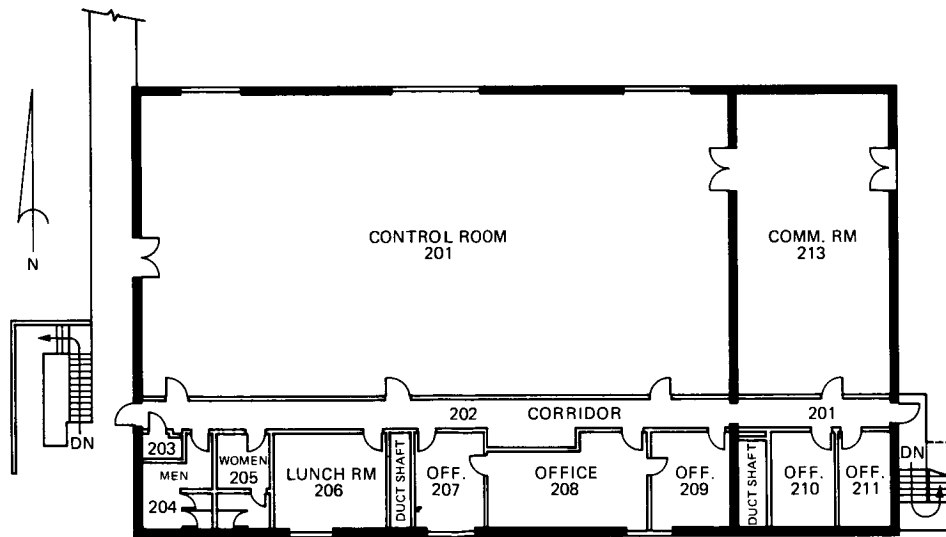


Fig. 2. Operations Support Building, second floor plan

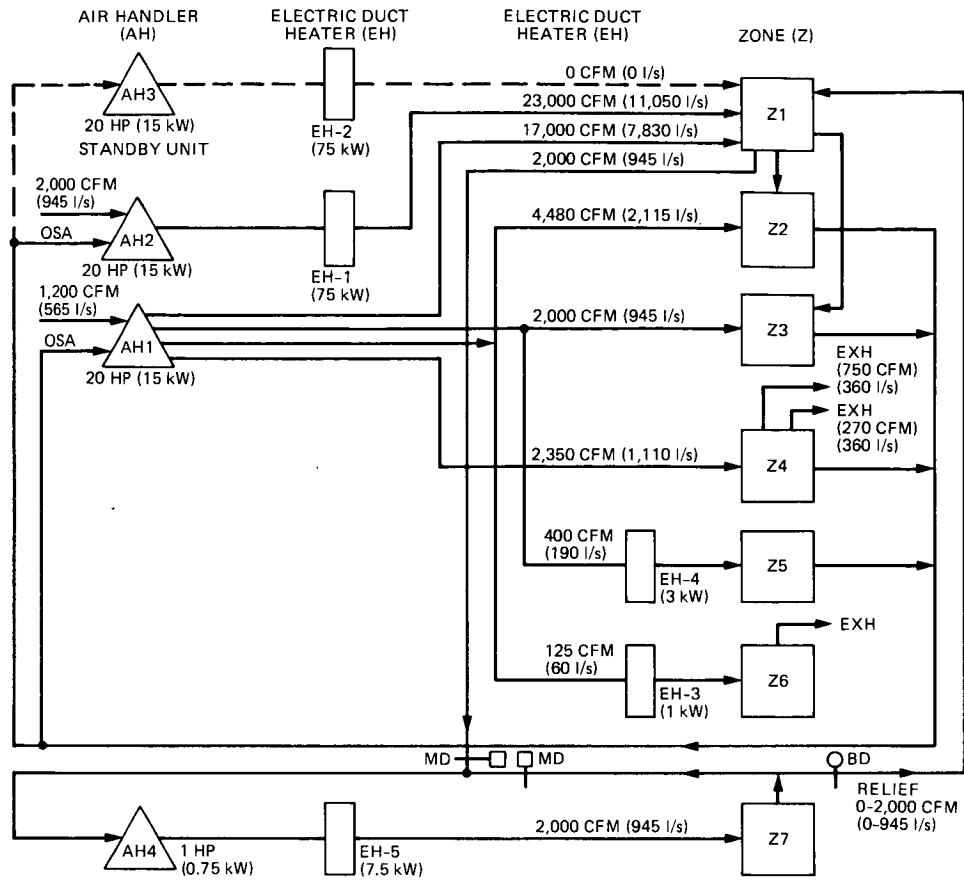


Fig. 3. Original HVAC zoning and air flow configuration

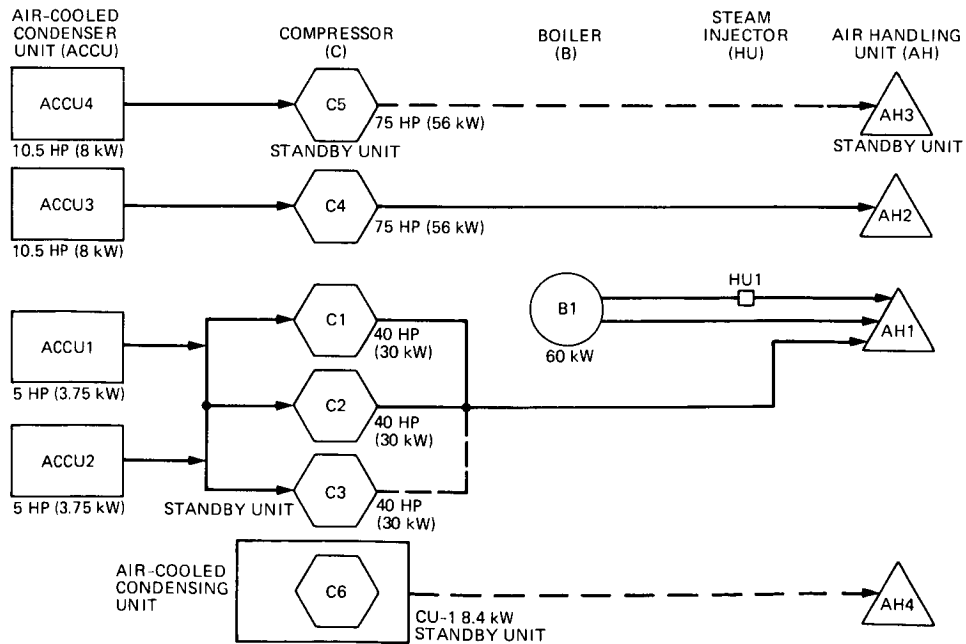
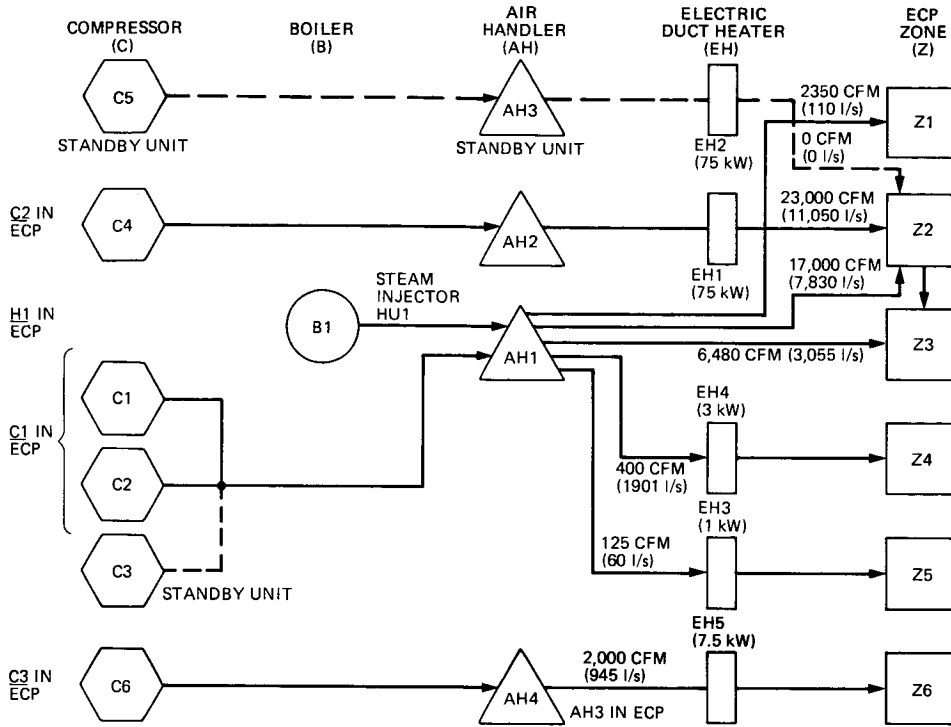


Fig. 4. Original cooling and heating equipment configuration



- NOTES: 1. ALL STANDBY UNITS ARE NOT MODELED BY ECP.
 2. ELECTRIC DUCT HEATERS EH1, EH2, EH3, EH4 AND EH5 ARE NOT ECP MODELED.
 3. RETURN/RELIEF/EXHAUST FROM ZONES ARE NOT SHOWN FOR CLARITY.

Fig. 5. Original HVAC configuration (ECP modeling)

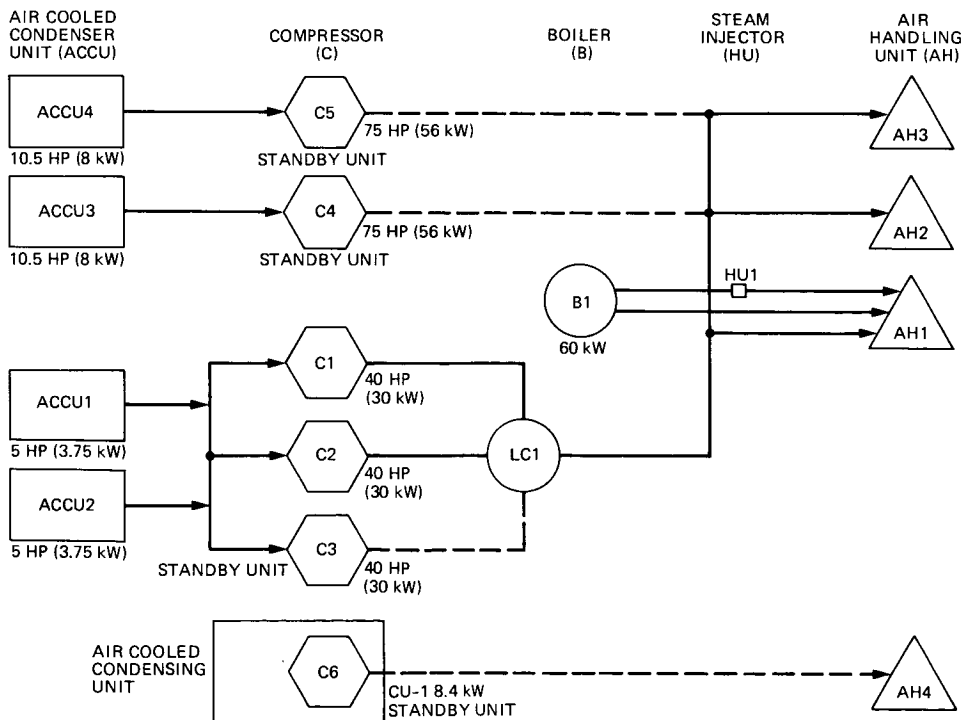


Fig. 6. Modified cooling and heating equipment configuration

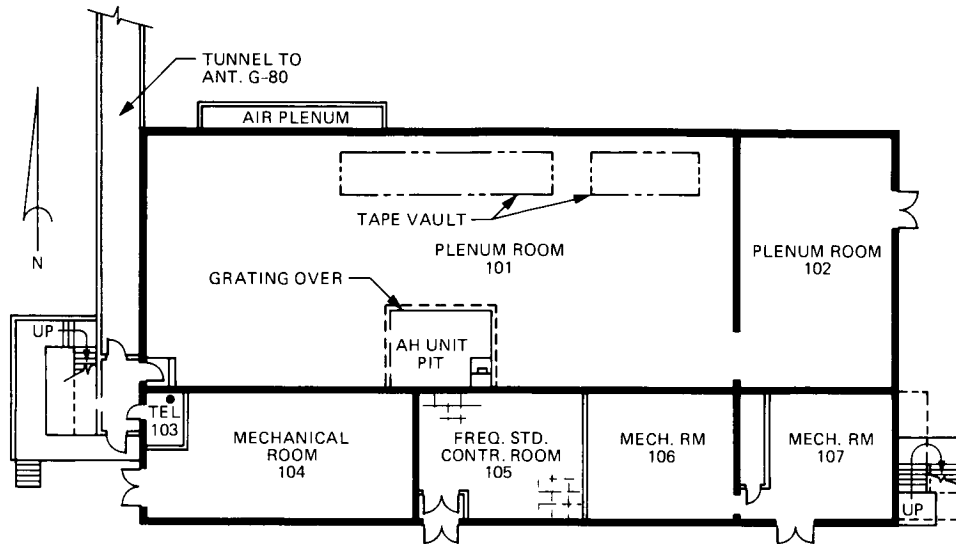


Fig. 7. Operations Support Building, first floor plan, modified

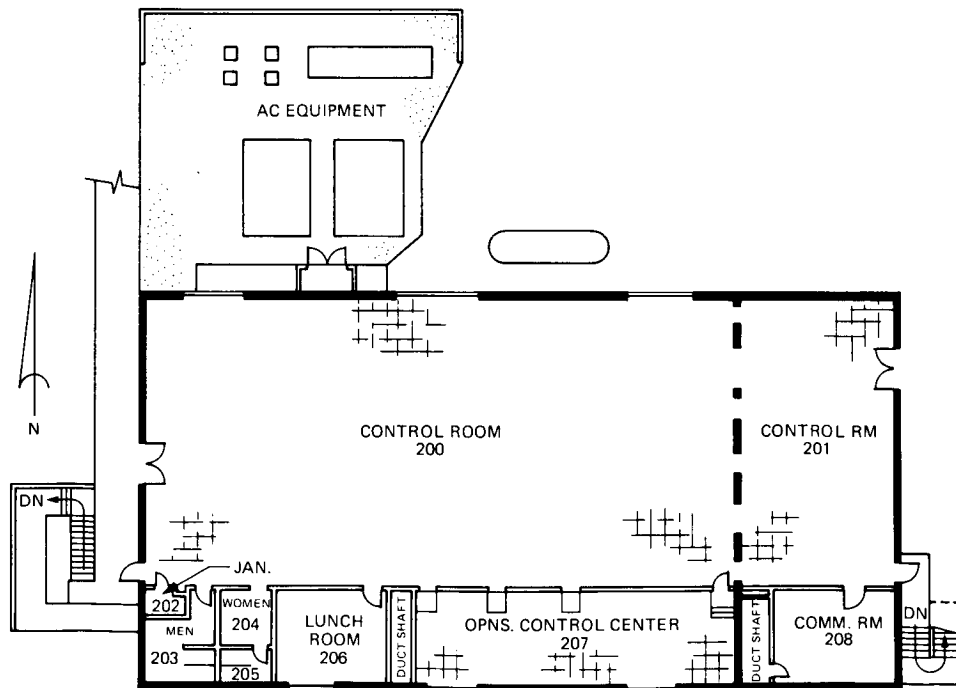


Fig. 8. Operations Support Building, second floor plan, modified

ORIGINAL PAGE IS
OF POOR QUALITY

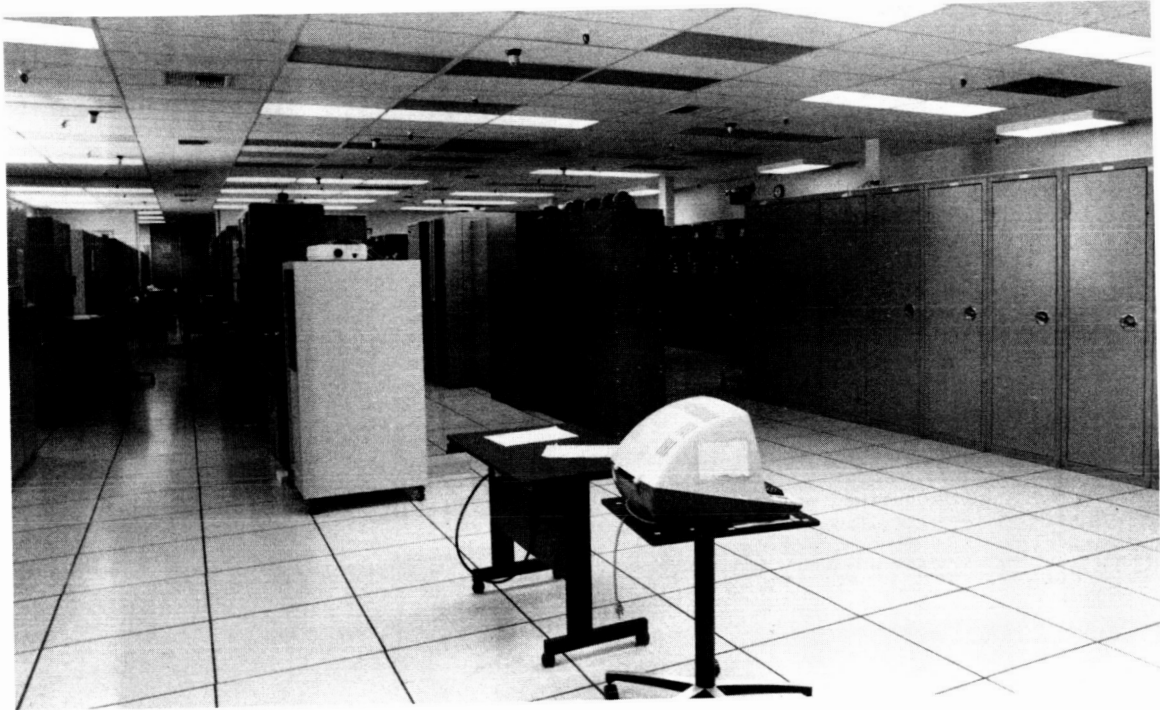
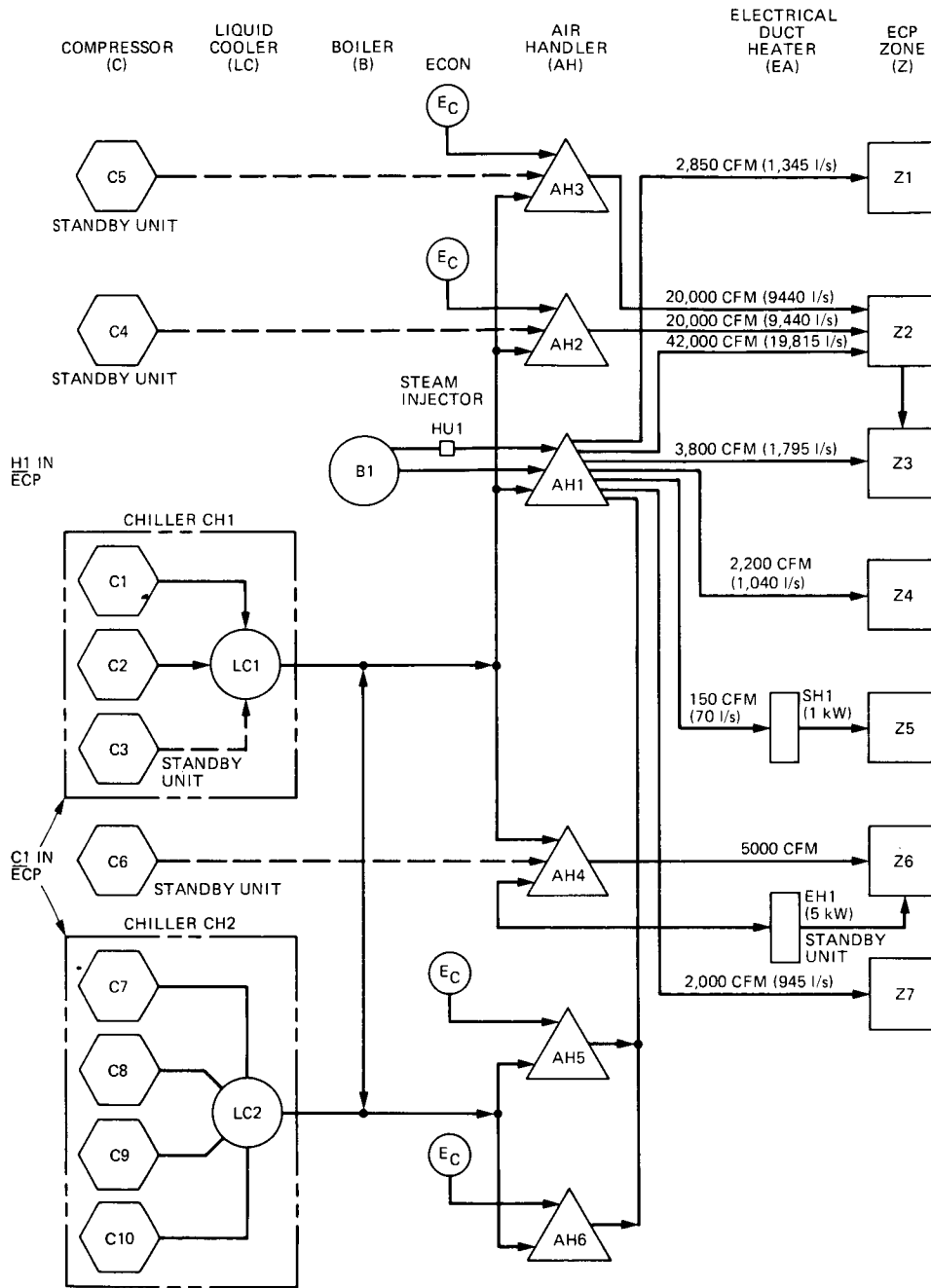


Fig. 9. View of actual control room (201)



- NOTES: 1. ZONE 7 (NO LOAD) IS INTRODUCED IN THE COMPUTER MODEL AS A REQUIREMENT FOR UNIT AH1 TO OPERATE IN THE STABLE PART OF THE FAN CURVE (11,000 CFM/5,190 l/s MIN.).
 2. ELECTRIC DUCT HEATER EH3 FROM PHASE I IS NOW RENAMED SH1.
 3. ALL STANDBY UNITS ARE NOT ECP MODELED.
 4. RETURN/RELIEF/EXHAUST FROM ZONES ARE NOT SHOWN FOR CLARITY.

Fig. 10. Actual HVAC configuration

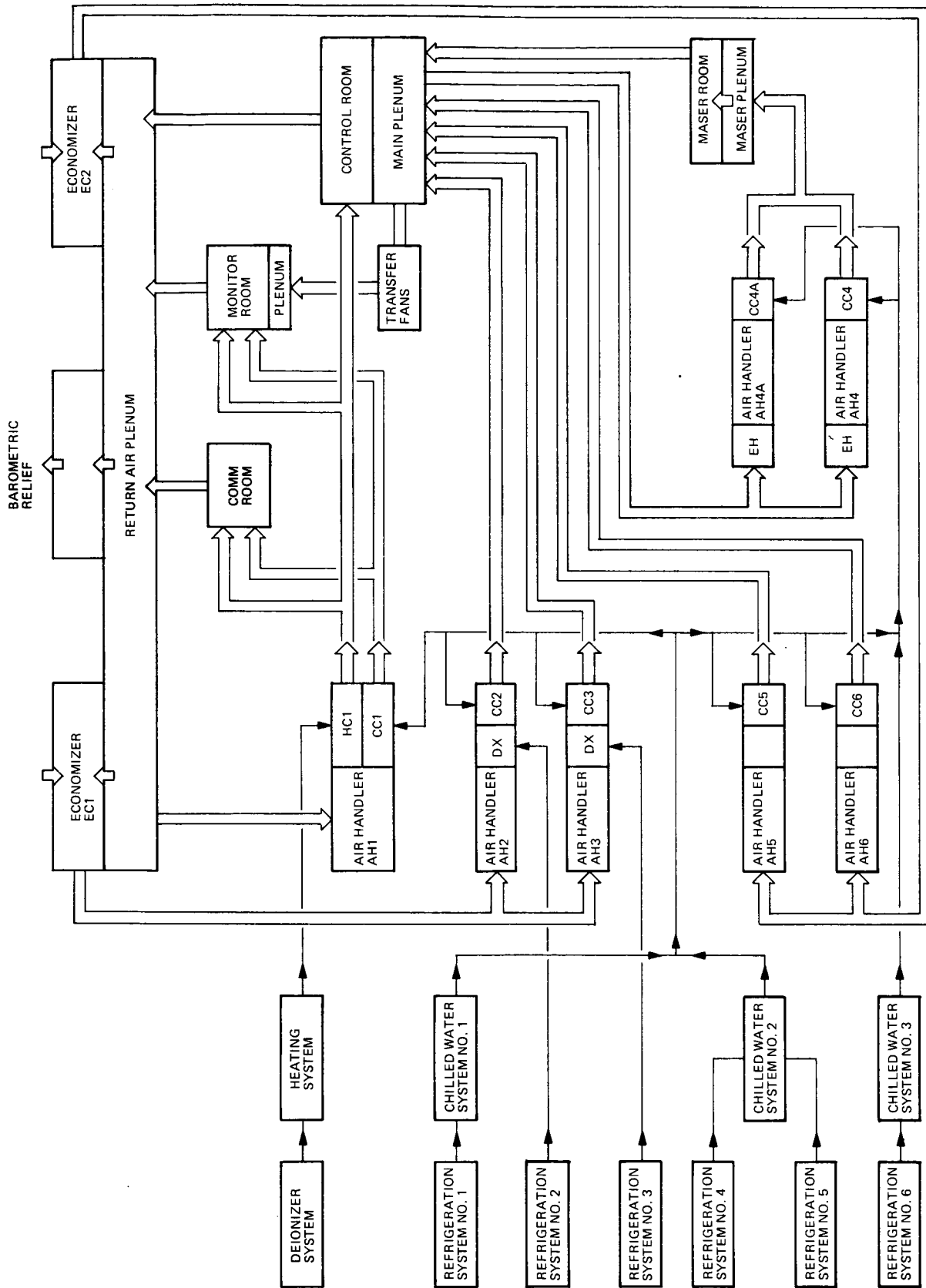


Fig. 11. HVAC, functional block diagram

C-3

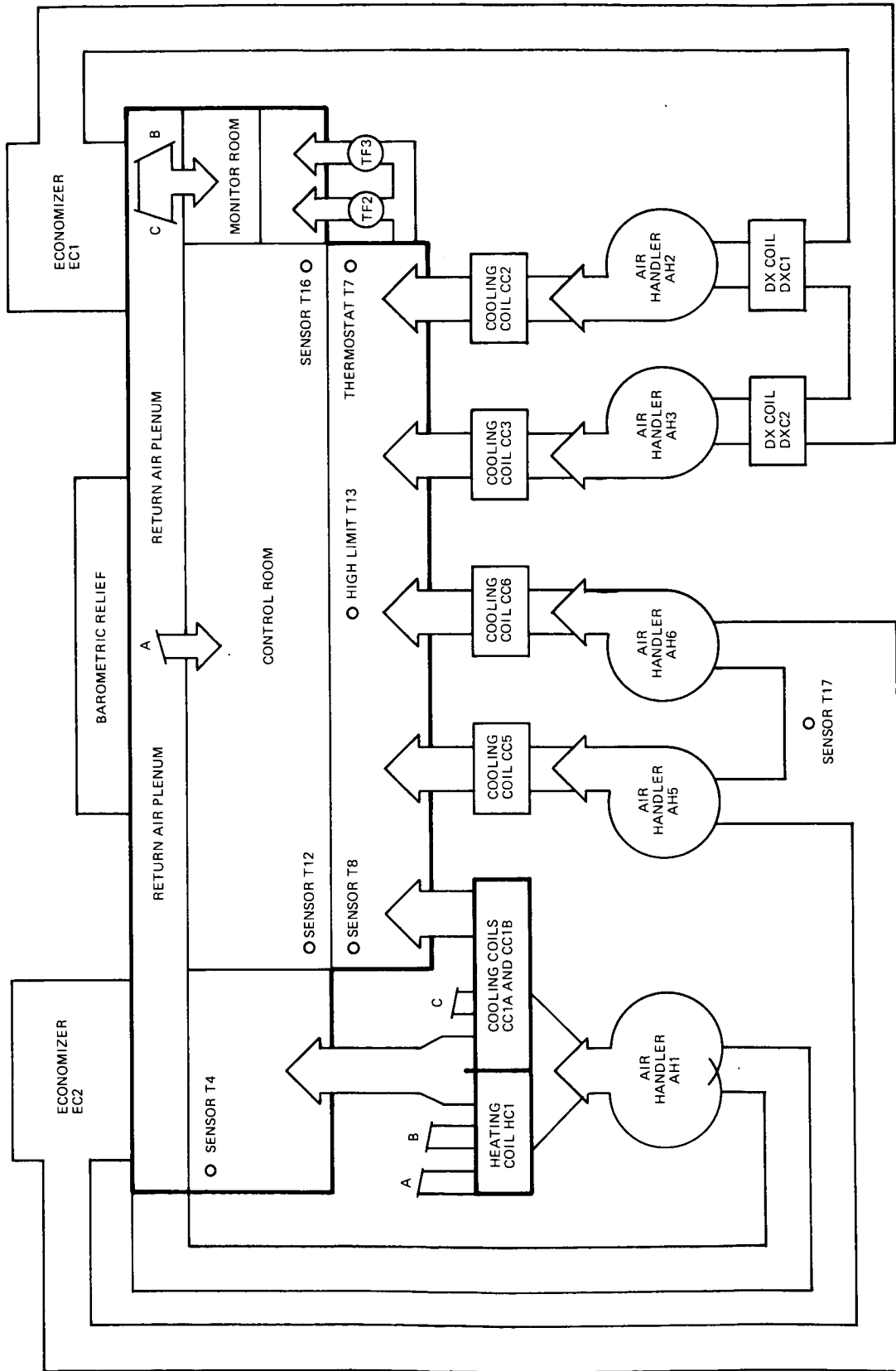


Fig. 12. Air distribution, functional block diagram

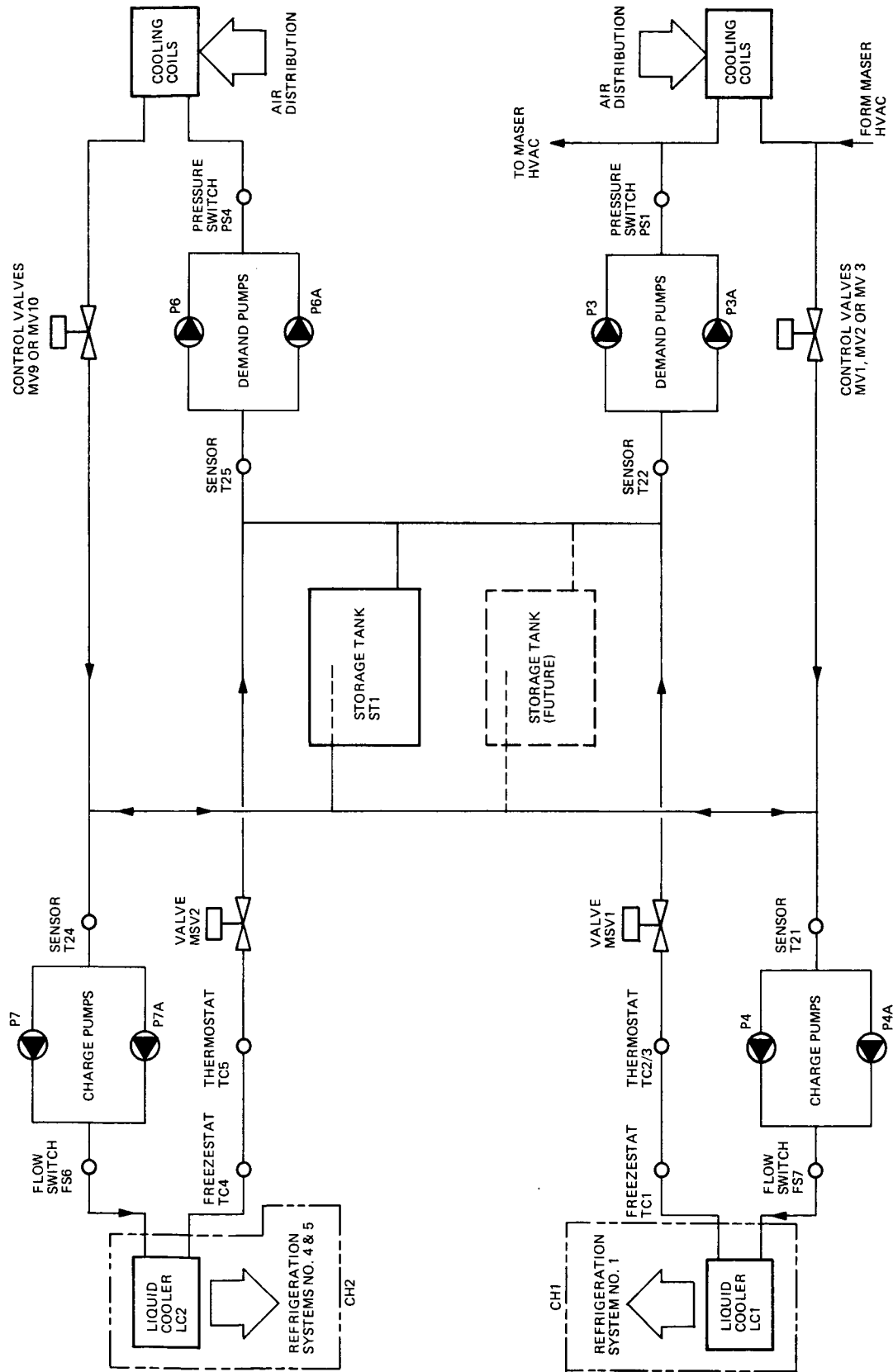


Fig. 13. Chilled water, functional block diagram

ORIGINAL PAGE IS
OF POOR QUALITY

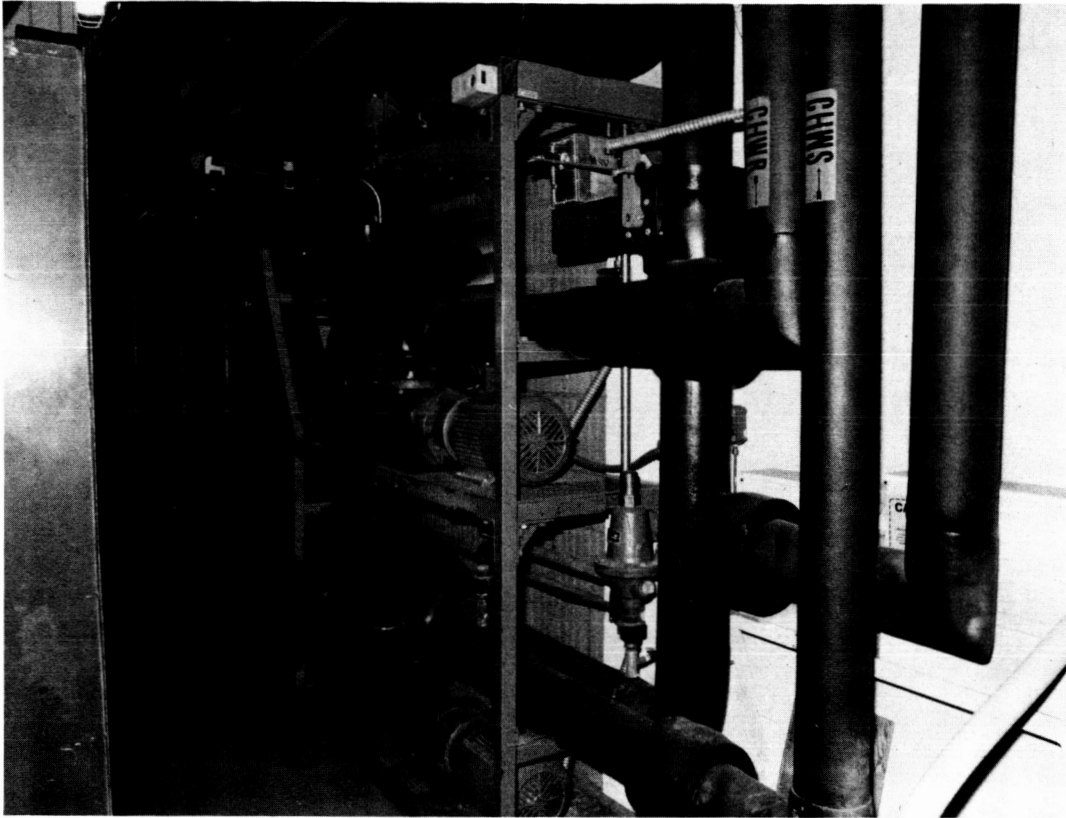


Fig. 14. Liquid Cooler LC1, Pumps P3, P3A, P4 and P4A assembly

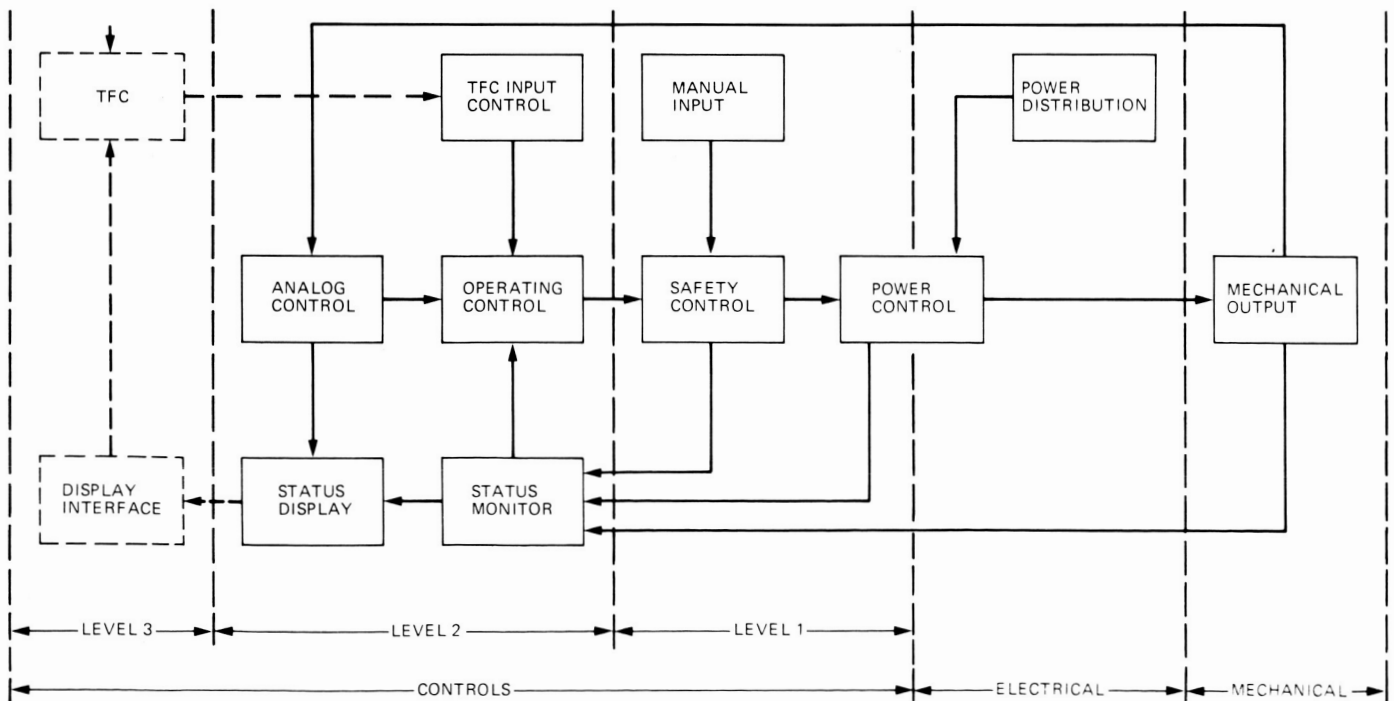


Fig. 15. HVAC controls, functional block diagram

ORIGINAL PAGE IS
OF POOR QUALITY

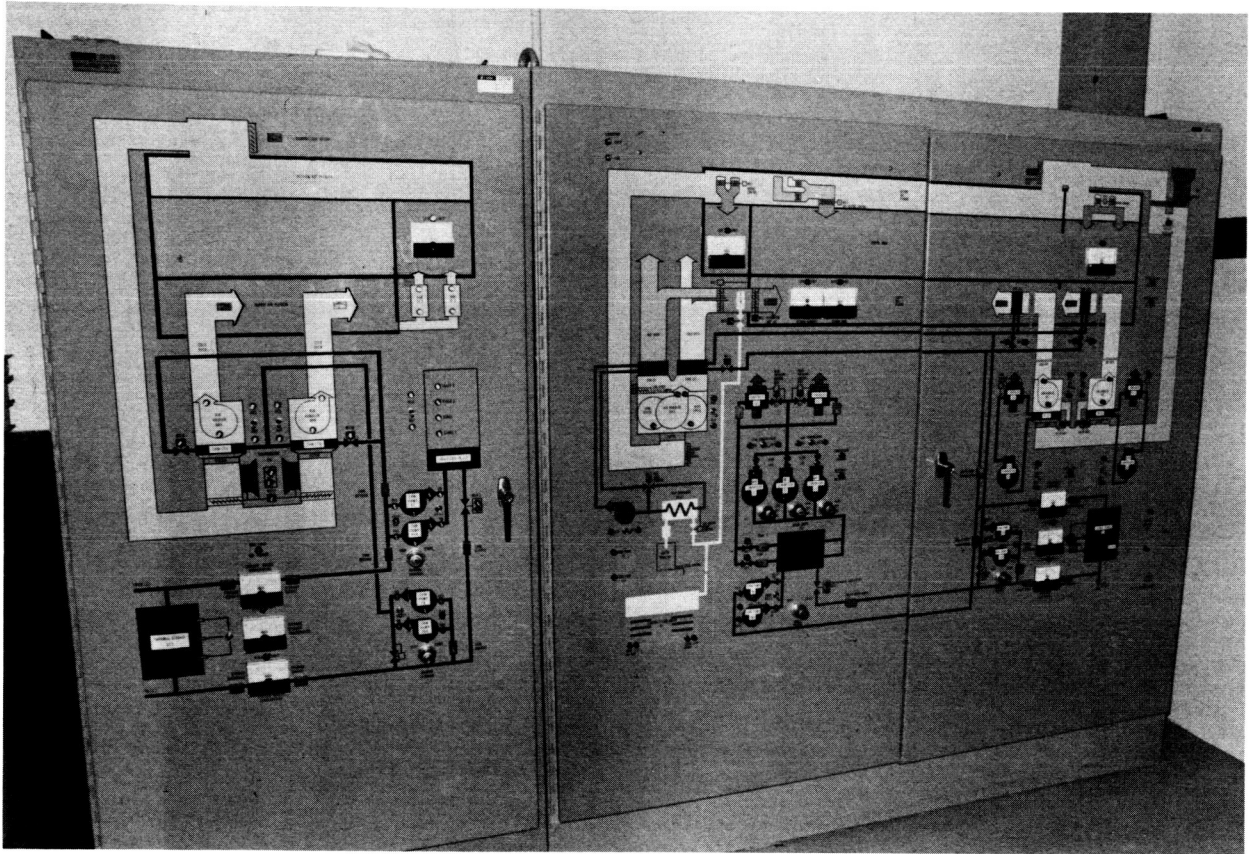


Fig. 16. HVAC status panel

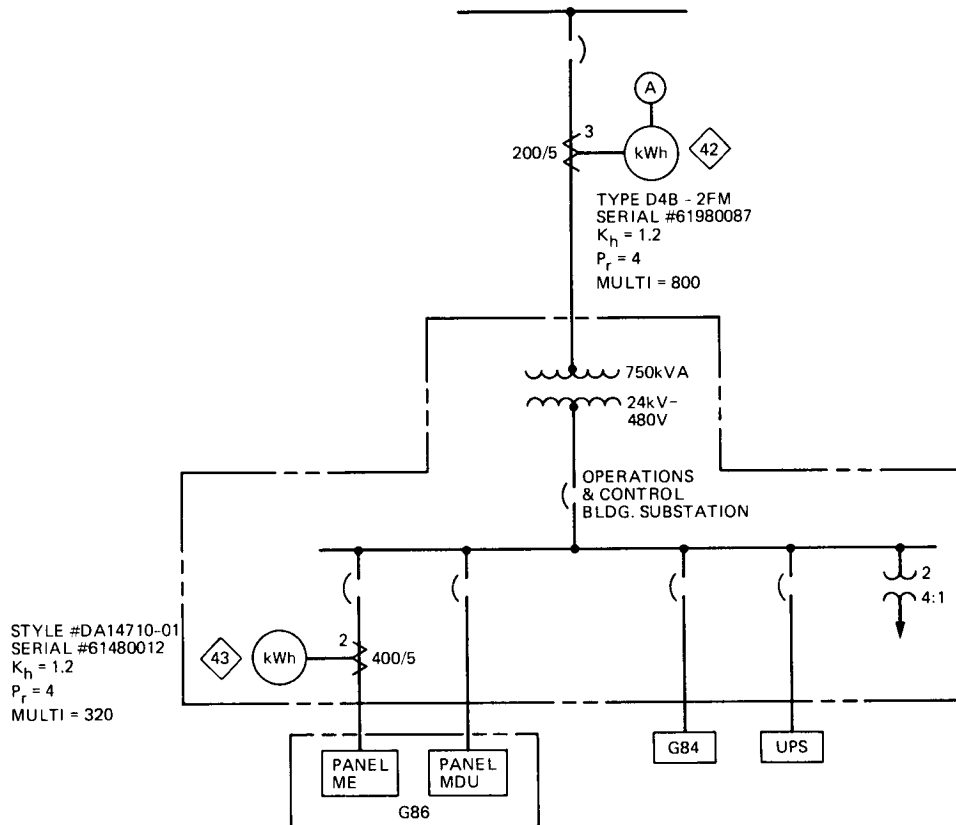


Fig. 17. Electric meters for Operations and Control Substation and for Building G-86

13160

Reverse Osmosis Water Purification System

H. G. Ahlstrom, P. S. Hames, and F. J. Menninger
Ground Antenna and Facilities Engineering Section

A new reverse osmosis water purification system, which uses a programmable controller (PC) as the control system, was designed and built to maintain the cleanliness and level of water for various systems of a 64-m antenna. The installation operates with other equipment of the antenna at the Goldstone Deep Space Communication Complex. The reverse osmosis system was designed to be fully automatic; with the PC, many complex sequential and timed logic networks were easily implemented and are modifiable. The PC monitors water levels, pressures, flows, control panel requests, and set points on analog meters; with this information various processes are initiated, monitored, modified, halted, or eliminated as required by the equipment being supplied pure water.

I. Introduction

A reverse osmosis water purification system was designed and installed for the Goldstone Deep Space Communication Complex, California. This article describes the water treatment requirements, control philosophy, and hardware and software specifications.

The moving part of the 64-m antenna shown in Fig. 1, a complex structure weighing over 3.2×10^6 kg (7×10^6 lb), rotates horizontally on a film of oil 0.2 mm (0.008 in.) thick beneath three large pads. The risk of losing a spacecraft track is high if the hydrostatic bearing fails due to insufficient cooling.

There are three requirements for pure water for systems that support the antenna operation. The first is cooling water for the hydraulic system that maintains the critical film of oil beneath each pad. The second requirement is for pure coolant water for the high-power transmitter. The third pure water use is for make-up water for the boilers and chilled-

water loop of the air conditioning system. Water supplied to the station is pumped from nearby underground wells. The chemical composition and quality are not adequate for direct use; therefore, a purification system is necessary to meet the specifications.

II. Functional Requirements

The performance and functional requirements for the pure water system can be summarized as follows:

The two principal design criteria for the water purification system are reliability and flexibility — reliability is derived from the mission requirements and flexibility from the need for versatility in monitoring and control, to permit unattended operation. This versatility must meet constantly changing process requirements, which include such events as placing an operation on "hold" to perform another process, and sensing the proper conditions for returning to the original operation.

Without automatic controls, such variations would require labor-intensive attention to the equipment.

Several water purification systems were considered, including gas/oil fired water distillation, solar stills, reverse osmosis, and purchasing purified water from a commercial water supplier. The stringent cleanliness standards for the product of this system, as well as the reliability required, led to the selection of reverse osmosis as the type of purification preferred. The need for reliability and flexibility resulted also in the selection of a programmable controller to manage the operation. The reverse osmosis system is shown in Fig. 2.

It was required that the plant be nearly maintenance free. The new design should have process error checking and fully automated operation, should automatically perform routine "housekeeping" functions, and should be capable of remotely controlled operation.

III. Reverse Osmosis Principles of Operation

Osmosis is the spontaneous passage of a liquid from a dilute to a more concentrated solution through a semipermeable membrane, which allows passage of the liquid but not of dissolved solids. Reverse osmosis (R.O.) is the forced reversal of this natural phenomenon, usually accomplished by applying enough pressure to the concentrated solution to overcome the natural pressure (osmotic pressure) of the less concentrated solution.

This property of some membrane materials makes them ideal for water purification. In general application, the membrane unit is made up of either a bundle of fibers approximately the diameter of a human hair, or a spiral-wound membranous material, within an epoxy tube. In either case, the membrane surrounds a central core, within which the clean, or "product" water flows after permeating through the membrane to the core.

The reject water, or "concentrate," emerges from the outside membrane material on the same side where the raw water entered. No chemical reactions or phase transitions are involved. One of the principal advantages of semipermeable membranes over other methods of separating water from its contaminants is that, with proper care, the membranes can be expected to last from three to five years.

This article focuses on the application of a programmable controller (PC) to control the R.O. process. It is therefore necessary to be aware of the constraints on the operation of the system and the process variations to take advantage of the flexibility the programmable controller provides.

IV. The Reverse Osmosis Process

The water purification process at the Goldstone antenna is divided into three stages: pretreatment, reverse osmosis, and post-treatment. The process is controlled by a programmable controller. The controller's actions are determined by the status of switches on the control panel and various sensors on the process equipment. An instrumentation panel monitors various analog signals and reports out-of-bounds conditions to the PC.

Figure 3 is a simplified flow diagram of the R.O. system. Many essential controls are omitted for simplification; the diagram is not intended as a complete representation but only as an aid to the discussion.

A. Pretreatment Stage

The reverse osmosis unit processes raw water from either the local water supply (demand tank fill) or the cooling tower sump water (tower recycle). The water cannot be run directly into the R.O. membranes; it must first go through preliminary processing so as not to damage the membranes. This pretreatment involves flowing the water through a sand filter (to remove large dirt particles) and a carbon filter (to remove chlorine, which would oxidize the membranes), injecting acid to control pH level to a slightly acidic condition (excess alkalinity can foul membranes), and flowing the water through a 10-micron prefilter and then past sensors that check for pH level and the presence of chlorine. (Raw water typically has a pH of 8.5 to 11.5; the R.O. membranes require the pH to be approximately 6.0.) Now the water contains very few nondissolved solids, but is still high in dissolved solids. It is now ready for the reverse osmosis treatment.

B. Reverse Osmosis Treatment Stage

The reverse osmosis treatment section consists of pressure switches, flow controls, conductivity ratio sensors, flow meters, R.O. membranes, pressure gauges, and a main pump. Each of these is critical to the production of purified water.

The inlet pressure to the pump must remain above 10 psi to avoid cavitation in the pump. The inlet pressure to the membranes must stay below 400 psi; otherwise the membranes will be damaged. Pressure switches monitor these critical items.

The flow controls are adjusted to maintain a ratio of 50 percent product water and 50 percent reject water, with a production flow of 15 gallons per minute. The reject water contains all the impurities removed from the product water and drains into the sewer.

The conductivity ratio sensors are part of the membrane efficiency meter, shown in Fig. 4, measuring the amount of dissolved solids in the water. The total dissolved solids in feedwater are typically 500 to 600 parts per million (ppm). Product water typically contains less than 45 ppm. The meter determines what percentage of dissolved solids is being rejected by the membranes; when it drops below 90 percent, the **PRODUCT WATER LOW REJECT RATIO** error signal is generated.

C. Post-Treatment Stage

Product water flows through an ultraviolet sterilizer, and then to either the demand tank by way of a degassifier, or to the cooling tower for sump recycle. The ultraviolet sterilizer kills bacteria in the water. The degassifier is a tall chamber above the demand tank, filled with saddle packing; water flows down over these saddles as air is simultaneously blown up over them removing dissolved gasses.

From the degassifier, product water flows into the demand tank until it reaches a preset level, monitored by a level switch. The demand tank can then drain to either the shutdown flush pump, or the demand pump. The shutdown flush pump supplies product water to the main pump for a cleaning flush of the membranes after every operation. The demand pump supplies water to the additional PC-controlled functions.

V. Additional Control Functions of the PC

In addition to processing water through the R.O. unit, the PC manages the water level of the cooling tower, a transmitter coolant storage tank, and an air conditioning chilled water storage tank. In addition, it manages the cleanliness of the cooling tower. The demand pump pumps water to three places, as selected by solenoid valves: the heating and air conditioning system (make-up water), the cooling tower sump, or the transmitter coolant system storage tank through a deionizer.

A. Cooling Tower Functions

A front panel switch, as shown in Fig. 5, tells the PC whether to refill the sump with raw water, purified water from the R.O., or nothing. The cleanliness of the tower water is monitored by a conductivity meter on the instrument panel. When a preset high limit in the conductivity meter is reached, the PC starts a cleanup process as determined by another front panel switch, which tells the PC whether to recycle the sump water through the R.O. or to pump it to the drain (blow down). Blow down is the operation of removing water from the sump and replacing it with fresh water. The controller blows down the sump by pumping water to drain and

replacing the lost water with either raw or R.O. water, as selected. (If neither recycle nor blow down is selected, an alarm is generated.) When conductivity reaches the low limit, the PC ends the cleanup process.

In recycle mode, the R.O. returns only 50 percent of the water it removes from the tower. If the refill switch is on R.O., then the other 50 percent is furnished from the demand tank. Since the R.O. must be flushed after each water producing cycle, there must be enough water in the demand tank to flush the R.O. membranes. Therefore, when the demand tank is below this middle level switch the PC will first fill the demand tank before proceeding with the recycle request.

B. Transmitter Tank Fill Function

The front panel switch selects between **MANUAL—OFF—AUTOMATIC** refill of the transmitter coolant tank. In automatic, a level switch indicates to the PC the need for water. (In manual, the level switch is overridden.) If the demand tank is not empty and the tower is not being refilled, the demand pump is turned on and a valve opens to send water to the transmitter coolant tank through a deionizer. The deionizer further purifies the water to a resistivity of at least 2 megohms/centimeter. (With a fresh deionizer, the output can be as high as 16 megohms/centimeter.) The water is monitored by a resistivity meter that has a preset low-level trip point, at which the **XMTR WATER LOW RESISTIVITY** error signal is generated when the water is too conductive. To prevent excess water from being pumped to the transmitter, this function can be active for only ten hours. Then the system must be reset before more water will be pumped to the transmitter.

C. Air Conditioning System Fill Function

In normal operation, a manual valve is opened and water is allowed to flow down to a chilled-water storage tank at the control building for the air conditioning system and to the humidifiers. (There is an elevation difference of approximately 30 feet.) If a large quantity of water is required, the demand pump may be turned on and the line to the storage tank pressurized (**G-86 PRESSURIZE** front panel indicator on). This function has the lowest priority, and is interruptible by the tower-refill-with-R.O.-water process or the transmitter-tank-fill process. To prevent excess water from being pumped to the storage tank, this function is active for only 10 hours. Then the system must be reset before more water may be pumped.

VI. Housekeeping Functions

At the end of each water-producing operation, the system automatically goes into a "shutdown flush" cycle. The flush pump pumps product water from the demand tank to the

main pump and then to the reverse osmosis unit. The product water from this operation returns to the demand tank or sump, depending on the production cycle that was just finished. The purpose of this flush is to feed very pure water into the membranes so as to flush out any contaminants.

A high-flow flush is performed once each day. (This is different from a shutdown flush and is performed even if no water production cycles have taken place that day.) A solenoid valve is opened to bypass the reject flow control valve; the reduced backpressure causes 90 percent of the water to go out the reject ports, thus flushing any solids from the surface of the membranes. The high-flow flush of the membranes lasts for fifteen minutes. In addition, once a week the sand filter and the carbon filter are backflushed, one at a time. Each of these filters is also backflushed when a high pressure drop exists across the filter.

All of these operations are part of programmed maintenance activities, independent of any other actions, and are initiated by the programmable controller's software clock. They are, however, subject to the same monitoring and alarm controls that accompany all other operations. The timing is part of the PC program; no additional hardware is required.

The sand filter and carbon filter backflush and the high-flow flush may be activated manually by using the power of the PC. This capability was accomplished without the use of an additional front panel switch. When all process selector switches are turned to OFF, and the ALARM ACKNOWLEDGE button is pushed twice, all three flushes are enabled. The sand filter is flushed first, followed by the carbon filter, and then the high-flow flush. At any time, each flush can be canceled by pushing the ALARM ACKNOWLEDGE button twice. This action establishes a form of reset, in which the first push holds everything, preventing the machine from running; the second push resets all sequences.

VII. Process Alarms

If any of eleven parameters is out of limits, an alarm sequence is initiated. Once a process is started, each instrument can generate an error signal, after a time delay has been satisfied to allow for transient water conditions. Once an error signal is generated, it will create an error routine that shuts off the applicable process. The eight processes of the R.O. system for purposes of alarm shutdown are demand tank fill, tower refill, tower recycle, tower blowdown, transmitter tank refill, air conditioning system pressurize, high-flow flush, and shutdown flush. After a five-minute delay, the controller will attempt to restart the interrupted process. This allows for the air bubbles that can get into the water supply. The delay

can be manually overridden by pushing the ALARM ACKNOWLEDGE button twice. If, after two restart attempts, the error still exists, the interrupted process will be shut off until it is manually reset by operator action (pressing the ALARM ACKNOWLEDGE button twice). The error is now a fatal error. When a fatal error occurs, an alarm is sent by the controller to a console at the communications center of the complex.

When an operator acknowledges an alarm, the system is placed in a "hold" condition with a 30-minute allowance for maintenance. If someone should forget to reactivate the system, the hold condition is canceled; if no reset has been input by this time, the system goes into SYSTEM SHUTDOWN mode and transmits an alarm.

VIII. Process History

The PC has been programmed to restart the system and continue, if an error does not reappear. This feature makes it difficult for maintenance personnel to determine whether there have been any errors since the last time the system was checked. Maintenance personnel may not check on the system for up to a week or two at a time. Repetition of a certain error can be a telltale signal that a certain section is becoming marginal and should be checked closely before it shuts the system down. As a maintenance feature, each error increments its own counter inside the PC when it shuts the system down.

There are also counters assigned to each process. Some count the number of times a process has occurred, and others count the number of five-minute increments each is on. These are useful in analyzing how the machinery has been used since the last time it was checked. The number of five-minute increments a process has been on can be multiplied by a constant to give an accounting of how much water was sent for each use; this number is within ten percent of the actual number and does not require costly totalizing flow meters to report back to the PC. There are two totalizing flow meters, one for the product water and one for the reject water, but they do not report back to the PC.

IX. The Programmable Controller Rationale

The large number of control and monitoring actions required in a system such as this makes the programmable controller an ideal choice for control methods. The necessity to effect the control actions, make the control change decisions, and provide the requisite isolation of sensor inputs from control outputs could suggest a completely computer-controlled system. But the sophistication of expensive computer hardware would constitute control "overkill" in this case, and the

cost would be compounded by the environmental protection necessary for most computer installations. The programmable controller modules are rugged and provide the ideal compromise, with cost savings on both ends.

For example, during pre-treatment, the water is monitored for excessive pressure drop at three stages, as well as for high or low pH or the presence of chlorine. If any sensor detects an out-of-limits condition, an error routine is generated and the condition is displayed on the appropriate analog meter. At the same time, corrective action is started by the PC. If another process was in progress at the time, it might continue, or be placed on "hold," depending on the relative importance of the two actions. Note that the relative importance can change; the first priority of the system is to keep the cooling tower sump filled; if the sump is not low, and another process, for instance the production of pure water, is ongoing and a high pressure drop occurs, the process would be suspended until the excessive pressure drop is corrected by a backflush of the offending tank. If, however, the cooling tower water level is low, refilling to a specified level would take priority and the backwash itself would be put on "hold."

In this application, several different conditions enable various processes. There are 32 inputs, 64 outputs, 114 internal logic relays, and 77 storage registers. Only 44 of the 77 storage registers are used for time delays and time-outs. To implement this design in discrete components would require a relay panel that was cost prohibitive, not to mention labor intensive. Moreover, should a slight change in process requirements occur, the task of rewiring would be time consuming and costly.

From an extensive survey of commercial programmable controllers available for this application, the Square D SY/MAX-20 (Fig. 6) was selected. Following are two of the features that determined the selection.

A. Dual Memory

The dual memory fits the reliability philosophy of this subsystem, which must support a very critical and probably unrepeatable mission. The application memory combines the advantages of random access memory (RAM) and electrically alterable read-only memory (EAROM) to ensure both the program flexibility offered by the RAM and the memory-saving characteristic of the EAROM. Program information stored in the EAROM is retained in the event of power failure, and even if the memory module is removed from the processor. The memory can be reprogrammed as often as desired, the change being as small as one contact or as large as the entire program.

These memory modules had several features unlike those of other manufacturers, at the time of purchase. The memory was programmed, when installed in the PC, with a command from the program to transfer the contents of the RAM to the EAROM. The memory was encased in a steel box with a rugged connector on the back. The connector configuration prevented the memory module from being inserted incorrectly into the PC.

B. Computer Interface Module

Another important feature is the computer interface module, which permits remote control and monitoring, as well as communication with the programmer. In this application all inputs, outputs, internal relays, and storage registers are accessible to a computer at a remote location. A modem in the PC cabinet is used to transmit this data to the computer terminal 14 miles from the pure water system installation. The computer can request any data that is stored in the PC at any time; and the PC can be called up as desired. This allows a historical record of how the system has been performing, and can indicate the development of trends in the process, such as gradually decreasing time between carbon filter backwashes, indicating the approach of the need to replace the carbon.

The computer interface allows access to information in the PC through a non-proprietary serial port. Any computer with a serial port could be programmed to communicate with the Square D processor.

X. Summary

The reverse osmosis water purification system for the NASA/JPL 64-meter antenna has been designed and installed. Utilization of a programmable controller made it possible to meet stringent performance requirements. The system has operated successfully since July 1982, with little or no preventive maintenance. Due to this increased reliability performance, the cooling system of the antenna has been much more reliable and has required significantly less maintenance.

One advantage of the programmable controller was the ability to make small program changes quickly during system startup: RAM could be modified and tested operationally before it was transferred to EAROM.

The successful experience gained by this PC installation led to the selection of PCs for control of other facilities at the Deep Space Communications Complex. Examples are as follows:

- (1) A 15-foot diameter mobile antenna used in the Orion earthquake research program: The SY/MAX-20 PC

controls antenna deployment, storage, and leveling of the trailer and antenna, making it possible to assemble and disassemble the system in 20 to 30 minutes.

- (2) The electrical power generating station at the Echo Station (DSS 12): This installation, with five 500-kW diesel generators, is also controlled by a SY/MAX-20.
- (3) Air conditioning for three buildings at DSS 12, buildings G26 (control room), G34 (hydromechanical building), and G35 (antenna): This complex system, designed

to meet the varying needs of three very different structures, utilizes a Square D Model 500 programmable controller, which simplifies control of a highly automated and energy efficient system.

The reverse osmosis water purification system, under programmable controller management, has met all of its principal design objectives: a cost-effective, high reliability, maintenance-free plant that incorporates fully automated operation, process error checking, automatic performance of routine housekeeping functions, and capability of remotely controlled operation.

ORIGINAL PAGE IS
OF POOR QUALITY

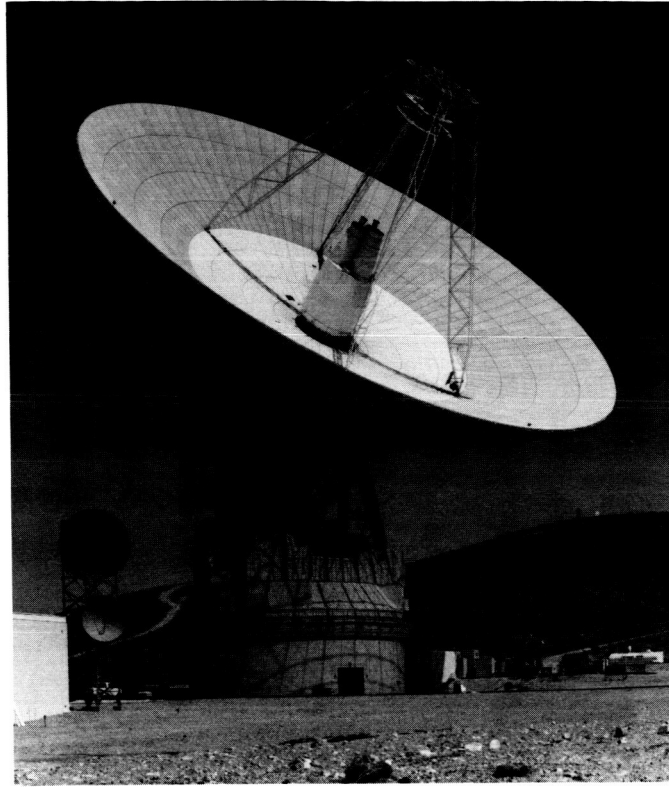


Fig. 1. The 64-m antenna at Goldstone, California

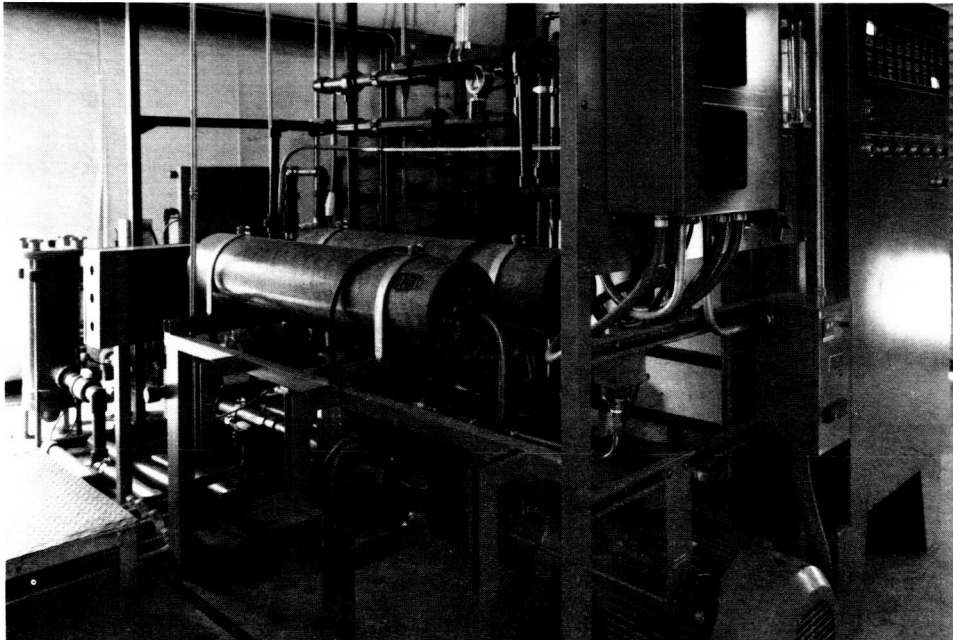


Fig. 2. Reverse osmosis water purification system

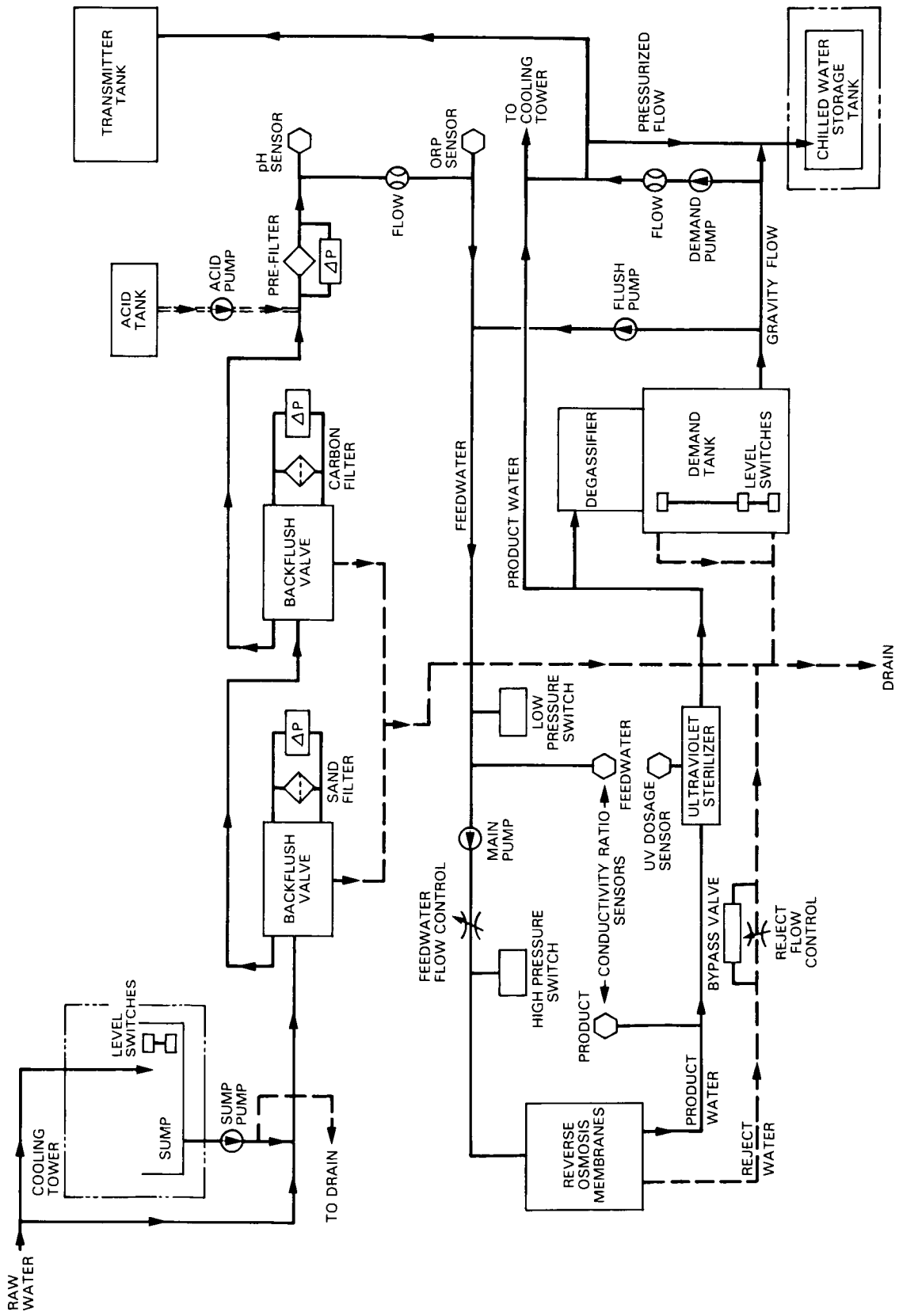


Fig. 3. Simplified flow diagram of the R.O. system

ORIGINAL PAGE IS
OF POOR QUALITY

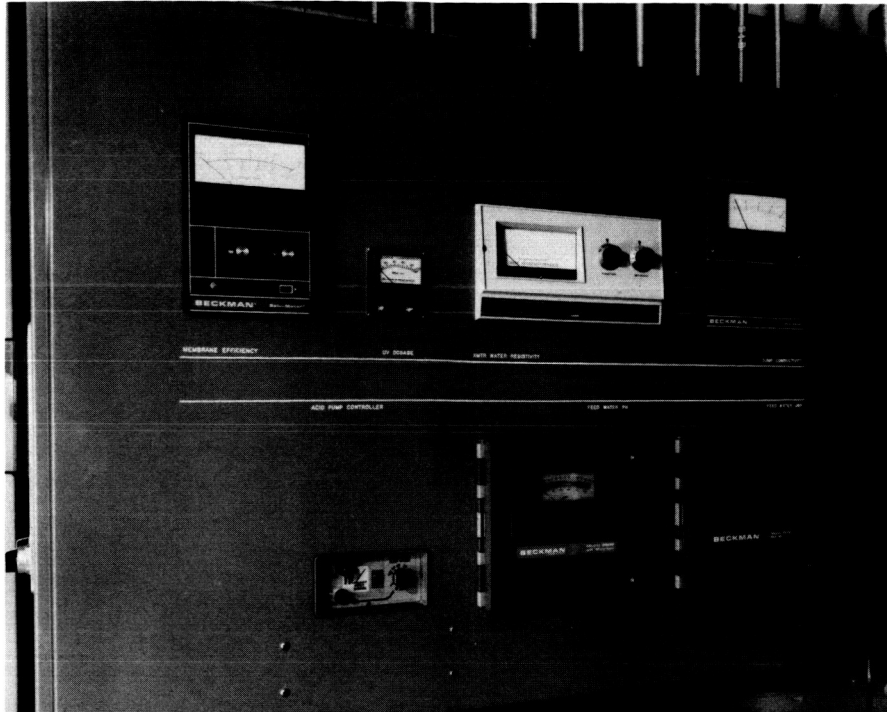


Fig. 4. R.O. instrument panel

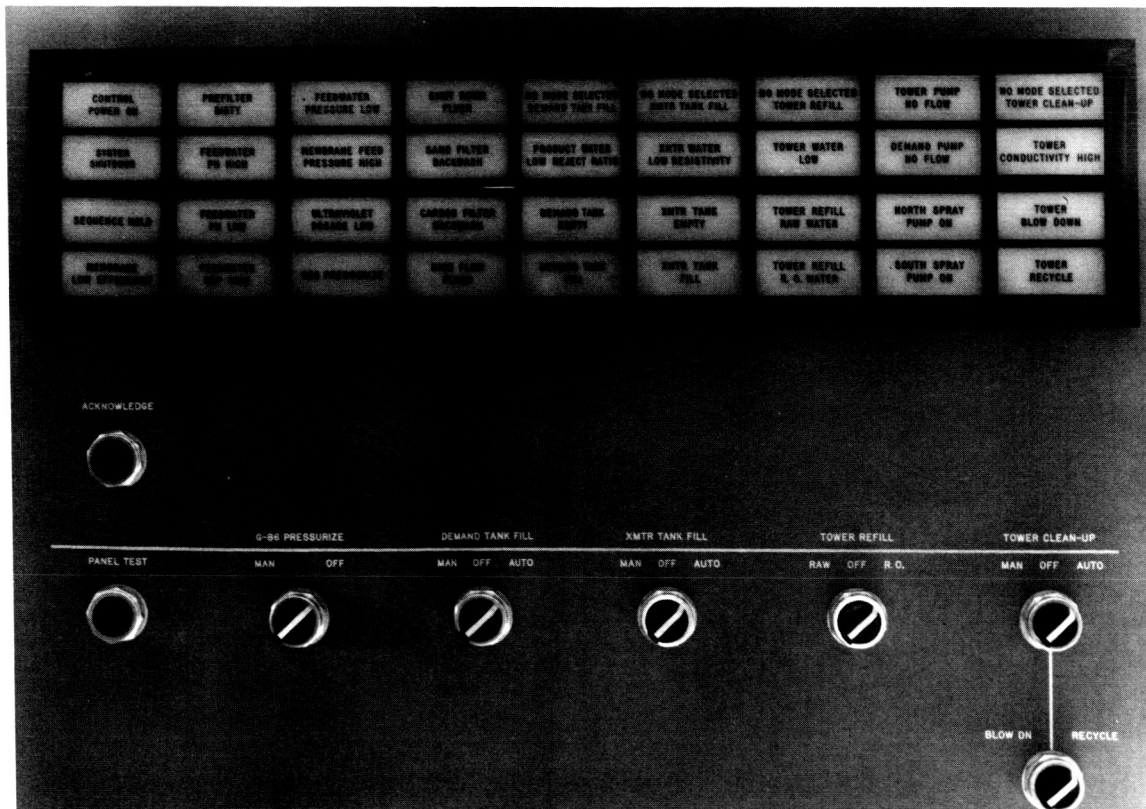


Fig. 5. R.O. control panel

ORIGINAL PAGE IS
OF POOR QUALITY.

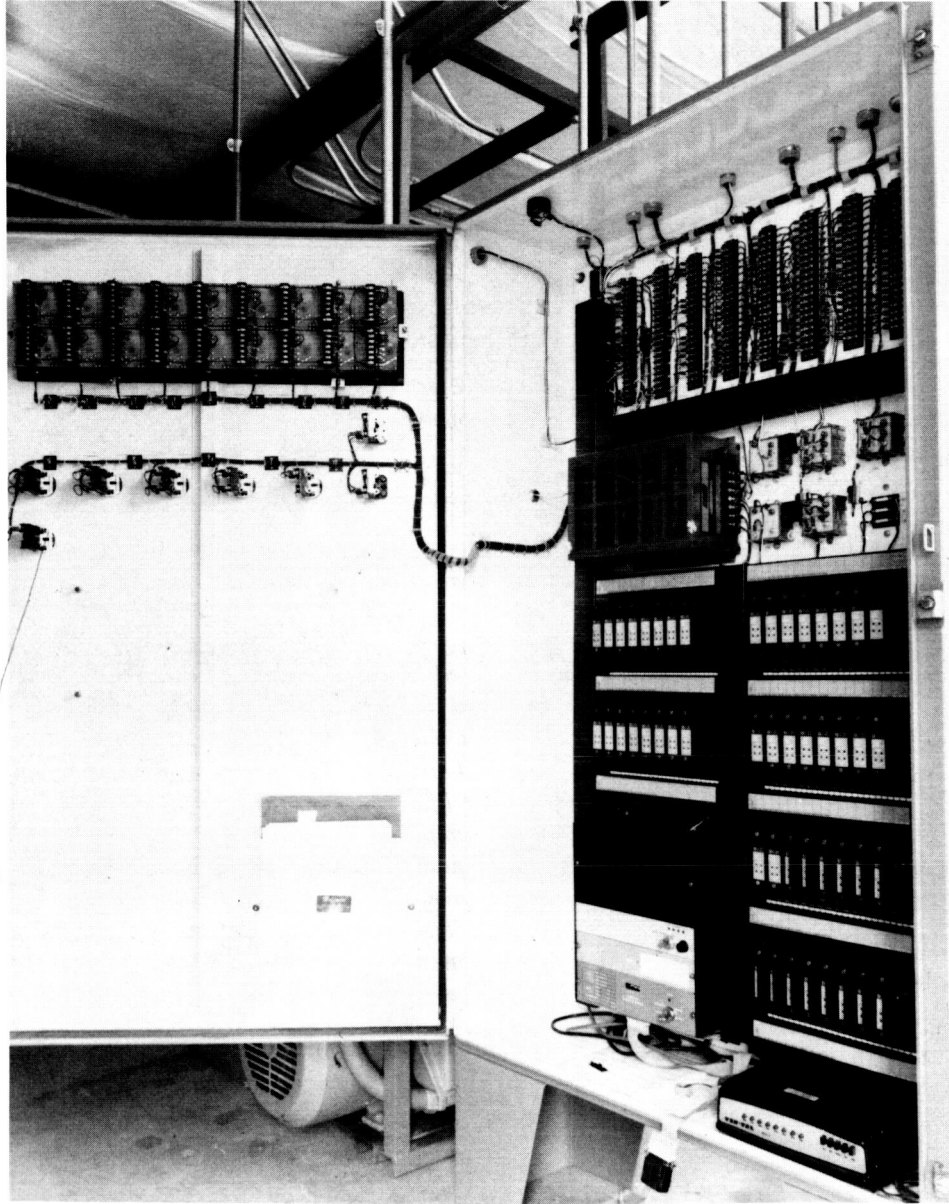


Fig. 6. Programmable controller installation

The Venus Balloon Project

C. T. Stelzried

TDA Mission Support and DSN Operations

R. A. Preston and C. E. Hildebrand

Tracking Systems and Applications Section

J. H. Wilcher

TDA Technology Development

J. Ellis

Navigation Systems Section

On June 11 and 15, 1985, two instrumented balloons were released from the Soviet VEGA 1 and VEGA 2 spacecraft and deployed in the atmosphere of Venus. The VEGA probes flew by the planet on their way to a rendezvous with comet Halley in March 1986. Drifting with the wind at altitudes of 54 km, the balloons traveled one-third of the way around the planet during their 46-hour lifetimes. Sensors on-board the gondolas made periodic measurements of pressure, temperature, vertical wind velocity, cloud particle density, ambient light level, and frequency of lightning. The data were transmitted to Earth and received at the DSN 64-m stations and at several large antennas in the USSR. Approximately 95 percent of the telemetry data were successfully decoded at the DSN complexes and in the Soviet Union, and were provided to the international science team for analysis.

Very Long Baseline Interferometry (VLBI) data were acquired by 20 radio observatories around the world for the purpose of monitoring the Venus winds. The DSN 64-m subnet was part of a 15-station VLBI network organized by the Centre National d'Etudes Spatiales (CNES) of France. In addition, five antennas of the Soviet network participated in the experiment. VLBI data from the CNES network are currently being processed at the Jet Propulsion Laboratory.

I. Introduction

In December 1984 the Soviet Union launched two spacecraft on the VEGA mission to comet Halley. On June 11 and 15, 1985, the spacecraft flew by Venus and deployed two instrumented balloons into the planet's atmosphere. The balloons floated at an altitude of 54 km, and traveled approxi-

mately one-third of the way around the planet during their 46-hour lifetimes (Fig. 1). *In situ* measurements were transmitted directly to Earth with a primary telemetry data rate of 4 bits per second at a carrier frequency of 1667.914 MHz. Complete descriptions of the VEGA mission and the balloon experiment are given in Refs. 1 through 5.

Ground data acquisition during the balloon experiment consisted of three activities, all of which were supported by the DSN 64-m subnet:

- (1) Balloon telemetry – Telemetry data acquisition and decoding, also supported by several stations in the USSR.
- (2) VEGA flyby orbit determination – Acquisition and processing of one-way Doppler and Delta DOR (Delta Differential One-way Range) from the VEGA spacecraft. VEGA orbit determination was performed at JPL using the DSN data, and independently in the Soviet Union using the DSN data and two-way Doppler and range acquired by selected Soviet stations at a ground-receive frequency of approximately 6 GHz.
- (3) Balloon position and velocity determination – Acquisition and processing of differential Very Long Baseline Interferometry (VLBI) measurements on each balloon and the corresponding VEGA spacecraft. VLBI data acquisition was also supported by a global network of radio observatories.

The balloon experiment is a cooperative venture of France and the Soviet Union. The French space agency Centre National d'Etudes Spatiales (CNES) was responsible for organization, implementation (as required), and operation of 15 of the 20 antennas of the worldwide network of radio observatories, which included the DSN 64-m subnet (Fig. 2). CNES also constructed some of the balloon instrumentation and established a Venus balloon science center at the Centre Spatiale de Toulouse. During the encounter periods and pre-encounter ground data system tests, CNES personnel manned the VEGA Project Operations Center at Toulouse to coordinate real-time activities between the Network Operations Control Center at JPL and the Space Research Institute in Moscow. Currently, CNES is coordinating telemetry and VLBI data exchange and analysis. Intercosmos, a branch of the USSR Academy of Sciences, has the responsibility for Soviet participation in this activity. Intercosmos made available all technical information required to conduct the ground-based portion of the experiment, and is responsible for providing to CNES all telemetry and VLBI data acquired by the five-station Soviet network.

The roles of the participating agencies are formalized by a Memorandum of Understanding between NASA and CNES, and by agreements between CNES and Intercosmos. According to these agreements, all data are to be analyzed by an international science team composed of members from France, the United States, and the Soviet Union. First results from joint analysis of the telemetry data are reported in Refs. 6 through 9.

II. Telecommunications

Radio signals were transmitted by each balloon and VEGA spacecraft bus at L-band (centered at 1667.914 MHz). Crystal oscillators were employed as on-board frequency references. The signal spectra varied in time according to a preset sequence which was re-initialized each time the L-band transmitters were turned on. At a given time, the signal took one of three forms:

- (1) Pure carrier.
- (2) Carrier with telemetry sidebands.
- (3) Suppressed carrier and first harmonics of a 3.25-MHz square wave phase modulation (the "VLBI" tones).

Balloon telemetry data were modulated onto a subcarrier located 254.5 Hz away from the carrier, at rates of either 1 or 4 bits per second. The VLBI tones were provided mainly for the purpose of determining the position of the balloon relative to the VEGA bus, but were also used in the acquisition of Delta DOR data from the bus and an angularly nearby quasar.

The balloon transmissions occurred in bursts with durations of 330 seconds, either once or twice per hour, in order to conserve battery power. The bus transmission sequence was essentially the same as the balloon's, except that the bus transmitted continuously during the Venus encounter phase. The telemetry modulation on the bus consisted of a pre-determined bit stream for testing purposes.

The balloon and bus L-band transmitters were identical. The radiated power levels were approximately 4.5 watts, and signal polarization was left circular. The peak bus antenna gain was 10 dB; the balloon omni-antenna gain varied from -3 dB to 0 dB, depending on orientation (maximum gain was achieved near the sub-Earth point, and minimum near the limb).

Implementation of the DSN 64-m subnet for reception of the balloon signals included installation of cooled FET amplifiers, L-band feeds, and upconverters to translate the 1668 MHz received signals to 2288 MHz (J. R. Withington, personal communication). The RF bandwidth of this system is 18 MHz, and the zenith noise temperature is approximately 30 K. Special equipment was also provided for downconverting the signal spectrum from IF to baseband in support of VLBI data acquisition. This hardware made it possible to record the signal spectra in the National Radio Observatory Mark II format, an international standard. Portions of this equipment were replicated by the Observatoire de Paris-Meudon in France and provided to other stations of the global network.

Prior to the encounter, the phasing of the balloon and bus transmission sequences was adjusted as required for the differ-

ential VLBI measurements. That is, for a given transmission, both spectra contained either a carrier or a pair of VLBI tones.

Balloon carrier received power as measured at the DSN 64-m subnet is shown in Fig. 3 (S. E. Borutzki, personal communication). These values are in good agreement with the estimated levels of -165 to -162 dBm.

III. Balloon Telemetry

Balloon telemetry data were provided by the DSN on computer-compatible magnetic tape in two forms: the original recorded spectra (level 0) and the demodulated and decoded data streams (level 1). Implementation details are described in Refs. 10 and 11. The science team also received estimates of the observed balloon frequency derived from telemetry processing for the purpose of obtaining preliminary estimates of zonal wind speed.

The balloon transmission sequence is illustrated in TDA document 870-20.¹ Each balloon had 46 telemetry transmissions, designated A-1 through A-46 (balloon 1) and B-1 through B-46 (balloon 2). The DSN obtained level 0 recordings for all telemetry sessions except A-45, A-46, and B-30, which were lost due to station hardware problems. DSN level 1 recordings were obtained for all recorded telemetry transmissions except A-1, B-1, B-45, and B-46. The first recordings on both balloons were not decoded by the DSN due to large signal variations resulting from erratic balloon motions. For the last two recordings from balloon 2, battery power was too low to yield the signal-to-noise ratio required for decoding. Most DSN level 1 data were produced by personnel at the Deep Space Complex near Madrid, Spain.

The Soviet network obtained level 0 recordings for the telemetry transmissions missed by the DSN. In addition, Soviet personnel produced level 1 recordings for sessions B-1 and B-30. Of the combined data set, only five telemetry transmissions have not been decoded (A-1, A/B-45, and A/B-46). The data have been analyzed by Soviet, French, and U.S. scientists, and preliminary results have been published in *Science* (Refs. 6-9).

IV. VEGA Flyby Orbit Determination

Components of the position and velocity of each balloon relative to the corresponding VEGA bus were measured using

¹Owen, E. L., *Venus Balloon Project, DSN Preparation Plan*, TDA document 870-20, JPL D-1111, Mar. 1, 1985 (JPL internal document).

VLBI techniques. In order to obtain information on the Venus wind velocity from these differential measurements, the VEGA spacecraft orbits relative to Venus must be accurately known.

Determination of the VEGA orbits at JPL depended only on one-way data acquired at L-band by the DSN 64-m subnet as described in Ref. 12. Soviet two-way range and Doppler were not used. The DSN provided Doppler from each station and Delta DOR observations from the Goldstone-Madrid and Goldstone-Canberra baselines. Delta DOR data essentially are VLBI measurements of the spacecraft angular position relative to an angularly nearby extragalactic radio source (EGRS). Candidate L-band radio sources were selected from the DSN EGRS source catalogue, which is derived from VLBI observations at 2.3 and 8.4 GHz. Observing sessions were conducted prior to the Venus encounter to validate source strengths at 1.7 GHz.

VEGA flyby orbit estimates were based on data gathered during the maneuver-free phase from two days before Venus closest approach to thirteen days after. Within this period, there were nine successful Delta DOR acquisitions on VEGA 1, and thirteen on VEGA 2 (see Table 1 for the Delta DOR performance summary). The overall Delta DOR measurement success rate was 85 percent.

For the determination of the Venus wind velocity from differential VLBI measurements, only errors in the VEGA spacecraft position and velocity relative to Venus that are perpendicular to the Earth-Venus line (i.e., the "transverse" components) are important. The formal standard deviations of these errors for the duration of the balloon experiment are given in Fig. 4. For VEGA 1, these uncertainties are always below the balloon position and velocity accuracy goals of 15 km and 1 mps. For VEGA 2, the position errors exceed the goal about 30 hours into the experiment, but the maximum error is less than 24 km.

The VEGA 2 errors tend to be larger than those for VEGA 1 for two reasons: the orbit geometry was not as favorable as that for VEGA 1, and the VEGA 2 one-way Doppler accuracy was degraded by jumps in the frequency of the spacecraft reference oscillator.

V. Balloon Position and Velocity Determination

Balloon position and velocity estimates will be obtained from reduction of the following data:

- (1) Balloon received frequency, which is a measure of velocity along the line-of-sight.

- (2) VLBI measurements of the angular position and velocity of each balloon relative to the corresponding bus as observed from Earth.
- (3) Estimates of VEGA bus orbits relative to Venus.
- (4) Estimates of balloon altitude and altitude rate based on *in situ* measurements of atmospheric pressure.

Acquisition of useful differential VLBI data was possible because the balloon and bus were simultaneously within the antenna beam at each station.

For complete determination of balloon transverse position and velocity in two dimensions from VLBI measurements, simultaneous observations from at least three stations are necessary. Maximum accuracy is achieved when the distances between stations are as large as possible (typically, several thousand kilometers). The global network yielded good observing geometry for approximately 22 hours each day.

Many of the world's most sensitive radio telescopes were part of the Venus balloon network, including eight with aperture diameters of 64 m or larger. Continuous coverage by highly sensitive antennas was required because of the low power level of the balloon transmissions. Integration times that are short compared to the signal coherence time can be used to extract signal phase from data recorded at these stations. With this information it is possible to compensate for signal phase fluctuations in order to obtain coherent detection from stations with poorer signal-to-noise characteristics.

Of the 69 transmissions from each balloon, there were only two for which DSN hardware problems caused loss of VLBI data. These were telemetry frame B-30 and the following VLBI transmission, which are expected to be recovered from VLBI recordings made at other stations of the CNES network. For balloon 1, eight transmissions are of marginal use for position and velocity determination because the bus antenna was not pointed to Earth. Two additional transmissions are probably not usable due to low signal power at the end of the balloon lifetime. For balloon 2, the bus signal was not observed for four transmissions because the spacecraft was occulted by Venus; four other transmissions are probably unusable due to low balloon signal levels. Thus, differential VLBI measurements were obtained for 120 of the balloon transmissions, out of a total of 138.

In addition to VLBI data acquisition, the DSN is supporting the processing of VLBI recordings from the CNES network. Analysis of quasar observations made by the network during the encounter period has yielded information on network clock synchronization to required levels. Time histories of balloon and bus received phase have been obtained for the majority of the DSN recordings (after a format conversion) using the hardware correlation capabilities of the Network Operations Control Center VLBI Processor.

In the next stage of processing, balloon and bus phase histories for all stations of the CNES network will be produced by the JPL/CIT VLBI Processor (Block II). These data and similar results derived from recordings made by the Soviet network will be given to the science team for further analysis.

References

1. Balebanov, V. M., et al., *Venus-Halley Mission*, Imprimerie Louis-Jean, Publications scientifiques et littéraires 05002 GAP, May 1985.
2. Preston, R. A., et al., "The Venus Balloon Project," *TDA Progress Report 42-80*, pp. 195-201, Jet Propulsion Laboratory, Pasadena, Calif., Feb. 15, 1985.
3. Sagdeev, R. Z., et al., "The VEGA Venus Balloon Experiment," *Science*, Vol. 231, No. 4744, pp. 1407-1408, Mar. 21, 1986.
4. Kremnev, R. S., et al., "VEGA Balloon System and Instrumentation," *Science*, Vol. 231, No. 4744, pp. 1408-1411, Mar. 21, 1986.
5. Sagdeev, R. Z., et al., "Overview of the VEGA Venus Balloon in Situ Meteorological Measurements," *Science*, Vol. 231, No. 4744, pp. 1411-1414, Mar. 21, 1986.
6. Preston, R. A., et al., "Determination of Venus Winds by Ground-Based Radio Tracking of the VEGA Balloons," *Science*, Vol. 231, No. 4744, pp. 1414-1416, Mar. 21, 1986.
7. Linkin, V. M., et al., "VEGA Balloon Dynamics and Vertical Winds in the Venus Middle Cloud Region," *Science*, Vol. 231, No. 4744, pp. 1417-1419, Mar. 21, 1986.
8. Linkin, V. M., et al., "Thermal Structure of the Venus Atmosphere in the Middle Cloud Layer," *Science*, Vol. 231, No. 4744, pp. 1420-1422, Mar. 21, 1986.
9. Blamont, J. E., "Implications of the VEGA Balloon Results for Venus Atmospheric Dynamics," *Science*, Vol. 231, No. 4744, pp. 1422-1425, Mar. 21, 1986.
10. Urech, J. M., Chamarro, A., Morales, J. L., and Urech, M. A., "Venus Balloon Project Telemetry Processing," *TDA Progress Report 42-85*, this issue.
11. Jurgens, R. F., and Divsalar, D., *A Proposed Technique for the Venus Balloon Telemetry and Doppler Frequency Recovery*, JPL Publication 85-68, Jet Propulsion Laboratory, Pasadena, Calif., Apr. 15, 1985.
12. Ellis, J., "Deep Space Navigation with Noncoherent Tracking Data," *TDA Progress Report 42-74*, pp. 1-12, Jet Propulsion Laboratory, Pasadena, Calif., Aug. 15, 1983.

Table 1. VEGA Delta DOR performance

1985 Date (MM/DD)	1985 DOY	VEGA bus	DSN baseline	Status
6/08	159	1	CS	F
			CA	P
6/10	161	1	CS	F
			CA	P
6/11	162	1	CS	P
			CA	P
6/12	163	1	CS	P
			CA	F
		2	CS	P
			CA	P
6/14	165	2	CS	P
			CA	P
6/15	166	2	CS	P
			CA	P
6/16	167	2	CS	P
			CA	P
6/17	168	1	CS	P
			CA	P
		2	CS	P
			CA	P
6/18	169	1	CS	P
			CA	P
6/20	171	2	CS	P
			CA	F
6/21	172	2	CS	P
			CA	P

P = Processed
 F = Failure to correlate
 DOY = Day of Year
 CS = California/Spain
 CA = California/Australia

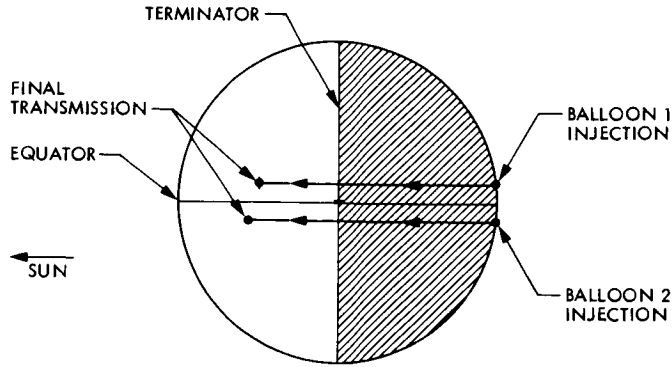


Fig. 1. Paths of balloons across Venus as viewed from Earth



LOCATION	DIAMETER (m)	LOCATION	DIAMETER (m)	LOCATION	DIAMETER (m)
1. PENTICTON, BRITISH COLUMBIA	(26)	8. ATIBAIA, BRAZIL	(14)	15. SIMEIZ, USSR	(22)
2. BIG PINE, CALIFORNIA	(40)	9. MADRID, SPAIN	(64)	16. PUSHINO, USSR	(22)
3. GOLDSTONE, CALIFORNIA	(64)	10. JODRELL BANK, ENGLAND	(26)	17. MEDVEZHI OZERA, USSR	(64)
4. FORT DAVIS, TEXAS	(26)	11. EFFELSBURG, FED. REP. GERMANY	(100)	18. ULAN-UDE, USSR	(25)
5. NORTH LIBERTY, IOWA	(18)	12. ONSALA, SWEDEN	(26)	19. USSURISK, USSR	(70)
6. WESTFORD, MASSACHUSETTS	(37)	13. HARTEBEEESTHOEK, SOUTH AFRICA	(26)	20. CANBERRA, AUSTRALIA	(64)
7. Arecibo, Puerto Rico	(305)	14. EUPATORIA, USSR	(70)		

Fig. 2. Venus Balloon Project International Network

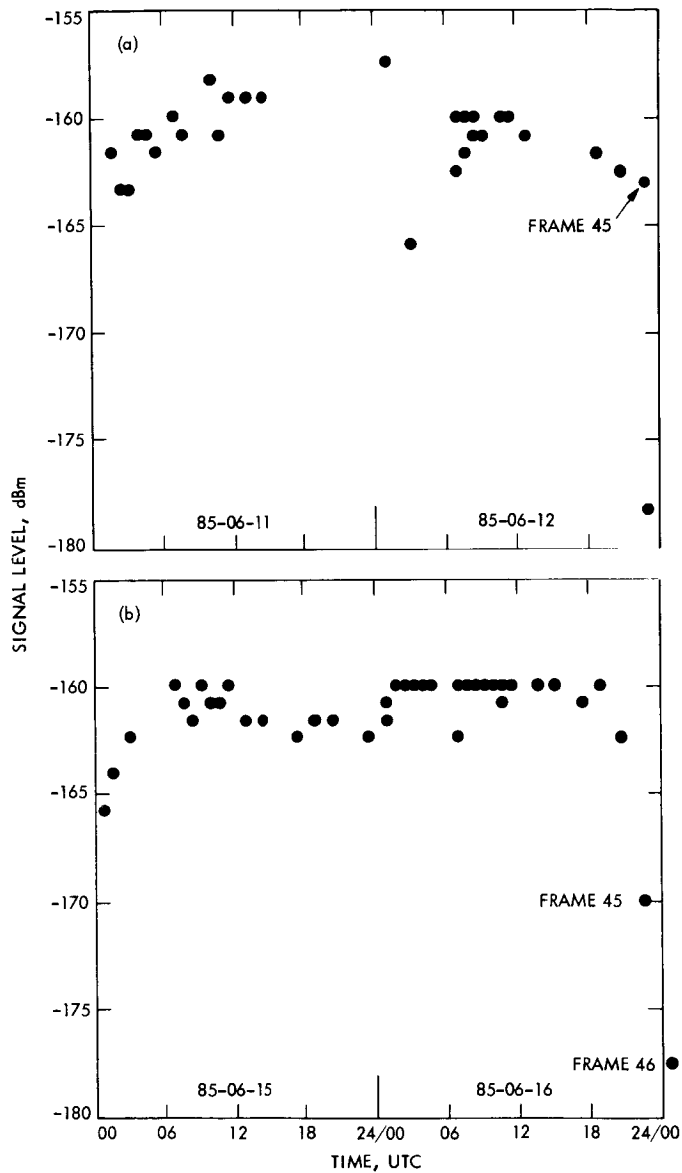


Fig. 3. Received signal level (carrier only) at DSN 64-m subnet: (a) balloon 1, (b) balloon 2

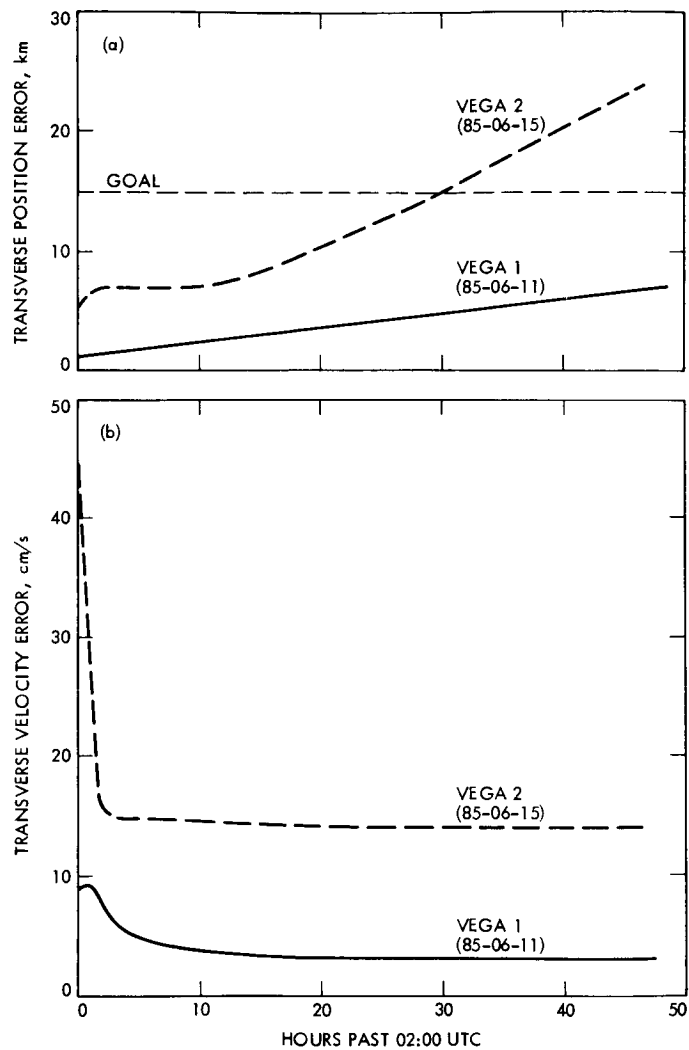


Fig. 4. Standard deviations of transverse position and velocity of VEGA bus relative to Venus: (a) position, (b) velocity

The Venus Balloon Project Telemetry Processing

J. M. Urech, A. Chamarro, J. L. Morales, and M. A. Urech
Madrid Deep Space Communications Complex

The peculiarities of the Venus Balloon telemetry system required the development of a new methodology for the telemetry processing, since the capabilities of the DSN telemetry system do not include burst processing of short frames with two different bit rates and first bit acquisition. The MDSCC engineering staff was tasked to produce a software package for the non-real time detection, demodulation, and decoding of the telemetry streams obtained from an open loop recording utilizing the DSN spectrum processing subsystem-radio science (DSP-RS). ~~This~~ the article contains a general description of the resulting software package (DMO-5539-SP) and its adaptability to the real mission's variations.

I. Introduction

The Venus Balloon telemetry consisted of 330 seconds of 1.67-GHz emissions every 30 minutes, one hour, or two hours, depending on the mission encoder phase. The 330-second emission sequence began with 30 seconds of carrier only (TM1 mode), followed by 270 seconds of telemetry data (TM2 mode), and ended with another 30-second period of carrier only.

During the first 210 seconds, the telemetry data rate was 4 bits/sec, and the last 60 seconds, the rate was 1 bit/sec (see Fig. 1). This telemetry data was convolutionally coded ($K = 6$, $V = 1/2$), and thereafter Manchester encoded with a subcarrier derived from the carrier (1667.9 MHz) divided by 6,553,600, resulting in an approximate subcarrier of 254.5 Hz (see Fig. 2).

The DSN spectrum processing-radio science (DSP-RS) recorded 20K samples/sec sampled spectra on magnetic tapes (level 0). These tapes were processed by DMO-5539-SP (Venus Balloon telemetry software), thus obtaining the decoded data (level 1) tapes.

II. Telemetry Software Description

The telemetry software package ran in a DSN spectrum processing (DSP) environment with three additional peripherals: a local terminal, a hard copy device, and a color display. These peripherals enabled a stand-alone operation isolated from other station activities.

A. Design Criteria

Design parameters were given as (a) signal strength: nominal 18 dB (1 Hz bandwidth), with uncertainty as low as 13 dB; and (b) 1.67 GHz carrier stability:

$$\frac{\Delta f}{f} \cong 10^{-11}$$

The 1.67-GHz carrier uncertainty was estimated in ± 2 kHz, Doppler rate 0.05 Hz/sec. Based on these parameters, the design was concentrated on the detection of weak signals highly stable in frequency and affected by moderate Doppler variations.

Due to the carrier uncertainty, the bandwidth of the radio science open-loop receiver (MMR) analog filter selected was 4091 Hz for frames A-2 to A-6, B-2 to B-46, and A-1 and B-1 (the first frames of every Balloon); when uncertainty was higher, the filter selected was a 8182-Hz bandpass filter. The first Balloon was designated as "A" and the second as "B." Telemetry frames for each Balloon were numbered 1 through 46.

With these constraints in mind, the software was designed with sophisticated algorithms to confirm the presence of the 1.67-GHz carrier under noisy conditions and proved to work satisfactorily with 6 dB less than the nominal case during the compatibility tests with the spacecraft prototype test simulator (PTS). During the real mission, the received signal strength was close to nominal, but the frequency stability and Doppler variations were worse than anticipated by several orders of magnitude. The software was highly modular, and its adaptability to the real situations was relatively simple, although the processing of several "pathological" frames required some interactive operation.

B. Preprocessing

The DSP-RS recorded tapes were selectively transferred to a large capacity disk (LCD) from which the spectrum data was further processed. During this transfer, only 350 seconds of recorded data were copied from the magnetic tape onto the LCDs containing the 330-second emission of the Balloon.

This transfer also performed a 1/2 decimation, reducing the 20K samples/sec to 10K samples/sec. The determination of the MMR filter shape was also possible at this stage. The resulting volume of data to be processed was 3.5 millions of samples (8 bits wide) per Balloon emission.

C. Telemetry Processing

A typical process consisted of the following major steps:

- (1) Carrier confirmation
- (2) Carrier estimation
- (3) Doppler estimation
- (4) Carrier demodulation
- (5) Subcarrier demodulation
- (6) Symbol and frame synchronization
- (7) Viterbi decoding

1. Carrier Confirmation. The purpose of this step was to determine whether a Balloon telemetry frame existed in the recorded data or not. To this end, the carrier confirmation module used 30 seconds of recorded data starting from a

hypothesized carrier-only period, which is to occur in the beginning of each telemetry frame (see Fig. 1).

The process was initiated computing 4096-point FFTs every 0.5 sec of recorded data, thus obtaining 60 power spectra. Then the ten maxima method is applied, forming a histogram from the 60 sets of 10 maxima of each spectrum. In this histogram, the confirmation module may find a zone where n consecutive bins contain a cumulative occurrence of maxima. After an ascending time search of the 60 power spectra, a maxima belonging to that zone satisfying a threshold value ν is a candidate for the searched carrier bin. If m consecutive power spectra contain maxima in the same zone, the presence of carrier is confirmed; if not, the first power spectrum of the set of 60 is discarded, the hypothesized time start is delayed by 0.5 sec, a new FFT is computed for the next 0.5 sec of recorded data, and a new set of 60 power spectra is analyzed with the maxima method. This process is repeated until either the carrier is confirmed or a recording time limit is reached. Figures 3 through 6 illustrate a nominal case and weak signal plots. (Typical values of parameters n , ν , and m were 10, 15 and 2, respectively.)

Once the carrier start time has been determined, the maximum of each of the 60 FFTs is passed to the following module.

2. Carrier Estimation. In this step, the software performs the initial estimation of the carrier frequency and rate using the maxima of the previous step, whenever they correspond to the zone of bins determined there.

Bin numbers are converted to Hertz, thus obtaining the translated 1.66-Hz carrier frequency referenced to the origin of the MMR filter used to condition the DSP-RS discretization process. These frequencies are fitted to a straight line using the least squares method. The resulting regression line provides then the initial estimations of carrier frequency and rate during the first 30 seconds of the Balloon telemetry emission. If the error of a particular point (i.e., its distance to the regression line) is greater than a Δf parameter (typically equal to 5 Hz), then the point is eliminated, and the fitting is repeated.

3. Doppler Estimation. After the initial estimation of carrier frequency and rate obtained in the first 30 seconds of the telemetry transmission by the previous module, the Doppler estimation module worked over the entire 330-second period of the Balloon emission.

In this case, the software algorithm was based on a least squares non-linear regression process with the following model:

$$M_i(t) = A_i \sin(\gamma_i + f_i t + \frac{1}{2} \gamma_i t^2)$$

The model was applied over spans of recorded data with lengths of 10, 4, and 2 seconds, respectively, chosen depending on the observed carrier stability and Doppler rate. In addition to a complete run over the 330 second period, the software was able to be directed to repeat the process on individual spans or groups of variable numbers of spans, with different span lengths or initial parameters.

Each span overlapped the precedent one by 50 percent. The stepping from one span to the next one was based on the SNR of the fitted model; if it violated a pre-established threshold, the model was iterated with a spiral search pattern until the SNR threshold was satisfied. The whole process is detailed in Appendix A, and illustrated in Figs. 7 through 10.

4. Carrier Demodulation. The carrier estimated by the previous module is demodulated from the recorded data samples, S_i , using the following method to maintain phase continuity.

$$S_i = S_i [(1 - \lambda_i) \cos \hat{\omega}_{n-1}(t_i) + \lambda_i \cos \hat{\omega}_n(t_i)]$$

where

$$\lambda_i = \frac{t_i - t_{n-1}}{t_n - t_{n-1}}, \quad n - 1 \leq i < n$$

$$\hat{\omega}_n(t) = \text{carrier estimate in span } n$$

The DC component is removed before and after the demodulation in groups of 5000 samples. After this process, the demodulation samples are reduced from 10K samples/sec to approximately 2500/samples/sec, using a running averages method. The resulting bandwidth is then approximately 1250 Hz.

5. Subcarrier Estimation. The first step in this module is to establish the coherency between the spacecraft timing (in subcarrier cycles) and the ground station timing, from which the data has been synchronized during the sampling and recording by the DSP-RS. Computing the received carrier from the open-loop receiver local oscillator frequency and the translated signal in the MMR filter, we then obtain the actual spacecraft subcarrier frequency by dividing the detected carrier frequency by 6,553,600.

After this frequency is known, the sampled data is arranged so that each subcarrier cycle contains 10 samples, as follows:

$$S_{sci} = \frac{1}{t_s} \int_{t_i}^{t_i} B(t) dt$$

where

$$S_{sci} = \text{subcarrier sample}$$

$$B(t) = \text{modulated subcarrier}$$

$$t_s = \frac{\text{sample rate}}{10 \times \text{subcarrier frequency}}$$

From this point on, every pseudosymbol in the last 60 seconds of the telemetry frame contains 640 subcarrier samples, and in the first 210 seconds contains 160 subcarrier samples.

The software now focuses on the last 60 seconds of the telemetry frame, and to estimate the subcarrier phase, uses five subcarrier models with a relative delay of one tenth of a pseudosymbol (i.e., 64 subcarrier samples) and computes the correlation function of the five models in groups of 64 subcarrier samples over the 60 second period of 1 bit/sec (or 4 pseudosymbols/sec) (see Fig. 11). The model of maximum correlation determines the subcarrier phase delay in samples and a first estimation of the pseudosymbol start in tenths of pseudosymbols.

6. Subcarrier Demodulation. The demodulation process is accomplished by taking groups of 10 subcarrier samples (one subcarrier cycle) and inverting the last five, using the subcarrier phase information provided by the previous module. At the same time, a bandwidth reduction is performed averaging the 10-sample groups. The resulting bandwidth is 128 Hz.

7. Symbol Synchronization. This module continues to use the 60 seconds of 1 bit/sec (4 pseudosymbols/sec) to determine the symbol synchronization. The method is based on averaging two half-pseudosymbols (i.e., two groups of 32 samples) centered on the estimated crossing from a positive pseudosymbol to the adjacent negative pseudosymbol.

The difference between the two averages is proportional to the crossing estimation error, which is iteratively corrected until the crossing error is less than or equal to five samples. This process also keeps track of sign transitions to determine the correct pseudosymbol pairing (the two pseudosymbols of the same symbol must have opposite signs.)

The final estimation of the symbol start delay is obtained after computing the pseudosymbol SNRs with a variation of up to 24 samples from the last crossing estimation.

When this symbol synchronization process is completed, the frame is normalized to 16 samples per second (this timing is referred to the spacecraft timing using the determination of the subcarrier coherency in subsection 5). The frame has been now reduced to 5280 samples.

8. Frame Synchronization. The Balloon telemetry frame consists of 900 bits with the following distribution:

48 bits (synch pattern) transmitted at 4 bits/sec

792 bits from 22 measurements of 6 instruments (6 bits each), transmitted at 4 bits/sec

60 bits of 10 data channels (6 bits each), transmitted at 1 bit/sec

The 96 symbols of the frame synch information are contained in 384 samples of the reduced set. This software module looks for the synch pattern correlating the sample set starting at 500 different sample positions around the expected point. The maximum correlation indicates the position of the synch word in the sample set (see Figs. 12 and 13).

From this position, the 1680 symbols corresponding to the 4 bits/sec are computed by removing the Manchester encoding. The 120 symbols corresponding to the 1 bit/sec are obtained in a similar fashion from the remaining samples, averaging four samples per pseudosymbol.

9. Viterbi Decoding. This module performs the convolutional decoding of the 1800-symbol frame using a standard algorithm.

After completing the decoding, the resulting bits are convolutionally encoded to obtain a symbol reference frame, which in turn is used to compute the symbol error distribution. This is presented together with the decoded frame as the end of the overall process.

The analysis of the synch word pattern permits the detection of a data bar condition. Final results are given in data that are true and decommutated (see Fig. 14).

III. Adaptability to the Real Conditions

During the mission, the spacecraft received signal presented the following characteristics:

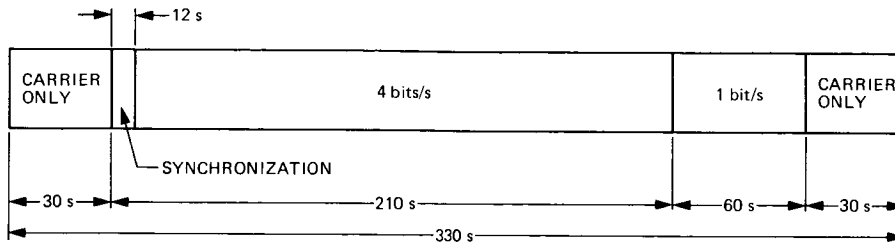
- (1) Average carrier SNR in a 1-Hz bandwidth approximately 20 dB (expected value 18 dB)
- (2) Average symbol SNR approximately 7.5 dB (expected 6.0 dB)
- (3) Frequency variations expected 0.05 Hz/sec
- (4) Frequency variations received up to 3.0 Hz/sec

Frames processed with the antenna near horizon and toward the end of spacecraft battery's lifetime have lower SNR.

The software was able to cope with the above frequency variations after creating new configurations with existing or modified modules and optimizing Doppler estimation parameters. These software modifications resulted in an average degradation of 0.5 dB.

ORIGINAL PAGE IS
OF POOR QUALITY

TM MODE (TELEMETRY)



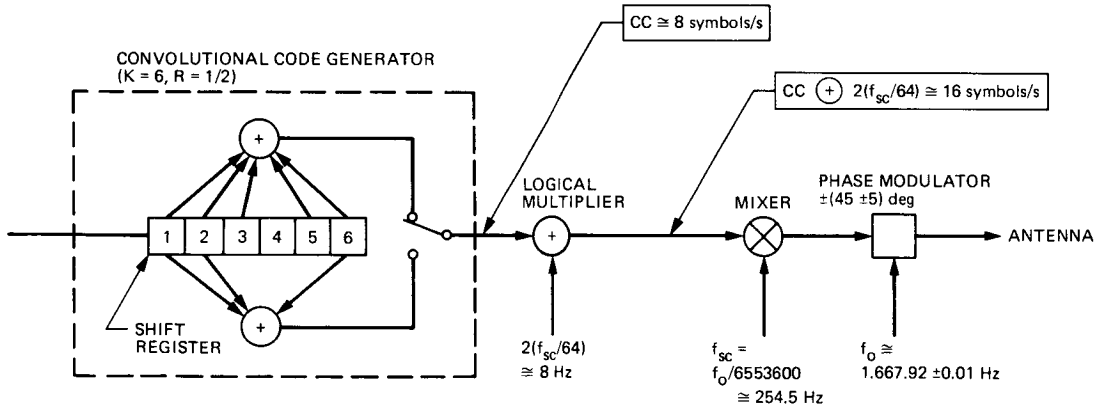
SYNCHRONIZATION WORD IS FIRST 48 bits

SYNCHRONIZATION WORD: 12 (0), 5 (0), 5 (1), 3 (0), 2 (1), 1 (0), 3 (1), 1 (0)
1 (1), 1 (0), 1 (1), 4 (0), 1 (1), 2 (0), 1 (1), 1 (0),
2 (1), 2 (0)

4 bits/s RESULT IN 16 symbols/s

1 bit/s RESULT IN 4 symbols/s

Fig. 1. Telemetry mode sequence



LEGEND:

⊕ = LOGICAL MULTIPLIER

CC = CONVOLUTIONAL CODE GENERATOR OUTPUT (8 symbols/s)

f_o = CARRIER FREQUENCY ($\cong 1667.92$ MHz)

f_{sc} = SUBCARRIER FREQUENCY ($\cong 254.5$ Hz)

Fig. 2. Telemetry modulation scheme

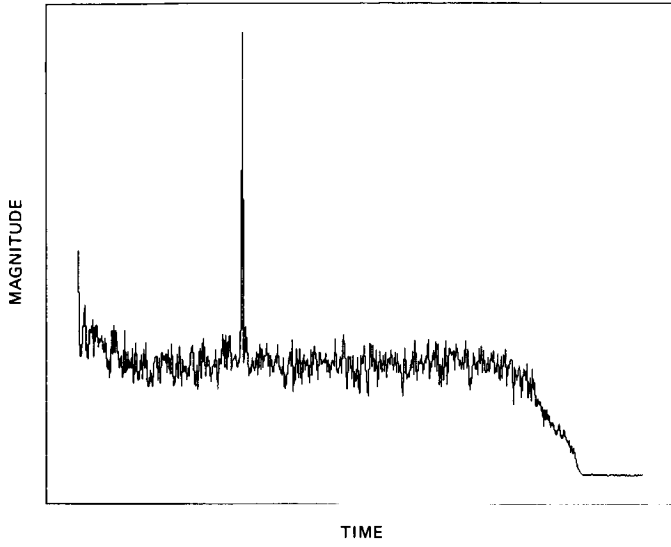


Fig. 3. Carrier detection FFT, nominal signal

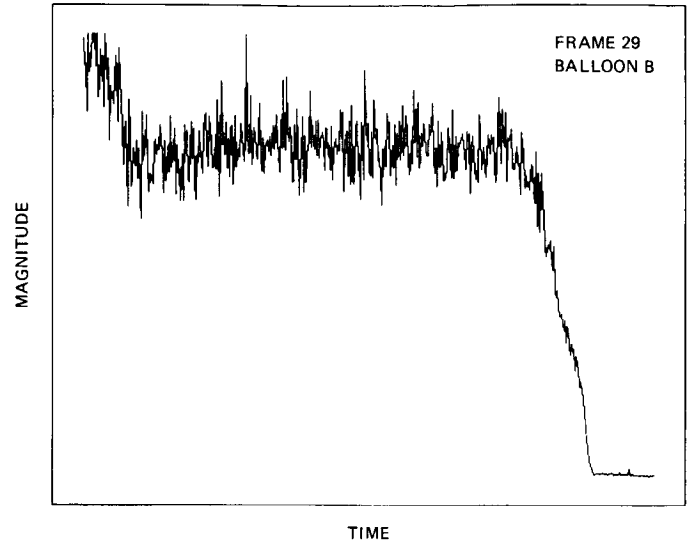


Fig. 5. Carrier detection FFT, weak signal

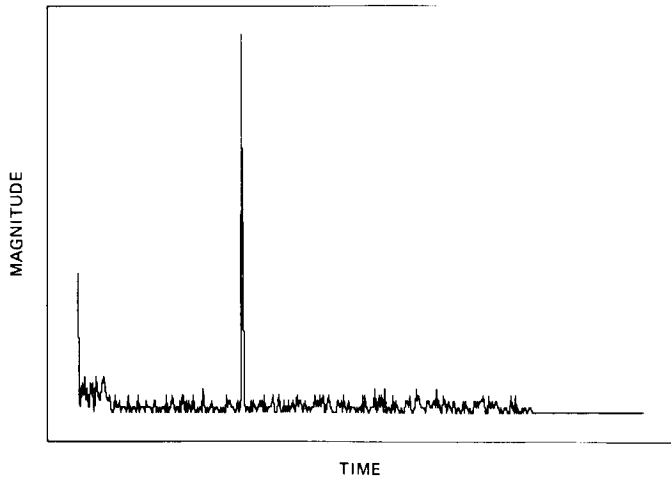


Fig. 4. Carrier detection histogram, nominal signal

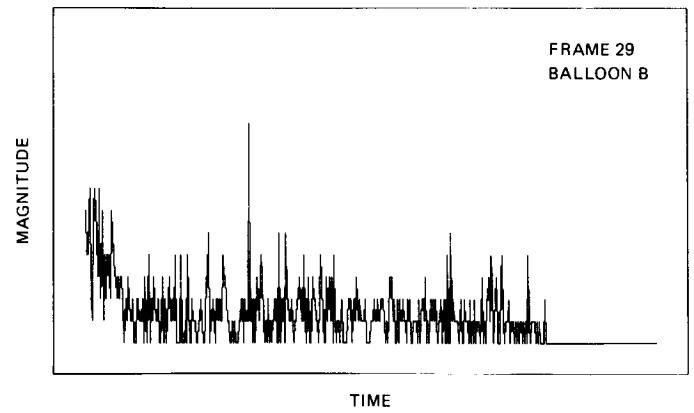


Fig. 6. Carrier detection histogram, weak signal

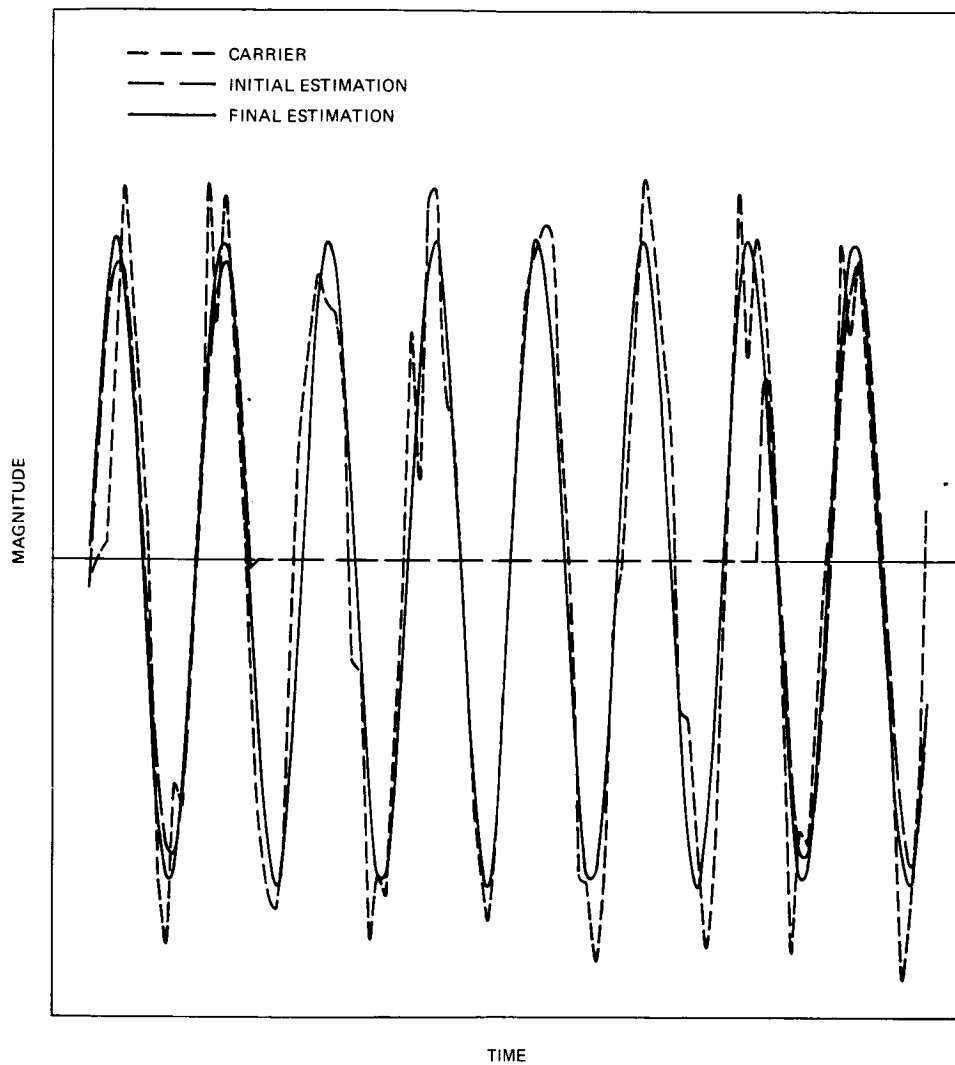


Fig. 7. Doppler estimation, 10 sec span

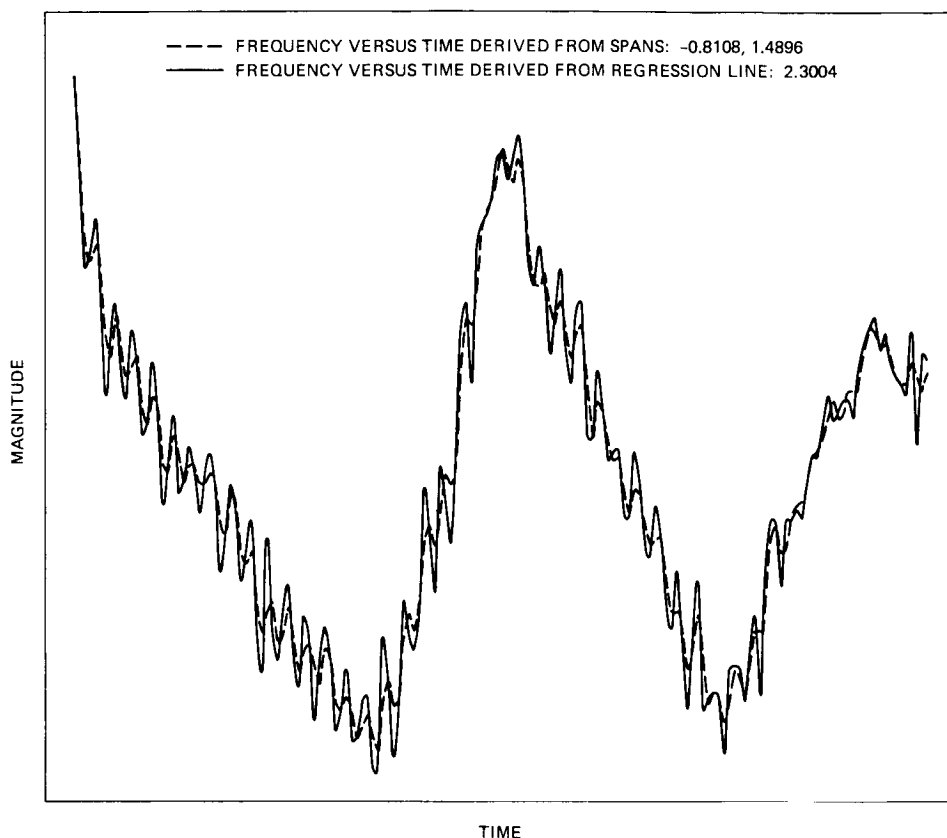


Fig. 8. Carrier frequency vs time (Balloon A2)

TIME	162	4	23	45.80	SPAN	80	PHASE	317.88	FREQ.	1454.15	RATE	-2.6321	AMP.	0.088	SNR	17.00
TIME	162	4	23	46.80	SPAN	81	PHASE	297.11	FREQ.	1450.50	RATE	-0.4855	AMP.	0.092	SNR	17.52
TIME	162	4	23	47.80	SPAN	82	PHASE	81.29	FREQ.	1448.77	RATE	2.1105	AMP.	0.100	SNR	17.99
TIME	162	4	23	48.80	SPAN	83	PHASE	25.79	FREQ.	1450.40	RATE	3.2802	AMP.	0.123	SNR	21.11
TIME	162	4	23	49.80	SPAN	84	PHASE	7.72	FREQ.	1454.28	RATE	-2.0219	AMP.	0.097	SNR	14.63
TIME	162	4	23	50.80	SPAN	85	PHASE	21.18	FREQ.	1457.71	RATE	-0.7964	AMP.	0.101	SNR	14.72
TIME	162	4	23	51.80	SPAN	86	PHASE	63.95	FREQ.	1458.10	RATE	-3.1915	AMP.	0.082	SNR	16.22
TIME	162	4	23	52.80	SPAN	87	PHASE	216.56	FREQ.	1455.21	RATE	-3.7863	AMP.	0.092	SNR	18.84
TIME	162	4	23	53.80	SPAN	88	PHASE	16.68	FREQ.	1450.52	RATE	-2.0800	AMP.	0.089	SNR	17.11
TIME	162	4	23	54.80	SPAN	89	PHASE	283.68	FREQ.	1447.10	RATE	0.2466	AMP.	0.076	SNR	16.14

Fig. 9. Partial listing of Doppler estimation (Balloon A4)

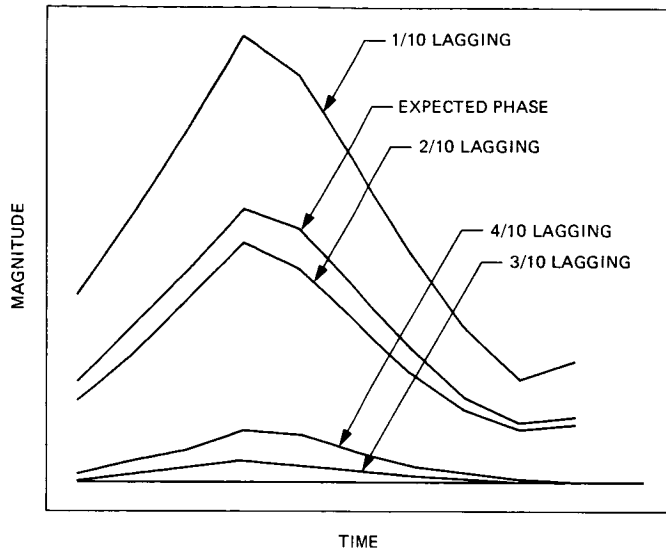


Fig. 10. Subcarrier and symbol correlations

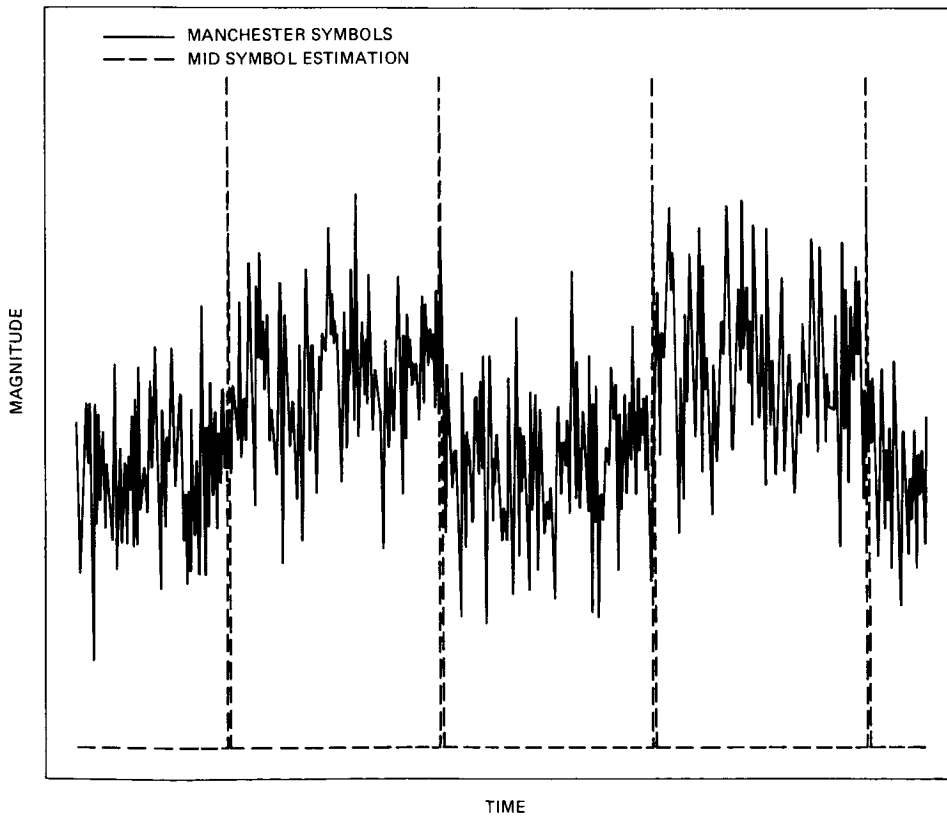


Fig. 11. Mid-symbol estimations

ORIGINAL PAGE IS
OF POOR QUALITY

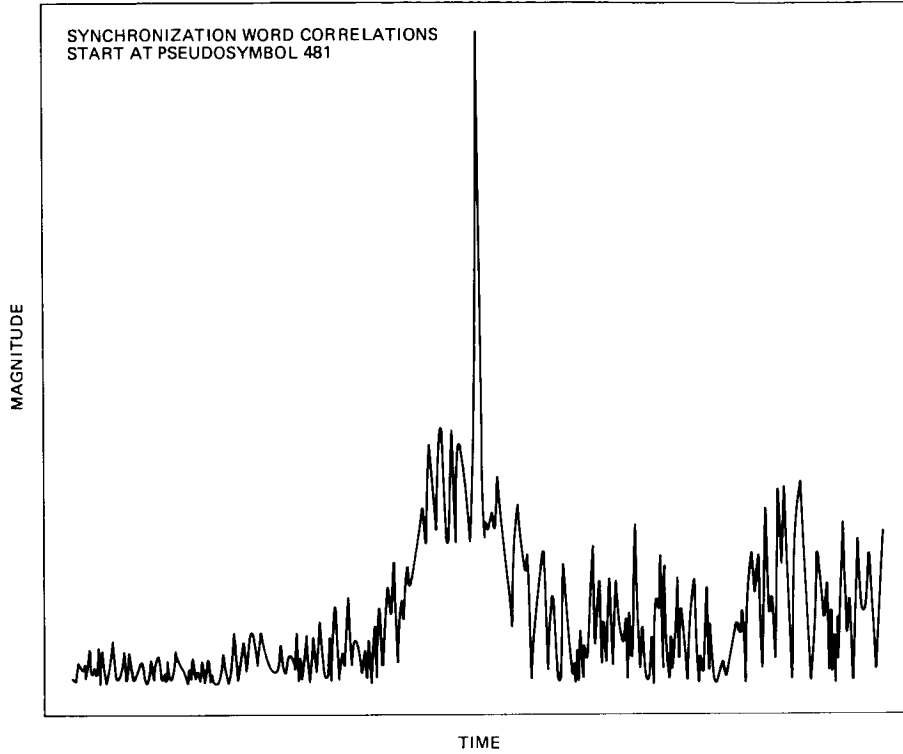


Fig. 12. Frame synch word detection

- DECOMMUTATED DATA -

RECORDING 163 4 30 54.80
SYNC WORD AT 163 4 31 29.38

FRAME SYNC : 0 7C6E A12C

1	0	7	5	8	31	1C	0	13	20	7	6	8	1F	3A	0
2	10	7	3	38	24	2C	2	14	10	7	5	29	1F	39	0
3	0	7	5	9	2E	4	0	15	30	7	3	39	11	9	0
4	20	7	5	28	29	C	0	16	30	7	4	6	1C	39	0
5	10	7	3	19	1F	3C	0	17	0	7	2	17	22	9	0
6	20	7	6	9	15	1C	0	18	10	7	4	18	1D	19	0
7	20	7	4	6	15	2B	0	19	10	7	3	29	14	4	0
8	30	7	5	17	1F	1C	0	20	20	7	10	30	1C	15	0
9	10	7	0	17	5	1C	0	21	1C	1F	37	0	1C	17	0
10	10	7	5	3	3A	7	0	22	F	25	37	0	1C	12	1
11	0	7	2A	9	2F	24	0	23	9	3D	1A	0	1E	2C	0
12	20	7	3	1E	F	1A	0	24	27	3A	12	0	0	0	0

- SYMBOL ERROR RATE = 0.00168

Fig. 13. Decommuted frame

Appendix A

Doppler Estimation Span Processing

The received signal (PCM/PSK/PM) can be represented mathematically by (Refs. A-1, A-2):

$$S(t) = \sqrt{2P} (\sin \omega(t) \cos \theta + \cos \omega(t) \sin \theta B(t))$$

This signal is mixed with a local estimate:

$$S_m(t) = \cos \hat{\omega}(t)$$

and the result, after a low pass filter provides S_i samples that are a function of the difference $\omega - \hat{\omega}$. The process is as follows.

Mixing (see Fig. A-1):

$$\begin{aligned} S(t) \cdot S_m(t) &= \sqrt{2P} (\sin \omega(t) \cos \theta + \cos \omega(t) \sin \theta B(t)) \\ &\quad \times \cos \hat{\omega}(t) \\ &= \sqrt{2P} \left[\frac{1}{2} (\sin (\omega(t) - \hat{\omega}(t)) \cos \theta + \frac{1}{2} \right. \\ &\quad \times (\sin (\omega(t) + \hat{\omega}(t)) \cos \theta) \\ &\quad + \sqrt{2P} \left[\frac{1}{2} ((\cos (\omega(t)) - \hat{\omega}(t) + (\cos (\omega(t) \right. \\ &\quad \left. + \hat{\omega}(t))) \sin \theta B(t) \right] \end{aligned}$$

Filtering:

$$S_i = \int_{t-\Delta t/2}^{t+\Delta t/2} S(t) \cdot S_m(t) dt$$

This filter cancels terms with $(\omega(t) + \hat{\omega}(t))$ and terms with $B(t)$, resulting in:

$$S_i = \frac{\sqrt{2P}}{2} \sin [\omega(t) - \hat{\omega}(t)] \cos \theta$$

and calling:

$$A = \frac{\sqrt{2P}}{2} \cos \theta$$

$$\omega_D(t) = \omega(t) - \hat{\omega}(t) = \psi + ft + \frac{1}{2} \gamma t^2$$

The problem now is to minimize

$$\sum (S_i - M_i)^2$$

Since S_i is equal to the reduced sample set

$$M_i = A \sin (\omega_D(t_i)) = A \sin \left(\psi + ft_i + \frac{1}{2} \gamma t_i^2 \right)$$

that is equivalent to solving the non-linear system:

$$-2 \sum (S_i - M_i) \frac{\gamma M_i}{\gamma X_k} = 0$$

where

$$1 \leq k \leq 4$$

$$x_1 = A$$

$$x_2 = \psi$$

$$x_3 = f$$

$$x_4 = \gamma$$

Expanding this expression, we obtain the system in explicit form:

$$\sum_i (S_i - A \sin \omega_d(t_i)) \sin \omega_d(t_i) = 0$$

$$\sum_i (S_i - A \sin \omega_d(t_i)) A \cos \omega_d(t_i) = 0$$

$$\sum_i (S_i - A \sin \omega_d(t_i)) A t \cos \omega_d(t_i) = 0$$

$$\sum_i (S_i - A \sin \omega_d(t_i)) \frac{A t^2}{2} \cos \omega_d(t_i) = 0$$

After sample trigonometric operations, the system is expressed with the following non-linear functions: $\sin \omega_d$, $\cos \omega_d$, $A \sin 2\omega_d$, $A \cos 2\omega_d$. This non-linear system is linearized to approximate the above functions by their Taylor series expansions.

After establishing a linear system of four equations with four unknowns (ψ, f, γ, A), the solution is obtained by iteration from a starting point ($\psi_0, f_0, \gamma_0, A_0$). Iteration increments for f and γ are obtained in a spiral way (see Fig. A-2), where negative values of f are avoided.

Limits of the spiral way are:

$$f \geq 0, |f - f_b| \leq f_{lim} \quad |\gamma| \leq \gamma_{lim} \quad f + t_s \gamma \leq BW$$

where

$$t_s = \text{span length in seconds}$$

BW = low pass filter bandwidth

Typical values are: $f_b = 0.8$ Hz, $f_{lim} = 0.8$ Hz, $\gamma_{lim} = 0.05$ Hz/sec. The initial values for the other two unknowns are:

$$A_0 = \frac{\sqrt{2}}{N} \sum_i^N |S_i|$$

(initial amplitude)

$$\psi_0 = K \psi_{20}$$

with K such that it maximizes:

$$\left| \sum_i^N S_i \sin \left(K \psi_{20} + f_0 t_i + \frac{1}{2} \gamma_0 t_i^2 \right) \right|$$

for $1 \leq K \leq 18$ and ψ_{20} = phase corresponding to the first step of 20 degrees.

The iteration process is started with an initial vector:

$$X_0 = (\psi_0, f_0, \gamma_0, A_0)$$

and an incremental vector:

$$\Delta X_0 = (\Delta \psi_0, \Delta f_0, \Delta \gamma_0, \Delta A_0)$$

in the usual way:

$$X_1 = X_0 + \Delta X_0 \rightarrow \Delta X_1$$

⋮

⋮

⋮

$$X_N = X_{N-1} + \Delta X_{N-1} \rightarrow \Delta X_N$$

The process finishes when:

$$|\Delta X_{NK}| \leq 10^{-5}, \quad 1 \leq k \leq 4$$

If this limit is not reached, the sequence is aborted when N is greater than the other limit (typically 60). Then, new initial values are obtained from the spiral search and the process is resumed.

If the convergence to 10^{-5} is obtained, a carrier SNR is computed and tested against a threshold value. If the test passes, this vector (ψ, f, γ, A) is considered a valid solution. If the test fails, the process is repeated with new initial values from the spiral search until a solution is found, or the spiral way is exhausted. When the latter happens, the solution with higher SNR is adopted.

Multiplicity of Solutions: If (ψ, f, γ, A) is a solution, ($-\psi, -f, -\gamma, -A$) and ($\psi_{+N}, -f, -\gamma, A$) are possible solutions that must be discarded. The set ($-\psi, -f, -\gamma, -A$) is easily detected by checking the sine of the amplitude (A). The set ($\psi_{+N}, -f, -\gamma, A$) is avoided by mixing with a frequency lower than the one estimated (typically 0.8 Hz lower), so that after mixing the difference will always be positive.

References

- A-1. Yuen, J. H., *Deep Space Telecommunications Systems Engineering*, Jet Propulsion Laboratory, Pasadena, Calif., 1982.
- A-2. Lindsey, W. C., and Simon, M. K., *Telecommunications Systems Engineering*, Englewood Cliffs, N.J.: Prentice-Hall, 1973.

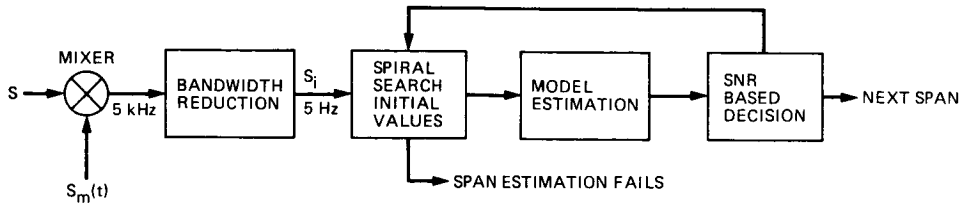


Fig. A-1. Doppler estimation span processing

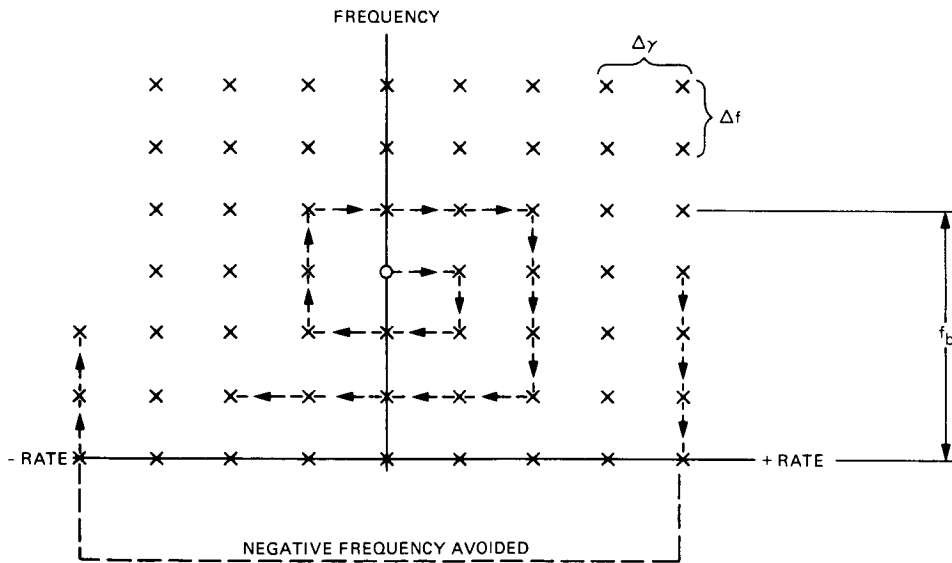


Fig. A-2. Spiral searching

019-43
78

N86-28294

13163

The March 1985 Demonstration of the Fiducial Network Concept for GPS Geodesy: A Preliminary Report

J. M. Davidson, C. L. Thornton, T. H. Dixon¹,
C. J. Vegos, L. E. Young, and T. P. Yunck
Tracking Systems and Applications Section

The first field tests in preparation for the NASA Global Positioning System (GPS) Caribbean Initiative were conducted in late March and early April of 1985. GPS receivers were located at the POLARIS VLBI stations at Westford, Massachusetts; Richmond, Florida; and Ft. Davis, Texas; and at the Mojave, Owens Valley, and Hat Creek VLBI stations in California. Other mobile receivers were placed near Mammoth Lakes, California; Pt. Mugu, California; Austin, Texas; and Dahlgren, Virginia. These sites were equipped with a combination of GPS receiver types, including SERIES-X, TI-4100 and AFGL dual frequency receivers. The principal objectives of these tests were the demonstration of the fiducial network concept for precise GPS geodesy, the performance assessment of the participating GPS receiver types, and to conduct the first in a series of experiments to monitor ground deformation in the Mammoth Lakes-Long Valley caldera region in California. Other objectives included the testing of the water vapor radiometers for the calibration of GPS data, the development of efficient procedures for planning and coordinating GPS field exercises, the establishment of institutional interfaces for future cooperative ventures, the testing of the GPS Data Analysis Software (GIPSY, for GPS Inferred Positioning SYstem), and the establishment of a set of calibration baselines in California. Preliminary reports of the success of the field tests, including receiver performance and data quality, and on the status of the data analysis software are given.

I. Introduction

The development of geodetic surveying systems based on the Global Positioning System (GPS) satellites is motivated by the promise of high performance, mobility and low cost. The large number of measurements which can be economically made using GPS-based systems will enable the resolution of

many geophysical questions which are inaccessible to the more costly VLBI or laser techniques. However, the use of GPS receivers for high-precision geodesy is still in its infancy, and much work remains in assessing system performance and understanding sources of error. Two major system components are still in the developmental or validation stage. These are the water vapor radiometers (WVRs) and the GPS receivers themselves. A third system element, the fiducial network, has received considerable investigation via covariance analysis (e.g.,

¹Geology and Planetology Section

Ref. 1²) but has not yet been tested in the field. The WVRs are currently undergoing extensive testing.

In this article, we report the results of recent field tests of the GPS receivers and of the fiducial network concept. These tests took place between March 28 and April 4, 1985. GPS receivers were placed at the NOAA/NGS POLARIS VLBI stations (Ref. 2) in Westford, Massachusetts; Richmond, Florida; and Ft. Davis, Texas; and at the Mojave, Owens Valley, and Hat Creek stations in California. Additional GPS receivers located near Mammoth Lakes, California, Austin, Texas, and Dahlgren, Virginia (Fig. 1) also recorded data during the test. The sites were equipped with a combination of GPS receiver types, including SERIES-X, TI-4100 and Air Force Geophysical Laboratory (AFGL) dual-frequency receivers. Three of the sites in California were equipped with WVRs (Table 1). In all, seventeen different institutions made contributions to this test (Table 2).

II. The Fiducial Network Concept

The accuracy of GPS-based baseline measurements depends in part on the accuracies with which the GPS satellite orbits are known. For baselines of 100 km length, simple geometric arguments show that orbit accuracies of the order 2.5 m are required to attain a baseline accuracy of 1 cm (Fig. 2). For baselines lengths of several hundred km or more, orbit accuracies of better than 50 cm are required. Currently available GPS ephemerides are in error at the level of ten meters or more. Hence, results of geodetic quality are limited to baselines of no more than a few tens of km, unless a method of improving satellite ephemerides is devised.

A fiducial network approach has been proposed by JPL for improving satellite orbit accuracy (Ref. 3; J. L. Fanselow and J. B. Thomas, 1983, private communication). In the fiducial network approach, three or more GPS receivers are placed at sites, called fiducial stations, whose positions are well established by an independent geodetic technique, such as VLBI or satellite laser ranging (SLR). Other receivers, called mobile receivers, are placed at sites of geodetic interest. During a GPS geodetic experiment, the fiducial receivers record data jointly with the mobile receivers (Fig. 3), enabling the simultaneous determination of accurate GPS satellite orbits and geodetic baselines. The effectiveness of the fiducial approach depends strongly on the locations of the fiducial receivers and on the accuracy with which the fiducial baselines are

known a priori. Covariance analysis has shown that orbit accuracies of better than 3 meters are attainable using current systems, involving the POLARIS VLBI sites as fiducial stations and integrated GPS carrier doppler as the data type. Orbit accuracies of better than 50 cm could be attainable using a system which delivers unambiguous carrier ranging data and which may include a fiducial station located in the northern part of South America (Refs. 4, 1). The feasibility of such a system is currently being investigated at JPL (Ref. 5). If it proves feasible, and if planned receiver developments proceed smoothly, such a system could be operational by 1989.

It should be noted that the location of the fiducial receivers at VLBI stations has the advantage of automatically placing the GPS satellite orbits in the coordinate frame of the quasi-stellar radio sources. This has the aesthetic appeal of tying the GPS results to an absolute frame of reference. Further, it unifies the VLBI and GPS geodetic frames, enabling simultaneous display and easy intercomparison of GPS and VLBI three-dimensional baseline results.

III. Test Site Selection

The relative locations of the fiducial stations must be known to a few centimeters. Practical considerations limit the choices to locations which have some past history of VLBI (or SLR) measurement. For this reason, the VLBI stations of the POLARIS Project at Westford, MA, Richmond, FL, and Ft. Davis, TX, were chosen. (Fiducial stations for future GPS experiments may include additional sites which presently at least have the facilities available for making these measurements.)

The selection of the mobile sites was done to establish a set of calibration baselines and initiate a series of measurements to monitor ground deformation in the Long Valley caldera region of California. The stations at Mojave, Owens Valley and Hat Creek were selected as the endpoints for the calibration baselines. These stations were selected because of their easy access from JPL and from most of the participating organizations and because they involve colocations with VLBI and SLR geodetic systems. Hence, high geodetic quality intercomparison data are available. Further, baselines between these three sites are approximately colinear. For this case, errors in the baselines due to orbit uncertainties will be similar in character, but will scale with baseline length (Fig. 2) and should be separable from other error sources.

The Mammoth Lakes site was established as part of a JPL-Caltech program designed to supplement ongoing geodetic measurements by the U.S. Geological Survey. Part of this program consists of leveling surveys, designed to monitor

²Thornton, C. L., Davidson, J. M., Beckman, B. C., Young, L. E., Thomas, J. B., Dixon, T. H., Trask, D. W., System Study for Global Positioning Satellite (GPS) Geodesy in the Caribbean, D-941 (internal document), Jet Propulsion Laboratory, Pasadena, Calif., 1983.

vertical motion associated with the uplift of a resurgent dome in the Long Valley caldera. This is thought to be due to an intrusion of magma into a shallow (< 10 km) crustal reservoir, and represents a potential volcanic hazard. Because leveling surveys are expensive and error prone, it is desirable to develop supplemental techniques to monitoring vertical motion.

IV. Test Results

A. Receiver Performance

Three receiver types were involved in these field tests: the SERIES-X, the TI-4100 and the AFGL dual-frequency receivers. The SERIES-X receivers were built at JPL under the sponsorship of the Oceanic Processes Office of NASA's Office of Space Science and Applications; the TI-4100 receivers were developed by the Texas Instruments Corporation; and the AFGL dual-frequency receivers were developed by Macrometrics Incorporated for the Air Force Geophysical Laboratory (AFGL). Each of the ten participating stations in the test was equipped with one or more of these receivers (Table 1). All three receivers recorded data at both L-band frequencies (1.57542 GHz and 1.22760 GHz) broadcast by the GPS satellites, thus enabling reduction of ionosphere corruption of the data. Data were recorded each day by all receivers throughout a six-hour viewing window when the current constellation of seven usable GPS satellites was visible over North America. This six-hour window extended from approximately 5:00 to 11:00 GMT (9:00 P.M. to 3:00 A.M. PST). The TI-4100 receivers recorded data for two hours more than the others, beginning at 3:00 GMT. During this window, the TI-4100 and the AFGL receivers recorded data from six GPS satellites; the SERIES-X receivers recorded data from all visible satellites. Throughout the eight days of the test, WVRs at Mojave, Owens Valley and Hat Creek recorded data continuously, with no data loss. A map of the Western Hemisphere, showing fiducial and mobile stations, satellite ground tracks for the full eight-hour viewing period, and 15-deg horizon masks is presented in Fig. 4. In all, 106 station days of data recording were scheduled. Of these, only six station days of data were not recorded for various reasons. In general, the receivers operated smoothly and without technical problems. Tape changes were required only once every six hours with all receivers. Hence, tape changes were required only once a day. The acquisition of new satellites as they rose was fully automated by the field system computers, as was the deacquisition of setting ones. It was particularly noted by the authors, all of whom have experience with VLBI systems, that the operation of the GPS receiver systems seemed relatively uneventful, even dull.

At this writing, most of the data recorded appears to be of very high quality. Initial processing is currently under way at JPL. Data from all satellites has been successfully recovered for the first few days of the test and the receivers appear to have operated properly.

B. Fiducial Network Performance

The principal objective of the March 1985 field test was the demonstration of the feasibility of the fiducial network concept. The proof will lie in the degree to which the accuracy of the mobile station baselines is improved over that attainable in the absence of a fiducial network. Considerable analysis remains before this question can be answered. In the mean time, it is instructive to describe the improvement expected based on covariance analysis. Figure 5 presents results for the Mojave/Owens Valley baseline, based on the actual observing scenario for the March field tests. The error model assumptions made in this analysis were as follows. Data noise was taken to be 2 cm; zenith troposphere calibration was taken to be 2 cm at stations where there were WVR's and 5 cm otherwise; fiducial baseline accuracy was taken to be 3 cm in all coordinates; a priori satellite position and velocity at epoch were taken to be 10 meters and 1 mm/sec, respectively; uncertainty in geocenter location was taken to be 20 cm in all coordinates; modeling of solar radiation pressure on the GPS spacecraft was assumed to be accurate to within 5% of the total effect; the product of GM was taken to be accurate to a part in $1.E+08$; and the error in the gravity model was taken to be 10% of the difference between the GEM6 and APL5.0 models; the elevation angle cutoff at each station was taken to be 15 degrees; and the data type used was carrier phase. These error model assumptions are standard ones for the current systems and are justified in detail elsewhere (Ref. 6). Two analyses of the March scenario were run, one in which the satellite epoch states were estimated (i.e., using the fiducial network) and one in which they were fixed at their a priori values (i.e., as if it were a two-station experiment with no fiducial network). An intermediate case in which there are ten GPS stations in the network and in which satellite orbits are estimated, but in which none of the GPS receivers have a priori known relative locations, gives results between the two extremes shown in Fig. 5. As Fig. 5 shows for the case of the Mojave/Owens Valley baseline, the use of a fiducial network is expected to improve accuracy for this baseline by factors of from five in the vertical to forty in the north. This improvement is dependent on baseline length and orientation and in general increases with baseline length.

C. Other Test Objectives

As outlined earlier, it was also among the objectives of the March field tests to develop efficient procedures for conduct-

ing large-scale GPS field operations and to establish institutional interfaces for future cooperative ventures. We feel that these objectives were attained.

Data from the field test are being used to test the GIPSY Software. The software tests began several months ago.

D. Delivery of Data

The raw data (observables, uncertainties and time tags) from this test has been made available to all participating organizations. In addition, important ancillary information (WVR and meteorology data, site eccentricities and fiducial baseline vectors) are available. Processed results (calibrated observables, ionosphere data, GPS satellite orbits and station locations and observables) will also be available to the test

participants, but the delivery of these will lag the raw data delivery by several months.

V. Conclusions

The March 1985 field tests described in this article were conducted as preparation for the NASA GPS Caribbean Initiative. It would be premature at this time to make any definitive evaluation of the data quality or of the feasibility of GPS as a geodetic technology. However, as of now, the overall effort seems to have been a success, indicating the possibility of an initial deployment to one of the Caribbean countries. Re-occupation of most of the sites involved in the March test, as well as deployment to Baja California and mainland Mexico, took place in November 1985. As with the recently completed test, their efforts were collaborative.

References

1. Kroger, P. M., Thornton, C. L., Davidson, J. M., Stephens, S. A., and Beckman, B. C., Sensitivity of GPS Caribbean Baseline Performance to the Location of a Southerly Fiducial Station, *Proc. First International Symposium on Positioning With the Global Positioning System*, U.S. National Oceanic and Atmospheric Administration, Rockville, Maryland, 1985.
2. Carter, W. E., Robertson, D. S., Pettey, J. E., Tapley, B. D., Schutz, B. E., Eanes, R. J., and Lufeng, M., Variations in the Rotation of the Earth, *Science* 224, 957-961, 1984.
3. Kroger, P. M., Davidson, J. M., and Gardner, E. C., Mobile VLBI and GPS Measurement of Vertical Crustal Motion, *Journal of Geophysical Research* (in press), 1986.
4. Thornton, C. L., Davidson, J. M., Wu, S. C., Beckman, B. C., Kroger, P. M., Allen, S. L., Determination of GPS Satellite Orbits Using a VLBI-Based Fiducial Network, *Transactions of the American Geophysical Union* 65, 856, 1984.
5. Yunck, T. P., A GPS Measurement System for Precise Satellite Tracking and Geodesy, *Proceedings Conf. on Precision Electromagnetic Measurements*, p. 8, August 20-24, 1984, Delft, The Netherlands, 1984.
6. Davidson, J. M., Thornton, C. L., Beckman, B. C., Kroger, P. M., Stephens, S. A., and Wu, S. C., Covariance Analysis for Geodetic Measurements in the Caribbean Utilizing the Global Positioning System Satellites, *Journal of Geophysical Research* (in preparation), 1986.

Table 1. Receiver, WVR deployment

Austin, TX	ARL TI-4100
Dahlgren, VA	ARL TI-4100
Ft. Davis, TX	TDH TI-4100
Hat Creek, CA	TI TI-4100, DSN R04 WVR
Mammoth Lakes, CA	ARL TI-4100
Mojave, CA	SERIES-X, TI TI-4100, CDP Retrofit WVR
Owens Valley, CA	SERIES-X, TI TI-4100, CDP Prototype WVR
Pt. Mugu, CA	PMTC TI-4100
Richmond, FL	AFGL dual-frequency, ARL TI-4100
Westford, MA	AFGL dual-frequency, ARL TI-4100

Table 2. Participating institutions and organizations

NASA Geodynamics Program
Applied Research Laboratory
Air Force Geophysical Laboratory
Bendix Corporation
California Institute of Technology
Crustal Dynamics Project
Defense Mapping Agency
Goddard Space Flight Center
Haystack Observatory
Interferometrics Incorporated
Jet Propulsion Laboratory
National Geodetic Survey
Naval Surface Weapons Center
Pacific Missile Test Center
Texas Department of Highways
Texas Instruments Corporation
United States Geological Survey
University Navstar Consortium

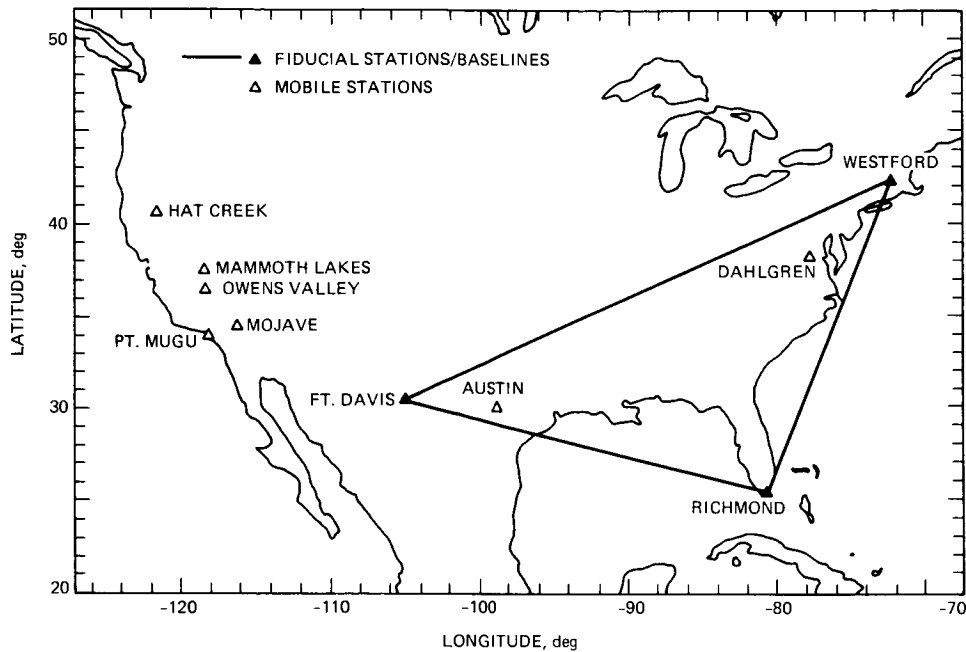


Fig. 1. The locations of the fiducial and mobile GPS receivers in the March 1985 demonstration

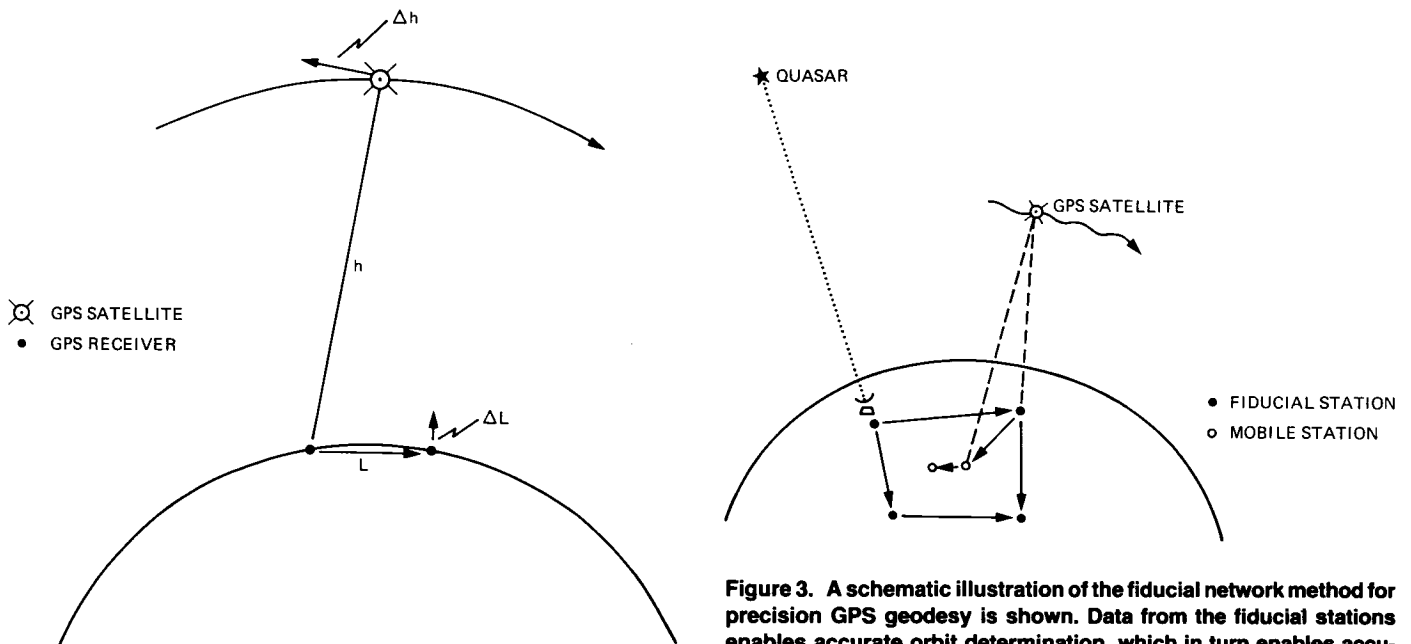


Fig. 2. The qualitative dependence of baseline accuracy on orbit accuracy is illustrated. Ground Stations track a GPS satellite. An error Δh in the satellite position results in an error ΔL in the baseline vector, such that $\Delta L \approx L/h * \Delta h$, where L is the baseline length and h is the satellite altitude. For $L = 100$ km, $\Delta L \approx \Delta h/250$.

Figure 3. A schematic illustration of the fiducial network method for precision GPS geodesy is shown. Data from the fiducial stations enables accurate orbit determination, which in turn enables accurate mobile baseline determination. VLBI observations from the fiducial sites (not necessarily simultaneous with the GPS observations) determine fiducial baselines and tie the GPS results to the inertial frame of the quasistellar radio sources.

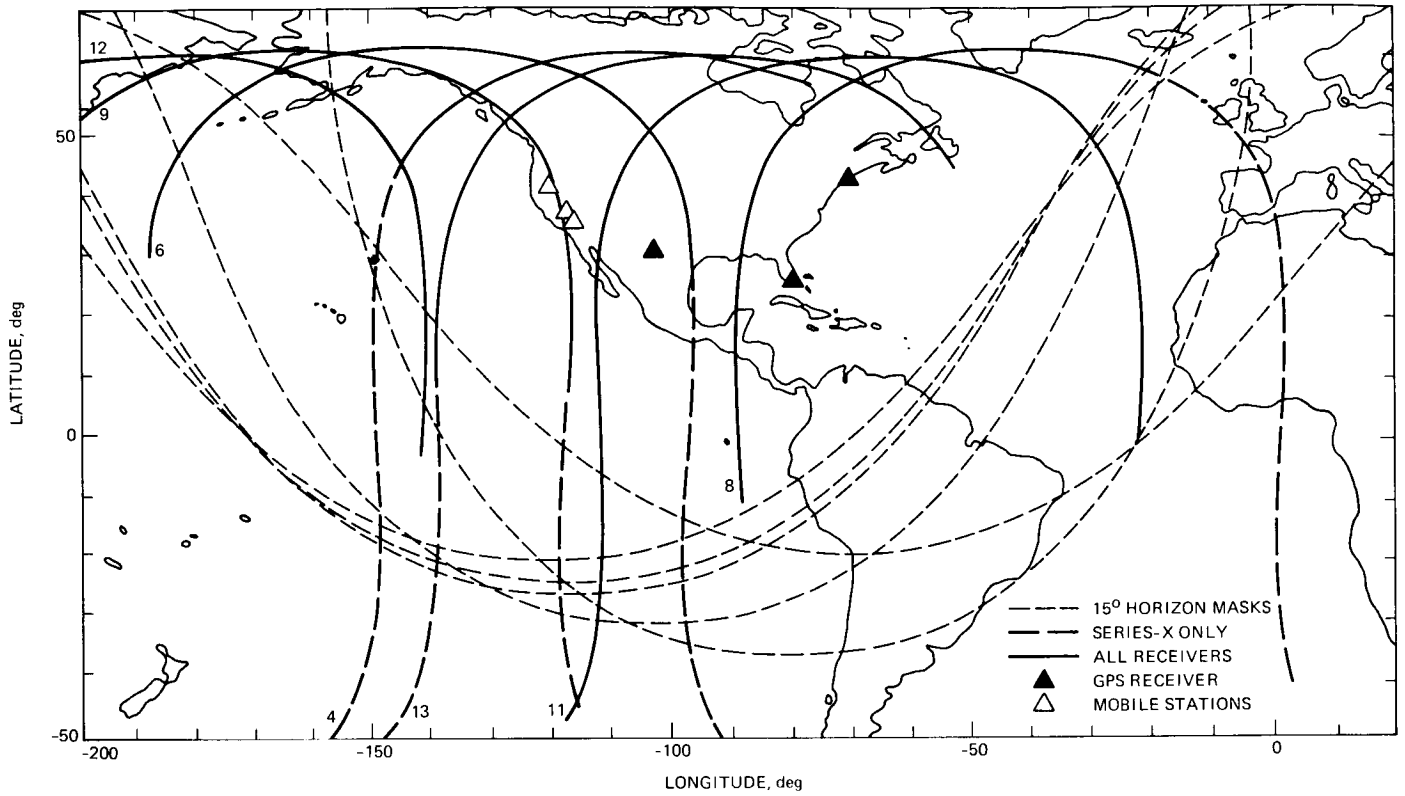


Figure 4. A map of the Western Hemisphere is shown, with stations at Westford, Richmond, Ft. Davis, Mojave, Owens Valley, and Hat Creek indicated. The short dashed lines denote the fifteen-degree horizon masks for these six stations. GPS satellite ground tracks are denoted by solid or long dashed lines. The solid lines indicate when the satellites were scheduled for viewing by all three receiver types; the dashed lines indicated where the satellites were viewed only by the SERIES-X receivers. The GPS satellite number is given at the beginning of each track.

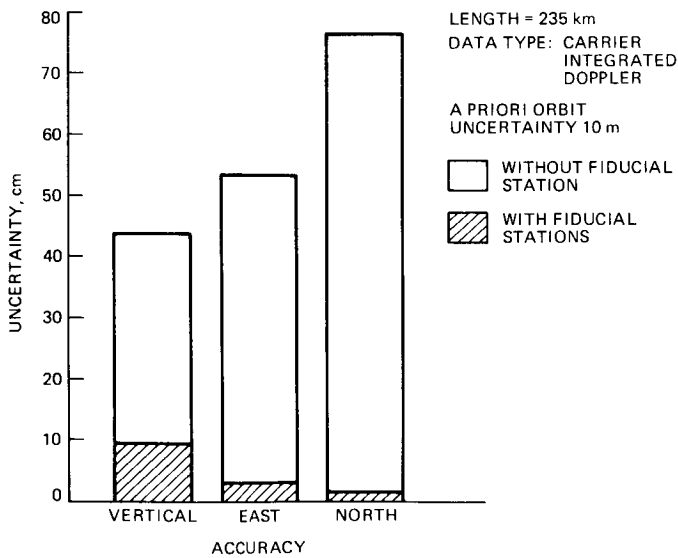


Figure 5. Covariance analysis results show expected baseline accuracies from the March 1985 field tests for the Mojave/Owens Valley baseline. Two scenarios are displayed, illustrating the improvement in accuracy expected as a result of the utilization of a fiducial station network.

TECHNICAL REPORT STANDARD TITLE PAGE

1. Report No. TDA PR 42-85		2. Government Accession No.		3. Recipient's Catalog No.	
4. Title and Subtitle The Telecommunications and Data Acquisition Progress Report 42-85				5. Report Date May 15, 1986	
				6. Performing Organization Code	
7. Author(s) E.C. Posner, ed.				8. Performing Organization Report No.	
9. Performing Organization Name and Address JET PROPULSION LABORATORY California Institute of Technology 4800 Oak Grove Drive Pasadena, California 91109				10. Work Unit No.	
				11. Contract or Grant No. NAS7-918	
				13. Type of Report and Period Covered TDA Progress Report Jan. - Mar. 1986	
12. Sponsoring Agency Name and Address NATIONAL AERONAUTICS AND SPACE ADMINISTRATION Washington, D.C. 20546				14. Sponsoring Agency Code	
15. Supplementary Notes					
16. Abstract This publication, one of a series formerly titled The Deep Space Network Progress Report, documents DSN progress in flight project support, tracking and data acquisition research and technology, network engineering, hardware and software implementation, and operations. In addition, developments in Earth-based radio technology as applied to geodynamics, astrophysics and the radio search for extraterrestrial intelligence are reported. <p style="text-align: center;">ORIGINAL PAGE IS OF POOR QUALITY</p>					
17. Key Words (Selected by Author(s)) Astronautics Communications Mathematical and Computer Sciences Space Science			18. Distribution Statement Unclassified -- Unlimited		
19. Security Classif. (of this report) Unclassified		20. Security Classif. (of this page) Unclassified		21. No. of Pages vi + 218	22. Price